Studies on recently identified activities of the Jumonji-C oxygenase JMJD4 and the bacterial class D nucleophilic serine β-lactamases

Kristina Aertker

Chemistry Research Laboratory

St. Hilda's College, University of Oxford

Michaelmas Term, 2020/21

A thesis submitted to the board of the Faculty of Physical Sciences of the University of Oxford in partial fulfilment of the requirements for the degree of Doctor of Philosophy

ABSTRACT

Studies on recently identified activities of the Jumonji-C oxygenase JMJD4 and the bacterial class D nucleophilic serine β-lactamases

The Jumonji-C oxygenase JMJD4 and the bacterial class D nucleophilic serine β-lactamases (SBLs) have been recently found to catalyse unprecedented cyclisation reactions. Biochemical, biophysical, and inhibition studies were carried out to investigate the formation of β-lactones from carbapenems by class D SBLs, and the JMJD4 catalysed γ-lactam ring formation of eukaryotic release factor 1 (eRF1). **Chapter 1** gives an introduction to the β-lactamase and oxygenase enzyme families to which the class D SBLs and JMJD4 belong, respectively.

The mechanism of β-lactone formation by class D SBLs was investigated through biochemical studies with variants of wild-type OXA-48 and OXA-23 in which active site residues not directly involved in catalysis were substituted (**Chapter 2**). The results reveal that active site residues that interact with the carbapenem-derived C-6 hydroxyethyl side chain impact both activity and product profile. OXA-23 V128L and the clinically observed variant OXA-48 V120L were observed to extend the β-lactone formation activity of class D SBLs to 1β-hydrogen substituted carbapenems.

β-Lactones are capable of re-acylating the nucleophilic serine residues in the active sites of some SBLs and could act as inhibitors. Inhibition studies revealed the Δ^1 imine tautomers of β-lactones derived from meropenem were less potent than their parent carbapenem meropenem (**Chapter 3**). Analyses employing NMR, and mass spectrometry indicated that the complex derived from class D SBLs and β-lactones can (re-)form β-lactones to a greater degree than observed with the corresponding complex derived from carbapenems.

Carbapenems bearing electron-donating and electron-withdrawing C-2 thiophenol side chains were used to investigate the mechanism of class D SBL carbapenemase activity (**Chapter 4**). It was proposed that the electronic properties of this C-2 side chain might influence kinetics and product distribution. The NMR studies showed differences in the turnover rate and the extent of β-lactone formation with carbapenem analogues.

Studies on the human JMJD4-catalysed oxidative γ-lactam ring formation with eRF1 are described in **Chapter 5**. eRF1 is responsible for translation termination and functional studies have shown that hydroxylation of eRF1 improve translation termination efficiency. Although the initial (4*R*)-hydroxylation of eRF1 by JMJD4 is established, less is known about the process by which Lys63 is modified to form a γ-lactam ring. Biochemical studies confirmed that γ-lactam ring formation depends on catalytic activity of JMJD4, and that Fe(II) and 2-oxoglutarate are required for and that *L*-ascorbate promotes its formation. Functional analysis of the mouse JMJD4 orthologue demonstrated that the oxidative γ-lactam ring formation is conserved; however, the yeast orthologue showed only hydroxylation activity.

Overall, the research described in this thesis provides new insights into the molecular mechanisms of β-lactone formation catalysed by class D SBLs and γ-lactam ring formation catalysed by JMJD4.

ACKNOWLEDGEMENT

I would like to thank Professor Christopher J. Schofield for giving me the opportunity to work on fascinating projects under his supervision, guidance, enthusiastic encouragement and the chance to learn from his ideas and curiosity. I would like to express my great appreciation to Christopher T. Lohans for introducing me to the OXA enzyme world and providing incredible guidance, useful critiques and suggestions. I want to thank SABS CDT for funding my work.

Many of my colleagues and collaborators were extremely supportive over the past years with my projects: Warmest thanks to: Professor Wyatt Yue for our regular project exchange and his support with protein production, Suzana Markolovic for introducing me to the JMJD4 world and experimental biochemistry and microbiology, Eidarus Salah for his help with crystallisation trials and protein production, James Wickens, Elisabete Pires, Svenja Hester and Roman Fischer, for their expertise in mass spectrometry, Adam Hardy, Zahn Gower and Jenny Houlsby for making sure that the lab runs smoothly, my students Emily Freeman, Fraula Daka and Ciondi Bess for their contributions, motivation and willingness to learn. A huge thanks to Christopher Lohans, H. T. Henry Chan, John-Paul Bukowski and Chiara Maniaci for proofreading my thesis.

Thanks as well to whole Schofield group for laughter and kindness inside and outside the lab, especially, Joanna Bonnici, Patrick Rabe, Tony (Tongri) Liu, Xiao Liu, Kerstin Lippl and many others. Thank you very much for the support provided by my friends in Oxford including Simon Nadal, Yuliya Dubianok, Daniel Quetschlich and Vilma and Edward Duller and many others. A special thanks to Mpho Makola, Corentine Laurin and Susan Leung for our regular St. Hilda's dinners.

Most importantly, I want to thank my family and Daniel's family for their support during my DPhil studies and my boyfriend Daniel Meusburger for his unwavering encouragement and love.

TABLE OF CONTENTS

ABBREVIATIONS

2OG	2-oxoglutarate
2OG oxygenase	Fe(II)- and 2OG-dependent oxygenases
AEC	Acyl-enzyme complex
ALKBH8	AlkB Homologue 8
AMR	antimicrobial resistance
CAS	clavaminate synthase
CD	circular dichroism
cryo-EM	cryogenic electron microscopy
DHP-I	human renal dehydropeptidase I
DSBH	distorted double-stranded β-helix core fold
DTT	dithiothreitol
E. coli	*Escherichia coli*
EDTA	ethylenediaminetetraacetic acid
eRF1	eukaryotic release factor 1
eRF1-FL	full-length eRF1
eRF1-ND	N-domain of eukaryotic release factor 1
eRF1-ND-30 Da	+30 Da modified N-domain of eukaryotic release factor 1
eRF1-ND+OH	hydroxylated N-domain of eukaryotic release factor 1
eRF3	eukaryotic release factor 3
ESBL	extended-spectrum β-lactamases

ESI	electrospray ionisation
GDP	guanosine diphosphate
GTP	guanosine triphosphate
HEPES	2-[4-(2-hydroxyethyl)piperazin-1-yl]ethanesulfonic acid
His6	polyhistidine-tag
IMP	Imipenem-resistant *Pseudomonas aeruginosa* producing metallo-β-lactamase
IPNS	isopenicillin N synthase
IPTG	isopropyl-β-*D*-1-thiogalactopyranoside
JmjC	Jumonji-C
JMJD	Jumonji domain-containing
K_D	dissociation constant
KDM	histone lysine demethylase
K. pneumoniae	*Klebsiella pneumoniae*
LIC	ligation independent cloning
LC-MS	liquid chromatography mass spectrometry
LC-MS/MS	liquid chromatography tandem mass spectrometry
MBL	metallo-β-lactamase
MDR	multidrug-resistant
MINA53	Myc-induced nuclear antigen 53
mRNA	messenger RNA
MS	mass spectrometry

NAG	*N*-acetylglucosamine
NAM	*N*-acetylmuramic acid
NDM	New Delhi metallo-β-lactamase
NMR	nuclear magnetic resonance
NO66	nucleolar protein 66
NOG	*N*-oxalylglycine
OGFOD1	oxygenase domain-containing protein 1
PBP	penicllin-binding protein
PCR	polymerase chain reaction
PDB	Protein Data Bank
PHD	prolyl hydroxylase domain proteins
PTM	post-translational modification
S. pombe	*Schizosaccharomyces pombe*
SBL	serine β-lactamase
SDM	site-directed mutagenesis
SDS-PAGE	sodium dodecyl sulphate polyacrylamide gel electrophoresis
SEC	size exclusion chromatography
SPE	solid-phase extraction
Tris	2-amino-2-hydroxymethyl-propane-1,3-diol
tRNA	transfer RNA
TYW5	tRNA wybutosine-synthesising protein 5

U2AF65	U2 auxiliary factor 65 kDa subunit
VIM	Verona integron-encoded metallo-β-lactamase
IMP	Imipenem-resistant *Pseudomonas aeruginosa* producing metallo-β-lactamase

Chapter 1 – General Introduction

Part I

1.1 Antibiotic history

In 1928, the activity of penicillin was observed by Sir Alexander Fleming. With the subsequent first clinical use of penicillin to treat human infections in the 1940s, a period of 30 years, known as the golden age of antibiotic drug discovery, led to the development of new classes of antibiotics, which collectively have saved millions of lives (1). The use of antibiotics against infectious diseases is now an essential component of modern medicine. With antibiotics, infectious diseases such as pneumonia, gonorrhoea, or rheumatic fever are normally treatable. In addition, with antibiotic prophylaxis, bacterial infections associated with cancer treatments and invasive surgical procedures can be prevented, lowering the risk of suffering and death.

Clinically used antibiotics operate via a rather limited set of mechanisms of action. These can be grouped based on whether they directly kill bacteria (bactericidal), or inhibit bacterial growth without killing them (bacteriostatic) (2). The specific targets of the major classes of antibiotics range from protein synthesis (macrolides and tetracyclines), DNA replication machinery (quinolones), folic acid biosynthesis (trimethoprim) to cell wall synthesis (β-lactams) (**Table 1**) (3). Due to the development of several highly potent antibacterial classes, it was widely believed that bacterial infections would be managed indefinitely, and so the discovery of new antibiotics became less of a medical need (4, 5). However, even in the 1940s, Sir Alexander Fleming warned that the incorrect use of

antibiotics can lead to the development of resistance (6). This is because bacteria are continuously evolving, resulting in the evolution of antibiotic resistance, so rendering common antibiotics increasingly ineffective. Combating multidrug-resistant bacteria, so-called 'superbugs,' is one of the major challenges of the 21st century.

Table 1. Examples of antibiotic targets and major antibiotic classes (adapted from (7)).

Antibiotic target	**Primary target**	**Antibiotic class**	**Drug**
Folic acid biosynthesis	Tetrahydrofolic acid synthesis pathway	Trimethoprim, sulfonamindes	Co-trimoxazole (trimethoprim and sulfamethoxazole combined in a 1:5 ratio)
Cell wall synthesis	Penicillin-binding proteins	β-Lactams	Penicillins (penicillin, oxacillin), cephalosporins (cefazolin, cefepime), carbapenems (imipenem, meropenem), and monobactams (aztreonam)
	Peptidoglycan precursors (*D*-Ala-*D*-Ala termini)	Glycopeptides, glycolipopeptides	Vancomycin; teicoplanin
DNA repair	Topoisomerase II (DNA gyrase), topoisomerase IV	Quinolones	Nalidixic acid, ciprofloxacin, levofloxacin, and gemifloxacin
Protein synthesis	30S ribosome	Tetracycline, aminoglycosides	Tetracycline, streptomycin, and kanamycin
	50S ribosome	Phenicols, macrolides	Chloramphenicol, erythromycin

1.2 β-Lactam antibiotics

More than half a century after the first clinical use of penicillin, the β-lactam antibiotics remain one of the most important antibiotic classes because of their low toxicity, low cost, and high efficacy (**Figure 1A**) (8). Approximately 62% of all antibiotics consumed globally contain a β-lactam ring, with slight variations of consumption in different countries (1). The clinically used β-lactam antibiotics, which may have narrow or broad-spectrum antibiotic activities, are grouped into four different subclasses: the penicillins, cephalosporins, monobactams, and carbapenems. Whilst the penicillins and cephalosporins are the most widely used classes, their efficacy varies depending on the bacteria being targeted. Monobactams, for which aztreonam is the only clinically available member, are pathogen-specific because they are only effective against Gram-negative bacteria (9). Carbapenems exhibit broad-spectrum activity and high efficacy and are therefore often used as last resort drugs.

Many β-lactam antibiotics are naturally occurring and are produced by different bacterial and fungal species as defences against other bacterial species in the environment. Sir Alexander Fleming accidentally found that the penicillin-producing mould, *Penicillium chrysogenum*, present as a contaminant produced something which killed a culture of staphylococci. Ultimately, this observation resulted in the discovery of the penicillins. This led to the screening of soil and other extracts to identify other antibiotic-producing species, resulting in the identification of other classes of β-lactam antibiotics. The cephalosporin antibiotics were first identified in *Cephalosporium* spp. and later in *Cephalosporium salmosynnematum* (10). All clinically used penicillins or cephalosporins are produced by direct fermentation, or from fermentation derived materials.

A

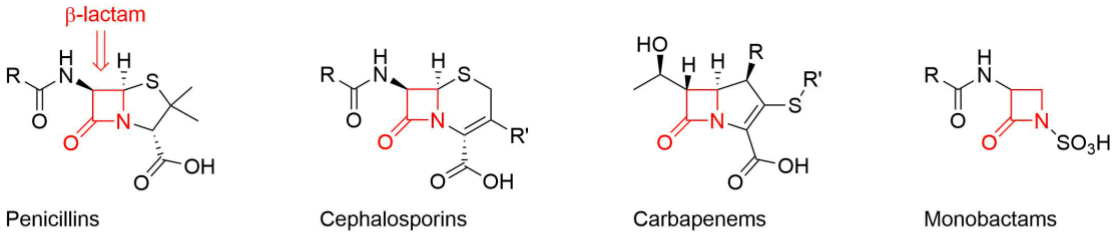

B

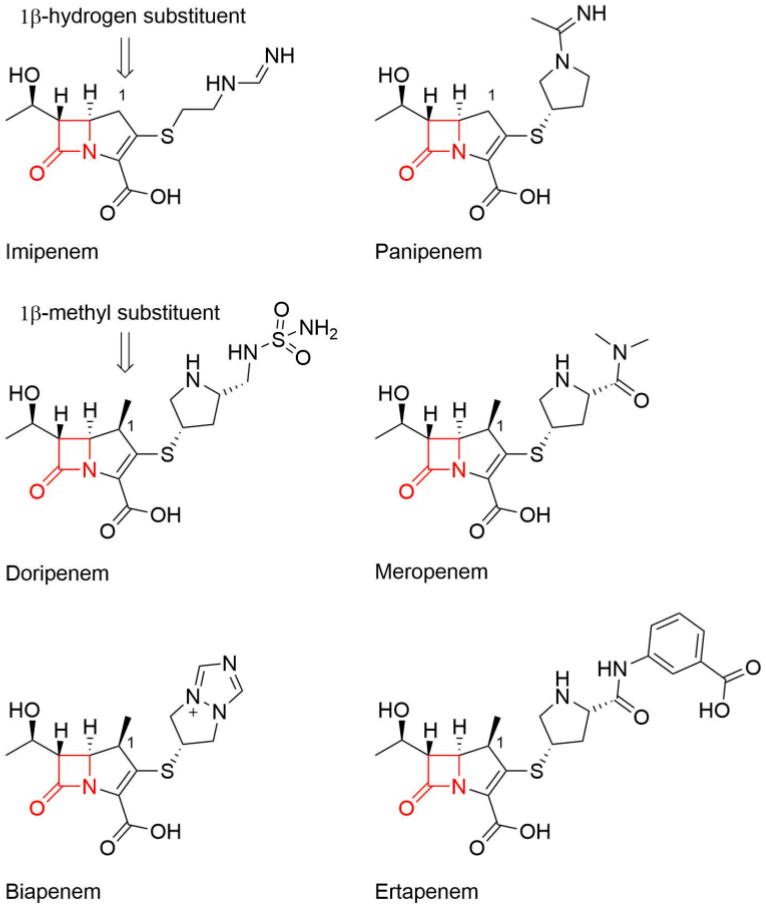

Figure 1. β-Lactam antibiotics. A. General structures of the four major β-lactam antibiotic subclasses: penicillins, cephalosporins, carbapenems, and monobactams. **B.** Chemical structures of important clinically used carbapenems.

The first examples of monobactams were the nocardicins which are produced by *Nocardia uniformis* subsp. *tsuyamanensis* (11). In the 1970s, the extensive screening efforts resulted in discovery of a fourth class of clinically useful β-lactam antibiotics. Thienamycin, a carbapenem with high antibacterial potency, was found in *Streptomyces cattleya*. Due to

the instability of thienamycin, the derivative imipenem was developed (12, 13). As imipenem has low stability in humans due to degradation by the human renal dehydropeptidase I (DHP-I) enzyme, imipenem is prescribed in combination with the DHP-1 inhibitor, cilastatin (14). To overcome this susceptibility to hydrolysis while preserving the high antibacterial potency, more carbapenem analogues were developed. Intrinsic carbapenem stability against DHP-1 was achieved by the introduction of a 1β-methyl substituent (e.g. meropenem, doripenem, ertapenem, and biapenem) rather than a 1β-hydrogen substituent (e.g. imipenem and panipenem) (**Figure 1B**) (14).

1.3 Penicillin-binding proteins

Bacteria have relatively rigid cell walls, which play an essential role in protecting them against hostile environments and tolerating osmotic pressures (15). Bacteria are classified as Gram-positive or Gram-negative bacteria depending on the structure of the cell wall. Gram-negative bacteria are enveloped by two lipid membranes (i.e. the inner membrane and the outer membrane), between which is a thin layer of peptidoglycan in the periplasmic space. The surface of Gram-positive bacteria are encircled by an inner lipid membrane which is surrounded by a thick layer of peptidoglycan (16).

The peptidoglycan layer is typically composed of a network of polysaccharide/glycans motifs, consisting of alternating *N*-acetylmuramic acid (NAM) and *N*-acetylglucosamine (NAG) residues (17, 18). The NAM residues are connected to pentapeptide chains with an often conserved amino acid sequence: *L*-alanine, γ-*D*-glutamic acid, *L*-lysine, *D*-alanine, and *D*-alanine, in which the *L*-alanine is bound to the glycan strands. These glycan strands are crosslinked by peptide chains, forming an interconnected network. These short peptide chains are usually 4,3 cross-linked, such that the fourth amino

acid residue, *D*-alanine, of one peptide chain is covalently connected by a peptide bond to the third amino acid residue, *L*-lysine, of an adjacent peptide chain. The formation of these peptide bonds are catalysed by enzymes known as penicillin-binding proteins (PBPs), which have *D*,*D*-transpeptidase activity (**Figure 2A**). To catalyse the formation of the 4,3-peptidoglycan link, the PBP employs a nucleophilic serine residue. The nucleophilic serine residue of PBP forms a covalent acyl-enzyme complex (AEC) with the fourth residue of a peptide chain, *D*-alanine, releasing the terminal *D*-alanine residue. The third amino acid residue, *L*-lysine of an adjacent peptide chain reacts with this AEC, resulting in the formation of a peptide bond with *D*-alanine, the fourth amino acid residue (**Figure 2A**) (19).

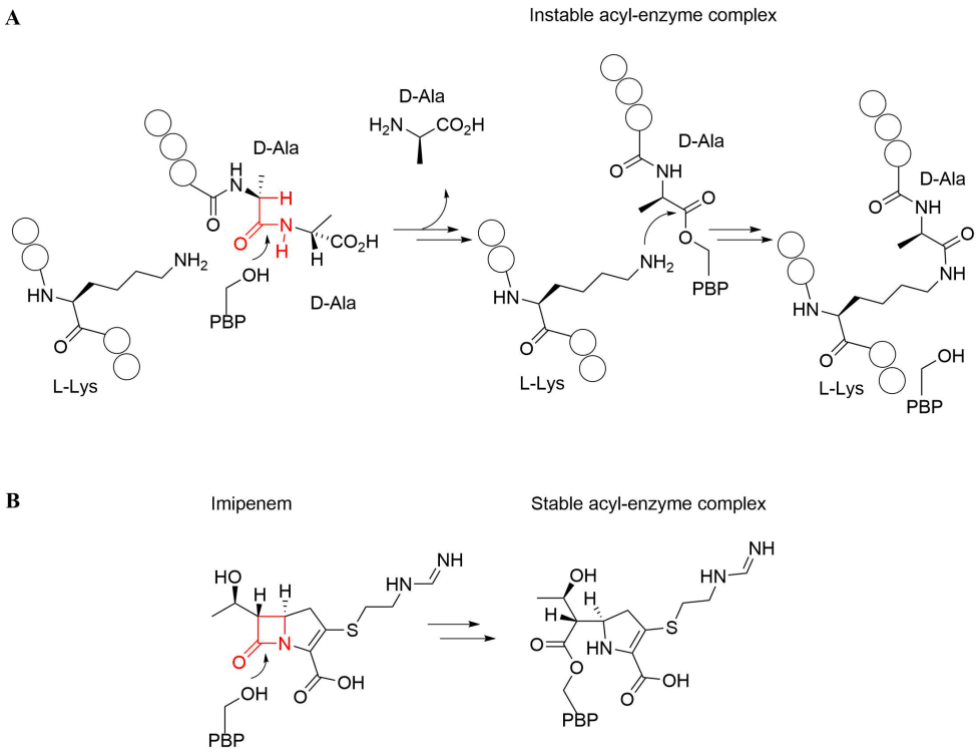

Figure 2. Outline mechanism and inhibition of *D*,*D*-transpeptidases. A. *D*,*D*-Transpeptidase activity of PBPs. **B.** Acylation of the PBP nucleophilic serine residue by the carbapenem imipenem results in (near) irreversible inhibition. The β-lactam ring has been proposed to be a structural mimic of the acyl-*D*-alanyl-*D*-alanine motif according to the Strominger hypothesis (20). Their structural similarity is in red.

PBPs are important antibiotic targets, as their inhibition disrupts cell wall biosynthesis (19, 21). Consequently, without an intact cell wall, bacteria cannot survive. In addition, PBPs are good antibacterial targets due to their location in the bacterial cell, such that antibiotics are not required to reach the cytoplasm to be active. Another advantage of targeting the cell wall is that peptidoglycan does not exist in other organisms such as animals and plants. That implies that the enzymes involved in cell wall biosynthesis do not have close human analogues, decreasing the side effects associated with antibiotics targeting PBPs (22). The main class of antibiotics that target PBPs are the β-lactams, which form irreversible covalent complexes with the PBP nucleophilic serine residues (**Figure 2B**) (23–25). It is proposed that the β-lactam motif is a structural mimic of the natural PBP substrate (a conformationally strained form), resembling the acyl-*D*-alanyl-*D*-alanine terminus occurring in the peptide chains of peptidoglycans (20).

1.4 Antibiotic resistance

As mentioned in **Section 1.1**, bacteria are able to efficiently mutate or undergo horizontal gene transfer, thereby becoming antibiotic-resistant. The current situation is exacerbated, as the identification and development of new antibiotics is quite limited. Consequently, infections caused by multidrug-resistant (MDR) pathogens are emerging, and the number of patients who die of those untreatable infections is growing. The World Health Organisation (WHO) has identified antimicrobial resistance (AMR) as a major global health threat (26).

Innate and acquired resistance mechanisms against β-lactam antibiotics have been identified (27). Innate resistance refers to the natural resistance of specific species to specific antibiotics; acquired resistance may occur by mutations to genes or due to gene transfer

between bacteria (28). There are four general strategies by which bacteria can develop drug resistance. These are: (I) alteration of the drug target, (II) antibiotic efflux pumps, (III) increased cell surface permeability barriers, and (IV) production of enzymes that change or inactivate the drugs.

(I) **Modified PBP genes.** Mutations to the genes that encode PBPs can result in altered PBP enzymes. While these modified PBPs maintain transpeptidase activity, they may demonstrate lower sensitivity to β-lactam antibiotics.

(II) **Decrease in cell permeability.** β-Lactam antibiotics are (normally) relatively hydrophilic small molecules and require nonspecific protein porin channels to travel through the outer membrane of Gram-negative bacteria. Therefore bacteria can achieve resistance by decreasing production of outer membrane porins, or through changes to the structures of these porin channels which impact their interactions with antibiotics (29–31).

(III) **Expulsion of antibiotics by efflux pumps.** A reduction in the concentration of β-lactam antibiotics in the periplasmic space can be accomplished by the export of β-lactams through the outer membrane by proteins known as efflux pumps. There are two underlying mechanisms: the increased production of efflux proteins, or substitutions in the efflux pumps which lead to more efficient transfer of antibiotics out of the bacterial cells (32).

(IV) **β-Lactamases.** β-Lactamases directly inactivate β-lactam antibiotics through a hydrolysis mechanism, preventing them from being able to target PBPs.

The primary resistance mechanisms against β-lactam antibiotics in both Gram-positive and Gram-negative bacteria are different (33). The primary resistance mechanism against β-lactams for Gram-positive bacteria involves the production of modified PBPs with

low affinity for β-lactams (34), while Gram-negative bacteria commonly achieve resistance through production of β-lactamases (33). The production of β-lactamases is often considered a secondary mechanism for Gram-positive bacteria.

1.5 β-Lactamases

The first penicillin-degrading enzyme (from *Escherichia coli* (*E. coli*)) was reported by Sir Edward Penley Abraham and Sir Ernst Borie Chain in 1940 (35, 36), 11 years after the discovery of the antibacterial activity of penicillins, but before their use in the clinic (37). Following the discovery of the β-lactamases, it was initially believed that they did not pose a threat to the clinical applications of β-lactam antibiotics. β-Lactamase-producing bacterial species have probably existed for millions of years, and these enzymes likely represent a natural defence system against β-lactam-producing bacteria (33). However, the potential impact of β-lactamases was probably underestimated until the 1960s. Increased selective pressure on resistance placed upon bacteria, in part caused by the large-scale antibiotic consumption and misuse of antibiotics, has accelerated resistance. To date, more than 5000 β-lactamases have been reported, and the number of such enzymes is continuing to grow at a rapid pace (38). In bacteria, there are chromosomal- (39, 40) and plasmid- (41–43) encoded β-lactamases. The latter contribute greatly to the spread of these encoded β-lactamases between different pathogenic species, accelerating the evolution of resistance.

β-Lactamases catalyse the hydrolysis of β-lactam antibiotics to different extents. Whilst the activity of many early identified β-lactamases is against a few β-lactam antibacterials, the increased use of the β-lactams has driven the production of new or modified β-lactamases with a broader substrate spectrum. One example of these new β-lactamases is the extended-spectrum β-lactamases (ESBLs), which are able to catalyse the hydrolysis of the penicillins, cephalosporins, and monobactams. Serious infections caused

by ESBL-producing organisms can only be treated with last resort drugs like carbapenems. However, bacteria can also become resistant to carbapenems through the production of carbapenem-hydrolysing β-lactamases (i.e. carbapenemases). ESBLs and carbapenemases are common causes of multidrug-resistant infections (44, 45).

β-Lactamases can be categorised according to their structure and mechanism based on the Ambler classification system. The Ambler classification approach had initially divided β-lactamases into two classes: class A, serine β-lactamases (SBLs) and class B, metallo-β-lactamases (MBLs) (**Figure 3**). Later, class A was further divided into classes A, C, and D to differentiate between enzymes which have similar catalytic mechanisms but differ in their structures. Class A, C and D SBLs contain a nucleophilic serine residue in their active sites. This serine reacts with the β-lactam ring to form an AEC, similar to complexes formed by PBPs with β-lactam antibiotics (46, 47). However, the AECs derived from SBLs with β-lactams are generally hydrolysed rapidly, whereas the AECs derived from PBPs are stable.

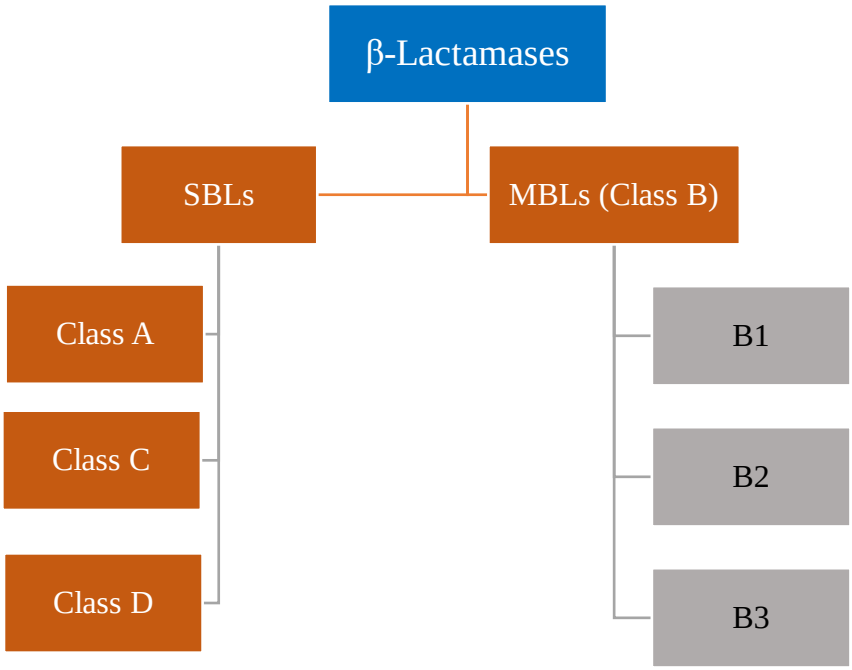

Figure 3. The Ambler structural classification of β-lactamases based on structural and molecular similarities. Classes A, C and D are SBLs and class B are MBLs, with subclasses B1, B2, and B3.

Most class A SBLs (e.g. TEM- and SHV-type enzymes) have penicillinase activity, although some class A enzymes have ESBL activity (44), or even carbapenemase activity, such as the *Klebsiella pneumoniae* carbapenemase (KPC enzymes) (48). In contrast to the class A penicillinases, class C SBLs (e.g. AmpC and CMY enzymes) prefer cephalosporins as substrates (49, 50).

Class D SBLs show a substantial variation in their substrate profiles with penicillins, cephalosporins, and carbapenems. A large group of class D SBLs are referred to as OXA enzymes because they prefer the hydrolysis of oxacillin over other penicillins (51, 52). Several OXA-10 variants with ESBL activity have emerged in *Pseudomonas aeruginosa*, due to a few amino acid substitutions in the parent enzyme OXA-10 (53, 54). The first reported carbapenem-resistant OXA enzyme was OXA-23. In 1985, the carbapenemase OXA-23 was isolated from a patient with an *Acinetobacter baumannii* infection; this was just one year after the clinical introduction of imipenem (55, 56). After carbapenemase activity of OXA-23 was identified, several other OXA enzymes were identified as carbapenemases, including OXA-48 and OXA-655 (variant of OXA-10).

Despite the fact that the carbapenemase activity of most OXA enzymes is relatively low, they are a major threat to the clinical use of carbapenems. That is because carbapenemase-producing bacteria commonly have other resistance mechanisms, and class D SBLs are able to rapidly mutate resulting in new class D variants with improved and/or new activity (57). The most prominent and widespread class D carbapenemase, OXA-48 can occur in *Klebsiella pneumoniae* (*K. pneumoniae*) with other *β*-lactamases and modified protein channels (58, 59).

A. KPC-2 (class A)

B. VIM-2 (class B)

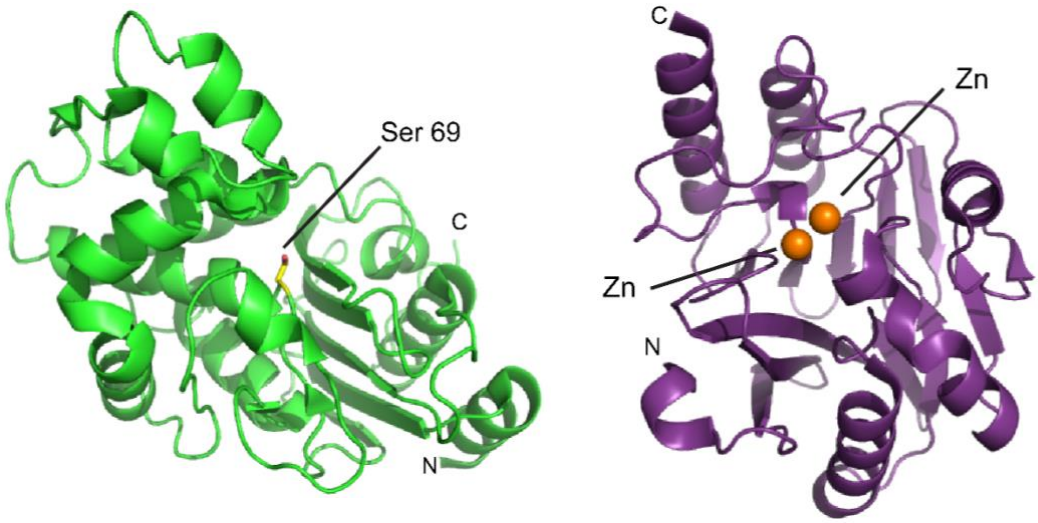

C. AmpC (class C)

D. OXA-48 (class D)

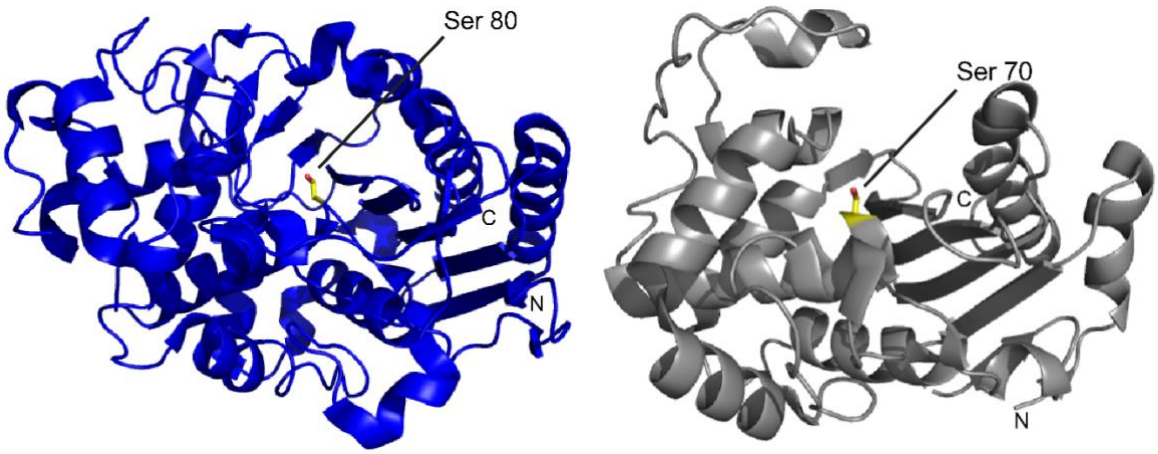

Figure 4. Views from crystal structures of a representative β-lactamase of each Ambler class. A. KPC-2, class A (PDB code: 3dw0) (60), **B.** VIM-2, class B (PDB code: 4nq2) (61), **C.** AmpC, class C (PDB code: 1ke4) (62), **D.** OXA-48, class D (PDB code: 3hbr) (63). The nucleophilic serine residues of KPC-2, Amp-C, and OXA-48 are in yellow and their conformations indicate similarity of these enzymes; however, note that the overall folds are substantially different. VIM-2 employs two zinc ions (orange) in the active site and like other MBLs has a different fold to the SBLs.

In the context of enzyme structure and mechanism, the class B MBLs differ greatly from the three classes of SBLs (**Figure 4**). MBLs have one or two zinc ions in their active sites, which bind hydroxide ions. The hydroxide ions act as a nucleophiles and open the β-lactam rings (64). The zinc-ion coordinated complexes derived from reaction between β-lactams and MBLs is in some ways analogous to the covalent AECs found in SBLs and PBPs. Class B MBLs generally possess a broad-spectrum of activity, and many MBLs are able to efficiently degrade penicillins, cephalosporins, and carbapenems (65). MBLs may be further divided into the B1, B2, and B3 MBL subclasses, which differ in terms of their structures and mechanisms (66, 67). The most well-studied MBLs, which are also of clinical relevance, include Verona integron-encoded metallo-β-lactamase (VIM), Imipenem-resistant *Pseudomonas aeruginosa* producing metallo-β-lactamase (IMP), and the New Delhi metallo-β-lactamase (NDM) (68).

1.6 Carbapenemases

The global rise of carbapenem consumption between 2000 and 2010 was about 45% (1). Carbapenems are often used as last resort antibacterial agents, and their enhanced consumption indicates an increase in the number of serious infections caused by multidrug-resistant Gram-negative bacteria. As a result of the increased clinical use of carbapenems, β-lactamases are emerging which have the ability to inactivate carbapenems, threatening the clinical efficacy of these drugs. From a clinical view, the most important carbapenemases include KPC (class A SBL), NDM (MBL), and OXA-48 (class D SBL) (69). Although all three carbapenemases have been involved in sporadic outbreaks worldwide, they are endemic to different geographical areas. KPC occurs in *K. pneumoniae* in the USA, Israel, Greece, and Italy, NDM arises in *K. pneumoniae* and *E. coli* in India, whereas OXA-48 is

commonly identified in *K. pneumoniae* and *E. coli* in North Africa and Turkey. KPC producers are usually isolated from nosocomial (hospital-acquired) infections, whilst NDM and OXA-48 producing species are often hospital- and community-acquired (70, 71).

1.7 Class D β-lactamases

Class D SBLs currently comprise several subfamilies, representing a broad diversity of amino acid sequences and enzyme activities. For example, OXA-1 has only a 18% sequence identify with OXA-58 (72). Sequence alignment analysis of class D SBLs reveals a high degree of homology in their active sites, and similarities between secondary structure elements (**Figure 5**). The overall structure of these enzymes encompasses two domains, an all helical domain and a mixed domain composed of a central six-stranded antiparallel β-sheet surrounded by α-helices (63, 73–75). The class D active site is deeply embedded between the two domains. At the N-terminus of all class D SBLs is a signal peptide region, which is essential for their secretion into the periplasmic space (76, 77). Sequence alignment also reveals a variety of deletions and insertions at the C- and N-terminus and in different loops. For example, the loop connecting two α-helices α3 and α4, the loop between α-helix α6 and β-strand β5 (known as the omega loop), and the loop linking two β-strands β7 and β8 are often extended or shortened.

Figure 5. Sequence alignment of representative OXA enzymes. α-Helices are in blue, and β-strands are with green arrows. The nucleophilic serine residues and lysine residues involved in catalysis are indicated in red boxes. The alignment was generated by Clustal Omega with the secondary structure elements of OXA-10 (74, 78).

The evolutionary relationship between class A, C, and D SBLs, which may have evolved from a common ancestral protein, is revealed by conserved active site elements (79). In class D SBLs, the active site nucleophilic serine and a conserved lysine residue are located in a S-X-X-K (X = any amino acid) tetrad motif located at the N-terminal end of α-helix α3. Analogous serine and lysine residues are also found in the active sites of class A and C β-lactamases (**Figure 6**). Notably, in class D SBLs, this lysine residue is carbamylated, and acts as a general acid/base during catalysis (**Figure 6B**). Protein carbamylation occurs when a lysine residue reacts with carbon dioxide/bicarbonate. The active site has a strong hydrophobic character, which is proposed to lower the pK_a of the

protonated lysine ε-amino group, thereby stabilising the carbamylated lysine (80). One of the residues contributing to the hydrophobic active site is a conserved valine residue (i.e. Val120 in OXA-48), which is located near the carbamylated lysine residue. By contrast, a hydrophilic asparagine residue occurs in a similar position in class A and C SBLs (e.g. Asn132 in class A SBL TEM-1 and Asn152 in class C SBL AmpC) (81). Crystallographic studies of class D SBLs have revealed that the carbamylated lysine is further stabilised by interactions with the side chain of the nucleophilic serine residue and a highly conserved tryptophan residue (82). The tryptophan residue is located in the loop between α-helix α6 and β-sheet β5, which is named the omega loop (82, 83). Class A SBLs employ the same conserved lysine and a glutamic acid residue as a general acid/base catalyst, while class C SBLs use a tyrosine residue which interacts with the conserved lysine residue (**Figure 6A, C**) (84, 85).

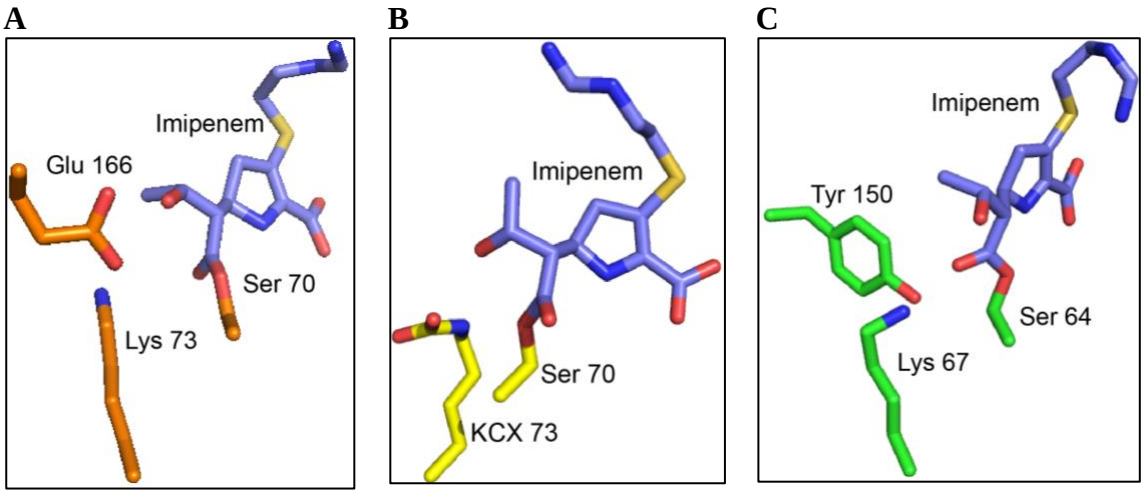

Figure 6. Comparison of SBL active site residues involved in catalysis. While all class A, C and D β-lactamases employ a nucleophilic serine residue, they use different complementary general acid/base residues. **A.** View of the active site of TEM-1 in complex with imipenem (PDB code: 1bt5) (86). **B.** View of the active site of OXA-48 in complex with imipenem (PDB code: 5qb4) (87). **C.** View of the active site of AmpC in complex with imipenem (PDB code: 1ll5). In class A SBLs different residues, including the conserved lysine residue and a glutamic acid residue, can contribute to acid/base catalysis. In class C SBLs, a tyrosine residue and the conserved lysine residue may be responsible for the general acid/base catalysis. In class D SBLs, the conserved lysine residue is carbamylated and acts as general/acid residue.

In spite of their different active site residues, SBLs are generally thought to degrade all three classes of β-lactams through broadly similar hydrolytic mechanisms (through fragmentation of the AECs can occur). However, the Schofield group has recently reported that class D SBLs degrade carbapenems to form the classical hydrolysis products in addition to previously unidentified β-lactones (88). While the acylation step is similar, the deacylation step bifurcates between hydrolysis and lactonisation pathways for carbapenems and class D SBLs. **Figure 7** shows the mechanism of the proposed acylation and deacylation steps during carbapenem degradation by class D SBLs. The following steps are proposed:

(A) Non-covalent binding of the carbapenem to the enzyme occurs; in the acylation step, the nucleophilic serine reacts with the carbonyl group of β-lactam ring.

(B) An anionic tetrahedral intermediate of the acylation step is formed, in which proton transfer occurs to the nitrogen atom of β-lactam ring.

(C) An AEC is formed. The carbapenem C-6 hydroxyethyl side chain may occur in different conformations, determining which products are formed.

(D) **(1)** Activated by the carbamylated lysine, the hydrolytic water molecule in the active site reacts with the ester carbonyl group. **(2)** Alternatively, the hydroxyl group of the C-6 hydroxyethyl side chain can undergo nucleophilic attack onto the ester carbonyl group to give a β-lactone ring.

(E) **(1)** **(2)** An anionic tetrahedral intermediate during the AEC hydrolysis or β-lactone is formed.

(F) **(1)** **(2)** Hydrolysed carbapenem and/or β-lactone is released; the β-lactone is able to react reversibly with the nucleophilic serine residue.

Interestingly, inhibition studies indicated that some β-lactones have inhibitory activity against some class D SBLs, although their potency is less than that of the parent carbapenems (88).

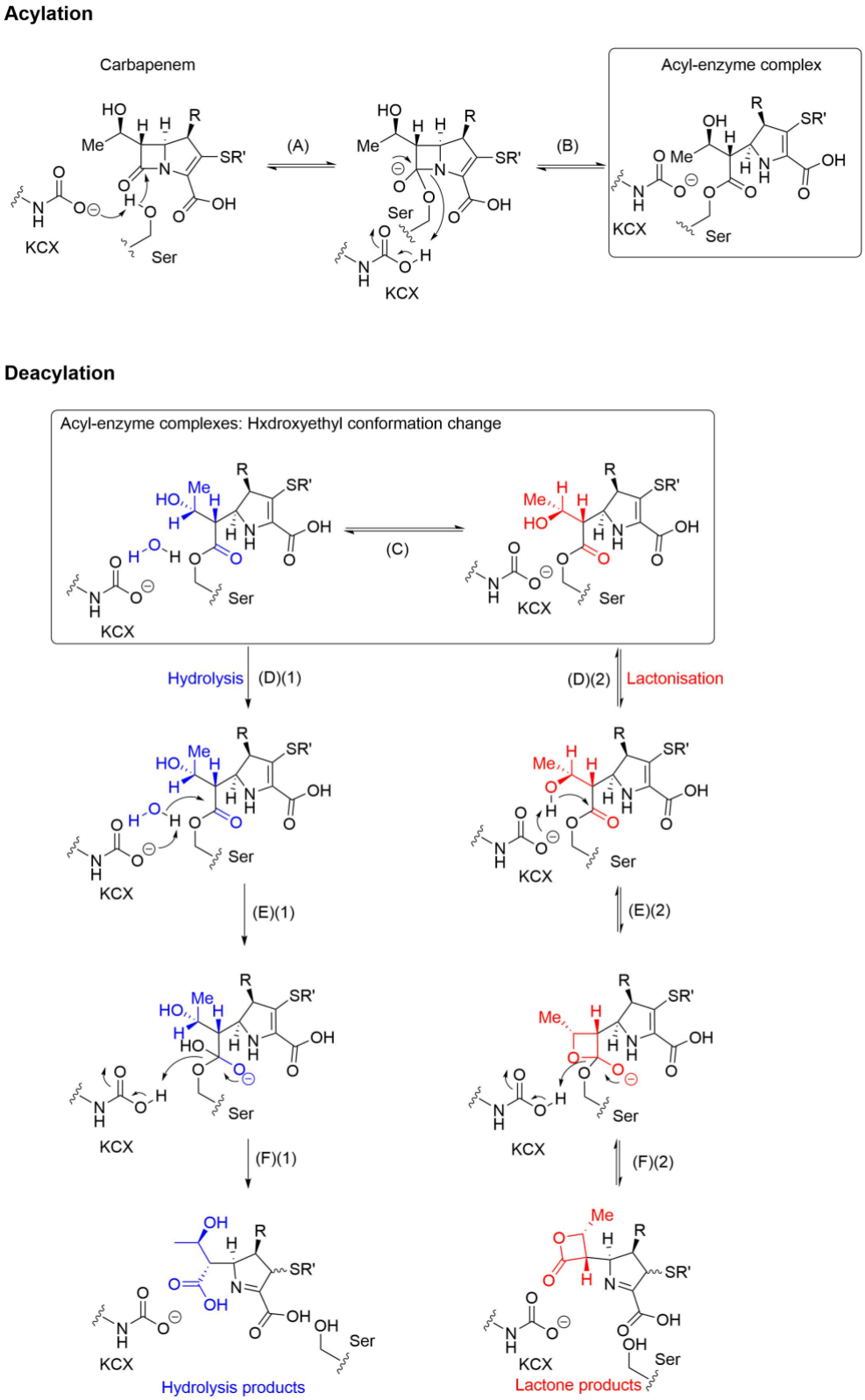

Figure 7. Outline of the proposed class D SBL carbapenem degradation mechanisms. The nucleophilic serine and carbamylated lysine residues in the active site are directly involved in catalysis. (**A**) and (**B**) show the reaction of carbapenem with the nucleophilic serine, forming the AEC. Subsequent deacylation is divided into hydrolysis and lactonisation pathways (**C**)-(**F**). Note that degradation of the AEC is proposed to be the rate limiting step of catalysis (89).

In the crystal structures of many class D SBLs, a hydrophobic bridge is observed. This involves the α3-α4 and β6-β7 loops located at the entrance of the active site (**Figure 8**). In the OXA-23 active site, a phenylalanine residue in the α3-α4 loop and a methionine residue in the β6-β7 loop form a hydrophobic bridge on the enzyme surface (90). However, OXA-48 and its variants belong to the only OXA subfamily which does not possess such a hydrophobic bridge. It is proposed that this hydrophobic bridge is involved in the binding of substrates/intermediates and in determining substrate selectivity (91).

A **B**

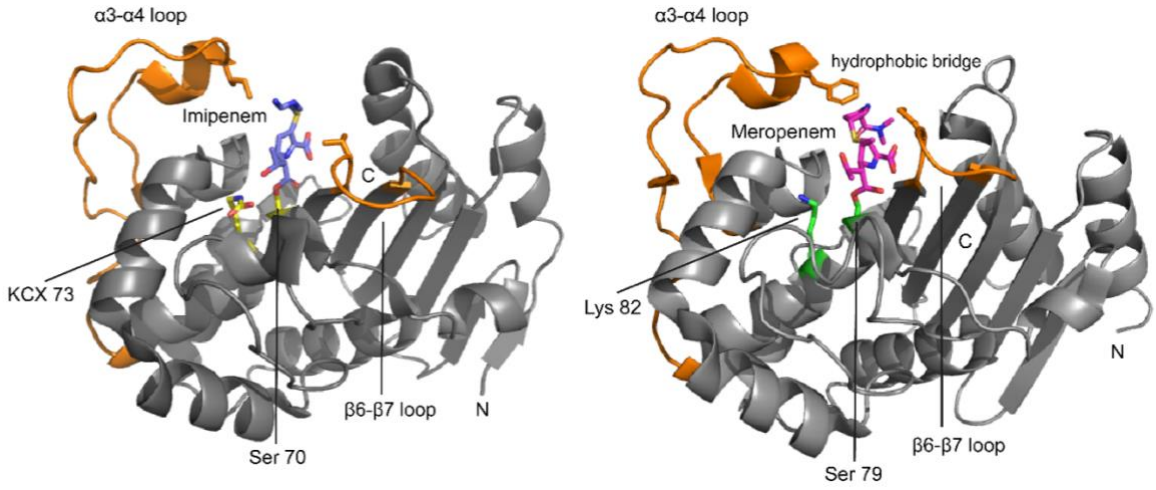

Figure 8. Comparison of the overall architecture of OXA-48 and OXA-23. A. Structural view of OXA-48 in complex with imipenem (PDB code: 5qb4) (87). **B.** Structural view of OXA-23 in complex with meropenem (PDB code: 4jf4) (90). The α3-α4 and β6-β7 loops in both crystal structures are in orange.

OXA enzymes typically occur in monomeric and dimeric forms. Most of the class D SBLs (e.g. OXA-10 and OXA-48) are dimeric and some enzymes (e.g. OXA-1 and OXA-24/40) exist principally in a monomeric form (92). As observed crystallographically, in the case of OXA enzymes, the dimer-dimer interface occurs between α-helix α8 and β-strand β6 of the two respected proteins (74). A broad range of dissociation constants have been reported for the OXA dimer/monomer equilibrium (92–94). The dimer/monomer dissociation constant (K_D) for OXA-10 was in the micromolar range, while for OXA-48 a

higher dimer affinity was found (<700 pM). The dimer affinity for OXA-10 can be enhanced by cations which bind at the dimer-dimer interface. Moreover, *in vivo* studies have revealed that the concentration of OXA-10 in two clinical strains of *Pseudomonas aeruginosa* was between 4–15 μM, indicating that the enzyme is present as a dimer under physiological conditions (93).

Biochemical studies on the class D SBLs have revealed biphasic burst kinetic behaviour with some β-lactams (95). Kinetic studies have led to the proposal that this biphasic behaviour can be attributed to the dimer/monomer equilibrium, as the dimer form is more active than the monomer form (94, 95). An alternative proposal suggests that the biphasic kinetic behaviour relates to an induced conformational change in the enzyme that occurs after substrate binding (93).

1.8 Objectives of the work described in Part I of this thesis

The class D SBLs play an important role in resistance against β-lactam antibiotics in Gram-negative bacteria. The recent discovery of β-lactones as carbapenem degradation products formed by class D SBLs, exemplifies the possibility of new discoveries in the mechanisms of clinically important class D SBLs. Therefore, a detailed understanding of the carbapenem degradation by class D SBLs is of clinical and basic science interest. In **Chapter 2** a mechanistic study on the two clinically important carbapenemases OXA-48 and OXA-23 is presented. The work aimed to develop an understanding of the factors involved in determining the balance between hydrolysis and β-lactone formation pathways.

Carbapenem-derived β-lactones can acylate class D SBLs and act as weak inhibitors (88). However, the inhibition of other SBLs and MBLs by carbapenem-derived β-lactones has not been studied. The work described in **Chapter 3** comprises an inhibition study on a panel of SBLs and MBLs and mechanistic work with β-lactones and class D SBLs.

The tautomerisation state of the carbapenem-derived pyrroline ring elements in the AECs derived from class D SBLs and carbapenems impact on carbapenemase activity. In **Chapter 4** new carbapenem analogues were tested with the aim of influencing the tautomerisation of carbapenem pyrroline ring during class D SBLs catalysis.

Part II

1.9 2-Oxoglutarate-dependent oxygenases

2-Oxoglutarate- and non-heme iron-dependent oxygenases (2OG oxygenases) belong to an enzyme superfamily that play important role in variety of biological functions, including collagen biosynthesis, DNA repair, DNA replication, transcriptional regulation, antibiotic biosynthesis, and protein translation (96–99). In animals and humans 2OG oxygenases are known to catalyse hydroxylation (e.g. lysyl hydroxylation) and/or demethylation (via hydroxylation) reactions of highly diverse substrates, e.g. nucleic acids, proteins, and small molecules (96, 97). In plants and microorganisms 2OG oxygenases catalyse a wide range of reactions, including halogenations, oxidative ring formations, and epimerisations of both small molecules and oligomers (100–104). Recent studies have controversially suggested that two human lysyl hydroxylases, Jumonji domain-containing 5 and 7 (JMJD7 and JMJD5) are endopeptidases and exopeptidases that cleave histones with methylated arginine and lysine residues (105, 106).

1.10 Structure and mechanism of 2OG oxygenases

There are about 60 human 2OG oxygenases in the human proteome. They can be classified according to their structures into two subfamilies, the Jumonji-C (JmjC) and the non-JmjC oxygenases (107, 108). JmjC oxgenases consist of JmjC hydroxylases and JmjC demethylases (KDMs) 2-7. The JmjC hydroxylases have been reported to catalyse the hydroxylation of proteins on amino acid residues lysine, asparagine, histidine and aspartic acid, and hydroxylation of nucleotides, e.g. tRNA. KDMs are thought to primarily catalyse N^{ε}-methyl lysine demethylation of methylated histones and, possibly, non-histone proteins. In some cases JmjC oxygenases show new N^{ω}-methyl arginine demethylation activity (109–

111). Jumonji domain- containing 6 (JMJD6) is reported to be a hydroxylase and more controversially, a demethylase (110, 112). Extensive biochemical work, including NMR and MS studies in Oxford provide evidence that recombinant JMJD6 acts as a lysyl C-5 hydroxylase with activity on different substrates, including U2AF65, RBM39, and LUC7L2 (113, 114).

2OG oxygenases have a distorted double-stranded β-helix core fold (DSBH, also described as a jelly-roll fold) which supports the active site (115, 116). The DSBH fold is comprised of two anti-parallel β-sheets made from 8 β-strands. The Fe(II) and 2-oxoglutarate (2OG) binding residues are sandwiched between the two β-sheets (**Figure 9**). The Fe(II) is commonly coordinated by two histidine residues and one carboxylate group from an aspartate/glutamate residue in a triad motif HX(D/E) … H (117). 2OG coordinates the Fe(II) in a bidentate manner and interacts via its C-5 carboxylate group with a basic active site residue. These active site residues binding 2OG C-5 carboxylate group can differ for JmjC and non-JmjC oxygenases. The JmjC oxygenases typically bind the 2OG carboxylate group with a lysine residue, whereas the non-JmjC oxygenases typically use an arginine residue for the 2OG stabilisation (115). Further variations are that JmjC oxygenases have additional domains. For example, a common structural feature of the JmjC oxygenases is N-terminal β-strands, which does not occur in non-JmjC oxygenases (118).

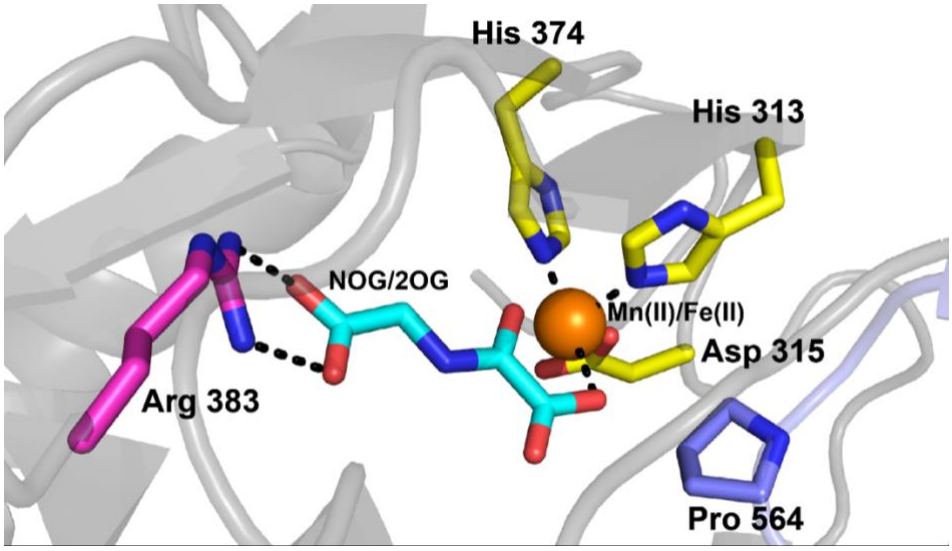

Figure 9. Conserved active site of 2OG oxygenases. View of an active site of a prolyl hydroxylase domain 2 (PHD2) complex (PDB code: 3hqr) (119). Mn(II) (orange), substitutes for Fe(II), and has an octahedral coordination. N-Oxalylglycine (NOG, cyan), substitutes for 2OG, binds in a bidentate manner to the Mn(II) and with the C-5 NOG/2OG carboxylate group to the arginine residue (Arg383, pink). A triad of residues including His 374, His 313 and Asp 315 and water (not shown) also coordinate Mn(II). This figure was adapted (120).

2OG oxygenases utilise 2OG and dioxygen, as co-substrates and Fe(II) as a co-factor to catalyse the two-electron oxidation of a wide range of substrates. Mechanistic studies on 2OG oxygenases have led to a consensus catalytic mechanism for the superfamily (104, 121) (**Figure 10**). Initially, 2OG binds in the active site and coordinates with Fe(II) in a bidentate manner resulting in a ternary complex (enzyme:Fe(II):2OG complex). Subsequent substrate binding leads to loss of a water ligand which was coordinated to the Fe(II), and allows coordination/binding of atmospheric dioxygen. Dioxygen binding enables the oxidation of Fe(II) to Fe(III) and the subsequent decarboxylation of 2OG giving succinate and carbon dioxide, which results in further oxidation of the iron to a reactive Fe(IV)=O intermediate.

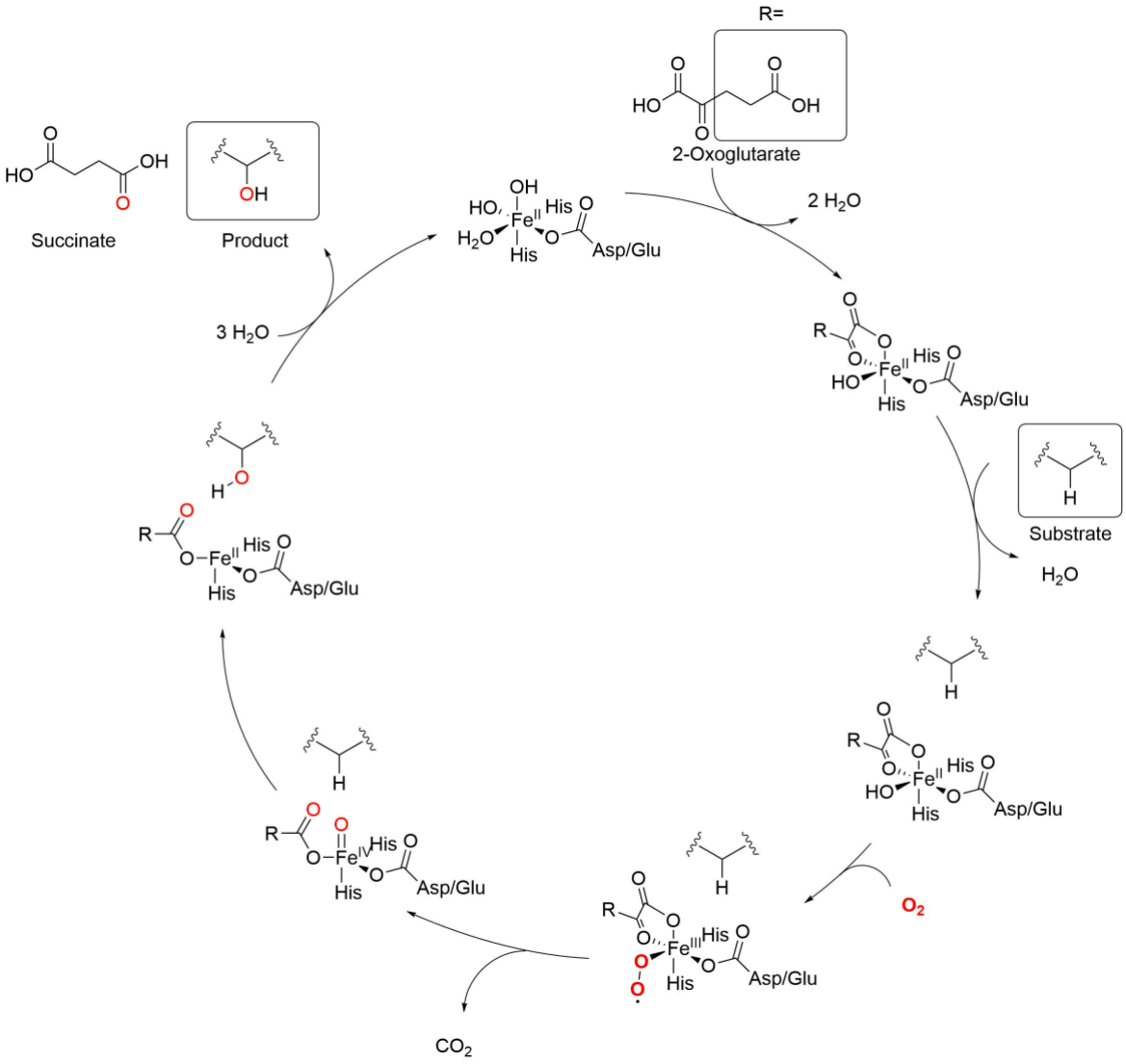

Figure 10. Simplified, proposed mechanism for the 2OG oxygenases. In the mechanism Fe(II) is octahedrally ligated by a triad of residues (two histidine residues and an aspartate/glutamate residue), 2OG, and water. Upon substrate binding, the water is displaced and dioxygen reacts with Fe(II) resulting in the reactive Fe(IV)=O intermediate. The Fe(IV)=O intermediate oxidises unreactive C-H group of prime substrates resulting in hydroxylated or demethylated products.

The Fe(IV)=O intermediate reacts with the prime substrate via a two-electron radical mechanism. The two-electron radical mechanism involves that the Fe(IV)=O intermediate abstracts a hydrogen atom from the prime substrate resulting in a Fe(III)-OH species and substrate radical and then the substrate radical reacts with the Fe(III)-OH species yielding the hydroxylated product. In the case of hydroxylation, the hydroxylated product and succinate are released from the active site. While demethylation of methylated lysine or

arginine residues occurs via an unstable hemiaminal intermediate. The hemiaminal intermediate spontaneously fragments into the demethylated product and formaldehyde.

1.11 2OG oxygenases involved in protein translation

Hydroxylation is one of the most abundant post-translational modifications (PTMs) in the human proteome (97, 122). Despite the small size of this PTMs, it has important functions in a range of biological processes. Eight human 2OG oxygenases play crucial roles in the regulation of protein biosynthesis, e.g. at the translational level (123–128). There are two tRNA hydroxylases: tRNA wybutosine-synthesising protein 5 (TYW5) and AlkB Homologue 8 (ALKBH8), three ribosomal protein hydroxylases: Myc-induced nuclear antigen 53 (MINA53/RIOX2), nucleolar protein 66 (NO66/RIOX1), and oxygenase domain-containing protein 1 (OGFOD1), a lysyl demethylase KDM4A and two lysyl hydroxylases, Jumonji domain-containing 4 (JMJD4) and Jumonji domain-containing 7 (JMJD7). All these 2OG oxygenase, except for ODFOD1 belong to the JmjC oxygenase subfamily.

1.12 Protein translation termination

Protein translation involves a complex machinery in which a messenger RNA (mRNA) molecule is decoded into a specific polypeptide sequence. The process is mediated by ribosomes which are located in the cytosol or attached to the endoplasmic reticulum. The translational process is organised into three phases: initiation, elongation, and termination (129). After the initiation phase the polypeptide sequence is extended by recruitment of an aminoacyl-transfer RNA (tRNA) bearing a specific amino acid. The interaction between an

anticodon, a region of the tRNA with a specific codon of mRNA mediates the elongation of the amino acid sequence. The termination of the translation takes place when a stop codon is found in the ribosomal aminoacyl site (A) site (**Figure 11**). The stop codons are not recognised by a tRNA but are recognised by class 1 eukaryotic translation terminating factor 1 (eRF1) (130, 131). eRF1 occurs in a ternary complex with eukaryotic release factor 3 (eRF3) and guanosine triphosphate (GTP). When eRF1 detects a stop codon in the ribosomal A site, GTP is hydrolysed by eRF3, forming guanosine diphosphate (GDP). eRF1 then promotes hydrolysis of the peptidyl-tRNA ester bond, resulting in release of the nascent polypeptide chain. Finally, ribosome/mRNA complex disassembly follows. In eukaryotic cells, the eRF1 interacts with all three stop codons (UAA-ochre, UAG-amber and UGA-opal), whereas in prokaryotic cells, there are two prokaryotic class 1 release factors (RF1 and RF2) with preferred stop codons. RF1 binds to UAA and UAG and RF2 binds to UAA and UGA mRNA stop codons, respectively (132).

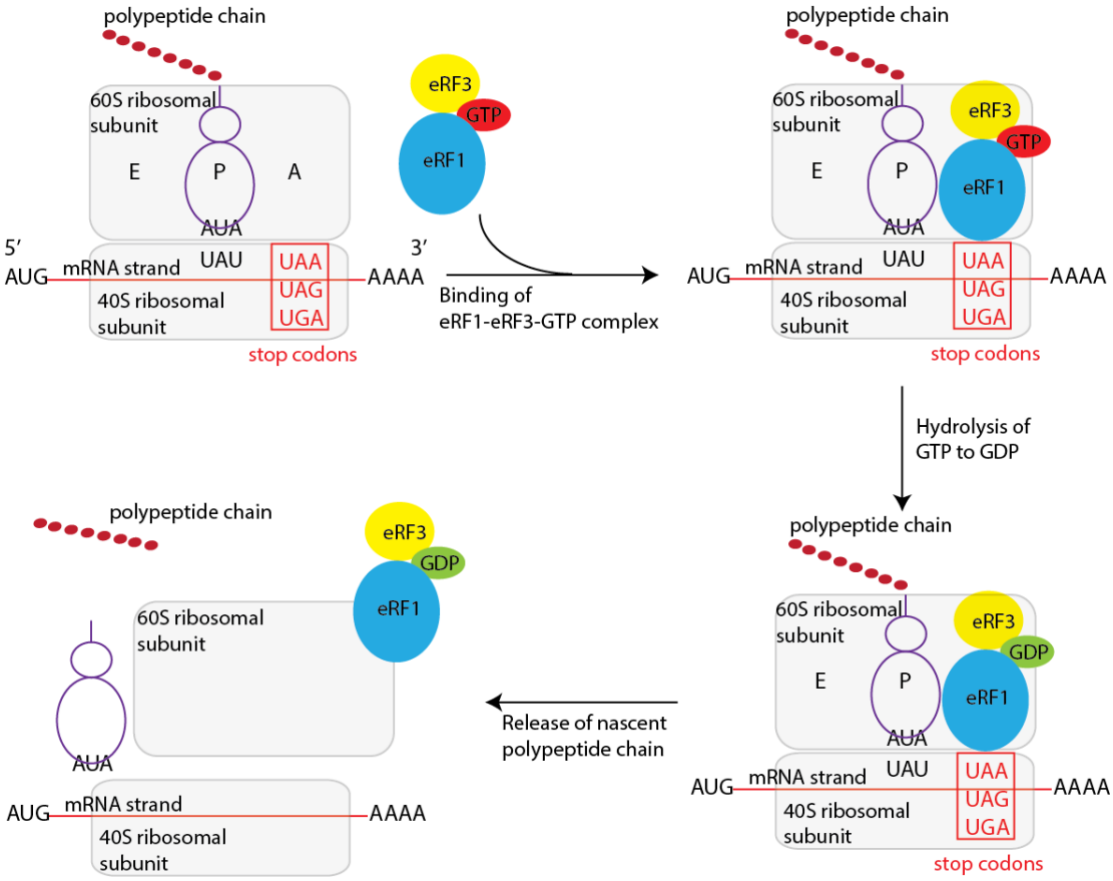

Figure 11. Schematic illustration of the termination step of translation, as mediated by the eRF1-eRF3-GTP ternary complex. Recognition of the stop codons by the eRF1-eRF3-GTP ternary complex in the ribosomal A site, followed by release of the synthesised polypeptide chain by hydrolysis.

1.13 Class 1 eukaryotic translation termination factor 1 (eRF1)

eRF1 mimics the tRNA in the ribosomal A site to trigger termination of protein synthesis. eRF1 comprises of three domains, i.e. N-terminal (N-), middle (M-), and C-terminal (C-) domains (133) (**Figure 12**). The N-domain contains stop codon binding sites (134), M-domain support the release of the polypeptide chain (135, 136), and C-domain interacts with eRF3 (137, 138) . In the N-domain, the highly conserved $NIKS_{61-64}$, GTS_{31-33}, and $YxCxxxF_{125-131}$ motifs can recognise all three stop codons. Amino acid substitution of Ile62, Lys63, and Ser64, which are part of the NIKS motif cause decreased eRF1 ribosome binding and eRF1 activity (139). More detailed information about the function of the NIKS motif was provided by cross-linking experiments. Lys63 of the NIKS motif was crosslinked

with the invariant uracil of all three stop codons (134), which suggest that this residue is responsible for binding and recognition of invariant uracil in the first position of the stop codon. Additional cross-linking studies revealed that the second and third positions of the stop codon are recognised by GTS_{31-33} (140, 141) and $YxCxxxF_{125-131}$ (141).

A better understanding of the translation termination complex and its network of interactions was provided by a cryogenic electron microscopy (cryo-EM) structure of the pre-termination complex. The cryo-EM structure of a human ribosomal pre-termination complex containing eRF1-eRF3-GTP analogue complex revealed the interaction of N-domain of eRF1 and the decoding centre of the 40S ribosomal subunit (138). In addition, NMR structural studies suggest rearrangement of the N-domain of eRF1 facilitates ribosome binding (142, 143).

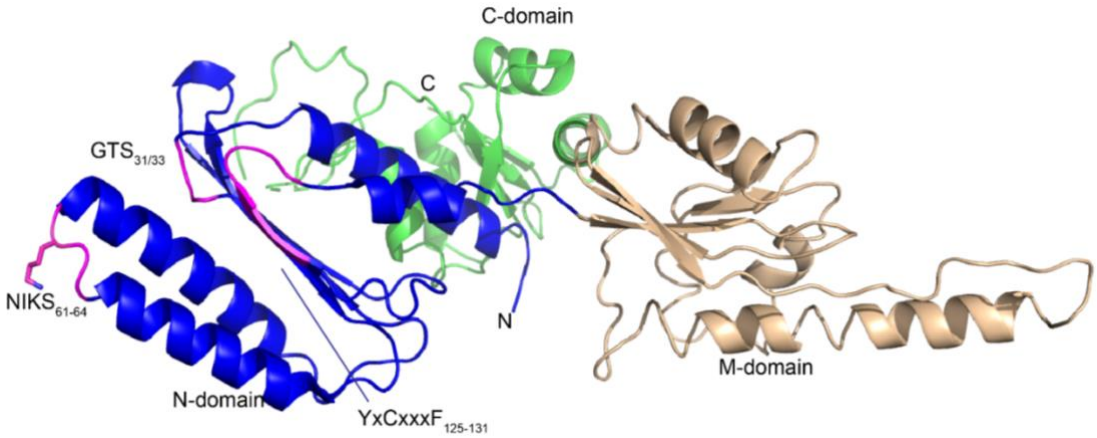

Figure 12. View from a crystal structure of full-length of eRF1 (PDB code: 1dt9) (133)**.** eRF1 contains three different domains: N-domain (in blue), M-domain (beige) and C-domain (green). The stop codon binding motifs are in pink.

1.14 JMJD4

JMJD4 is reported to catalyse C-4*R* hydroxylation of the lysine residue, Lys63 of the eRF1 (**Figure 13**) (144, 145). In human cell lines, e.g. HEK293T, A549, and U2OS and various mouse tissues over 90% of eRF1 was observed to be hydroxylated (measured by

MS-based techniques), showing that the majority of cellular eRF1 contains this PTM. A cell-based stop codon readthrough reporter assays, i.e. Renilla:stop:firely luciferase assays were performed using siRNA-mediated knockdown of eRF1 or JMJD4 expression in HeLa cells. The knockdown of eRF1 and JMJD4 resulted in promoted readthrough of all three stop codons. A complimentary translation kinetic assays revealed that hydroxylation of eRF1 (> 60%) increased translation termination efficiency relative to wild-type eRF1 and eRF1 K63R variant. This observation suggests that JMJD4 regulates translation termination by hydroxylation of eRF1.

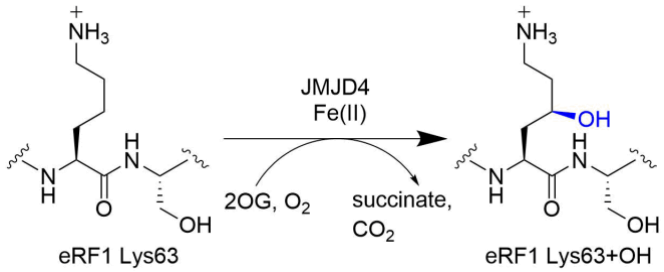

Figure 13. (4*R*)-hydroxylation of the lysine residue, Lys63 of eRF1 is catalysed of JMJD4.

In a disease related context, it was found that the Jmjd4 gene is amplified in cancer types, including breast, liver, and codon carcinomas (146, 147). However, further investigations are required to validate the role of JMJD4 in cancer. Jmjd4-knockout mouse studies suggest that the Jmjd4 gene is not essential for normal animal development and therefore could be an attractive therapeutic target (148).

Recent unpublished NMR structural data of eRF1 show that beyond the JMJD4-catalysed hydroxylation of eRF1, JMJD4 can further modify eRF1 resulting in an oxidative γ-lactam ring formation (**Figure 14**) (149), this modification is the focus of the work described in this thesis and is further described in **Chapter 5**.

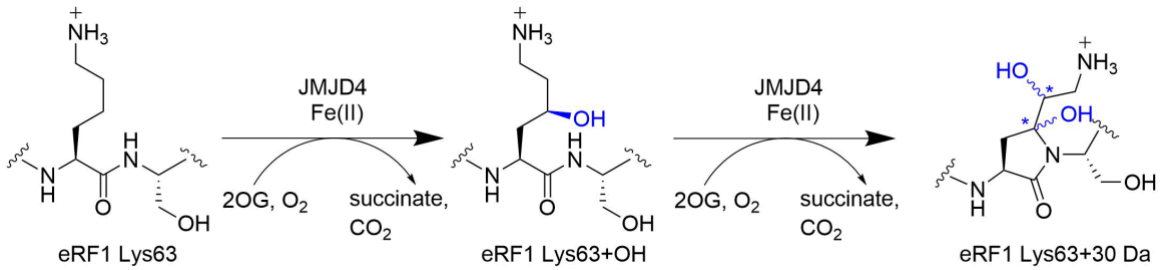

Figure 14. Two JMJD4-catalysed reactions: hydroxylation (eRF1+OH) and γ-lactam ring formation (eRF1+30 Da).

1.15 Objectives of the work described in Part II of this thesis

In animals, 2OG oxygenases catalyse the hydroxylation and/or demethylation of substrates in diverse biological processes including protein biosynthesis, oxygen sensing and gene expression. Beyond animals, 2OG oxygenases can catalyse halogenation, rearrangements, and oxidative ring formations. In Schofield group a new modification of eRF1 in presence of human JMJD4 is formed. The protein modification was identified as γ-lactam ring. The objectives of **Part II** of the work described in this thesis which are presented in **Chapter 5** were:

a. To validate the finding that the γ-lactam ring formation is catalysed by JMJD4 and investigate its co-substrate/co-factor dependency.
b. To conduct mechanistic studies on γ-lactam ring formation.
c. To evaluate if the hydroxylation and γ-lactam ring formation are conserved in the evolutionary process by using JMJD4 and eRF1 orthologues from *Mus musculus* (mouse) and from *Schizosaccharomyces pombe* (*S. pombe*, fission yeast).
d. To use physiologically related conditions to investigate γ-lactam formation as human PTM.

Chapter 2 – Mechanistic studies of class D serine β-lactamase catalysed β-lactone formation

Much of the work described in this chapter has been published and can be found in a modified form in Aertker, K. M. J., Chan, H. T. H., Lohans, C. T., and Schofield, C. J. (2020) Analysis of β-lactone formation by clinically observed carbapenemases informs on a novel antibiotic resistance mechanism. *J. Biol. Chem.* 295, 16604–16613.

2.1 Introduction

2.1.1 Class D SBLs with carbapenemase activity

Carbapenems are an important antibacterial β-lactam containing drug class, which are often used to treat multidrug-resistant infections (52). Class D SBLs, especially OXA-48, are a major threat due to their efficient degradation of carbapenems and their high worldwide prevalence (150). The initially reported class D SBLs showed a narrow substrate profile, preferentially degrading penicillins such as oxacillin, hence the description of these enzymes as oxacillinases (52). However, many new class D SBLs, including variants which differ by only a few point mutations from their parent enzymes, have emerged which manifest much improved carbapenemase activity (151–153).

Some clinically relevant class D SBL variants are associated with increased carbapenemase activity compared to their parent enzymes, including OXA-519, OXA-655, OXA-83, and OXA-110 (151–154) (155). A common substitution found in these carbapenemases is a Val-to-Leu substitution at residue 120 (OXA-48 numbering), which is present in in OXA-519 (OXA-48 V120L) and OXA-655 (OXA-10 V116L T26M; note that the T26M substitution does not apparently contribute to the increased carbapenemase

activity) (151, 152) (**Figure 15**). Minimum inhibitory concentrations (MICs) for *E. coli* strains producing OXA-519 and OXA-655 have lower carbapenem susceptibility in comparison to the strains producing the parent enzymes, OXA-48 and OXA-10 (151, 152). Additionally, the Ile-to-Leu substitution at residue 120 (OXA-48 numbering) is found in OXA-83 (OXA-66 I129L) and OXA-110 (OXA-69 I129L) (154). The parent enzymes, OXA-66 and OXA-69 belong to the OXA-51 subfamily and are reported to be weak carbapenemases. The MICs for Acinetobacter baumannii strains producing OXA-83 and OXA-110 are also increased for carbapenems. The same effect is not found for strains producing the parent enzymes OXA-66 and OXA-69 (155).

Another substitution linked to improved carbapenemase activity is the Leu-to-Val substitution at residue 158 (OXA-48 numbering) in the OXA-51 subfamily (**Figure 15**). This Leu-to-Val substitution occurs in OXA-82 and OXA-107 (153, 155, 156).

Two rational protein design studies have identified other regions important for the carbapenemase activity of class D SBLs. The OXA-51 W222M variant producing bacterial strain has increased MIC values than wild-type OXA-51 producing bacterial strain (157). Residue Trp222 in OXA-51 (OXA-48 numbering, Thr213) interacts directly with the carbapenem in the AEC (**Figure 15**). In addition, when the β7-β8 loop (OXA-48 numbering residues 211-220) of the poor carbapenemase OXA-10 was artificially substituted with the β7-β8 loops from OXA-23, OXA-48, and OXA-24, all three novel engineered enzymes showed improved carbapenemase activity (**Figure 15**) (158).

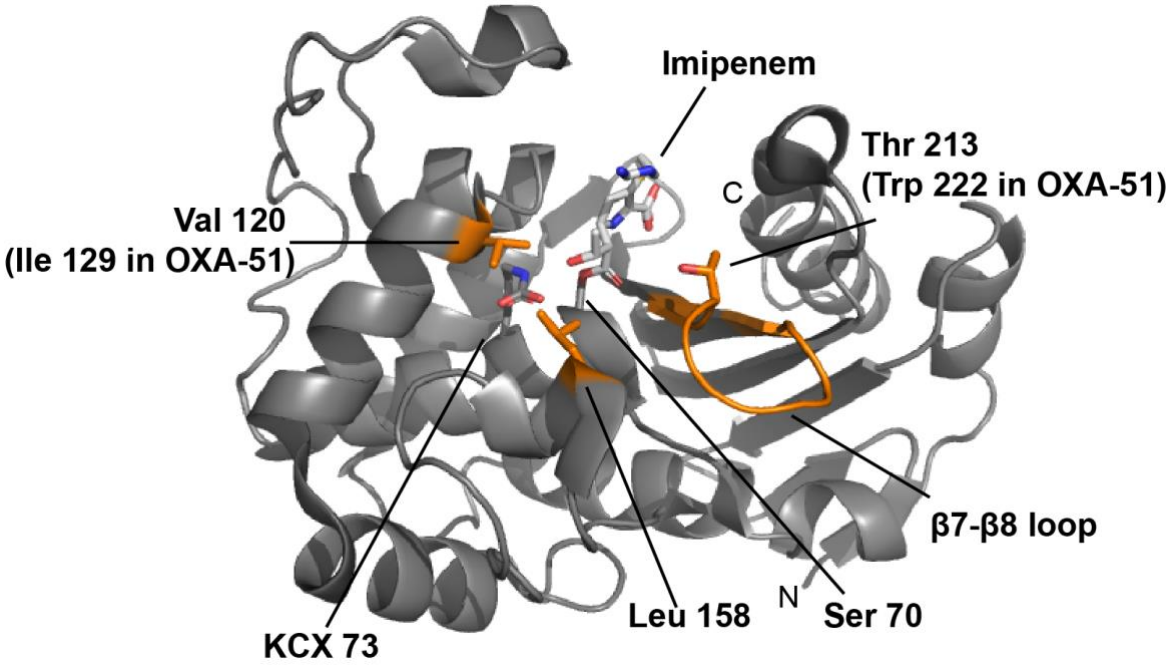

Figure 15. Positions of residues related to improved carbapenemase activity in a crystal structure of OXA-48 complexed with imipenem (PDB code: 5QB4). The residues Val120, Leu158, Thr213 (Trp222 in OXA-51) and the β7-β8 loop, which are in orange, are associated with improved carbapenemase activity in different class D SBLs. Imipenem is in white and carbamylated lysine (KCX73) and nucleophilic serine are in grey.

2.1.2 Mechanisms of class D SBLs

As described in the **General Introduction, Section 1.7**, 1β-methyl substituted carbapenem degradation by class D SBLs can be divided into two processes: an acylation step, and a bifurcating deacylation step. Whilst the degradation of carbapenems bearing a 1β-methyl substituent yield a mixture of β-lactones and hydrolysis products, degradation of those bearing a 1β-hydrogen substituent is reported to result in the hydrolysis products (88).

The C-6 hydroxyethyl side chain of the clinically used carbapenems, which is involved in β-lactone formation, has a unique 6α-stereochemistry amongst β-lactam antibiotics, and is thought to contribute to the resistance of carbapenems to SBL-mediated degradation. It is proposed that this side chain sterically hinders the entry of the water molecule required for hydrolysis into the active site (159). Recent density functional theory

(DFT) non-covalent interaction calculations on carbapenems have provided insights into the potential steric clashes of 1β-methyl substituent with the C-6 hydroxyethyl side chain. Complementary molecular dynamics (MD) simulations suggest that the 1β-methyl substituent limits the conformational flexibility of the C-6 hydroxyethyl side chain (88).

The aim of the work described in this chapter was to investigate the mechanism of carbapenem degradation by class D SBLs, focusing on the bifurcating pathway that forms both classical hydrolysis products and the recently identified β-lactones. It was envisaged that the work would investigate whether β-lactone formation by class D SBLs contributes to carbapenem-related antibiotic resistance.

2.1.3 Selection and production of OXA-48 variant enzymes

Analysis of crystal structures of class D SBLs with carbapenems revealed that there are active site residues which interact with the C-6 hydroxyethyl side chain of the carbapenem-derived AEC, i.e. Trp105, Val120, and Leu158 (87). To investigate the role of these residues in the enzymatic mechanism of OXA-48, several variants of this enzyme, i.e. W105A, W105F, V120I, V120L, L158V, and L158I, were prepared and characterised. The position of the single residue substitutions are shown in a view from crystal structure of OXA-48 with imipenem (PDB code: 5qb4) (**Figure 16**) (87).

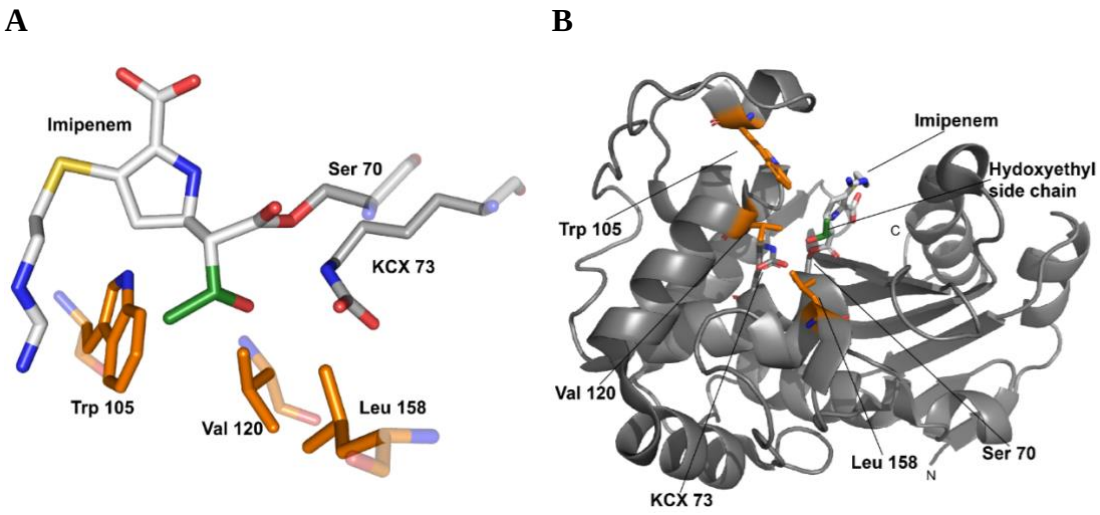

Figure 16. View from a crystal structure of OXA-48 complexed with imipenem. A. Three residues, Trp105, Val120, and Leu158, are positioned to interact with the imipenem C-6 hydroxyethyl side chain as observed in the crystal structure of OXA-48 with imipenem (PDB code: 5qb4). **B.** View of the AEC of OXA-48 with imipenem showing the positions of the residues Trp105, Val120, and Leu158. The imipenem C-6 hydroxyethyl side chain is in green, the nucleophilic serine, Ser70, and carbamylated lysine, KCX73, are in grey, and the residues Trp105, Val120, and Leu158, which were chosen for substitution studies, are in orange. Some parts of this figure are adapted from Aertker, K. M. J. et al. (2020) *J. Biol. Chem.* **295**, 16604–16613.

Mechanistic studies on the degradation of carbapenems by OXA-48 were carried out as summarised below:

1. To understand the link between state-steady kinetics of variants and wild-type Class D SBLs enzymes and NMR-based product profile analyses,
2. To analyse the conformation of the C-6 hydroxyethyl side chain in the crystallographically observed AECs of class D SBLs with carbapenems,
3. To perform bioinformatic analyses of class D SBL sequences focusing on the residues in position 120 (OXA-48 numbering).

2.2 Results

2.2.1 Mutagenesis, production and purification of wild-type OXA-48 and OXA-48 variants

Genes encoding for OXA-48$_{23\text{-}265}$ (referred as OXA-48) variants (V120I, V120L, L158V, L158I, W105A, W105F) were prepared by site-directed mutagenesis (**Material and Methods**, **Section 6.2.1.3**) using the primers defined in **Section 6.2.1.1**. Ms. Ciondi Bess, an internship student under my laboratory supervision, prepared the constructs encoding for OXA-48 W105A and W105F. The N-terminally His$_6$-tagged OXA-48 variants were produced in *E. coli* and purified by Ni(II)-affinity chromatography and size exclusion chromatography (SEC), as described in the **Material and Methods**, **Section 6.3**. The procedure was adapted from the established protocol for wild-type OXA-48$_{23\text{-}265}$ (referred as OXA-48) (160). Purified wild-type OXA-48 and OXA-48 V120L, V120I, L158I and L158V proteins were kindly provided by Mr. H. T. Henry Chan. The purity of the variants was assessed by SDS-PAGE, and the substitutions were confirmed by intact ESI-LC-MS analysis (**Figure 17**).

OXA-48	Calculated mass (Da)	Observed mass (Da)
Wild-type	30830.9	30830.6
V120I	30844.9	30848.5
V120L	30844.9	30847.0
W105A	30715.8	30716.5
W105F	30791.9	30792.3
L158V	30816.9	30818.5
L158I	30830.9	30833.5

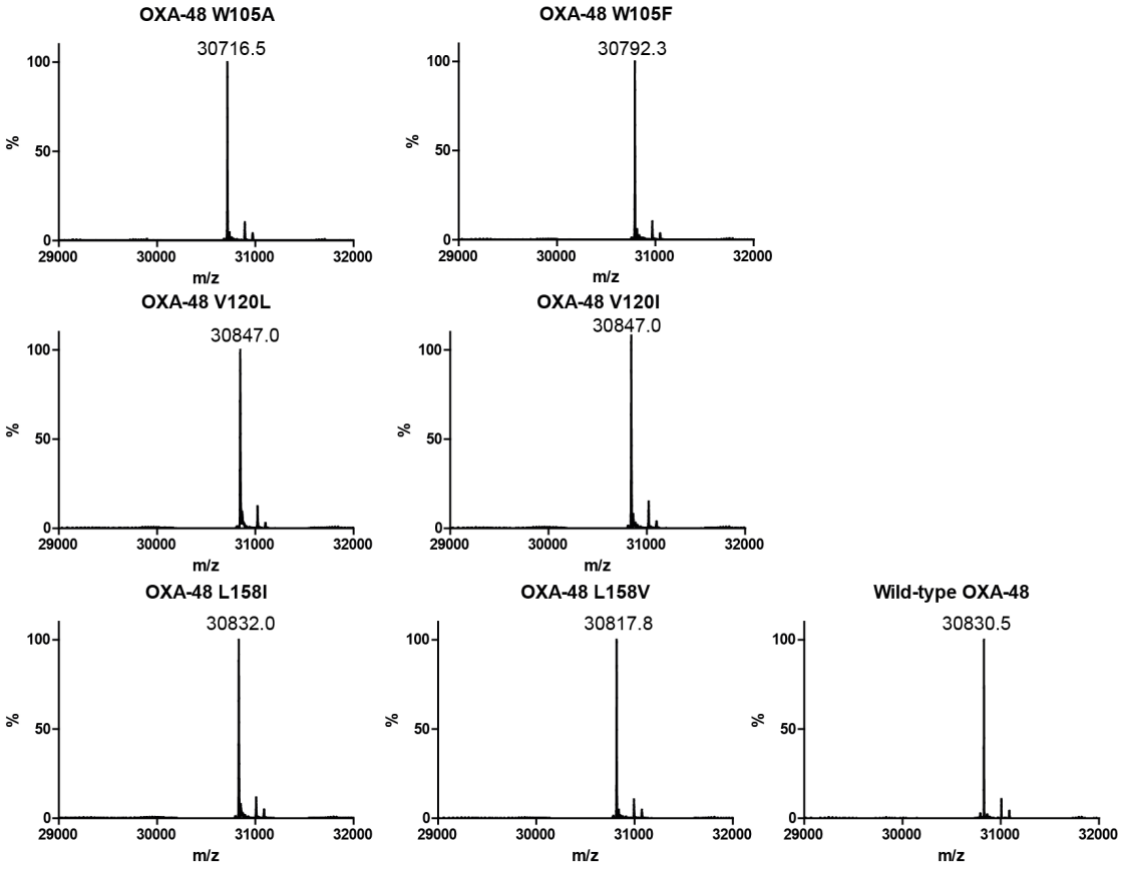

Figure 17. Deconvoluted protein mass and Coomassie-stained SDS-PAGE gel for wild-type OXA-48 and its variants. Calculated protein masses based on amino acid sequence using the ExPASy ProtParam tool, and deconvoluted protein masses based on mass spectrometry. Smaller adducts (+177.8 Da, +257.9 Da) were also observed, likely resulting from α-*N*-6-phosphogluconoylation of the His-tag, as previously identified (161). The proteins are >95% pure after nickel affinity chromatography and SEC. Some parts of this figure are adapted from Aertker, K. M. J. et al. (2020) *J. Biol. Chem.* **295**, 16604–16613.

A comparative analysis of wild-type OXA-48 and its variants, evaluating secondary structure and thermal stability, was carried out by circular dichroism (CD) spectroscopy. The two different types of secondary structures, α-helices and β-sheets of proteins have characteristic absorption of left and right circularly polarised light in the far UV region (185-260 nm). The thermal stability of the enzymes was studied by exposing them with to a temperature gradient (20-85 °C) (162, 163), while monitoring the absorption region corresponding to α-helical secondary structure (222 nm) (163, 164).

Initial CD measurements with wild-type OXA-48 were conducted to optimise the protein concentration for sufficient signal; the measurements revealed 0.2 mg/mL as a suitable concentration. The CD spectra for the OXA-48 variants (W105A, W105F, L158I, V120L, and V120I) all closely resemble that of wild-type OXA-48, with only a slight shift in the characteristic α-helix region for the L158V variant. In spite of this, the apparent T_m for the L158V variant was very similar to that of wild-type OXA-48. Furthermore, the W105A variant had an apparent ΔT_m difference of 6 °C relative to the wild-type enzyme, whereas the CD spectrum for this variant showed no evidence for substantial changes in the protein fold compared to wild-type OXA-48. These results indicate that all of the variants, expect for W105A, have similar stabilities and overall folds compared to wild-type OXA-48 (**Figure 18**).

A

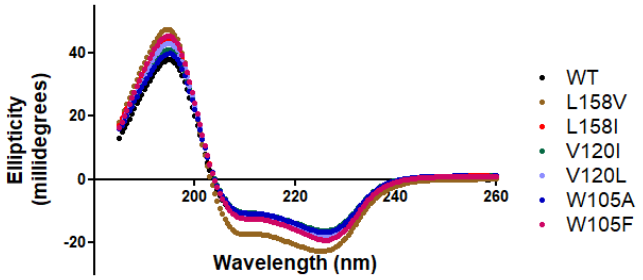

B

OXA-48	**T_m (°C)**
wild-type	58.3 ± 0.07
V120I	56.6 ± 0.09
V120L	60.3 ± 0.1
L158I	58.8 ± 0.08
L158V	57.2 ± 0.06
W105A	51.9 ± 0.2
W105F	54.6 ± 0.1

Figure 18. CD spectroscopic analysis of protein fold and apparent T_m for wild-type OXA-48 and its variants. A. CD spectra in the far UV region (185-260 nm) were measured in triplicate, averaged, and smoothed. **B.** Apparent melting temperatures were obtained by three measurements at a wavelength of 222 nm, then averaged, normalised, and fitted to a Boltzmann sigmoidal curve. Based on these data, these substitutions have only a marginal impact on overall protein stability. The figure is adapted from Aertker, K. M. J. et al. (2020) J. Biol. Chem. **295**, 16604–16613.

2.2.2 Steady state kinetics

The kinetic properties of the OXA-48 variants were investigated to understand how the active site amino acid substitutions impact on catalytic activity. The catalytic properties of the different enzymes were determined by Michaelis-Menten type analysis, calculating kinetic parameters, K_M, k_{cat}, and k_{cat}/K_M. The Michaelis constant, K_M, describes the substrate concentration at which the enzymatic rate is half of the maximal value, and is independent of enzyme and substrate concentration. k_{cat} reflects the enzyme rate at maximal catalytic turnover. Under saturating substrate concentrations, the enzyme converts substrate into product at the maximal rate. When the substrate concentration is greater than K_M, the turnover number is close to k_{cat}. A third kinetic parameter, k_{cat}/K_M, combines both parameters, and is often used as a measure of catalytic efficiency.

For the steady-state kinetic analyses of the OXA-48 variants, three different substrates were used: nitrocefin, meropenem and imipenem (**Figure 19**). Nitrocefin was employed as a chromogenic cephalosporin-based reporter for β-lactamase activity assay with a well characterised reaction mechanism (165). The carbapenems were chosen due to the presence (meropenem) and the lack (imipenem) of a 1β-methyl substituent.

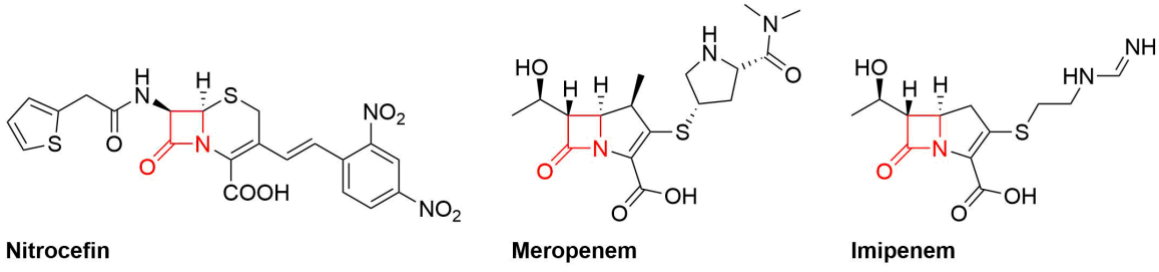

Figure 19. Structures of substrates used for kinetic analyses.

Prior to the kinetic analysis, the optimal enzyme concentrations were evaluated using a non-limiting substrate concentration, aiming to determine suitable linear ranges corresponding to the initial enzymatic velocities. The enzyme concentrations were optimised for each combination of substrate and enzyme (**Material and Methods, Section 6.7.1**). Product formation from nitrocefin and substrate depletion for meropenem and imipenem were monitored at 25 °C by UV-Vis spectrometry (**Table 2**, **Figure 78**).

All of the OXA-48 variants tested turned over the three substrates less efficiently than wild-type OXA-48, as judged by k_{cat}/K_M (**Table 2**). Furthermore, it was found that nitrocefin is a better substrate than the tested carbapenems for all of the OXA-48 variants, based on k_{cat} and k_{cat}/K_M values. Interestingly, the K_M values for carbapenems were generally lower than those for nitrocefin. Relative to wild-type enzyme, the K_M of nitrocefin for the V120L V120I, W105F, W105A variants were higher and for the L158V and L158I variants were lower.

The k_{cat} and k_{cat}/K_M values for the OXA-48 V120L and V120I variants varied for the two carbapenems, meropenem and imipenem (**Table 2**). Relative to wild-type OXA-48, the k_{cat} for meropenem was higher with the V120L and V120I variants, and higher for imipenem with the V120I variant, but lower for imipenem with the V120L variant. For the V120L and V120I variants, meropenem was a poorer substrate then imipenem, as judged by k_{cat}/K_M comparison.

With meropenem, the L158V, L158I, and W105F variants had a lower catalytic efficiency (k_{cat}/K_M) relative to the wild-type OXA-48 (**Table 2**). In addition, the K_M values were comparable for the L158V and W105F variants and was higher for the L158I variant than the wild-type enzyme. The degradation of meropenem by the W105A variant was too slow under the assay conditions to allow for accurate kinetic characterisation.

Table 2. Kinetic parameters of wild-type OXA-48 and variants with nitrocefin, meropenem, and imipenem, measured by UV-Vis spectrometry. Spectrophotometric assays were carried out using nitrocefin (5 - 1500 μM) and enzyme (25 - 500 pM) in 100 mM sodium phosphate pH 7.5, 0.01% Triton X-100, or meropenem (1.75 - 500 μM) or imipenem (5 - 500 μM) with enzyme (1.5 - 400 nM) in 50 mM sodium phosphate, pH 7.5, 0.01% Triton X-100, with 50 mM sodium bicarbonate. The reaction rates were plotted as a function of substrate concentration. The K_M and k_{cat} values are the mean, and the errors are the standard deviations of the mean (n = 3). The table is adapted from Aertker, K. M. J. et al. (2020) J. Biol. Chem. **295**, 16604–16613.

OXA-48	substrate	k_{cat} (s^{-1})	K_M (μM)	k_{cat}/K_M ($M^{-1}s^{-1}$) • 10^{-6}
wild-type	nitrocefin	593.2 ± 18.3	23.9 ± 3.5	24.8 ± 3.7
	meropenem	0.087 ± 0.01	<1.9[b]	>0.045[b]
	imipenem	11.4 ± 0.5	57.7 ± 9.3	0.20 ± 0.03
V120L	nitrocefin	287.1 ± 11.7	184.1 ± 22.8	1.5 ± 0.2
	meropenem	1.1 ± 0.08	51.0 ± 11.8	0.021 ± 0.005
	imipenem	0.49 ± 0.006	6.8 ± 0.6	0.071 ± 0.006
V120I	nitrocefin	323.2 ± 11.1	40.1 ± 4.9	8.1 ± 1.0
	meropenem	0.94 ± 0.01	10.6 ± 1.4	0.075 ± 0.008
	imipenem	17.9 ± 1.42	208.2 ± 45.2	0.086 ± 0.002
W105F	nitrocefin	178.1 ± 16.7	298.4 ± 37.8	0.60 ± 0.09
	meropenem	0.038 ± 0.0007	<1.75[b]	>0.022[b]
W105A	nitrocefin	70.72 ± 1.46	218.1 ± 9.5	0.32 ± 0.02
	meropenem[a]	-	-	-
L158V	nitrocefin	54.9 ± 4.3	16.1 ± 3.3	3.4 ± 0.8
	meropenem	0.0081 ± 0.0002	<2[b]	>0.004[b]
L158I	nitrocefin	59.8 ± 3.5	8.1 ± 2.2	7.4 ± 2.1
	meropenem	0.031 ± 0.005	7.1 ± 4.1	0.0017 ± 0.003

[a] Not determined. [b] K_M values reflect the lowest [S] that could be detected; the actual K_M values are lower than the given values, and the k_{cat}/K_M values are higher than the given values.

Comparison of the results with previously reported kinetic parameters show that the k_{cat} and k_{cat}/K_M values determined for wild-type OXA-48 are consistent with other studies (166). However, the kinetic parameters for OXA-519 (OXA-48 V120L) were not in

agreement with the reported data (meropenem, k_{cat} = 3.4 s^{-1}, K_M = 358 μM, k_{cat}/K_M x 10^{-3} = 9.5 $M^{-1}s^{-1}$, imipenem, k_{cat} = 2.1 s^{-1}, K_M = 982 μM, k_{cat}/K_M x $10^{-3•}$ = 2.1 $M^{-1}s^{-1}$) (151). This is likely due to different assay conditions, including the nature of the recombinant protein construct used.

2.2.3 OXA-48 W105A forms an acyl-enzyme complex with meropenem

Kinetic parameters for meropenem degradation by OXA-48 W105A could not be accurately determined due to the detection limits of the kinetic assay (**Table 2**). To investigate why the meropenem degradation was less efficient, an acylation assay was carried out to determine whether the acylation of OXA-48 W105A by meropenem was slow. Using ESI-MS, OXA-48 W105A was analysed in the presence and absence of meropenem with a 1:10 ratio of enzyme to substrate. Rapid formation of the meropenem-derived AEC was observed (**Figure 20**), suggesting that the deacylation step is disrupted in OXA-48 W105A.

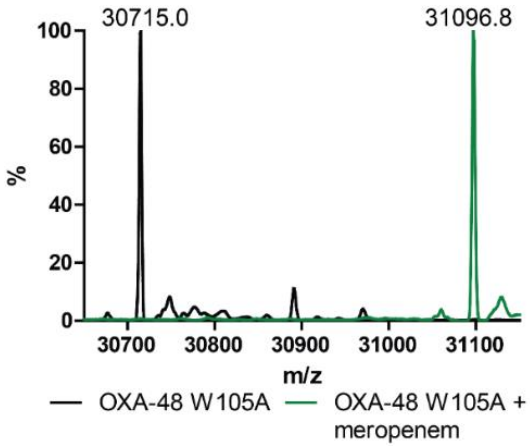

Figure 20. Mass spectrometric analysis of OXA-48 W105A with meropenem. Deconvoluted ESI-MS spectra of OXA-48 W105A in the absence (black) and in the presence of meropenem (green). The samples contained 1 μM OXA-48 W105A, with and without 10 μM meropenem, prepared in 50 mM sodium phosphate buffer pH 7.5. The figure is adapted from Aertker, K. M. J. et al. (2020) J. Biol. Chem. **295**, 16604–16613.

2.2.4 ^{1}H NMR turnover assays

The state-steady kinetic analyses demonstrate that the amino acid substitutions (W105A, W105F, V120L, V120I, L158V, and L158I) impact (on the catalytic activities of the OXA-48 variants with all three substrates (**Figure 19**, **Table 2**). To investigate how these results, relate to the ratio of hydrolysis to β-lactone formation, meropenem and imipenem degradation by the OXA-48 variants was measured by ^{1}H NMR (600 MHz) spectroscopy over 60 min.

To characterise the product distributions for these enzymes, resonances corresponding to the H-9 methyl group (1.19- 1.57 ppm, **Figure 21**) of the carbapenem substrate, the hydrolysis products, and the β-lactone products were monitored. The hydrolysis and β-lactone products can occur as mixture of epimeric (*S*)-Δ^1 imine and (*R*)-Δ^1 imine pyrroline forms, as well as a tautomeric Δ^2 enamine pyrroline form. A previous NMR study provided evidence that the Δ^2 enamine is the enzymatic product of β-lactones (as seems likely to be the case for the hydrolysis products) (167). For 1β-methyl substituted carbapenems, the Δ^2 enamine form rapidly tautomerises to the (*R*)-Δ^1 imine product as a kinetic product (non-enzymatic product), which subsequently converts to the thermodynamic (*S*)-Δ^1 imine product over time (167). The tautomerisation from (*R*)-Δ^1 imine to (*S*)-Δ^1 imine products likely occur via Δ^2 enamine product (167). In the NMR time courses with 1β-methyl substituted carbapenems, the (*S*)-Δ^1 imine product was the major form observed for both hydrolysis and β-lactone products with all the studied variants.

A

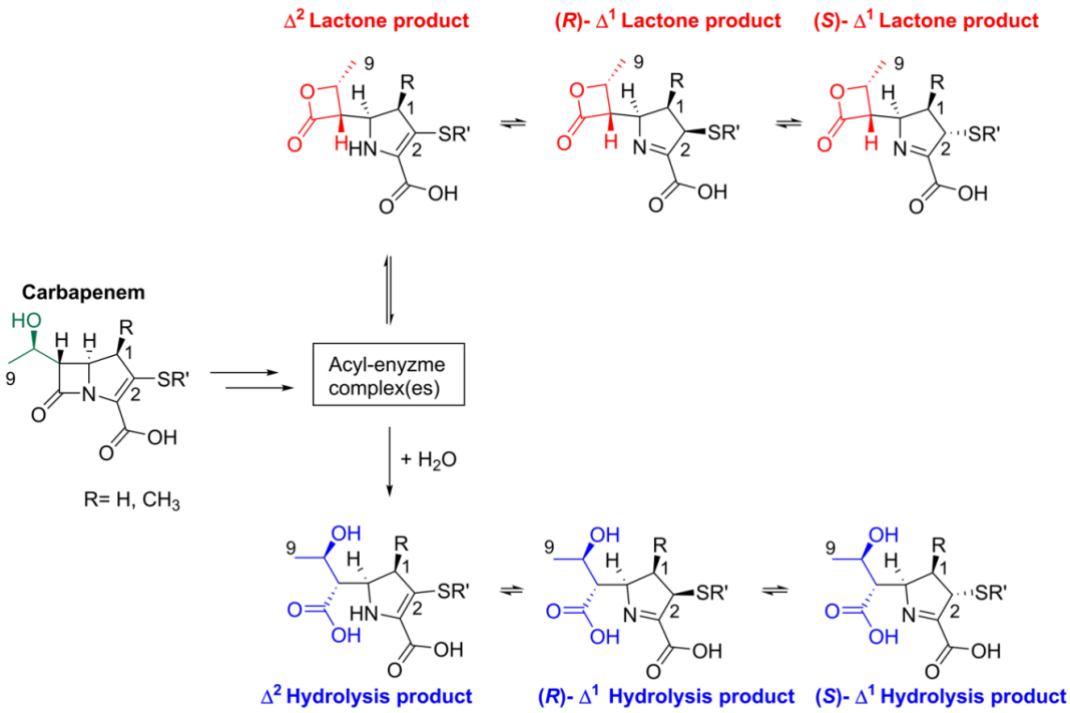

B

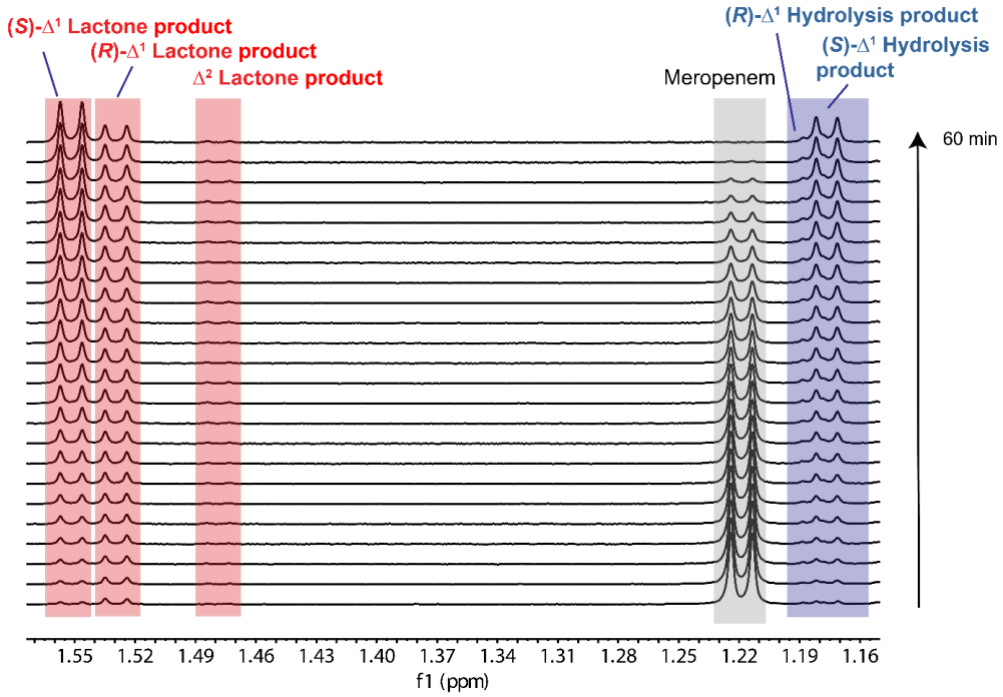

Figure 21. Class D SBLs form carbapenem-derived β-lactone and hydrolysis products. A. The different pyrroline ring isomers of the β-lactone and hydrolysis products are shown (167). **B.** Representative ^{1}H-NMR time course with meropenem and wild-type OXA-48 showing the different pyrroline forms of β-lactone and hydrolysis products. Assay conditions were 1 mM meropenem, 5 μM wild-type OXA-48, in 50 mM sodium phosphate buffer pH 7.5, 10% D_2O for 60 min. The figure is adapted from Aertker, K. M. J. et al. (2020) *J. Biol. Chem.* **295**, 16604–16613.

All of the OXA-48 variants tested turned over meropenem to form both β-lactones and hydrolysis products (**Figure 22**). A higher percentage of hydrolysis products relative to β-lactones was observed for the L158I, L158V, W105F, and V120I variants, with the V120I variant favouring hydrolysis to the greatest extent. However, wild-type OXA-48 and the V120L and W105A variants produced more β-lactones than hydrolysis products. Notably, the V120L variant, which is clinically relevant for carbapenem resistance, and is referred to as OXA-519 (151), produced the greatest amount of β-lactones.

These results suggest that active site substitutions which are not directly involved in the catalytic machinery, but which are in proximity to the carbapenem C-6 hydroxyethyl side chain in the AEC, impact on the ratio of hydrolysis to β-lactone. The observed differences in these product ratios were compared to the kinetic parameters for these enzymes (**Section 2.2.2**) indicating that there is not a direct correlation between product profile and kinetic properties.

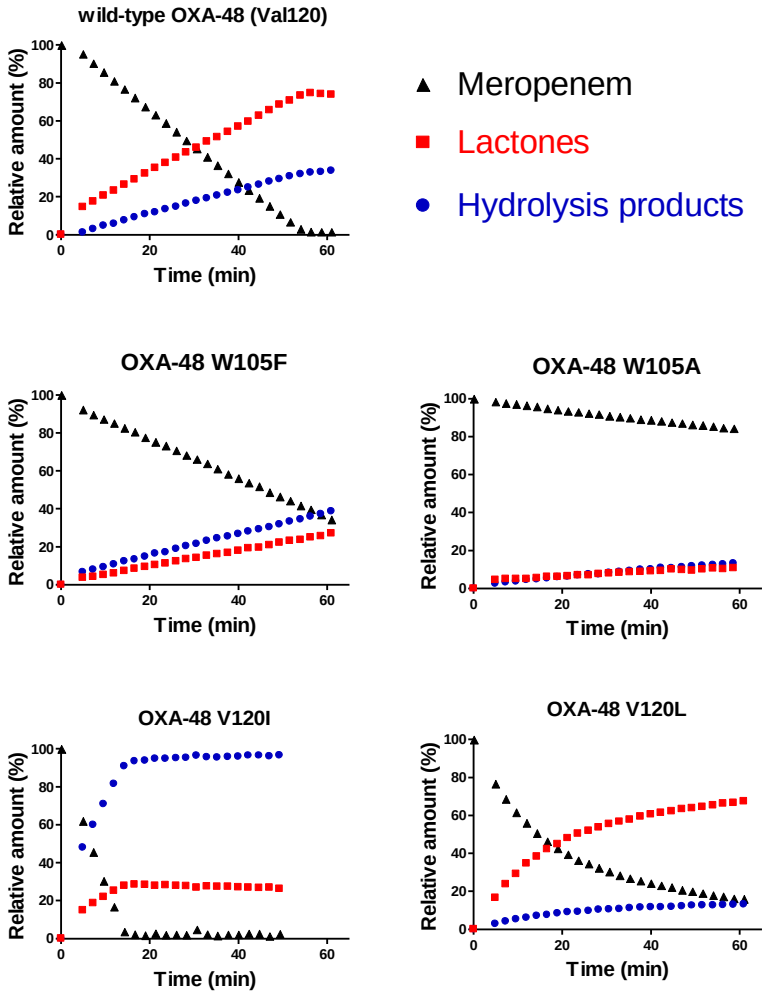

Figure 22. ^{1}H NMR time courses of meropenem degradation by wild-type OXA-48 and the OXA-48 variants. 1 mM meropenem was treated with varying enzyme concentrations (0.5 μM - 100 μM) in 50 mM sodium phosphate buffer pH 7.5 for 60 min. The product formation was monitored by ^{1}H NMR (600 MHz). The related NMR spectra of the time course of wild-type OXA-48 with meropenem is found in **Figure 21B**. The figure is adapted from Aertker, K. M. J. et al. (2020) *J. Biol. Chem.* **295**, 16604–16613.

OXA-48 V120L was next tested under the same NMR (600 MHz) assay conditions as used with other clinically used carbapenems, i.e. the 1β-methyl substituted carbapenems ertapenem and biapenem. The chemical shift assignments of the major (*S*)-Δ^1 imine products and minor (*R*)-Δ^1 imine products of the 1β-methyl substituted carbapenems have been

previously determined (88, 167). As with meropenem, degradation of all of these carbapenems by OXA-48 V120L favoured β-lactone formation (**Figure 23B**).

Previous work suggested that β-lactone products are not formed when wild-type OXA-48 degrades imipenem and panipenem, clinically important carbapenems which have 1β-hydrogen substituent (88). All the OXA-48 variants prepared in the present work were tested with imipenem. Under the standard NMR assay conditions, mixing imipenem or panipenem with the OXA-48 V120L variant, new products were observed by NMR (**Figure 23A**). Mr. H. T. Henry Chan kindly isolated and characterised the products, demonstrating that they correspond to the imipenem- and panipenem-derived β-lactones (H. T. Henry Chan Part II Thesis, University of Oxford, **Table 32 and Table 33, Figure 70 - Figure 77**).

A

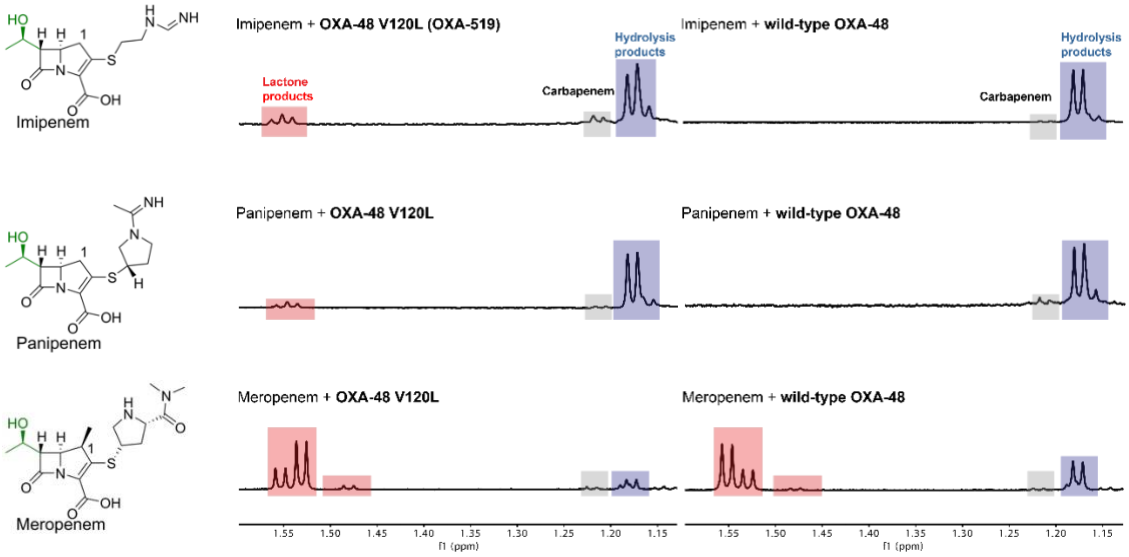

B

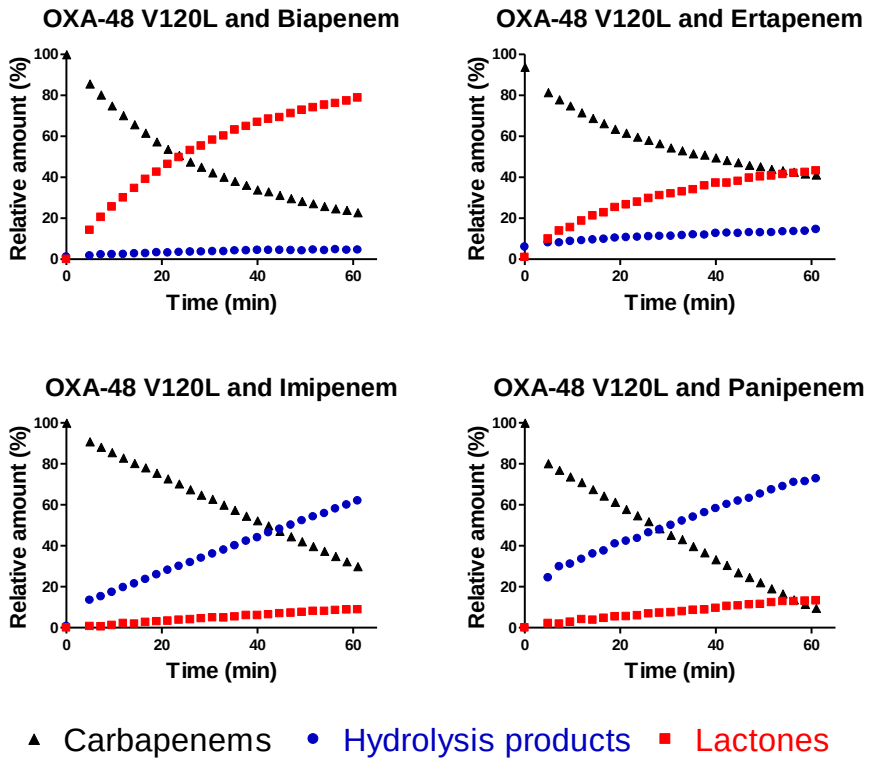

Figure 23. Clinically observed SBL OXA-519 (OXA-48 V120L) produced β-lactone products derived from all carbapenems tested. A. ^{1}H NMR spectrum showing the product mixture when less than 5% of the carbapenem was remaining. **B.** Product profiles of carbapenems such as ertapenem, imipenem, panipenem, and biapenem, with the OXA-48 V120L variant monitored by ^{1}H NMR (600 MHz) for 60 min. Conditions were 1 mM carbapenem and the OXA-48 V120L variant (varying enzyme concentrations) in 50 mM sodium phosphate buffer, pH 7.5 10% D_2O. The figure is adapted from Aertker, K. M. J. et al. (2020) *J. Biol. Chem.* **295**, 16604–16613.

2.2.5 Analysis of lysine carbamylation for wild-type OXA-48 and the V120L and V120I variants

In the catalytic mechanism of class D SBLs a carbamylated lysine acts as a general base/acid (80, 87) (**General Introduction, Figure 7**). It was investigated whether the carbamylation state of the active lysine is impacted by the active site substitutions in OXA-48 V120L and OXA-48 V120I. All three enzymes (i.e. wild-type OXA-48, OXA-48 V120L and OXA-48 V120I) were dialysed against degassed 50 mM sodium phosphate pH 7.5 for 18 h as described in the **Material and Methods**, **Section 6.6.3** and reported (80). The enzymes were mixed with isotopically labelled $NaH^{13}CO_3$ and the degree of lysine carbamylation was measured by ^{13}C-NMR (**Figure 24**). The ^{13}C-NMR spectra suggest that the extent of carbamylation for all three enzymes was comparable. It is important to point out that a disadvantage of this protein-observed ^{13}C-NMR method is that it has low sensitivity and therefore require large amount of protein and long acquisition times (160). In addition, the carbamylation observed under tested conditions might not reflect the carbamylation state during catalysis, because the level of lysine carbamylation was measured in absence of substrates.

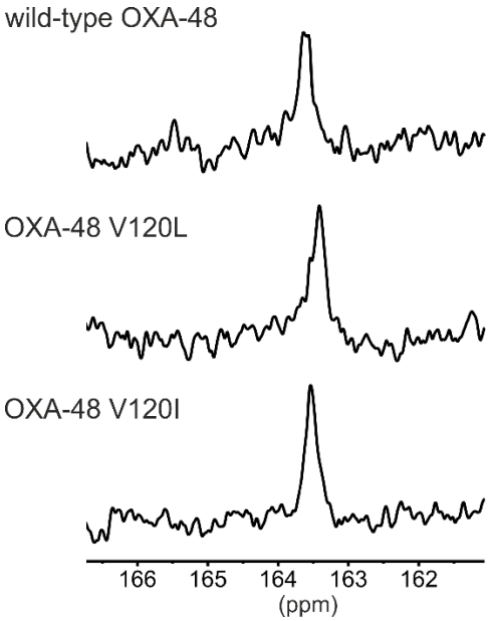

Figure 24. Monitoring lysine carbamylation by protein-observed ^{13}C NMR. ^{13}C-NMR (150 MHz) spectra revealing the lysine carbamylation states of the OXA-48 Val120 variants. Enzymes (700 µM) were incubated with 10 mM Na$H^{13}CO_3$ in 50 mM sodium phosphate pH 7.5 using an optimised, previously reported procedure (80). The figure is adapted from Aertker, K. M. J. et al. (2020) *J. Biol. Chem.* **295**, 16604–16613**.**

To understand better the impact Val-to-Ile (V120I variant) and Val-to-Leu (V120L variant) substitutions in OXA-48 on catalytic activity, steady state kinetics were performed with and without added sodium bicarbonate ($NaHCO_3$) to monitor the degradation of nitrocefin by these enzymes (**Table 3**, **Figure 78** and **Figure 79**). With added $NaHCO_3$, the k_{cat} values of wild-type OXA-48 and V120L and V120I variants were higher. The results suggest that lysine carbamylation is likely not or very little impacted by the conserved substitutions in position 120 (OXA-48 numbering).

Table 3. Lysine carbamylation of the OXA-48 Val120 variants is comparable to wild-type OXA-48. Kinetic parameters of wild-type OXA-48 and its V120I and V120L variants with nitrocefin in the presence and absence of 100 mM sodium bicarbonate. Assay conditions were nitrocefin (5 - 1500 μM) and enzyme (25-50 pM) in 100 mM sodium phosphate, pH 7.5, 0.01% Triton X-100, with and without 50 mM sodium bicarbonate. Errors are measured as standard deviations, n = 3. The table is adapted from Aertker, K. M. J. et al. (2020) *J. Biol. Chem.* **295**, 16604–16613.

OXA-48	k_{cat} **(s^{-1})**	K_M **(μM)**	k_{cat}/K_M **($M^{-1}s^{-1}$) x 10^{-6}**	**Addition of $NaHCO_3$**
wild-type	593.2 ± 18.3	23.9 ± 3.5	24.8 ± 3.7	-
V120L	287.1 ± 11.7	184.1 ± 22.8	1.5 ± 0.2	
V120I	323.2 ± 11.1	40.1 ± 4.9	8.1 ± 1.0	
wild-type	663.2 ± 17.8	34.6 ± 3.7	19.1 ± 2.1	+
V120L	320.6 ± 79.6	275.9 ± 62.2	1.2 ± 0.4	
V120I	356.8 ± 15.5	330.8 ± 38.7	1.2 ± 0.1	

2.2.6 Analyses of kinetics and product profile of wild-type OXA-23 and OXA-23 V128I and OXA-23 V128L variants

Based on the observation that residue 120 in OXA-48 plays in important role in determining the product distribution, the V128I and V128L variants of the carbapenemase OXA-23 were prepared. Site-directed mutagenesis was carried out to obtain plasmids encoding for these variants (**Material and Methods**, **Section 6.2.1.3**). The N-terminally His_6-tagged $OXA\text{-}23_{18\text{-}273}$ (referred to as OXA-23) variants were produced and purified as previously described for OXA-48 in the **Material and Methods**, **Section 6.3** and as reported (160). The identities of the new OXA-23 variants were confirmed by LC-ESI-MS (**Figure 25**). The N-terminally His_6-tagged wild-type $OXA\text{-}23_{18\text{-}273}$ (referred to as OXA-23) was kindly provided by Dr. Christopher Lohans.

OXA-23	Calculated mass (Da)	Observed mass (Da)
Wild-type	31062.8	31076.5
V128I	31076.8	31079.5
V128L	31076.8	31078.8

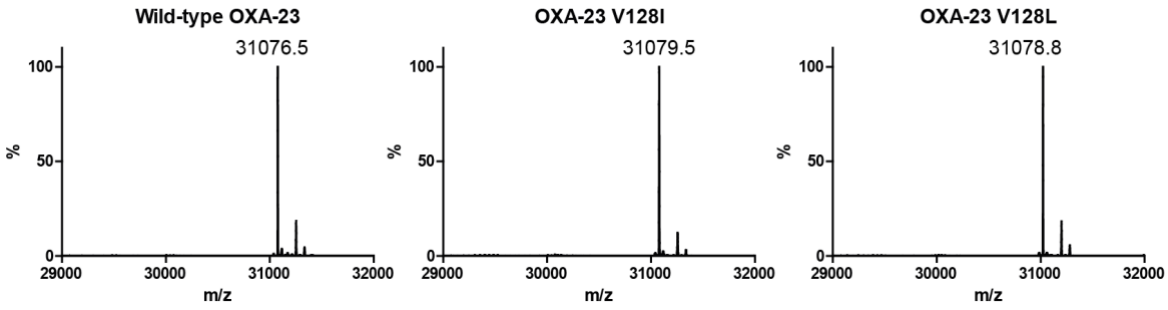

Figure 25. Mass spectrometric analysis of OXA-23 variants. Calculated and observed deconvoluted protein masses, as measured by LC-ESI-MS. The additional +177.8 Da and +257.9 Da adducts likely correspond to N-6-phosphogluconoylation of the His-tag sequence, as has been reported (161). Some parts of this figure are adapted from Aertker, K. M. J. et al. (2020) *J. Biol. Chem.* **295**, 16604–16613.

To evaluate the impact of the Val-to-Ile (V128I variant) and Val-to-Leu (V128L variant) substitutions on enzymatic activity, kinetic analyses with the three substrates, nitrocefin, meropenem, and imipenem were performed (**Table 4**, **Figure 80**). As observed for the OXA-48 variants, the k_{cat}/K_M values for the OXA-23 V128I and V128L variants with the cephalosporin nitrocefin were lower than that for wild-type OXA-23. The catalytic efficiency k_{cat}/K_M values were higher for imipenem than meropenem with wild-type OXA-23 and the V128I variant, which was consistent with what was observed for wild-type OXA-48 and the OXA-48 V120I variant. However, comparable catalytic efficiencies were observed for imipenem and meropenem with the OXA-23 V128L variant, as judged by k_{cat}/K_M values.

Table 4. Kinetic parameters for wild-type OXA-23 and variants (500 nM-0.1 nM) with nitrocefin, meropenem, and imipenem in 100 mM sodium phosphate pH 7.5, 0.01% Triton X-100. Error values are the standard deviation of the mean (n = 3). The table is adapted from Aertker, K. M. J. et al. (2020) *J. Biol. Chem.* **295**, 16604–16613.

OXA-23	Substrate	k_{cat} (s^{-1})	K_M (μM)	k_{cat}/K_M ($M^{-1}s^{-1}$) x 10^{-6}
wild-type	nitrocefin	260.3 ± 5.9	93.2 ± 6.6	2.79 ± 0.2
	meropenem	0.063 ± 0.002	3.4 ± 0.4	0.019 ± 0.002
	imipenem	0.59 ± 0.03	5.9 ± 0.9	0.10 ± 0.02
V128L	nitrocefin	119.1 ± 10.4	437.4 ± 85.5	0.27 ± 0.06
	meropenem	0.14 ± 0.009	8.2 ± 2.3	0.017 ± 0.005
	imipenem	0.094 ± 0.005	5.0 ± 1.3	0.019 ± 0.005
V128I	nitrocefin	30.1 ± 2.4	499.8 ± 115.2	0.06 ± 0.02
	meropenem	0.066 ± 0.003	1.9 ± 0.5	0.035 ± 0.01
	imipenem	0.54 ± 0.007	9.4 ± 0.6	0.057 ± 0.003

After obtaining the kinetic parameters for wild-type OXA-23 and the OXA-23 V128I and OXA-23 V128L variants, the product profiles for these enzymes were investigated. The wild-type OXA-23 and the OXA-23 V128L variant degraded meropenem

to preferentially β-lactones to a similar degree as was previously observed for wild-type OXA-48 and the OXA-48 V120L (**Figure 22**, **Figure 26A**). Consistent with what was seen for OXA-48 V120I, OXA-23-V120I also produced β-lactone products from imipenem and panipenem (**Figure 23**, **Figure 26B**). However, there were discrepancies in the product outcomes for OXA-23 V128I and OXA-48 V128I with meropenem, as the formation of hydrolysis products was less favoured by OXA-23 V128I.

Considering the observed hydrolysis: β-lactone products ratio and the steady-state kinetic analyses, these results suggests that there is not a direct correlation between the preferred reaction pathway and the kinetic parameters (i.e. k_{cat}, K_M, and k_{cat}/K_M values).

A

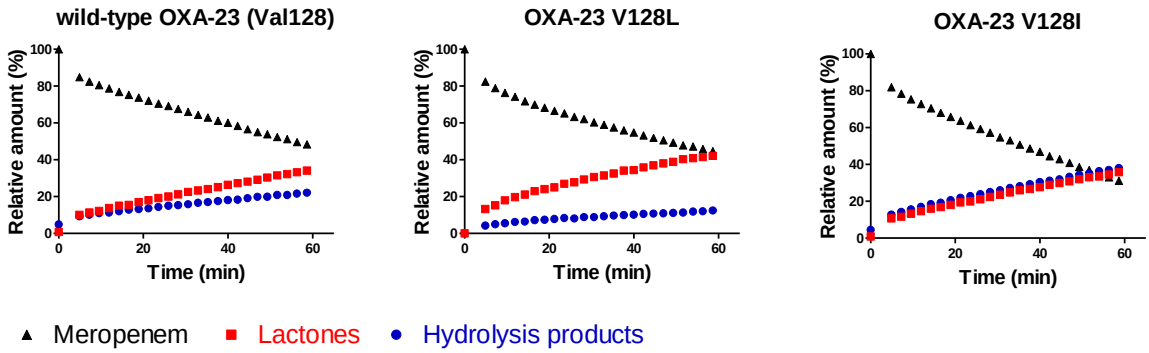

B

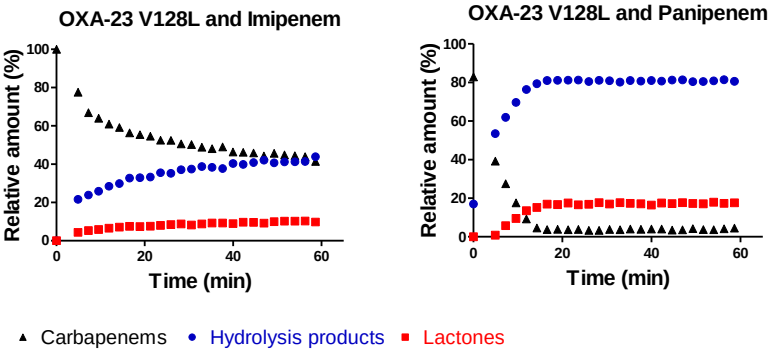

Figure 26. ^{1}H NMR (600 MHz) time courses of carbapenem degradation by wild-type OXA-23 and the OXA-23 variants. **A.** Product profile of meropenem degradation by wild-type OXA-23, OXA-23 V128L, and OXA-23 V128I. **B.** Product profiles of the 1β-hydrogen substituted carbapenems imipenem and panipenem with the OXA-23 V128L variant. Assay conditions were 1 mM carbapenem and varying enzyme concentrations in 50 mM sodium phosphate buffer, pH 7.5 10% D_2O. All assays were monitored by ^{1}H NMR (600 MHz) for 60 min. The figure is adapted from Aertker, K. M. J. et al. (2020*) J. Biol. Chem.* **295**, 16604–16613.

2.2.7 Conformation of the carbapenem C-6 hydroxyethyl side chain

To examine the roles of the active site residues in determining the mechanism of carbapenem (i.e. β-lactone vs hydrolysis), the entries in the Protein Data Bank (PDB) (listed in caption of **Figure 28**) that represent the AECs of class D SBLs with carbapenems were compiled and analysed. These structural analyses suggest that the carbapenem C-6 hydroxyethyl side chain in the AEC preferentially adopts three main conformations (**Figure 28**).

Conformation **I** is observed in the AEC derived from OXA-1 and doripenem (PDB code: 3isg) (168). In conformation **I**, the C-6 hydroxyethyl hydroxyl group is situated between the carbamylated lysine and the carbonyl group of the AEC. The C-9 methyl group is oriented near a valine residue (Val117 in OXA-1, Val120 in OXA-48, Val128 in OXA-23). The hydroxyl group and the AEC ester carbonyl are apparently positioned for favourable 4-exo-trig (using the Baldwin rule's (169)) cyclisation according to the Bürgi-Dunitz trajectory, which would result in β-lactone formation (**Figure 27**). In addition, this 'lactone-forming conformation' likely blocks the entry of water into the active site.

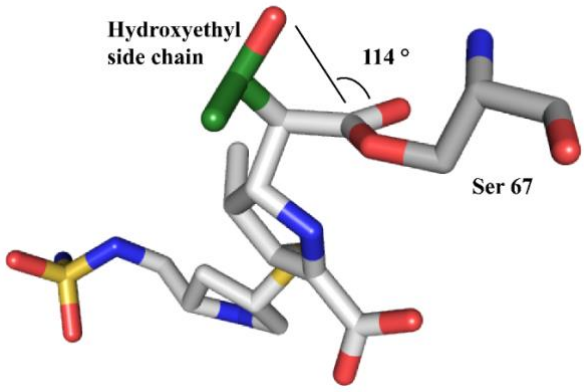

Figure 27. Orientation of the hydroxyl group of the C-6 hydroxyethyl side chain relative to the acyl-enzyme ester carbonyl in OXA-1 AEC with doripenem (PDB code: 3isg) (168)**.** Conformation **I** may represent a conformation close to that relevant for β-lactone formation, because this conformation positions the nucleophile at an angle close to the Bürgi–Dunitz trajectory (107°) (170). The figure is adapted from Aertker, K. M. J. et al. (2020) *J. Biol. Chem.* **295**, 16604–16613.

The C-6 hydroxyethyl conformation **II** is observed in PDB entries including that for OXA-1 with doripenem (PDB code: 3isg) (168) and for OXA-48 with imipenem (PDB 5qb4) (87). The hydroxyl group is oriented towards a valine residue (Val117 in OXA-1, Val120 in OXA-48, Val128 in OXA-23), and the H-8 of the C-8 of the C-6 hydroxyethyl side chain is oriented towards the anticipated position of the hydrolytic water.

Conformation **III** is observed in almost all of the AEC structures that lack a carbamylated lysine. However, there are recent AEC structures of OXA-10 with ertapenem and imipenem, and OXA-10 V117L with meropenem that adopt conformation **III** despite the presence of a carbamylated lysine (171). In conformation **III**, the hydroxyl group of the C-6 hydroxyethyl side chain is oriented towards the conserved tryptophan (Trp113 in OXA-23, Trp105 in OXA-48, Trp102 in OXA-1), and the C-9 methyl group is placed between the carbamylated lysine and the ester carbonyl of the AEC. Based on these analyses, neither conformation **II** or **III** is likely relevant for β-lactone formation, and conformation **II** likely reflects the most relevant conformation for hydrolysis of the AEC.

It is not clear to what degree these crystallographically observed structures resemble the catalytically relevant structures and conformations in solution. Notably, some of these structures do not have a carbamylated lysine due to the low pH used for crystallography, or due to substitution in the active site to generate a deacylation deficient enzyme (90, 172). The uncarbamylated structures are not expected to represent catalytically active complexes, as lysine carbamylation is critical for hydrolysis and β-lactone formation (173, 174). Furthermore, carbamylation is a reversible modification, and might be disfavoured in the crystalline state (80).

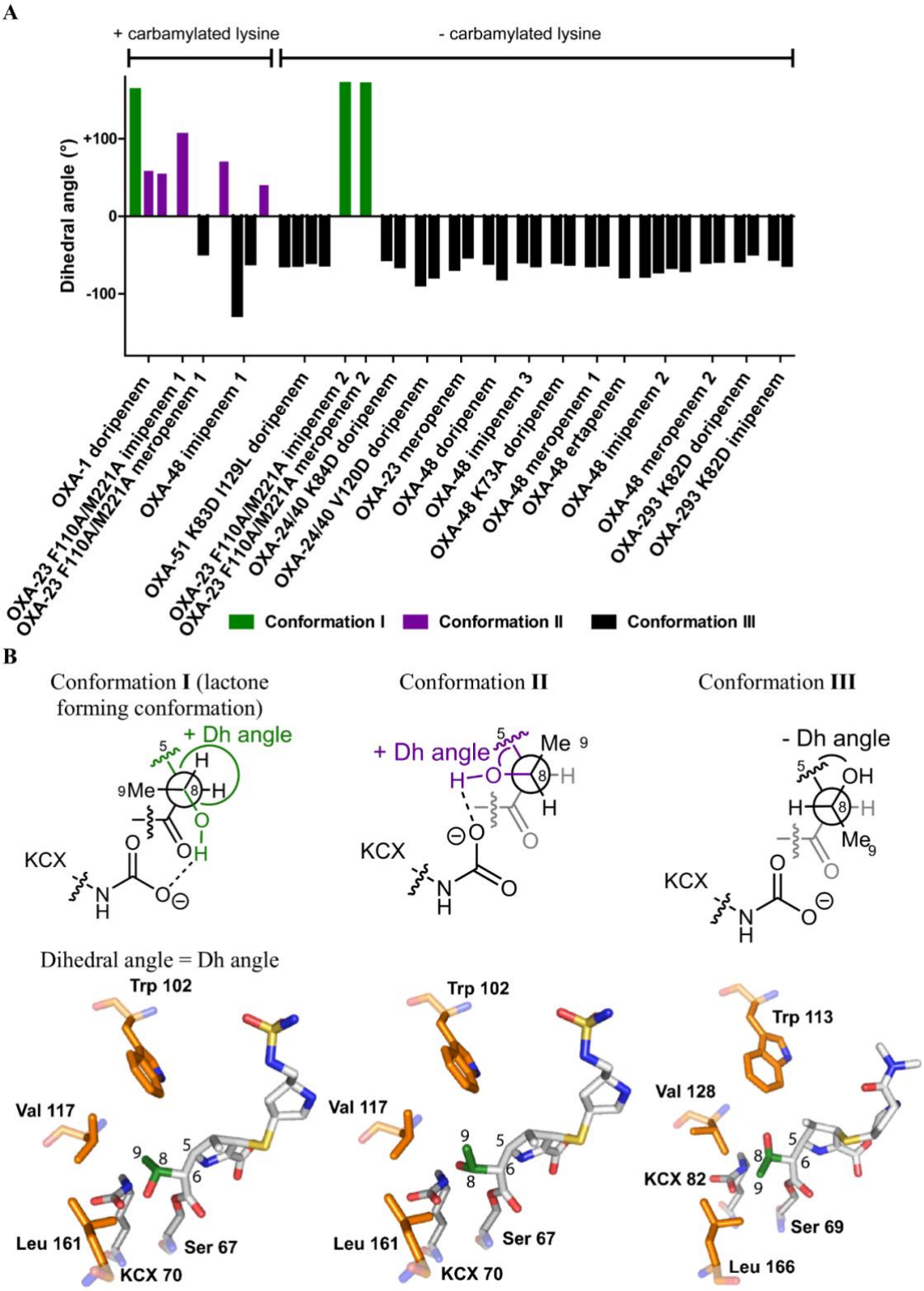
A
+ carbamylated lysine
- carbamylated lysine
Dihedral angle (°)
+100
0
-100
OXA-1 doripenem
OXA-23 F110A/M221A imipenem 1
OXA-23 F110A/M221A meropenem 1
OXA-48 imipenem 1
OXA-51 K83D I129L doripenem
OXA-23 F110A/M221A imipenem 2
OXA-23 F110A/M221A meropenem 2
OXA-24/40 K84D doripenem
OXA-24/40 V120D doripenem
OXA-23 meropenem
OXA-48 doripenem
OXA-48 imipenem 3
OXA-48 K73A doripenem
OXA-48 meropenem 1
OXA-48 ertapenem
OXA-48 imipenem 2
OXA-48 meropenem 2
OXA-293 K82D doripenem
OXA-293 K82D imipenem
Conformation I
Conformation II
Conformation III
B
Conformation I (lactone forming conformation)
Conformation II
Conformation III
+ Dh angle
- Dh angle
KCX
Dihedral angle = Dh angle
Trp 102
Val 117
Leu 161
Ser 67
KCX 70
Trp 113
Val 128
KCX 82
Ser 69
Leu 166

Figure 28. Crystallographically observed conformations of the carbapenem C-6 hydroxyethyl side chain. **A.** Dihedral angles (Dh angles) of the carbapenem hydroxyethyl side chain H-O C-8 C-6 C-5 in the AECs of class D SBLs and carbapenems, in the presence and absence of a carbamylated lysine. The crystal structures were analysed: OXA-1 with doripenem, pH 7.5 (PDB code: 3ISG) (168), OXA-23 F110A, M221A with imipenem, pH 7.0 (PDB code: 6N6X) (91), OXA-23 F110A, M221A with meropenem, pH 7.0 (PDB code: 6N6Y) (91), OXA-23 F110A, M221A with meropenem, pH 4.1 (PDB code: 6N6V) (91), OXA-23 F110A, M221A pH 4.1 with imipenem, (PDB code: 6N6U) (91), OXA-24/40 K84D with doripenem, pH 8.5 (PDB code: 3PAE) (173), OXA-24/40 V130D with doripenem, pH 8.5 (PDB code: 3PAG) (173), OXA-23 with meropenem, pH 4.1 (PDB code: 4JF4) (90), OXA-51 K83D, I129L with doripenem, pH 6.5 (PDB code: 5L2F) (175), OXA-13 with imipenem (PDB code: 1H5X) (176), OXA-48 with imipenem, pH 7.5 (1) (PDB code: 5QB4) (87), OXA-48 K73A with doripenem, pH 4.0 (PDB code: 6PXX) (174), OXA-48 with ertapenem, pH 4.0 (PDB code: 6P99) (172), OXA-48 with imipenem, pH 4.0 (3) (PDB code: 6P97) (172), OXA-48 with meropenem, pH 4.0 (1) (PDB code: 6P98) (172), OXA-48 with doripenem, pH 4.0 (PDB code: 6P9C) (172), OXA-48 with imipenem, pH 4.6 (2) (PDB code: 6PTU) (177), OXA-48 with meropenem, pH 4.6 (2) (PDB code: 6PT1) (178), OXA-239 K82D with doripenem, pH 4.2 (PDB code: 5WI7) (179), OXA-239 K82D with imipenem, pH 4.2 (PDB code: 5WIB) (179). This work indicates that the carbamylation of lysine impacts the conformation of the C-6 hydroxyethyl side chain. **B.** View of C-6 hydroxyethyl conformations in the OXA-1 AEC with doripenem (conformation **I** and conformation **II**) and the OXA-23 F110A/M221A AEC with meropenem (conformation **III**), showing the dynamic nature of the C-6 hydroxyethyl side chain. The figure is adapted from Aertker, K. M. J. et al. (2020) *J. Biol. Chem.* **295**, 16604–16613.

2.2.8 Bioinformatic analysis

The Beta-Lactamase DataBase (BLDB) is a publicly available database that compiles all clinically related and naturally occurring β-lactamases sequences, including all of the subfamilies and their variants (38). The BLDB currently comprises more than 930 class D SBLs, of which many are reported to be carbapenemases (last updated in June 2020). The identity of the residue in position 120 (OXA-48 numbering) in these sequences was analysed using the sequence alignment provided by the BLDB. The most common substitution is Val-to-Ile, which occurs in 39% (363 Class D SBLs) of all class D β-lactamases. This substitution occurs commonly in the OXA-51 and OXA-213 class D SBLs subfamilies and occurs once in the OXA-12 subfamily. This analysis also revealed that 2% (19 Class D SBLs) of all sequences have a Val-to-Leu substitution, which occurs in eight different class D SBLs subfamilies: OXA-51 (6 variants), OXA-62 (3 variants), OXA-153 (1 variant), OXA-157 (1 variant), OXA-156 (3 variants), OXA-493 (2 variants), OXA-48 (2 variants), and OXA-10 (1 variant).

2.3 Discussion

The work described in this chapter aimed to investigate the factors governing the mechanism of carbapenem degradation by class D SBLs, focusing on the amino acid residues that interact with the C-6 hydroxyethyl side chain of the carbapenems in the AEC (**Figure 16**). One of the obtained variants, OXA-48 V120L, is a clinically observed carbapenemase (151), and the studies on these enzymes may provide insight into the emerging carbapenem resistance associated with class D SBLs.

Previous mechanistic studies indicate that, at least for some class D SBLs (e.g. OXA-10), the deacylation of the AEC is the rate limiting step (89). This led to the proposal that β-lactone formation may occur when the lifetime of the AEC is relatively long. Although the stability of the AEC might play a role, the results of the work described, hence suggest that direct interactions between the C-6 hydroxyethyl side chain and active site residues influence the ratio of hydrolysis to β-lactone formation. In particular, the product outcome is likely determined by the ratio of C-6 hydroxyethyl conformation **I** (relevant for β-lactone formation) and C-6 hydroxyethyl conformation **II** (relevant for hydrolysis) (**Figure 28**).

The proposed molecular mechanism of carbapenem degradation is clearly reflected by substitutions at position 120 (OXA-48 numbering) which occur in a hydrophobic pocket important for the stability of the catalytically important carbamylated lysine residue (89). While OXA-48 V120L and wild-type OXA-48 favoured β-lactone formation, the V120I variant clearly favoured hydrolysis (**Figure 22**). Notably, the OXA-48 V120I variant showed the greatest extent of hydrolysis of the tested enzymes, and OXA-48 V120L (also known as OXA-519, a clinically observed enzyme) produced the largest amount of β-lactones of all the enzymes tested. In addition, OXA-519 also produced low level of β-lactones derived from carbapenems with 1β-hydrogen substituents (e.g. imipenem and

panipenem). Similar product profiles were observed for wild-type OXA-23 and the V128L and V128I variants (**Figure 26**).

Conservative substitutions were carried out for Leu158 in OXA-48. The OXA-48 L158I and L158V variants were both observed to have decreased carbapenemase activity, and to produce less β-lactones, suggesting that these substitutions disfavour the lactone-forming conformation **I** of the carbapenem C-6 hydroxyethyl side chain (**Figure 22**). Previous crystallographic studies on OXA-23 suggest that the leucine residue in this position may act as a "water-gate residue", which provides access of the hydrolytic water to the active site (25). The results presented in this chapter are consistent with this proposed role of Leu158. Isoleucine and valine residues both have β-branched side chains, whereas leucine has a branch further from the backbone on the γ-carbon. The bulky β-branched side chains may block the access of water to the active site, and stabilise the AEC resulting in a lower k_{cat} for the OXA-48 L158I and L158V variants.

The observations made for the OXA-48 Trp105 variants further validated the results with the other variants (OXA-48 V120I, V120L, L158V and L158I). Most class D SBLs have a so-called hydrophobic bridge over the active site, which involves the α3-α4 and β6-β7 loops and is responsible for substrate/intermediate interactions (**General Introduction**, **Section 1.7**) (91). While OXA-48 does not appear to have an analogous bridge (63), the α3-α4 loop which bears Trp105 may be involved in similar substrate/intermediate interactions. The W105F and W105A variants do not show preferential β-lactone formation (**Figure 22**), and OXA-48 W105A appears to be impaired with the deacylation step (**Figure 20**).

A significant difference in the rate of degradation of carbapenems with and without 1β-methyl substituent by class D SBLs was observed, with the latter being degraded significantly faster, consistent with previous studies (180). The steric hindrance associated

with the 1β-methyl substituent based on computational studies as described in **Section 2.1.2** appears to impact the rotational freedom of the C-6 hydroxyethyl side chain, potentially disfavouring the conformation **II** required for hydrolysis and favouring the β-lactone-forming conformation **I** (**Figure 28**).

Overall, the class D SBLs react via a two-stage process involving the formation an AEC. Subsequent deacylation of the AEC then occurs to produce hydrolysed carbapenem and β-lactones. The results presented here show β-lactone formation for all clinically used carbapenems, including those with a 1β-hydrogen substituent. The β-lactone forming process of deacylation is mechanistically interesting because it implies Class D SBLs can enable resistance without a hydrolytic step. Importantly, the clinically observed OXA-48 V120L variant (151) was observed to efficiently degrade carbapenems, while also substantially favouring β-lactone formation over hydrolysis. These results suggest that that SBL-catalysed β-lactam degradation via β-lactone rearrangement may represent a clinically relevant mechanism for antibiotic resistance. Future work could focus on investigating the potential link between β-lactone formation and carbapenemase activity and whether or not the β-lactone forming process for degrading the AEC is an evolving aspect of class D SBLs, and potentially, other β-lactamase classes.

Chapter 3 – Molecular Mechanism of 1β-methyl substituted β-Lactones with Class D SBLs and their Inhibition Activity

3.1 Introduction

To date, the most widely used class of antibiotics is the β-lactams (8). β-Lactamase-mediated resistance is the best characterised resistance mechanism against β-lactam antibiotics in Gram-negative bacteria. β-Lactamases are grouped into Ambler classes A, C and D SBLs and class B MBLs according to their molecular mechanisms, sequences, structures, and substrate selectivity, as described in the **General Introduction, Section 1.5** (181, 182). The SBLs (i.e. classes A, C and D) are proposed to have evolved from a common ancestor (79), whereas class B MBLs have a different evolutionary path.

Multidrug-resistant bacteria that produce ESBLs, carbapenemases, and/or multiple β-lactamases are becoming more prevalent, and are responsible for suffering, disability, and death (44, 45). The use of inhibitors to target β-lactamases is an important approach to overcome pathogens that produce β-lactamases. Therapy with a small molecule inhibitor of β-lactamases in combination with a β-lactam antibiotic is a common treatment for multidrug-resistant infections, and new combinations are currently in clinical trials (**Table 5**) (183–187).

Table 5. Combinations of β-lactamase inhibitors and β-lactam antibiotics that are clinically approved or are in clinical trials (adapted from (188)**.**

Class of inhibitor	**Inhibitor**	**β-lactam antibiotic**	**Approved or in clinical development**	**Inhibit**
β-Lactam	Clavulanic acid	Amoxicillin Ticarcillin	Approved (Augmentin) Approved (Timentin)	ESBLs
	Sulbactam	Ampicillin	Approved (Unasyn)	ESBLs
	Tazobactam	Piperacillin Cefepime Ceftolozane	Approved (Zosyn/Tazocin) Approved outside the US Approved (Zerbaxa)	ESBLs
	Enmetazobactam	Cefepime	Clinical trials	ESBLs
DBO	Avibactam	Ceftazidime	Approved (Avycaz/Zavicefta)	ESBLs, AmpC, KPC, OXA-48
		Aztreonam	Clinical trials	ESBLs, AmpC, KPC, OXA-48, MBLs
	Relebactam	Imipenem	Clinical trials	ESBLs, AmpC, KPC
	Nacubactam	Meropenem	Clinical trials	ESBLs, AmpC, KPC
	Zidebactam	Cefepime	Clinical trials	ESBLs, AmpC, KPC
	ETX2514	Sulbactam	Clinical trials	ESBLs, AmpC, KPC, OXA-48
Boronic acid	Vaborbactam	Meropenem	Approved (Vabomere)	ESBLs, AmpC, KPC
	VNRX-5133	Cefepime	Clinical trials	ESBLs, AmpC, KPC, OXA-48, MBLs

The first clinically approved β-lactamase inhibitor used in combination with a β-lactam antibiotic was clavulanic acid, a β-lactam containing natural product (**Table 5**, **Figure 29**)

(189). Clavulanic acid has insufficient antibacterial activity to be used alone against most bacteria but is a potent inhibitor of some class A SBLs. The mode of action of this β-lactamase inhibitor involves mechanism-based irreversible inhibition (190, 191). Clavulanic acid reacts with the nucleophilic serine in the active site of SBLs, forming a transient AEC. Subsequently, the clavulanic acid-derived AEC can undergo different reactions. One pathway yields hydrolysed clavulanic acid and catalytically active enzyme, while (an) alternative fragmentation pathway(s) lead(s) to inactivated enzyme complexes. The latter is responsible for the irreversible inhibition of class A SBLs by clavulanic acid. While clavulanic acid inhibits some SBLs, the clinical rise of other SBLs means that its activity is increasingly limited, e.g. it is a poor inhibitor of the class A carbapenemase KPC and other clinically important SBLs (191).

The clinical success of clavulanic acid inspired pharmaceutical companies to develop the β-lactam-based β-lactamase inhibitors sulbactam and tazobactam (**Figure 29**), which are proposed to act through related fragmentation mechanisms (192, 193). Both of these penicillin sulfone inhibitors have a similar activity profile to clavulanic acid (193–195). All three β-lactam-based inhibitors are approved for clinical use in combination with particular penicillins and cephalosporins (**Table 5**) (196–198).

Avibactam, the first clinically used non-β-lactam containing SBL inhibitor, has a diazabicyclo[3.2.1]octanone (DBO) core scaffold (**Figure 29**). In contrast to the established β-lactam containing SBL inhibitors, avibactam has a broader spectrum of activity and inhibits SBLs belonging to classes A, C, and, in some cases, class D. The inhibition mechanism for avibactam differs from that of the β-lactam-based inhibitors. Avibactam acts as a reversible inhibitor with a high binding affinity for the SBL active site, rapidly reacting with the nucleophilic serine (199). This covalent complex can undergo slow deacylation through a recyclisation mechanism, resulting in the recovery of catalytically active enzyme and intact

avibactam (199, 200). Avibactam has been approved for use in combination with ceftazidime, and has demonstrated efficacy against Enterobacterales and *Pseudomonas aeruginosa* that produce ESBLs, KPCs, AmpC, and the class D carbapenemase OXA-48 (201, 202) (**Table 5**). This inhibitor-antibiotic combination is an important alternative to carbapenems, which are often last resort drugs for the treatment of multidrug-resistant infections, e.g. carbapenem-resistant Enterobacteriaceae (CRE) (203, 204).

One promising class of new β-lactamase inhibitors are boronic acids (205) (**Figure 29**). Such inhibitors can interact with the active sites of both SBLs and MBLs, mimicking the anionic tetrahedral intermediate formed during β-lactam degradation. In 2017, the boronic acid vaborbactam was approved for use in combination with meropenem to treat infections caused by *E. coli*, *K. pneumoniae*, and *Enterobacter cloacae* (206). Vaborbactam is active against class A, C, and a few class D SBLs, but not against class B MBLs (207, 208) (**Table 5**). A bicyclic boronic acid VNRX-5133 demonstrates inhibitory activity against all classes of SBLs as well as some clinically important MBLs, such as VIM-1/2 and NDM-1 (209). The combination of cefepime and VNRX-5133 is currently in phase III clinical trials for the treatment of infections caused by Enterobacteriaceae and *P. aeruginosa* that produce ESBLs and carbapenemases.

Although β-lactamase inhibitors have been successfully used to tackle SBL-mediated resistance, resistance against these inhibitor-antibiotic combinations has emerged (210–212). There are no clinically used MBL inhibitors. Because of this, the development of new β-lactamase inhibitors remains an unmet medical need.

As mentioned in the **General Introduction**, **Section 1.7** class D SBLs have been recently reported to degrade 1β-methyl substituted carbapenems to yield β-lactones. *In vitro* inhibition studies with β-lactones (**Figure 29**) indicate that they can inhibit both SBLs and potentially some MBLs to varying degrees (88). These initial studies did not fully characterise

the inhibitory potency of β-lactones against β-lactamases. The aim of the work described in this chapter was to further investigate the inhibitory activity of carbapenem-derived β-lactones against SBLs and MBLs. Furthermore, the molecular interactions between class D SBLs and β-lactones remains to be fully explored. An understanding of the mechanisms may help to develop new strategies for β-lactamase inhibition, and possibly employing the β-lactone scaffold as a novel class of inhibitors.

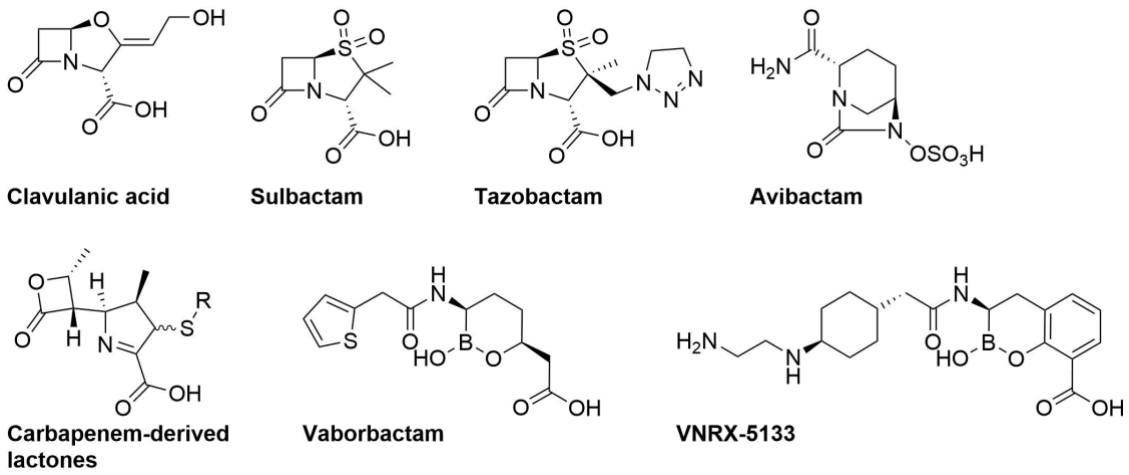

Figure 29. Structures of β-lactamase inhibitors.

Specific aims of this work were as follows:

1. To optimise the production and purification of carbapenem-derived β-lactones.

2. To investigate the inhibitory potency of carbapenem-derived β-lactones against SBLs and MBLs.

3. To understand the mode by which β-lactones inhibit class D SBLs with the sub-aims of:
    a. Evaluating the stability of β-lactones and carbapenems with class D SBLs.
    b. Developing an efficient mass spectrometric based assay that enables investigating on the acylation and deacylation of class D SBLs by β-lactones.

3.2 Results

3.2.1 Protein production

The recombinant β-lactamases OXA-10$_{20\text{-}266}$ (referred as OXA-10), OXA-48, OXA-23, TEM-1, VIM-1, VIM-2, IMP-1, NDM-1, and AmpC were provided by Mr. H. T. Henry Chan, Ms. Pauline Lang, Dr. Patrick Rabe, Dr. Christopher Lohans and Dr. Karina Calvopina Tapia.

3.2.2 β-Lactone production and purification

A procedure for the preparation of ertapenem-derived β-lactones (erta-β-lactones) had been previously developed by Dr. Christopher Lohans (88). This procedure involved production of the β-lactones with wild-type OXA-48 with subsequent purification by HPLC and resulted in relatively low yield. Furthermore, the procedure may leave residual levels of trifluoroacetic acid (TFA) from the HPLC purification, which was considered might interfere with inhibition assays and crystallographic studies. Previous work by Mr. H. T. Henry Chan and Dr. Christopher Lohans showed that the OXA-48 variant OXA-48 S70C reacted with carbapenems to preferentially give β-lactones rather than hydrolysis products to a greater extent compared to wild-type OXA-48 (unpublished data), meaning OXA-48 S70C would be a useful catalyst for β-lactone production.

To optimise the yield of β-lactones produced by OXA-48 S70C, different conditions for β-lactone production were screened by Ms. Emily I. Freeman under my laboratory supervision. To improve β-lactone production, the incubation time, incubation temperature, and varying enzyme:substrate ratios were optimised, assessing β-lactone formation by ^{1}H NMR (600 MHz) spectroscopy (**Figure 30**). Previous chemical shift assignments for

meropenem, (*S*)-Δ^1 and (*R*)-Δ^1 epimers of meropenem-derived β-lactones (mero-β-lactones) and hydrolysed meropenem products were used as a reference (167). The improved conditions for production of the mero-β-lactones involved a 48 h incubation of 25 µM OXA-48 S70C with 10 mM meropenem at room temperature (**Material and Methods**, **Section 6.4**; **Figure 30**). Under these conditions, meropenem was fully converted using a relatively small amount of OXA-48 S70C.

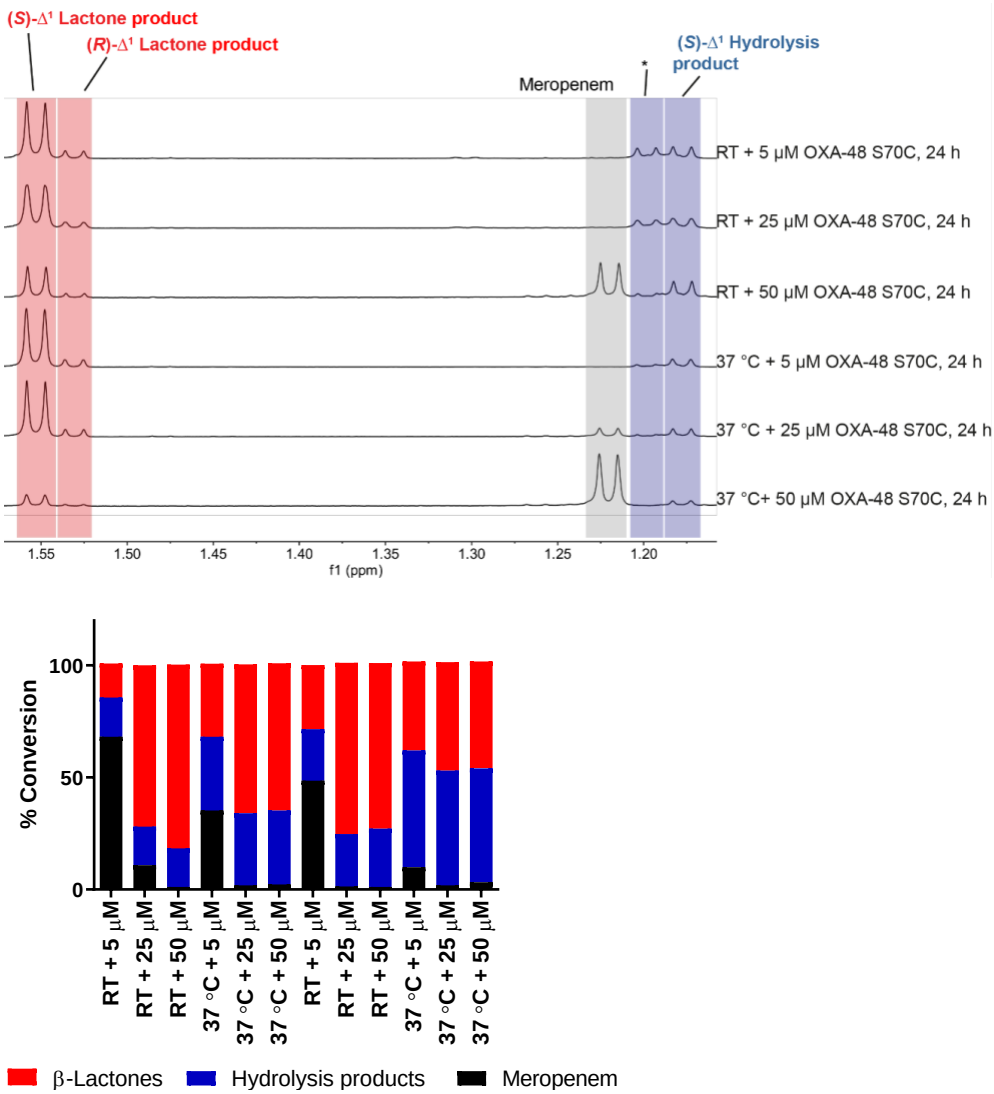

Figure 30. Optimisation of mero-β-lactones production. ^{1}H NMR spectra of different screening conditions. Different enzyme concentrations, temperatures, and incubation times were used. * indicates a new peak of apparent new product formed by OXA-48 S70C. This product was not further characterised. Peaks of meropenem, hydrolysis products and mero-β-lactones including new product were integrated using MestreNova 12.0.3. Optimised assay conditions for production of mero-β-lactones: 10 mM meropenem, 25 µM OXA-48 S70C in 50 mM phosphate pH 7.5, and 10% D_2O. RT = room temperature. The data have been generated with Ms. Emily I. Freeman Ms. Emily I. Freeman.

To obtain purified mero-β-lactones without TFA contamination, buffers, salts, and hydrolysis products were removed as described in detail in the **Material and Methods**, **Section 6.4**. In brief, in the first step, the enzyme was removed by collecting the filtrate of an Amicon ultracentrifugal filter. In the second step, a C18 Sep-Pak column was used to isolate the β-lactones. The reaction mixture was loaded onto the C18 Sep-Pak column and centrifuged, the mixture on the column was washed with water. Due to the more hydrophilic properties of the meropenem-derived hydrolysis products, these were first eluted from the C18 Sep-Pak column. Then, the mero-β-lactones on the column were eluted with 25% (v/v) aqueous acetonitrile (**Figure 31**). The yield of the purified mero-β-lactones was 44% from meropenem.

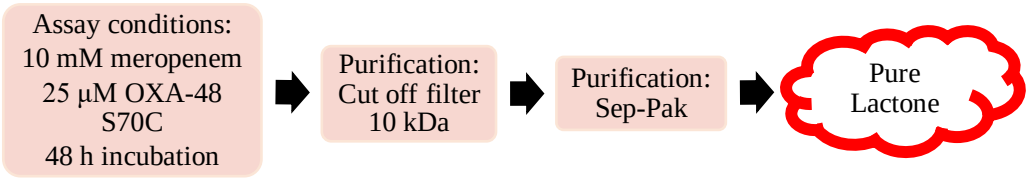

Figure 31. Mero-β-lactones purification strategy. This strategy provided >95% pure mero-β-lactones as determined by ^{1}H-NMR (600 MHz).

The purified mero-β-lactones were analysed by ^{1}H-NMR (600 MHz) to confirm that they had been separated from meropenem and meropenem hydrolysis products (**Figure 32A**). A 2D ^{1}H-^{1}H COSY spectrum was collected to confirm the absence of residual meropenem (**Figure 32B**), which would significantly impact inhibition and mechanistic studies. The ^{1}H-NMR and 2D ^{1}H-^{1}H COSY spectra revealed trace amount of hydrolysis product(s), but no evidence for the presence of meropenem (**Figure 32**). In addition, the NMR spectra revealed that mero-β-lactones exist as a mixture of (*S*)-Δ^{1} and (*R*)-Δ^{1} imine mero-β-lactones in a ratio of 5:1, which is consistent with what has been previously observed with the ertapenem-derived β-lactones (88). The separation by HPLC of the two (*S*)-Δ^{1} and (*R*)-Δ^{1} imine epimers of mero-β-lactones resulted in rapid tautomerisation giving the same 5:1 epimeric mixture of mero-β-lactones.

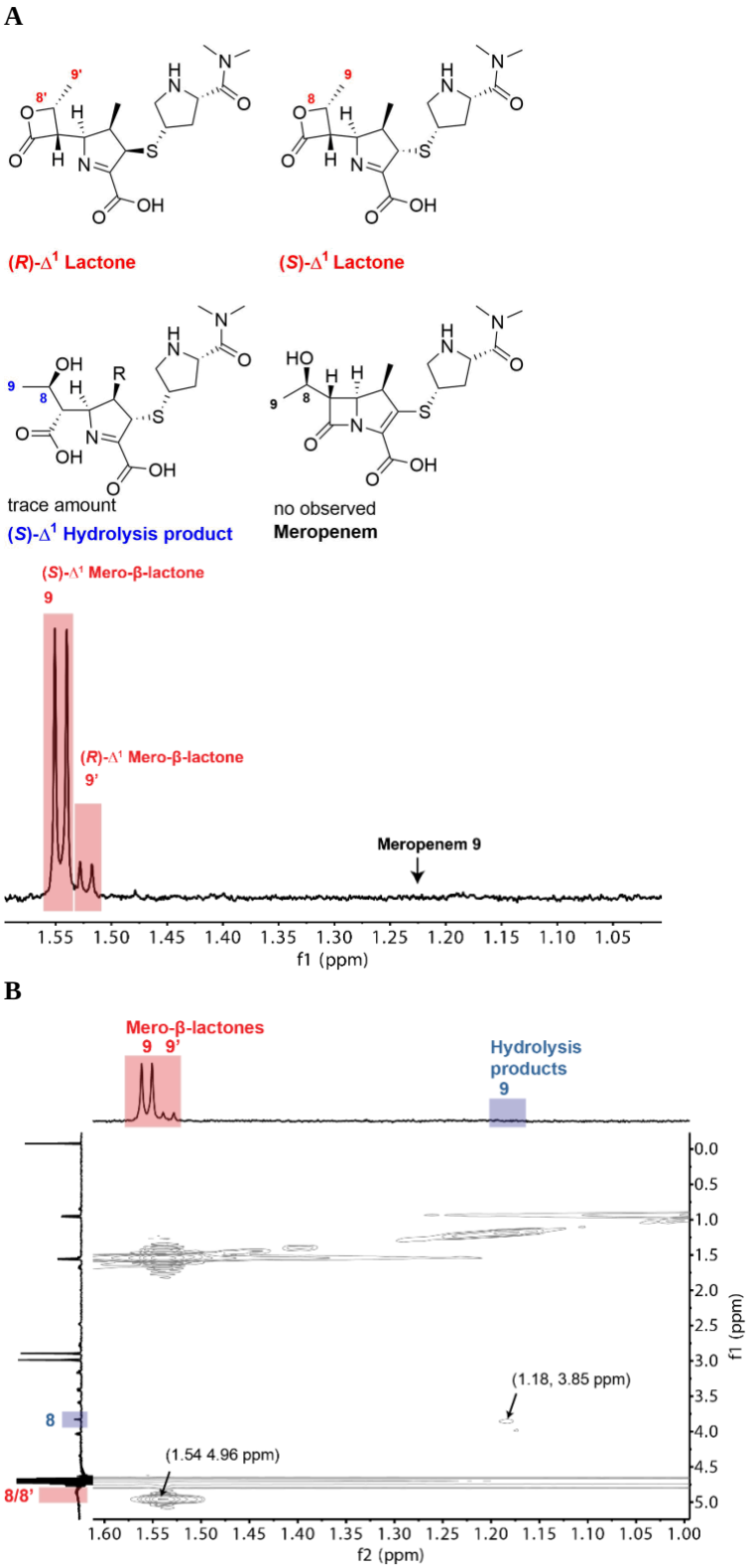

Figure 32. ^{1}H and 2D ^{1}H-^{1}H COSY NMR spectra of the purified mero-β-lactones. A. ^{1}H NMR (600 MHz) spectrum of purified mero-β-lactones showing the H-9 methyl region. **B.** The 2D ^{1}H-^{1}H COSY NMR spectrum revealed a correlation between H-9 (1.54 ppm) and H-8 (4.96 ppm) for mero-β-lactones, and a weak correlation between H-9 (1.18 ppm) and H-8 (3.85 ppm) for the meropenem hydrolysis products. There was no correlation of H-9 (1.23 ppm) and H-8 (4.19 ppm), which would indicate the presence of intact meropenem. Full ^{1}H NMR spectrum of mero-β-lactones is given in **Figure 81**.

3.2.3 Inhibition of SBLs and MBLs by β-lactones

The inhibitory potency of both the mero-β-lactones and meropenem against SBLs and MBLs, representing a broad range of β-lactamases were investigated. The panel of SBLs and MBLs tested included enzymes in Ambler classes A (TEM-1), B (VIM-1, VIM-2, IMP-1, and NDM-1), C (AmpC), and D (OXA-10, 23, and 48).

To quantify inhibitor potency, the negative log of the half maximal inhibitory concentration (pIC_{50}) was measured. The half maximal inhibitory concentration (IC_{50}) is defined as the inhibitor concentration that inhibits enzymatic activity by 50%. To determine the pIC_{50} of an inhibitor, the impact of different inhibitor concentrations on enzyme activity is determined and a dose-response curve is plotted. The dose-response experiments were performed by Dr. Karina Calvopina Tapia, using a previously reported fluorogenic assay (213). The impact of inhibitors on enzymatic activity was measured using a microplate reader by monitoring hydrolysis of the fluorogenic coumarin-linked substrate FC-5 under the following conditions (**Table 6**).

Several factors need to be considered for the measurement of pIC_{50} values:

- The influence of inhibitor on enzyme activity is measured at an enzyme concentration and time point in which the enzyme activity is linear.
- For pIC_{50} experiments with MBLs, the conditions were chosen to provide non-limiting conditions of the co-factor Zn(II), which is required for the activity.
- Note that pIC_{50} values are dependent on enzyme concentration and the assays were performed with different concentrations, hence the values cannot be directly compared amongst different enzymes, though K_i values can be calculated from pIC_{50}.

Table 6. Assay conditions for the determination of inhibitor pIC_{50} values with a panel of SBLs and MBLs using the fluorogenic substrate FC-5 (213).

Substrate	FC-5	5 µM
Enzyme	TEM-1*	1 nM
	VIM-1**	500 pM
	NDM-1**	20 pM
	VIM-2**	100 pM
	IMP-1**	20 pM
	AmpC*	500 pM
	OXA-10*	250 pM
	OXA-23*	12.5 nM
	OXA-48*	12.5 nM
Inhibitor	Highest [40 µM] Lowest [2 nM], 10 x 1 in 3 dilutions	

*100 mM Sodium phosphate, pH 7.4, 0.01% (v/v) Triton X-100 **50 mM Hepes, pH 7.2, 10 µM $ZnSO_4$, 1 µg ml^{-1} BSA, 0.01% (v/v) Triton X-100.

First, the dose-response curves for reported small molecule inhibitors were determined and compared with literature values. *L*-Captopril inhibits the class B1 MBLs, such as VIM-1, NDM-1, VIM-2, and IMP-1, while avibactam and the bicyclic boronate CB2 inhibits TEM-1, AmpC, OXA-10, OXA-23, and OXA-48 (**Figure 33**) (37, 40–42).

The measured potencies of the reported inhibitors were almost in agreement with previously reported pIC_{50} values (**Table 7**) (80, 88, 214, 215). The pIC_{50} value obtained for OXA-23 and avibactam was lower than the reported value (literature pIC_{50} 6.3 (80), measured pIC_{50} <4.4), potentially because the enzyme was degraded or aggregated. Due to the poor reproducibility of OXA-23 inhibition by avibactam, OXA-23 was excluded from further inhibition experiments. The pIC_{50} values of meropenem and the mero-β-lactones with the different SBLs and MBLs are shown in **Table 7** and the corresponding dose response curves are shown in **Figure 82**.

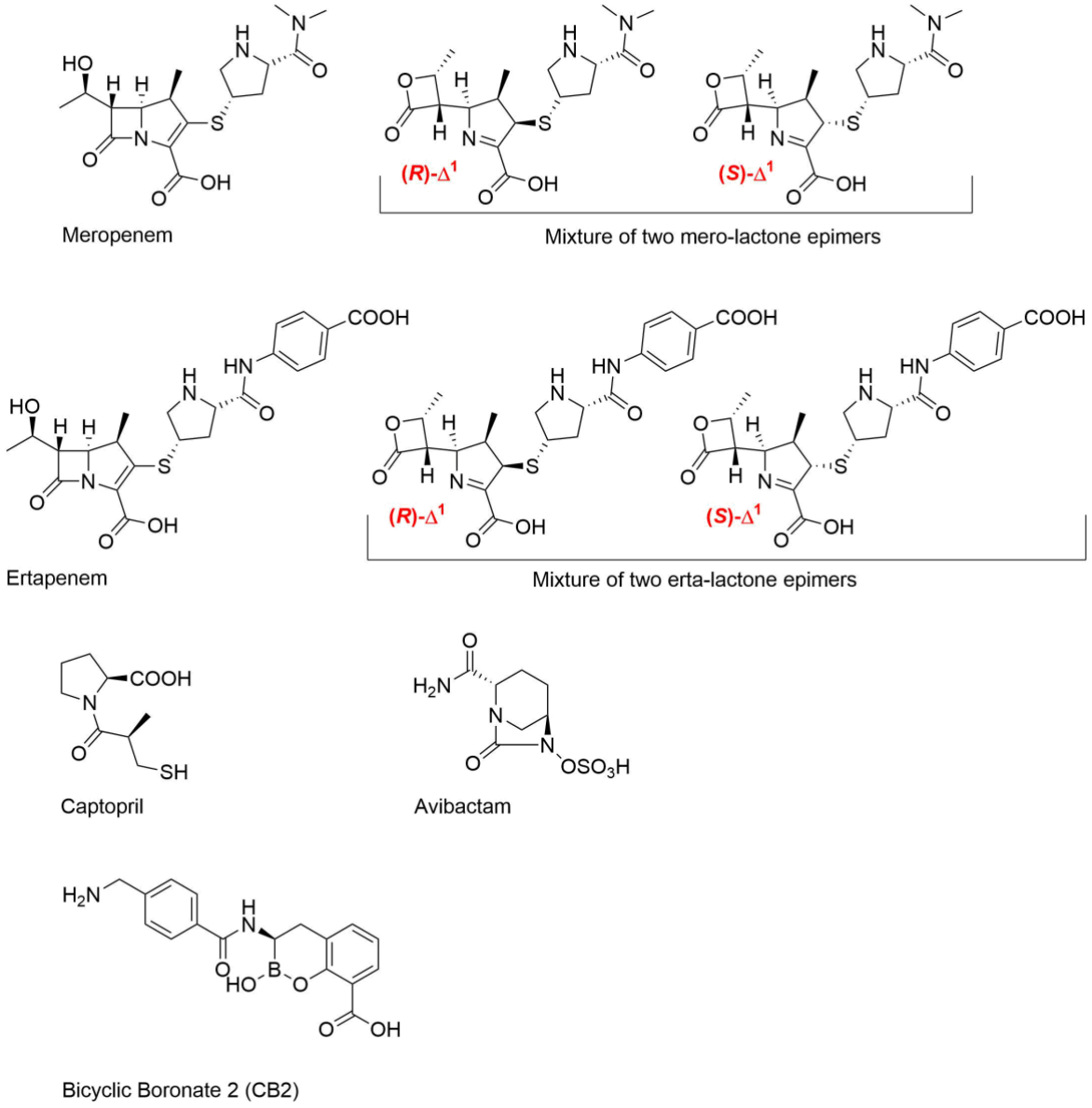

Figure 33. Structures of inhibitors related to work involving inhibition of SBLs and MBLs.

Table 7. **Inhibitory activity of mero-β-lactones and meropenem against a panel of SBLs and MBLs.** *L*-Captopril, avibactam, and CB2 were used as reference inhibitors. The assay conditions are described in **Table 6**. Errors were calculated as standard deviations of the mean of three or four independent measurements. The data have been generated by Dr. Karina Calvopina Tapia.

A

		pIC_{50}			
Incubation time (min)	Compound	TEM-1	Lit. values	AmpC	Lit. values
20	Avibactam	8.7 ± 0.12		6.9 ± 0.01	
	CB2	8.1 ± 0.02	8.4 (214)	6.9 ± 0.01	6.9 (216)
	Meropenem	6.3 ± 0.12		5.6 ± 0.01	
	Mero-β-lactones	<3.4 ± ND		<3.4 ± ND	

B

		pIC_{50}			
Incubation time (min)	Compound	VIM-1	NDM-1	VIM-2	IMP-1
20	*L*-Captopril	4.4 ± 0.04	4.4 ± 0.02	5.1 ± 0.04	5.3 ± 0.07
			(3.8)*	(5.4)*	(4.6)*
	Meropenem	4.1 ± 0.04	4.0 ± 0.04	5.2 ± 0.03	5.5 ± 0.06
	Mero-β-lactones	<3.4 ± ND	<3.4 ± ND	<3.4 ± ND	<3.4 ± ND

* Reported pIC_{50} values (215).

C

	pIC_{50}						
Incubation time (min)	Compound	OXA-10	Lit. values	OXA-23	Lit. values	OXA-48	Lit. values
0	Avibactam	<4.4 ± ND	<4 (80)	<4.4 ± ND	6.3 (80)	5.6 ± 0.02	5.8 (80)
	CB2	5.1 ± 0.05				4.8 ± 0.01	
	Meropenem	7.9 ± 0.01				6.3 ± 0.01	
	Mero-β-lactones	5.1 ± 0.04				5.1 ± 0.02	
	Ertapenem*	8.7				8.0	
	Erta-β-lactones*	6.1				6.0	
20	Avibactam	4.6 ± 0.02	4.7** (80)	4.8 ± 0.01	7.3** (80)	6.3 ± 0.02	6.3** (80)
	CB2	5.1 ± 0.04	5.2 (214)			4.8 ± 0.03	
	Meropenem	8.4 ± 0.02				6.0 ± 0.01	
	Mero-β-lactones	5.6 ± 0.02				5.0 ± 0.03	

* pIC_{50} values have been previously reported and were added for direct comparison (88). **pIC_{50} values were measured after 10 min incubation time with avibactam.

For all of the SBLs and MBLs tested, meropenem was a more potent inhibitor than the mero-β-lactones (**Table 7**). No inhibition of TEM-1, Amp-C, VIM-1, NDM-1, VIM-2, and IMP-1 was observed under tested assay conditions in the presence of the mero-β-lactones (pIC_{50} < 3.4) (**Table 7A**, **B**). The results imply that β-lactones derived from 1β-methyl substituted carbapenems do not interact, react transiently, or react reversibly with these enzymes.

Against the class A and C SBLs the pIC_{50} values for meropenem were 5.6- 6.3, whereas the inhibition of the selected MBLs by meropenem was weaker (pIC_{50} 4.0- 5.5) (**Table 7A**, **B**). These observations indicate that although meropenem generally acts as a substrate for some β-lactamases, it can also act as an inhibitor, potentially due to slow hydrolysis or β-lactone formation.

So far, class D SBLs are the only β-lactamases that have been observed to degrade carbapenems through β-lactone formation (88). Consequently, it is important to understand the potency of mero-β-lactones on OXA-10 and OXA-48, which are clinically important class D SBLs (63, 74). The results show that the mero-β-lactones were weak inhibitors of OXA-10 and OXA-48 (pIC_{50} 5.1 ± 0.04 and 5.1 ± 0.02, respectively), whereas under the same conditions, meropenem inhibited these enzymes more potently with pIC_{50} values of 8.4- 6.0 (**Table 7C**).

The previous inhibition study of ertapenem and erta-β-lactones with class D SBLs has shown that these compounds also inhibited OXA-10 (pIC_{50} 8.7 for ertapenem, pIC_{50} 6.1 for erta-β-lactones) and OXA-48 (pIC_{50} 8.0 for ertapenem, pIC_{50} 6.0 for erta-β-lactones) (**Table 7C**) (88). Overall, the meropenem and the mero-β-lactones demonstrate a slightly lower potency with class D SBLs as ertapenem and the erta-β-lactones. This might be due to faster binding of ertapenem and the erta-β-lactones lactones compared to meropenem and the mero-β-lactones.

Previous work indicated that carbapenem-derived β-lactones can form an AEC with class D SBLs (88). The amount of time that the inhibitors are pre-incubated with the enzymes may impact on the inhibition results, promoting the formation of AECs derived from mero-β-lactones and meropenem. The same fluorogenic assays (**Table 6**) with longer pre-incubation time (20 min) were used. The findings show that the time dependent effect on potency varied (**Table 7C**). The potency of mero-β-lactones inhibition was increased against OXA-10 (pIC_{50} 5.6 ± 0.02 compared to pIC_{50} 5.1 ± 0.04) by longer pre-incubation period, while the potency against OXA-48 was relatively unaffected (pIC_{50} 5.0 ± 0.03 compared to pIC_{50} 5.1 ± 0.02) (**Table 7C**). The inhibition of OXA-10 by meropenem was also increased with longer incubation times (pIC_{50} 8.4 ± 0.02 compared to pIC_{50} 7.9 ± 0.01), while decreased inhibition of OXA-48 with meropenem was observed (pIC_{50} 6.0 ± 0.01 compared to pIC_{50} 6.3 ± 0.01).

The poor inhibition of class D SBLs by the erta-β-lactones and the mero-β-lactones despite acylation of these enzymes led to the proposal that class D SBLs might quickly degrade β-lactones due to efficient hydrolysis of the β-lactones. This proposal was then investigated by NMR studies.

3.2.4 Comparison of the stability of β-lactones and carbapenems in the presence of class D SBLs

The results of inhibition studies show that meropenem and mero-β-lactones act as inhibitors of OXA-10 and OXA-48 (**Table 7**). To investigate the relative stabilities of mero-β-lactones and meropenem in presence of OXA-10 and OXA-48, they were incubated with both enzymes at a 10:1 substrate: enzyme ratio and their degradation was monitored by ^{1}H-NMR (600 MHz) spectroscopy (**Figure 34**)

OXA-48 with mero-β-lactones

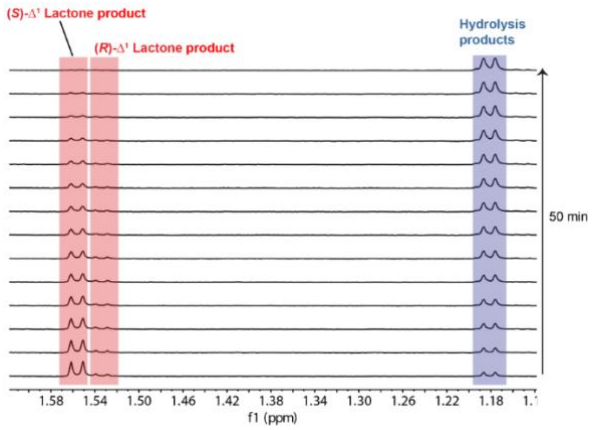

OXA-48 with meropenem

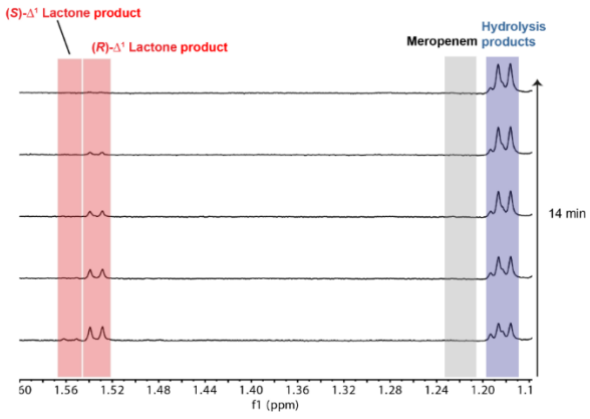

OXA-10 with mero-β-lactones

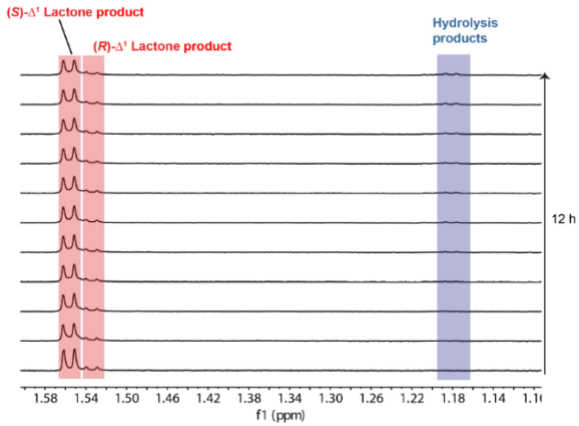

OXA-10 with meropenem

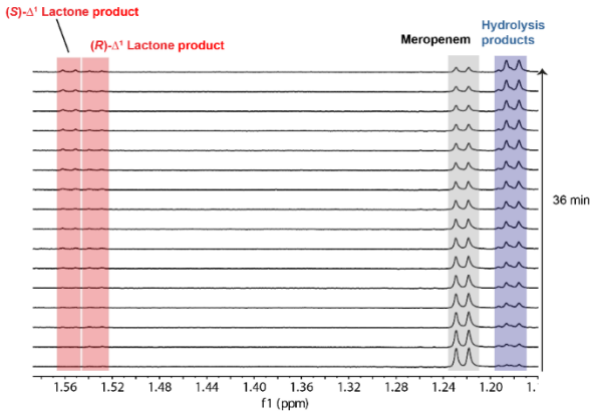

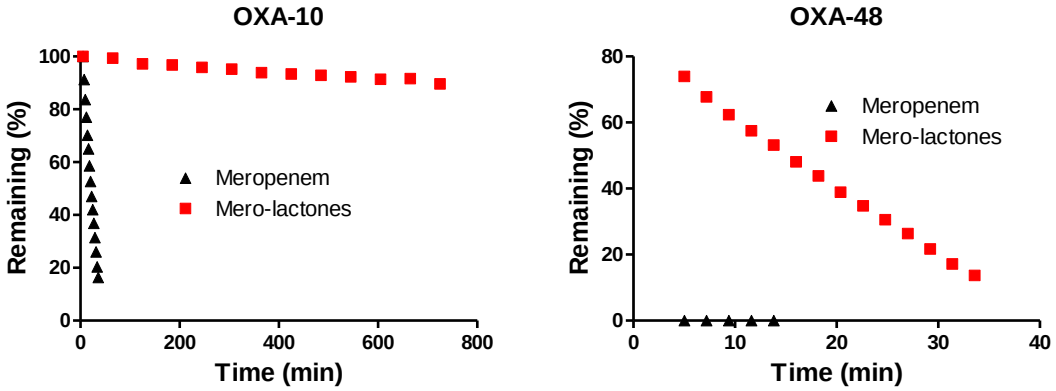

Figure 34. OXA-48 degrades meropenem and mero-β-lactones more efficiently than OXA-10. ^{1}H NMR (600 MHz) time courses of mero-β-lactones and meropenem in presence of OXA-10 and OXA-48 using a 10:1 ratio of β-lactones/carbapenem to enzyme. Conditions: 0.5 mM mero-β-lactones or meropenem, 50 μM enzyme in 50 mM sodium phosphate, pH 7.5 and 10% D_2O. The peaks of H-9 methyl group of meropenem and mero-β-lactones were monitored and integrated using MestreNova 12.0.3.

In the presence of OXA-10, >80% of the mero-β-lactones remained intact after 12 h, whereas meropenem itself was degraded in less than 2 h (**Figure 34**). Under the same NMR assay conditions with OXA-48, meropenem was completely degraded by OXA-48 at the first time point (5 min incubation) and the mero-β-lactones were hydrolysed within ~1 h. Overall, the mero-β-lactones were degraded more slowly than meropenem. Note that the Δ^2 enamine mero-β-lactone was not observed when mero-β-lactones reacted with OXA-10 and OXA-48, the only observed products were the epimers of the Δ^1 imine forms.

The results show that mero-β-lactones are more stable than meropenem with both OXA-10 and OXA-48 although, both meropenem and mero-β-lactones react with the enzymes. An implication of these observations is that meropenem and the mero-lactones react with OXA-48 and OXA-10 (potentially also other SBLs) to give different AEC(s). The previous proposal that mero-β-lactones are more efficiently degraded than meropenem is not supported by this NMR degradation study. The combined results including weak inhibition and slow degradation of the mero-β-lactones, led to a new proposal that β-lactones can react reversibly with class D SBLs. This was then investigated by mass spectrometry.

3.2.5 SPE-MS based acylation and deacylation assays

OXA-10 and OXA-48 can react with mero-β-lactones to form AECs (88). The NMR based degradation assays revealed that hydrolytic degradation by OXA-10 and OXA-48 was less efficient with mero-β-lactones than with meropenem. It was proposed that the mero-β-lactones were degraded at a different rate compared to meropenem because the mero-β-lactones can react reversibly. Hence, the acylation and deacylation reactions of class D SBLs by mero-β-lactones were studied.

To study the acylation and deacylation of class D SBLs an integrated autosampler/solid-phase extraction (SPE) RapidFire 365 system (RapidFire system) coupled to a sensitive iFunnel Agilent 6550 mass quadrupole time-of-flight (Q-TOF) mass spectrometer (SPE-MS) was used (**Figure 35**) (217). In contrast to reverse phase liquid chromatography column coupled to a mass spectrometer, the SPE-MS system has a SPE cartridge which enables very short runtimes of two measurement per minute. The SPE-MS can monitor the relative levels of apo-enzymes and AECs over time when mero-β-lactones and meropenem react with OXA-10 and OXA-48, respectively. The work was performed in collaboration with Dr. Anthony Tumber.

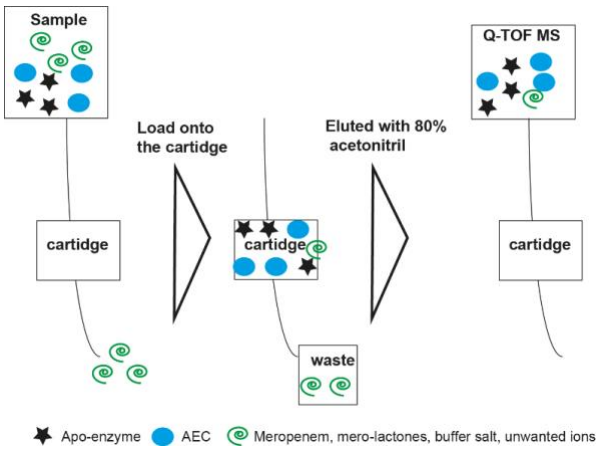

Figure 35. The solid-phase extraction-MS set-up.

Different concentrations of enzyme and inhibitor were tested to optimise the assay conditions for SPE-MS (**Figure 83A,** conditions 1 and 2). The results show that lowered small molecule concentrations (from 5 μM to 1 μM) with the same inhibitor to enzyme ratio of 10:1 lead to increased protein signals, likely because the strongly ionising mero-β-lactones and meropenem suppress the protein signal. Further improvement of protein signal intensity was achieved by preparing buffer with HPLC grade water instead of MilliQ water to minimise the presence of unwanted ionising ions. The optimised acylation assay conditions (**Figure 83**, condition 3) were 1 μM enzyme, 10 μM inhibitor, and 50 mM sodium phosphate in HPLC grade water, pH 7.5.

To carry out data analysis, the raw protein mass spectra were deconvoluted and the protein peak areas were integrated. Note that in the mass spectra shown (**Figure 84**), and for nearly all of the mass spectra obtained for AECs derived from carbapenems and β-lactones, a -44 Da mass was observed in addition to the AEC mass. This signal was proposed to correspond to the decarboxylation of the carboxylic acid on the carbapenem-derived and β-lactone-derived pyrroline ring (218).

The acylation reactions of OXA-10 and OXA-48 by the mero-β-lactones and meropenem with an enzyme to inhibitor ratio of 1:10 were monitored over 5-10 min by using the optimised SPE-MS conditions (**Figure 36**).

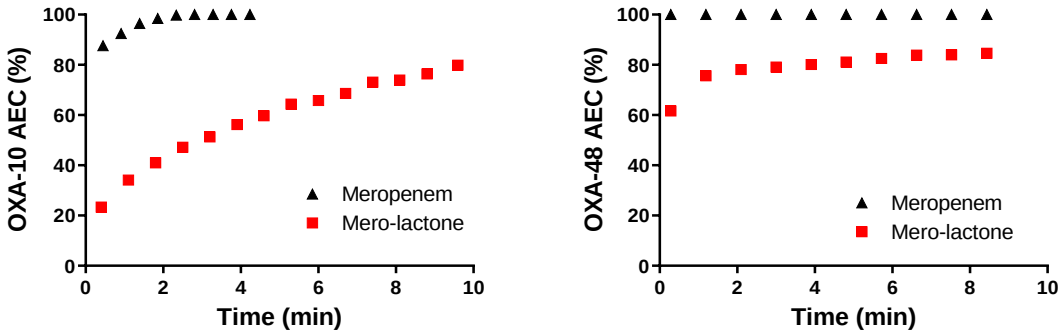

Figure 36. Formation of an AEC between OXA-10 and OXA-48 with meropenem or mero-β-lactones as monitored by SPE-MS. The assay conditions are described in **Figure 83**. For analysing the reaction, the peak areas for the apo-enzymes, AECs and -44 Da species were integrated. Supplementary deconvoluted spectra of OXA-48 with mero-β-lactones is in **Figure 83**.

The rate of formation of the AECs derived from the mero-β-lactones and OXA-10 was slower than that from meropenem. Similarly to OXA-10, formation of the AEC between OXA-48 and meropenem is faster than the formation of the corresponding complex with mero-β-lactones.

The rate of degradation of the AEC derived from mero-β-lactones with class D SBLs was next investigated. OXA-10 or OXA-48 were incubated for 10 minutes with the mero-β-lactones, and then mixed with the inhibitor/substrate ertapenem. The procedure allows the monitoring of both the degradation of the AECs derived from mero-β-lactones and the formation of the complex with ertapenem, because ertapenem and meropenem differ in their molecular weights. The first time point was measured immediately after adding ertapenem (**Figure 37**).

A

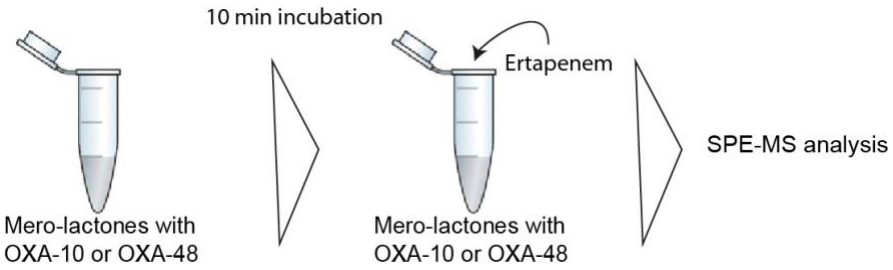

B

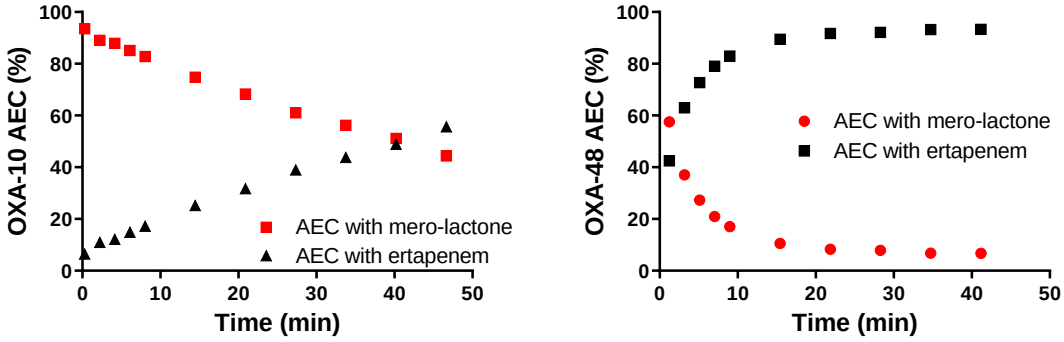

Figure 37. Mass spectrometric analysis of deacylation of the complex derived from mero-β-lactones with OXA-10 and OXA-48. A. Sample preparation for deacylation assays. **B.** Deacylation assay conditions: 1 µM enzyme and 10 µM mero-β-lactones were incubated for 10 min, then 100 µM ertapenem was added to the reaction mixture. For analysing the reaction, apo-enzymes, AECs, and -44 Da species were integrated.

The results of the mero-β-lactones/ertapenem deacylation assays reveal that the AECs derived from mero-β-lactones with OXA-10 and OXA-48 are relatively unstable, as AEC derived from ertapenem was observed immediately after addition of ertapenem. Overall, the result indicate that mero-β-lactones can acylate OXA-10 and OXA-48 and then deacylated the enzymes by re-formation of mero-β-lactones over hydrolysis.

3.3 Discussion

Understanding the β-lactamase-mediated antibiotic resistance mechanisms may be useful in combating resistance against β-lactams. One major strategy towards this goal is the development of new β-lactamase inhibitors. In this chapter, the potencies of the carbapenem-derived β-lactones mero-β-lactones against seven different SBLs and MBLs was studied, and mechanistic studies were carried out on the interactions of mero-β-lactones with class D SBLs.

Class A, B, and C β-lactamases TEM-1 AmpC, VIM-1, VIM-2, NDM-1, and IMP-1 were inhibited weakly by the mero-β-lactones, and were inhibited moderately or potently by meropenem (**Table 7A** and **B**). Previous studies on the turnover and interactions of the carbapenem-derived β-lactones with AmpC and NDM-1 have been described (88). In this study, the erta-β-lactones were used instead of the mero-β-lactones. Both β-lactones have the same β-lactone and pyrroline ring core, but differ in their C-2 thioether side chains (**Figure 33**). The observed poor inhibition of AmpC by mero-β-lactones is in agreement with previous work with erta-β-lactones and AmpC (88). The erta-β-lactones were not observed to acylate AmpC, nor did AmpC hydrolyse the erta-β-lactones. In the same study NDM-1 was not observed to hydrolyse the erta-β-lactones. Although a previous single dose inhibition study indicated weak inhibition of NDM-1 by the erta-β-lactones, this observation is not in agreement with the quantitative dose response inhibition study presented in this chapter using the mero-β-lactones and NDM-1. Taken together, the poor inhibition of these enzymes by the mero-β-lactones may result from poor or reversible acylation of class A and class C SBLs, and poor or reversible binding to the MBLs. However, this might not be the case for all class B MBLs, inhibition and, interestingly, no hydrolysis of the erta-β-lactones were observed with the class B MBL, L1 (88).

In contrast to the class A and C SBLs, pervious work has shown that class D SBLs, such as OXA-10 and OXA-48 can be acylated by the erta-β-lactones (88). This led to the proposal that mero-β-lactones inhibit class D SBLs. Kinetic studies confirmed that mero-β-lactones can act as an inhibitor of the class D SBLs, OXA-48 (pIC_{50} = 5.0) and OXA-10 (pIC_{50} = 5.6) (**Table 7C**). However, meropenem acts as a more potent inhibitor than mero-β-lactones against these enzymes OXA-10 (pIC_{50} = 7.9 ± 0.01) and OXA-48 (pIC_{50} = 6.3 ± 0.01) (**Table 7C**).

The difference in inhibitory activities of meropenem and the mero-β-lactones indicates different interactions of the parent carbapenems and their β-lactones with class D SBLs, i.e. meropenem and mero-β-lactones react to form different AECs. When meropenem reacts with class D SBLs, the nascent and catalytically most productive AEC is proposed to be in the Δ^2 enamine form, according to previous NMR studies (**Chapter 2**, **Section 2.2.7**) (167). The Δ^2 enamine AEC is proposed to be efficiently degraded through hydrolysis or β-lactone formation. In solution, the Δ^2 enamine form of the hydrolysis product and β-lactone tautomerise rapidly to give the (*R*)-Δ^1 and (*S*)-Δ^1 imine forms (**Figure 38**).

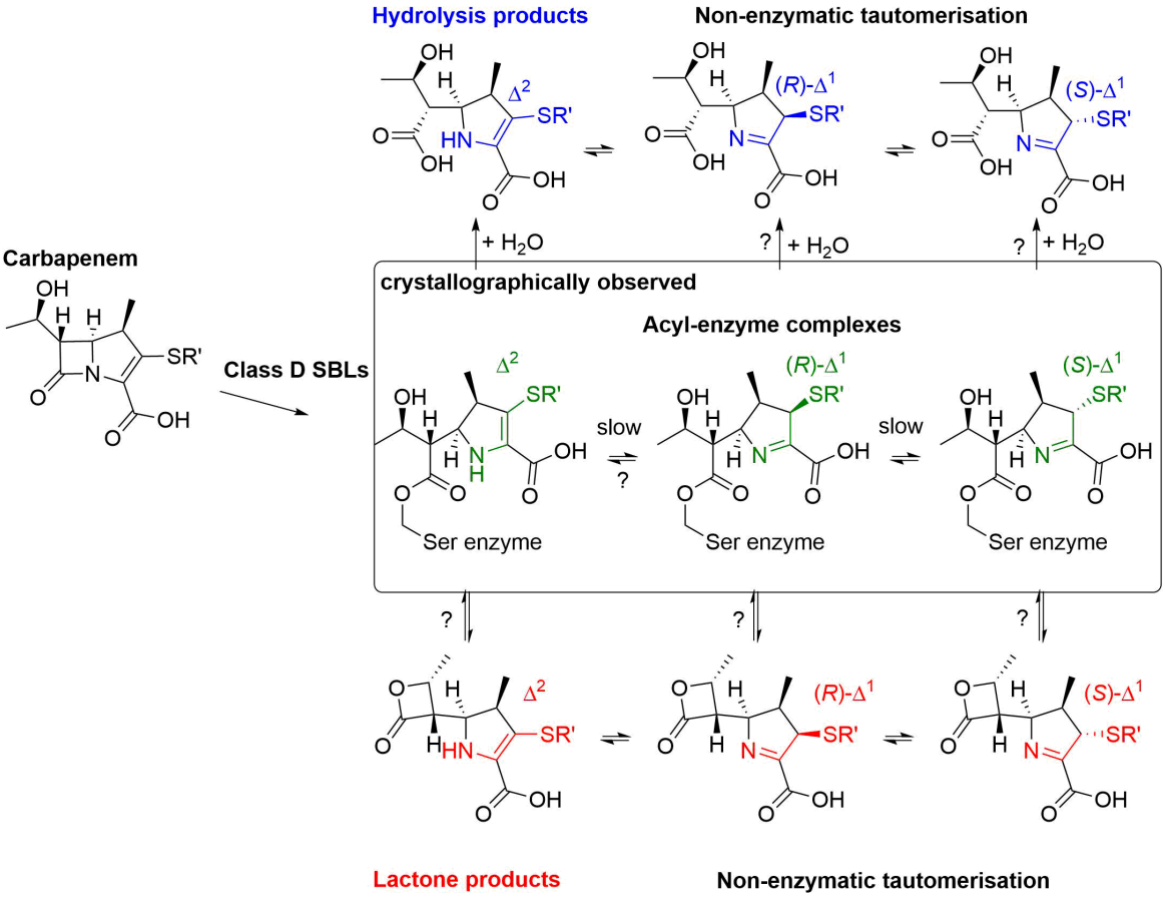

Figure 38. Meropenem is degraded to hydrolysis products and mero-β-lactones via an Δ^2 enamine AEC.

Structural analyses of class D SBLs with carbapenems have led to the observation that all three pyrroline isomers (Δ^2 enamine, (*S*)-Δ^1 imine and (*R*)-Δ^1 imine) can be found in the AECs (90, 168, 173). There are two potential explanations for the three crystallographically observed tautomeric forms: the carbapenem-derived Δ^2 enamine AEC may tautomerise on the enzyme resulting in (*S*)-Δ^1 imine and (*R*)-Δ^1 imine AECs. Alternatively, the two imine pyrroline forms may result from reacylation of the enzyme by β-lactones generated in either crystals or solution. 1β-Methyl substituted β-lactones occur as an equilibrium mixture of epimers in a 5:1 ratio of (*S*)-Δ^1 imine to (*R*)-Δ^1 imine form. To examine the pyrroline forms of AECs derived from β-lactones, crystallographic studies on mero-β-lactones and OXA-10 were conducted by Dr. Jürgen Brem (University of Oxford). The result reveals that an (*S*)-Δ^1 imine

AEC is formed (unpublished data). This (*S*)-Δ^1 imine AEC showed steric clashes between the C-2 side chain of the (*S*)-Δ^1 imine pyrroline ring in the AEC and the α3-α4 loop of OXA-10. In the preliminary structural work, there was no (*R*)-Δ^1 imine AEC derived from mero-β-lactones observed. This may be because the (*R*)-Δ^1 imine mero-β-lactone does not acylate OXA-10 as the (*S*)-Δ^1 imine form or crystal structures do not represent the interactions in solution.

According to the NMR based degradation study with the mero-β-lactones with OXA-10 and OXA-48 the Δ^2 enamine form was not observed, indicating that (*S*)-Δ^1 imine AEC is hydrolytically degraded via an analogous AEC. In addition, the combined results from degradation and acylation/deacylation work suggest that the (*S*)-Δ^1 imine AEC may be relatively unstable, and the steric clashes occurring in (*S*)-Δ^1 imine AEC may favour the formation of β-lactone (recyclisation) over hydrolysis more than the Δ^2 enamine AEC (**Figure 39**). Furthermore, the (*S*)-Δ^1 imine form of the pyrroline ring may promote a C-6 hydroxyethyl side chain conformation that favours β-lactone formation (as described in **Chapter 2**).

The results described in **Chapter 2** suggest that β-lactone formation by class D SBLs may represent a clinically relevant mechanism of carbapenem resistance. The evidence for fast recyclisation of β-lactones observed in this chapter explains why class D SBLs are not strongly inhibited by their carbapenem-derived β-lactones. However, this does not explain whether there are advantages to favour a specific carbapenem degradation pathway, i.e. β-lactone vs. hydrolysis pathways).

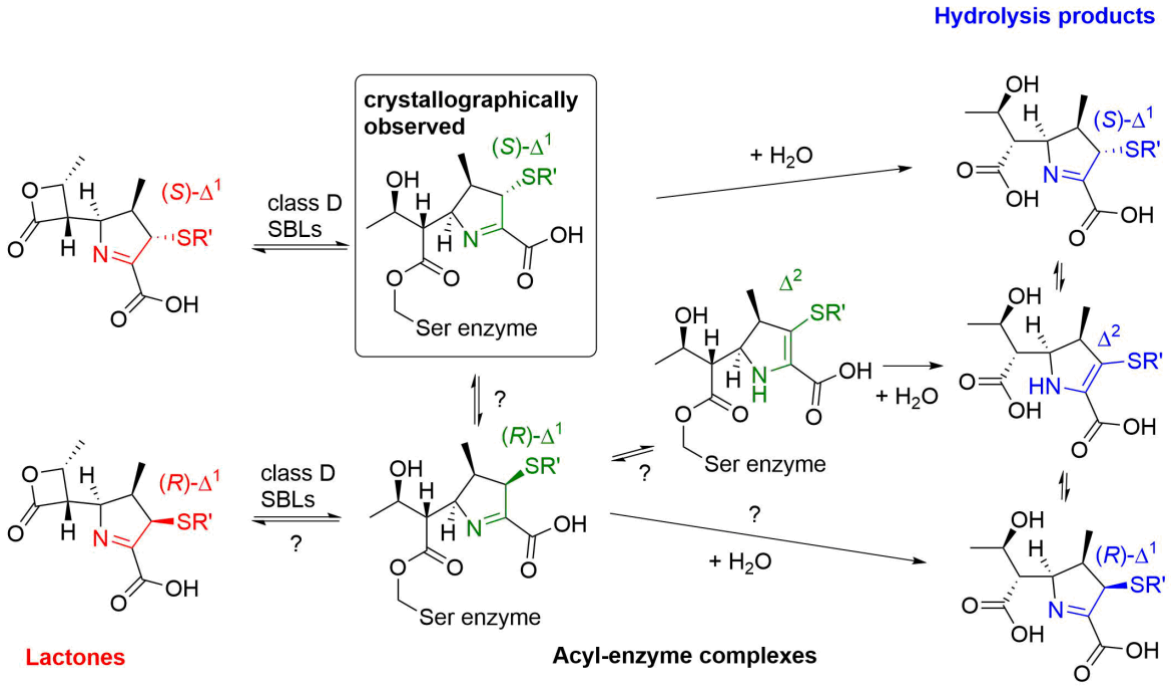

Figure 39. β-Lactones react reversibly with class D SBLs enzymes. Crystallography studies show that mero-β-lactones with OXA-10 form an (*S*)-Δ^1 imine AECs. The forms of the pyrroline ring in the AECs derived from carbapenems and β-lactones are not identical. The carbapenems degradation occurs via catalytically productive Δ^2 enamine AEC, whereas β-lactones degradation likely happens via (S)-Δ^1 imine AEC.

Further studies should focus on the molecular interaction of 1β-hydrogen substituted β-lactones with class D SBLs. These occur as a mixture of epimers in a 1:1 ratio of (*S*)-Δ^1 imine to (*R*)-Δ^1 imine forms. To compare inhibitory activity of 1β-hydrogen substituted and 1β-methyl substituted β-lactones may help to understand why 1β-methyl substituted carbapenems are favourably degraded by β-lactone formation, whereas 1β-hydrogen substituted carbapenems are hydrolysed by most clinically important class D SBLs. Furthermore, by altering the equilibrium of the pyrroline ring tautomers in the AECs of class D SBLs, it may be possible to make potent β-lactone SBL inhibitors.

Chapter 4 – Carbapenem Analogues

The biochemical work related to FDK023, FDK025, FDK027, and FDK036 described this chapter were performed by Ms Fraula Daka under my laboratory supervision and guidance and can be found in modified form in her Master's thesis (2019).

4.1 Introduction

Carbapenems are often considered as last resort drugs because of their clinical efficacy and relative stability against some β-lactamases (88). As described in **Chapter 2**, carbapenems can be degraded by SBLs and MBLs resulting in hydrolysis products and, in the case of class D SBLs, β-lactones (88, 167, 219). These degradation products occur as a mixture of three pyrroline isomers: epimeric (*S*)-Δ^1 imine and (*R*)-Δ^1 imine pyrroline forms and a Δ^2 enamine pyrroline form (167) (**Chapter 2**, **Section 2.2.4**). Previous NMR studies provided evidence that the Δ^2 enamine is the predominant nascent enzymatic product (88, 220). For 1β-methyl substituted carbapenems, the Δ^2 enamine product form undergoes rapid non-enzymatic tautomerisation to yield the (*R*)-Δ^1 imine form. Over time, the (*R*)-Δ^1 imine form tautomerises to give an equilibrium mixture that consists principally of the more thermodynamically stable (*S*)-Δ^1 imine epimer (**Figure 40**). This tautomerisation from (*R*)-Δ^1 imine to (*S*)-Δ^1 imine epimers likely proceeds via Δ^2 enamine form. The tautomeric process between these forms plays an important role in the molecular mechanism of carbapenem degradation by MBLs and SBLs (167).

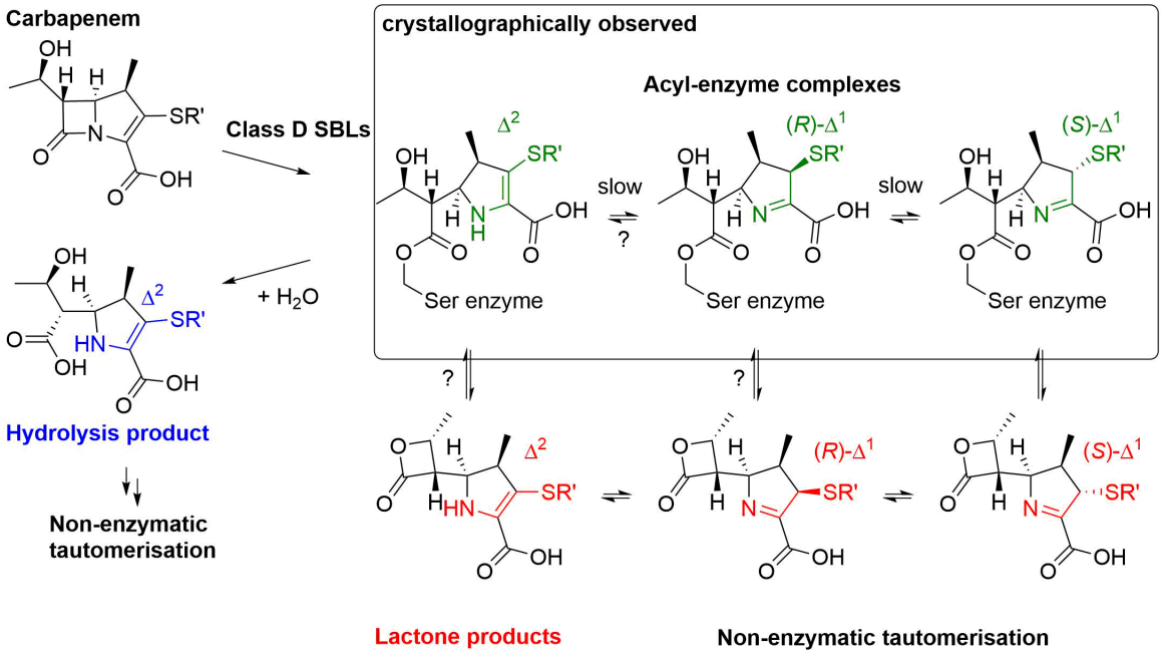

Figure 40. Class D SBLs form carbapenem-derived β-lactones and hydrolysis products. The carbapenem pyrroline ring occurs in different tautomeric forms, which interconvert over time in solution for the degradation products and also in the context of the AECs.

As described in **Chapter 3**, the reported crystallographic studies of the AECs derived from SBLs with carbapenems have shown that all three pyrroline ring forms can be formed, indicating that tautomerisation can occur in the crystallographically characterised AECs (**Figure 40**) (91, 168). Structural studies of the complex derived from class A SBL BlaC from *Mycobacterium tuberculosis* with ertapenem suggest that the Δ^2 enamine AEC is initially formed, which then interconverts over time to form the (*S*)-Δ^1 imine AEC (221). It is unclear whether the (*R*)-Δ^1 imine AEC act as an intermediate for the interconversion of the Δ^2 enamine to the (*S*)-Δ^1 imine form in the context of the enzyme active site which it likely observed in solution. In the case of class D SBLs, the crystallographically observed Δ^1 imine epimers may result from tautomerisation of the carbapenem-derived AEC, or from reacylation of the enzyme with carbapenem-derived β-lactones. In solution, at least under likely equilibrating conditions 1β-methyl substituted β-lactones are typically observed to

occur in an approximately 5:1 ratio of (*S*)-Δ^1 and (*R*)-Δ^1 imine epimers, as shown by the work in **Chapter 3**.

Previous studies on AECs derived from carbapenems and SBLs suggest that the conversion from the Δ^2 enamine AEC to the Δ^1 imine AEC may inhibit release of the product from the enzyme (222). The combined kinetic and spectroscopic analyses of class A SBL TEM-2 with carbapenems indicate that the Δ^2 enamine AEC is hydrolysed more quickly than the Δ^1 imine AEC(s) (223, 224). Mechanistic work (using Raman spectroscopy on crystals) on the interactions of class A SBL SHV-1 with carbapenems has led to the proposal that the Δ^1 imine AEC is stabilised due to the repositioning of the acyl-enzyme ester carbonyl group, resulting in less efficient hydrolysis (225). However, it is unclear whether it is the (*S*)-Δ^1 imine or the (*R*)-Δ^1 imine AEC that is responsible for this apparent inhibitory effect because Raman spectroscopy is not able distinguish between the two epimers. In **Chapter 3**, it was revealed that the (*S*)-Δ^1 imine AEC derived from 1β-methyl substituted β-lactones disfavoured hydrolysis and favoured recyclisation (through β-lactone formation). The weak inhibition of class D SBLs by the Δ^1 imine tautomers of β-lactones and the favoured recyclisation mechanism indicates that the (*S*)-Δ^1 imine form of the AEC is not responsible for a major reduction in class D SBL activity, which is reported for Δ^1 imine AEC forms of some other SBLs.

The aim of the work described in this chapter was to investigate the impact of the carbapenem C-2 side chain on the tautomerisation of the pyrroline ring. The electronic properties of this side chain might influence the tautomer equilibration of the pyrroline ring in the AEC formed with SBLs, potentially improving the properties of these carbapenems as SBL inhibitors. Six different carbapenem analogues differing in their C-2 thioether side chains were prepared and characterised by Mr. Tim Suits, Mr. Siegfried Thun-Hohenstein, and Ms. Fraula Daka (University of Oxford).

The specific aims of the work described in this chapter were:

- To obtain the NMR resonance assignment of the β-lactones and hydrolysis products derived from the carbapenem analogues.
- To analyse of the impact of the C-2 side chain on the mechanism of carbapenem degradation.
- To investigate the antibacterial properties of the carbapenem analogues.

4.2 Results and Discussion

4.2.1 Carbapenem analogues and OXA-48

With the aim of influencing the tautomerisation rate of the carbapenem pyrroline ring in the context of the AEC, new carbapenem analogues were designed. The bicyclic core of these carbapenem analogues, consisting of a β-lactam ring fused to a pyrroline ring, was functionalised with a C-1 β-methyl substituent and a C-6 hydroxyethyl side chain, as present in many clinically used carbapenems. The new compounds differ in the substitution patterns of their C-2 thiophenol side chains. Six different carbapenem analogues were synthesised by Mr. Tim Suits, Mr. Siegfried Thun-Hohenstein, and Ms. Fraula Daka (University of Oxford). The compound **TS01** contains an unsubstituted C-2 thiophenol side chain. The other compounds contain thiophenol group side chains bearing substituents with different electronic effects. The C-2 *para*-methoxy substituted thiophenol side chain in **TS02** is electron-donating, while the C-2 fluoro substituted thiophenol side chains in **FDK023**, **FDK025**, **FDK027**, and **FDK036** have electron-withdrawing effects. The interactions of these six carbapenem analogues with SBLs was compared to those of the clinically used carbapenem biapenem (**Figure 41**). These carbapenem analogues were tested with the clinically relevant class D SBL wild-type OXA-48. Wild-type OXA-48 was kindly provided by Mr. H. T. Henry Chan.

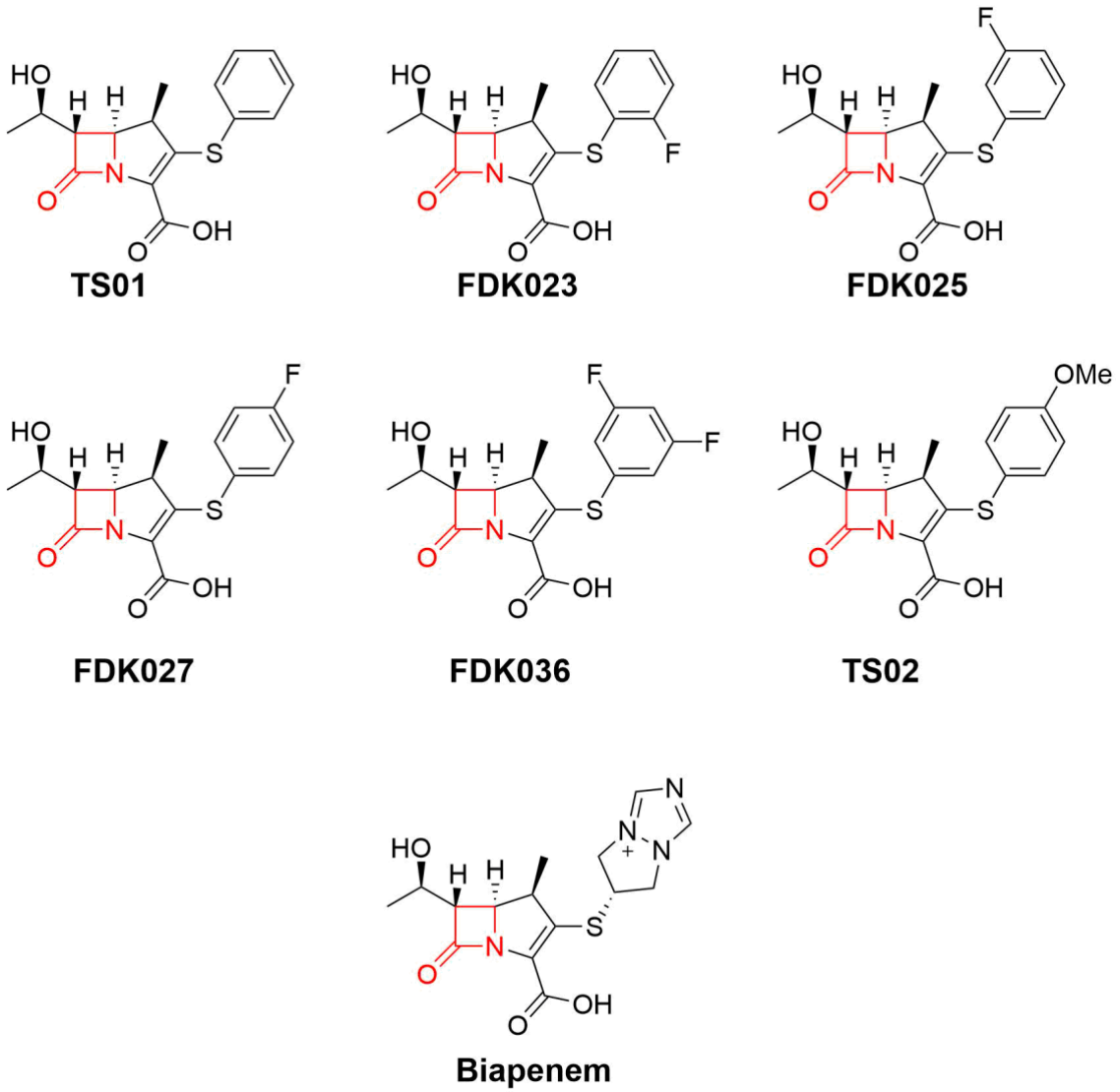

Figure 41. Structures of the six C-2 thiophenol substituted carbapenem analogues and biapenem. Six different carbapenem analogues were synthesised by Mr. Tim Suits, Mr. Siegfried Thun-Hohenstein, and Ms. Fraula Daka.

4.2.2 NMR turnover assays

To compare the interaction of the carbapenem analogues **FDK023**, **FDK025**, **FDK027**, **FDK036**, **TS01**, and **TS02** with class D SBLs, the analogues were incubated with wild-type OXA-48 and the mixture was monitored by ^{1}H-NMR (600 MHz) spectroscopy. The stability of the compounds was analysed by measuring the half-life ($t_{1/2}$), i.e. the time in which half of the compounds is degraded by wild-type OXA-48. Initial experiments with a compound:enzyme ratio of 40:1 suggested that there was little to no difference in how fast the compounds were degraded (data not shown). Therefore, the concentration of the enzyme was lowered such that the compound:enzyme ratio was 200:1 (**Figure 42**).

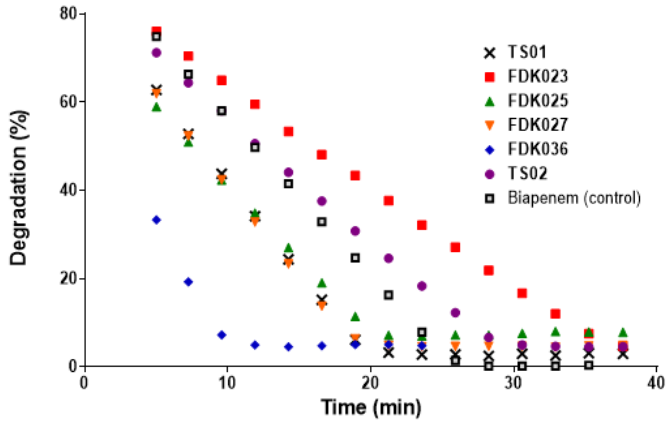

Compound	Half-life value ($t_{1/2}$) in min
TS01	11
FDK023	20
FDK025	11
FDK027	11
FDK036	6
TS02	15
Biapenem	13

Figure 42. Comparative analysis of the degradation of carbapenem analogues by wild-type OXA-48. The assay conditions were 1 mM compound and 5 µM wild-type OXA-48 in sodium phosphate buffer pH 7.5, 10% D_2O. The resonances of H-9 (methyl group of the C-6 hydroxyethyl side chain) of the carbapenem analogues and biapenem were monitored by ^{1}H-NMR (600 MHz) (**Figure 85**). The data with **FDK036**, **FDK025**, **FDK023**, and **FDK037** have been generated with Ms. Fraula Daka.

Compound **TS01**, which contains an unsubstituted thiophenol side chain, had a $t_{1/2}$ value of 11 min in presence of wild-type OXA-48 under the tested conditions (**Figure 42**). The stability of **FDK023**, **FDK025**, **FDK027**, and **FDK036**, which contain electron-withdrawing fluoro substituted thiophenol side chains, varied significantly. **FDK023** was

degraded more slowly than **TS01** by wild-type OXA-48 ($t_{1/2}$ value 20 min), whereas **FDK036** was degraded most quickly of all the tested compounds ($t_{1/2}$ value 6 min). The $t_{1/2}$ values of **FDK025** and **FDK027** were comparable with **TS01**. By comparison, **TS02**, which contains an electron-donating methoxy substituted thiophenol side chain, was turned over more slowly than **TS01** by wild-type OXA-48 ($t_{1/2}$ value 15 min vs. $t_{1/2}$ value 11 min), although it was degraded more quickly than **FDK023**. In comparison to the clinically used carbapenem biapenem, **FDK023** was more stable in the presence of wild-type OXA-48 ($t_{1/2}$ value 13 min vs. $t_{1/2}$ value 20 min), whereas **TS02** was degraded slightly slower than biapenem.

These results suggest that the C-2 substituents of the tested compounds have an impact on the catalytic efficiency of wild-type OXA-48. The $t_{1/2}$ values of the compounds containing C-2 fluoro substituted thiophenol side chains diverged, although they all likely have similar electron-withdrawing effects. Hence, the rate of carbapenem degradation may be impacted by other factors than electronic effects, e.g. specific active site interactions. In contrast to the C-2 fluoro substituted thiophenol side chain containing compounds, **TS02** was more slowly degraded than **TS01** with an unsubstituted thiophenol side chain. This observation may be because of the electron-donating effect of the methoxy substituent, which may impact the rate of pyrroline tautomerisation.

4.2.3 Characterisation of degradation products formed with wild-type OXA-48 and OXA-48 S70C

Prior to studying the tautomerisation of the degradation products derived from 1β-methyl substituted carbapenem analogues in presence of wild-type OXA-48, the degradation products were characterised by ^{1}H NMR (600 MHz) spectroscopy. As described in **Chapter 2**, clinically used 1β-methyl substituted carbapenems are degraded by wild-type OXA-48 as a mixture of β-lactones and hydrolysis products. However, with longer time periods β-lactones are ultimately converted into hydrolysis products. The products of carbapenem analogues with wild-type OXA-48 were first determined by using **FDK023**. 1 mM **FDK023** with 25 μM wild-type OXA-48 were mixed for 60 min. The resonances of the major product were assigned based on ^{1}H and 2D ^{1}H-^{1}H COSY experiments. In each case the major product was identified as the (*S*)-Δ^{1} imine hydrolysis product (**Table 8**).

As shown in **Chapter 3**, OXA-48 S70C preferentially degrades carbapenems to yield β-lactones. A mixture of 1 mM **FDK023** with 5 μM OXA-48 S70C was incubated for 60 min, and ^{1}H-NMR and 2D ^{1}H-^{1}H COSY spectra were then acquired. The observed major product was assigned as the (*S*)-Δ^{1} imine β-lactone of **FDK023** (**Table 9**). The chemical shift assignments of the β-lactones and hydrolysis products derived from **FDK023** are in agreement with previous NMR characterisation for clinically used 1β-methyl substituted carbapenems (88, 167).

Table 8. Chemical shift assignments for the FDK023 (*S*)-Δ^1 imine hydrolysis product. Full ^{1}H NMR spectrum is given in **Figure 86**. The data have been generated with Ms. Fraula Daka. The ^{13}C chemical assignments were obtained using ^{1}H ^{13}C correlations observed in ^{1}H ^{13}C HSQC and/or ^{1}H ^{13}C HMBC spectra. The chemical shift of C-10 was not observed.

Position	^{13}C NMR (ppm)	^{1}H NMR (ppm)
1	43.07	2.46
2	59.20	4.11
3	172.77	
5	72.54	3.99
6	55.65	2.48
7	180.18	-
8	67.93	3.87
9	20.41	1.12
10		-
11	14.26	0.89
12	162.53	-
13	163.60	-
14	135.70	7.49
15	124.69	7.12
16	130.88	7.35
17	115.77	7.13

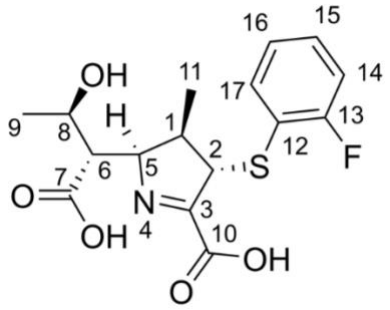

Table 9. Chemical shift assignments for the FDK023 (*S*)-Δ^1 imine β-lactone. Full ^{1}H NMR spectrum is given **in Figure 87**. The data have been generated with Ms. Fraula Daka. The ^{13}C chemical assignments were obtained using ^{1}H ^{13}C correlations observed in ^{1}H ^{13}C HSQC and/or ^{1}H ^{13}C HMBC spectra. The chemical shift of C-10 was not observed.

Position	^{13}C NMR (ppm)	^{1}H NMR (ppm)
1	42.03	2.55
2	59.68	4.04
3	174.10	
5	68.41	3.79
6	52.28	3.89
7	173.38	-
8	73.19	4.87
9	15.05	1.37
10		-
11	14.28	0.87
12	162.59	-
13	164.08	-
14	137.45	7.52
15	125.41	7.12
16	132.15	7.40
17	116.04	7.14

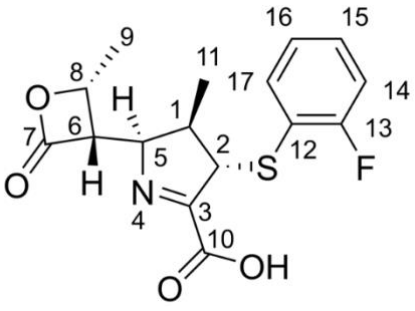

After assignment of the structures of the major degradation products, the reaction of **FDK023** with wild-type OXA-48 was monitored for 60 min by ^{1}H-NMR (600 MHz) to detect the other tautomeric forms of hydrolysis products and β-lactones. The signals corresponding to the H-9 methyl group of the products of **FDK023** were compared to products derived from clinically used carbapenems, e.g. meropenem and biapenem, as previously reported (167).

A recent study proposed that the Δ^2 enamine forms of the β-lactones and hydrolysis products are likely the nascent products formed during enzyme-catalysed carbapenem degradation (88). This is also likely the case for **FDK023** with wild-type OXA-48 (**Figure 43A**). After 5 min of incubation, the Δ^2 enamine β-lactone was the major product. In the same spectra, small amount of the (*R*)-Δ^1 imine β-lactone was present (**Figure 43A**).

Over time, the Δ^2 enamine form underwent non-enzymatic tautomerisation to yield the (*R*)-Δ^1 imine form, which subsequently interconverted to the more stable (*S*)-Δ^1 imine form. After 60 min, 4.7:1 equilibrium mixture of the (*S*)-Δ^1 and (*R*)-Δ^1 imine β-lactones was observed. In the case of the hydrolysis products, the (*S*)-Δ^1 imine form was favoured at all points during the time course. The rapid tautomerisation observed for the hydrolysis products likely results from intramolecular proton transfer from the new formed carboxylic acid group to the pyrroline ring (167).

The ^{1}H NMR chemical shifts of the H-9 methyl groups of all the β-lactones and hydrolysis products derived from the carbapenem analogues **FDK025**, **FDK027**, **FDK036**, **TS01**, and **TS02** were then assigned and compared to literature and the products of **FDK023** (**Figure 43B**).

A

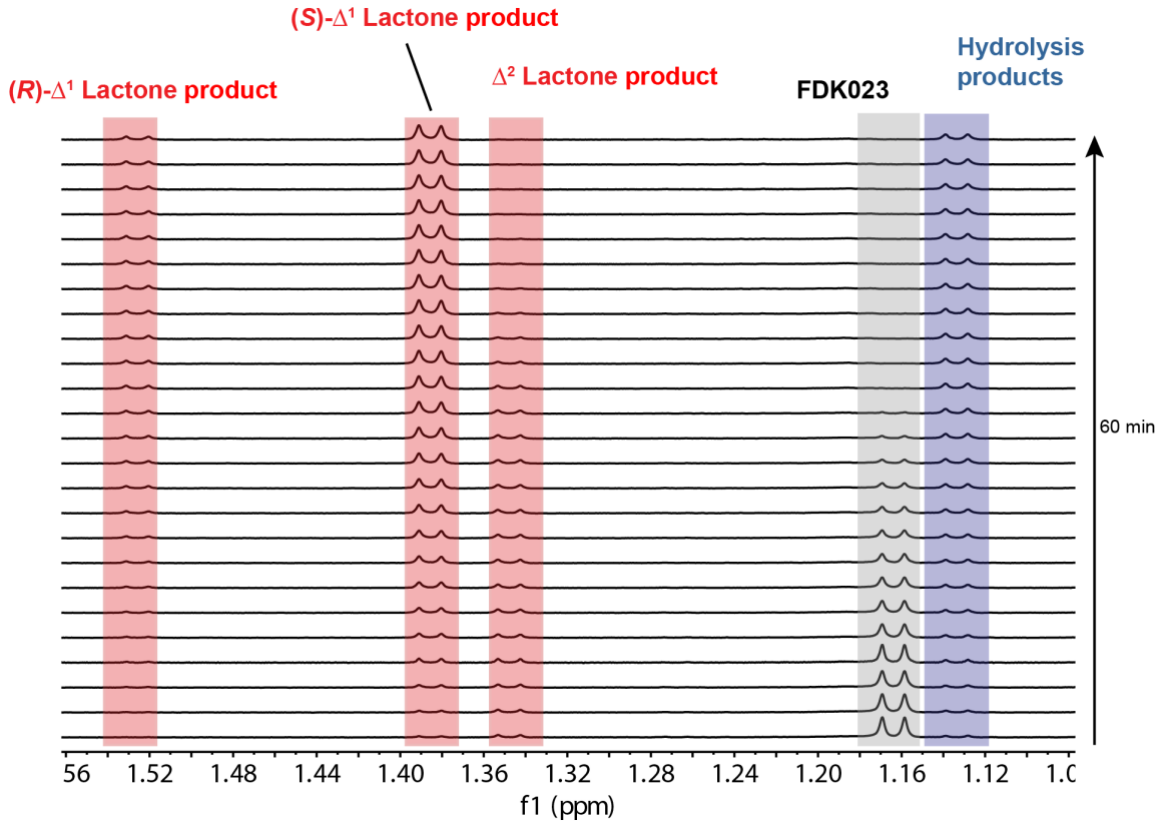

B

	^{1}H NMR (ppm)				
Compound	(*S*)-Δ^1 imine β-lactone	(*R*)-Δ^1 imine β-lactone	Δ^2 enamine β-lactone	(*S*)-Δ^1 imine hydrolysis product	(*R*)-Δ^1 imine hydrolysis product
TS01	1.33	1.52	1.35	1.12	1.18
TS02	1.29	1.51	1.32	1.10	1.13
FDK023	1.37	1.51	1.33	1.11	
FDK025	1.39	1.53	1.38	1.14	1.19
FDK036	1.45	1.54	1.41	1.15	1.19
FDK027	1.34	1.52	1.33	1.12	1.18
Biapenem*	1.58	1.56	1.49	1.26	1.27

***** Resonances of the H-9 methyl groups of biapenem-derived products have been reported previously (167).

Figure 43. NMR characterisation of the degradation products of C-2 thiophenol derived carbapenem analogues by OXA-48. A. Representative ^{1}H-NMR time course showing the degradation of **FDK023** by wild-type OXA-48. The other ^{1}H-NMR time courses are given in **Figure 85**. Assay conditions were 1 mM **FDK023**, 5 μM wild-type OXA-48, 50 mM sodium phosphate buffer pH 7.5, 10% D_2O. **B.** Chemical shift assignments for the H-9 methyl groups of the degradation products derived from the six carbapenem analogues and biapenem. The data with **FDK023**, **FDK025**, **FDK036**, and **FDK027** have been generated with Ms. Fraula Daka.

4.2.4 Investigating the Δ^2 enamine β-lactone intermediate product

To investigate the mechanism of degradation of the carbapenem analogues by class D SBLs, the extents of formation of the Δ^2 enamine β-lactones (i.e. the proposed nascent enzymatic product) were compared. The Δ^2 enamine β-lactones formed were monitored by ^{1}H NMR (600 MHz) spectroscopy, using a 200:1 ratio of the carbapenem analogues with wild-type OXA-48. The ^{1}H-NMR time courses show that the Δ^2 enamine β-lactones were constantly formed during the degradation of the carbapenem analogues by wild-type OXA-48. After the carbapenem analogues were completely depleted, the amount of Δ^2 enamine lactones gradually lowered (**Figure 43** and **Figure 85**). The Δ^2 enamine β-lactone was the major product for all carbapenems analogues after 5 min incubation. In the case of biapenem, the Δ^2 enamine β-lactone was only observed to be a minor product (**Figure 85**). The corresponding Δ^2 enamine hydrolysis product was not observed which is likely due to its rapid tautomerisation or possibly because the peaks for it were obscured. Note that biapenem forms a small level of Δ^2 enamine lactone with wild-type OXA-48, in which the other clinically used carbapenems form trace amount of this enzymatic product.

For the clinically used carbapenems the level of the enzymatic Δ^2 enamine β-lactone is low and hindering full peak assignments due to the long acquisition time of 2D NMR spectra (167). Considering the relatively high levels of Δ^2 enamine β-lactones derived from the carbapenem analogues, it was of interested to confirm that this is the Δ^2 enamine form. Hence it was desirable to optimise the conditions for a ^{1}H-NMR chemical assignment. For the proton assignment, coupling between protons can be analysed by 2D ^{1}H-^{1}H COSY. A 2D ^{1}H-^{1}H COSY experiment shows ^{1}H-^{1}H couplings that are two or three bonds away (226). Stereochemical analysis of the pyrroline ring can be accomplished by 1D ^{1}H-^{1}H-NOESY with selective irradiation of the 1β-methyl substituent (88). For the Δ^2 enamine product, the

H-11 protons of the 1β-methyl substituent would show through-space correlations to the H-5 and H-6 protons, and no proton signal for H-2 would be observed.

The proton peak assignments for the Δ^2 enamine β-lactone were limited by the acquisition times required for NMR experiments, and the low concentrations of the transient Δ^2 enamine β-lactone. To perform the 2D ^{1}H-^{1}H COSY and 1D ^{1}H-^{1}H-NOESY experiments, the transient Δ^2 enamine β-lactone must be present at a sufficient concentration for a period of at least 1.5 h. Therefore, the assay conditions were optimised with varying ratios of OXA-48 S70C and **FDK023** and varying buffer pH values (**Table 10**). The optimised conditions were a 1:143 ratio of OXA-48 S70C:FDK023 in 50 mM sodium phosphate buffer pH 8.0.

Table 10. Optimisation of conditions for the FDK023 Δ^2 enamine β-lactone chemical shift assignment. The spectra are given in **Figure 85.** The experiments were performed with Ms. Fraula Daka.

Condition	Ratio of enzyme: FDK023	Buffer pH	Note
1	1:100	7.5	Δ^2 Enamine β-lactone was stable for < 1 h
2	1:200	7.5	**FDK023** was not fully degraded within 1.5 h
3	1:143	7.5	Δ^2 Enamine β-lactone was present for 1.5 h
4	1:143	7.0	**FDK023** was not degraded within 1.5 h
5	1:143	8.0	Δ^2 Enamine β-lactone was present for 1.5 h, and at higher levels than with condition 3

Optimised assay conditions for production of the Δ^2 enamine β-lactone derived from **FDK023**: 1 mM **FDK023**, 7 μM OXA-48 S70C, sodium phosphate, pH 8.0, 10% D_2O. For the optimisation screen, 1 mM **FDK023** was used to minimise the amount of compound used.

The final changes to optimise the production of Δ^2 enamine β-lactone were to increase the concentration of carbapenem **FDK023** from 1 mM to 10 mM, and to increase the concentration of OXA-48 S70C from 7 μM to 70 μM, such that the concentration of the Δ^2 enamine β-lactone would be around 1 mM. With the 10-fold increases in compound and enzyme, the degradation of **FDK023** was slowed down, resulting in lower levels of Δ^2

enamine β-lactone present in the reaction mixture. Because of this, chemical shift assignments were only partially obtained (**Table 11**). This observation of decreasing OXA-48 S70C activity with increased enzyme concentrations may result from inadequate carbon dioxide in the solution, such that the active site lysine is not fully carbamylated.

Table 11. Partial chemical shift assignments of the FDK023-derived Δ^2 enamine β-lactone. The spectrum has been generated Ms. Fraula Daka

Position	**^{1}H NMR (ppm)**
1	2.70
2	
3	
4	
5	4.11
6	3.85
7	
8	4.88
9	1.32
10	
11	0.74

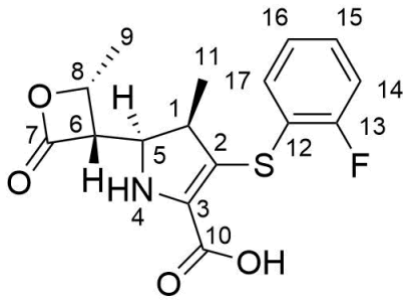

4.2.5 Degradation product analysis of carbapenem analogues

As described in **Chapter 2**, the Δ^2 enamine form of the AEC derived from 1β-methyl substituted carbapenems and wild-type OXA-48 is degraded to yield hydrolysis products and β-lactones, in which β-lactones are favoured. In contrast, as described in **Chapter 3**, the (*S*)-Δ^1 imine AEC derived from mero-β-lactones and OXA-10 is proposed to almost exclusively undergo recyclisation to re-form the β-lactone. Thus, it was of interest to study the ratio of β-lactones and hydrolysis products derived from the carbapenem analogues and biapenem, which have different C-2 side chains (**Figure 44**).

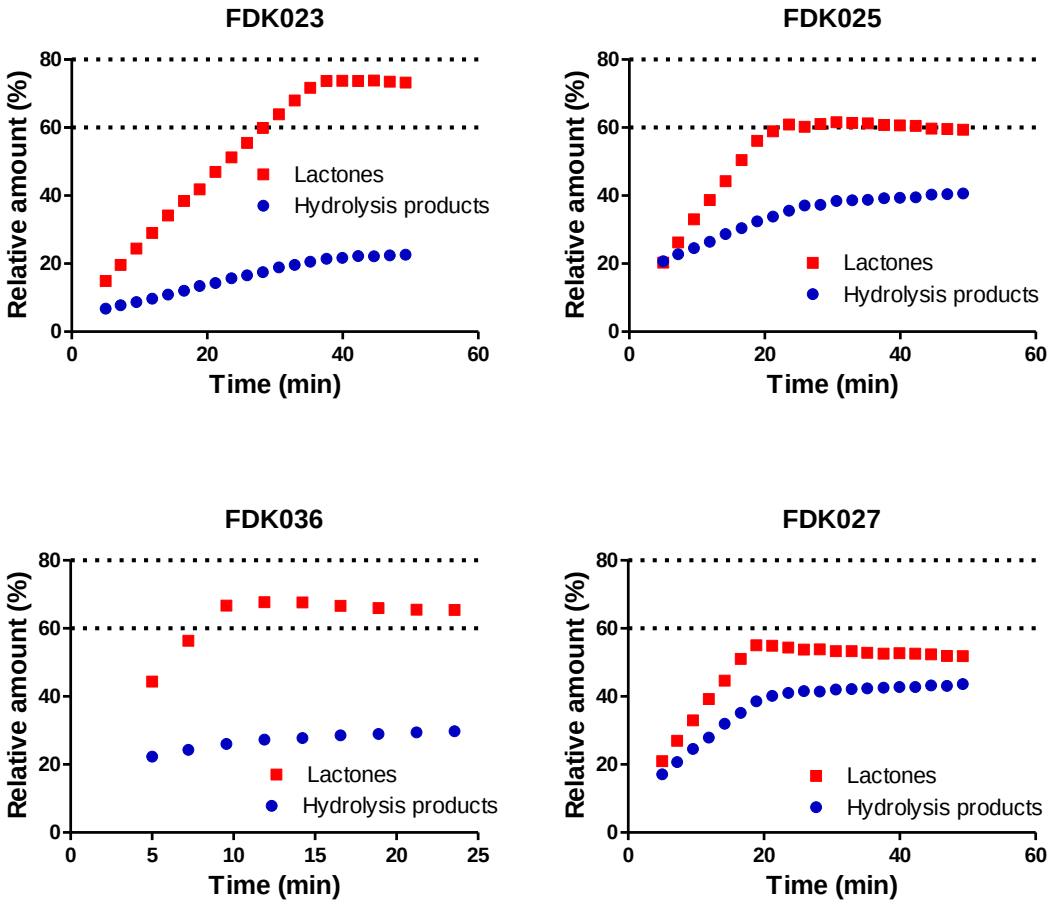

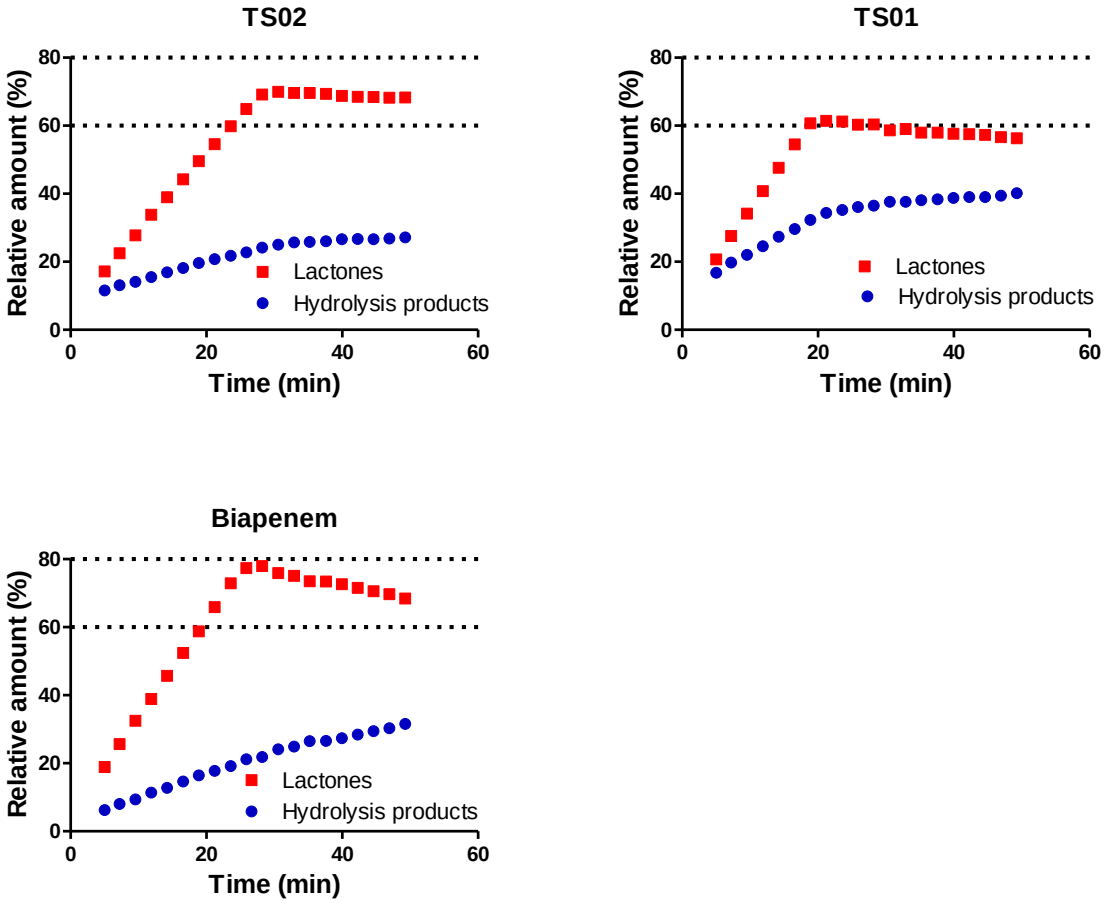

Compound	Time point when carbapenems were degraded	Ratio of β-lactones: hydrolysis products
TS01	21	1.8:1
FDK023	49	3.4:1
FDK025	35	1.7:1
FDK027	19	1.4:1
FDK036	12	2.4:1
TS02	31	2.8:1
Biapenem	28	3.6:1

Figure 44. ^{1}H NMR (600 MHz) time courses showing the degradation of the carbapenem analogues and biapenem by wild-type OXA-48. Conditions: 1 mM compound and 5 μM wild-type OXA-48 in 50 mM sodium phosphate pH 7.5 and 10% D_2O.

All the tested compounds were degraded by OXA-48 to preferentially form β-lactones over the corresponding hydrolysis products. The levels of β-lactone formation were higher with biapenem, **FDK023**, **FDK036,** and **TS02** (ratio of β-lactones: hydrolysis products 3.6-2.4:1) but lower with **FDK025** and **FDK027** (ratio of β-lactones: hydrolysis products 1.7-1.4:1) relative to **TS01** containing unsubstituted C-2 side chain (ratio of β-lactones: hydrolysis products 1.8:1). The results imply that the partition at the AEC between β-lactone formation and hydrolysis is affected by the nature of the C-2 thiophenol side chains. However, there is no direct link between the electronic properties of the C-2 thiophenol side chains and the ratios of β-lactones: hydrolysis products.

4.2.6 *In vitro* MIC assays

The antimicrobial properties of the six carbapenem analogues were evaluated using broth microdilution assays to determine their minimum inhibitory concentrations (MICs). The MIC indicates the lowest concentration of antibiotic that can fully inhibit bacterial growth. The six analogues were tested against Gram-negative *Escherichia coli* BW25113 and Gram-positive *Staphylococcus aureus* ATCC29213 (**Table 12**). The MICs were determined according to the Clinical Laboratory Standards Institute (CLSI) guidelines and were conducted by Dr. Karina Calvopina Tapia.

Table 12. MICs of FDK023, FDK025, FDK027, FDK036, ampicillin, and meropenem against *E. coli* BW25113 and *S. aureus* ATCC29213. The data have been generated by Karina Calvopina Tapia.

	MIC (µg/mL)	
Compound	***E. coli* BW25113**	***S. aureus* ATCC29213**
FDK023	128	128
FDK025	≥ 256	≥ 256
FDK027	64	64
FDK036	≥ 256	≥ 256
TS01	32	
TS02	128	
Ampicillin	4	4
Meropenem	0.25	

The results suggest that most of the carbapenem analogues do not have strong antibacterial properties against the tested Gram-negative and Gram-positive strains (**Table 12**). In the case of Gram-negative bacteria, the compounds must pass through the outer membrane to reach their target PBPs, which are located in the periplasmic space. It is reported that to reach the periplasmic space, the carbapenem analogues use non-specific porins like the OmpC porins (31). However, to pass through these porins, the carbapenems

would need a basic C-2 side chain, as present in biapenem and meropenem (31). In the case of the synthesised carbapenem analogues, they have neutral thiophenol side chains which likely limit their ability to traverse the outer membrane. The neutral thiophenol side chains of carbapenem analogues may also lead to different interactions with the target PBPs.

4.3 Conclusions

The goal of the work described in this chapter was to investigate the catalytic machinery of the class D SBLs using C-2 thiophenol side chain varied carbapenem analogues. Previous work had shown that the AECs of class D SBLs derived from carbapenems and β-lactones result in different product profiles, presumably due the formation of different AECs (88). Furthermore, the results described in **Chapter 2** suggest that the (*S*)-Δ^1 imine form of the AEC is relatively unsusceptible to hydrolysis, at least compared to the enamine AEC.

Analysis of the degradation products formed from the carbapenem analogues shows that different amount of the β-lactones and hydrolysis products were formed, though in all cases β-lactone formation was preferred (**Figure 44**). **FDK023**, **FDK036**, **TS02**, and biapenem favoured β-lactone formation over hydrolysis to a greater degree than **FDK025**, **FDK027**, and **TS01** (**Figure 44**). This observation may indicate that the substituents of these carbapenems influence the ratio of the different pyrroline isomers present in the AEC, which may in turn influence the amount of β-lactones formed. This contrasts with the observation that all carbapenem analogues show increased amounts of the nascent enzymatic products (the Δ^2 enamine β-lactones) relative to the amount formed by clinically used biapenem (based on the NMR assays) (**Figure 86**). This observation indicates that Δ^2 enamine form of the AEC was involved in β-lactone formation.

There was no clear correlation between the product profile and the catalytic degradation rates for the carbapenem analogues. **TS02** with an electron-donating C-2 methoxy substituted thiophenol side chain is degraded more slowly and gives a higher ratio of β-lactone to hydrolysis products relative to **TS01** with a C-2 unsubstituted thiophenol side chain. For the carbapenem analogues (**FDK023**, **FDK036**, **FDK025**, and **FDK027**) which contain an electron-withdrawing C-2 fluoro substituted thiophenol side chains the results

varied significantly. Consequently, more detailed kinetic studies are desirable. The combined results indicate that the difference in rates of product formation and in product distribution are likely caused by unidentified factors rather than, at least solely, by the different electronic effects of the thiophenol ring in the C-2 side chain although it might contribute to a certain extent.

Further mechanistic studies are required to understand how the nature of the carbapenem-derived pyrroline ring impacts the conformation of the C-6 hydroxyethyl side chain, which contributes to the bifurcation of carbapenem degradation through β-lactone formation and hydrolysis.

Overall, the insights into the catalytic machinery of Class D SBLs with carbapenem suggest that the AECs derived from carbapenem and β-lactones deacylate through β-lactone formation because it may prevent inhibition due to the formation of (*S*)-Δ^1 imine AEC. However, class A and C SBLs, particularly non-carbapenemases, may be inhibited by the (*S*)-Δ^1 imine form. Future research should study the reactions of carbapenems with other classes of SBL.

Chapter 5 – Characterisation of +30 Da modification of eRF1

5.1 Introduction

5.1.1 JMJD4 and proposed mechanism of γ-lactam ring formation

JMJD4 is reported to regulate translation termination by catalysing the (4*R*)-hydroxylation of lysine residue Lys63 of eRF1 (**Figure 45**) (144). eRF1 is involved in the recognition of stop codons in mRNA, that leads to termination of protein biosynthesis during ribosome-mediated translation (130, 131). When eRF1 binds to a stop codon, it effects the release of the synthesised polypeptide chain by promoting the hydrolysis of the ester bond linking the polypeptide chain with the peptidyl site of the tRNA (135). Studies have shown that the (hydroxylated) Lys63, which is part of a highly conserved NI**K**S$_{61\text{-}64}$ motif, interacts directly with the stop codon and hydroxylation of eRF1 improves translation termination efficiency (144). Beyond the (4*R*)-lysyl hydroxylation, JMJD4 may also catalyse another modification on the same Lys63 of eRF1. MS/MS and NMR studies and amino acid analysis have led to the conclusion that a unprecedented γ-lactam ring structure (+30 Da modification) might be occurring between Lsy63 and Ser64 residues of eRF1 (**Figure 45**).

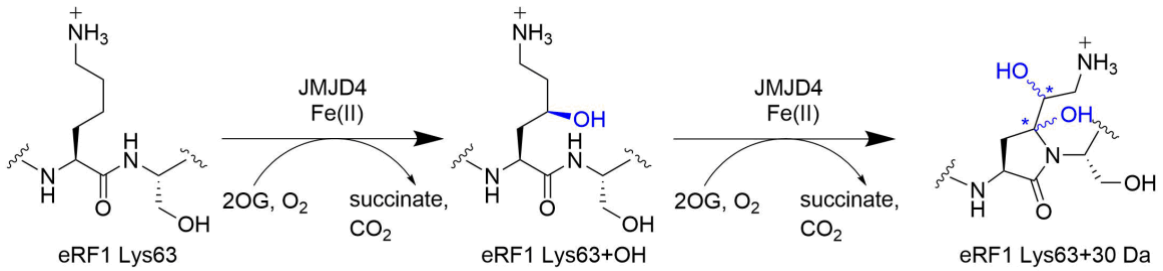

Figure 45. Representation of the two identified modifications of eRF1: initial C-4 hydroxylation (eRF1 Lys63+OH) and subsequent γ-lactam ring formation (eRF1 Lys63+30 Da) (adapted from the General Introduction, Section 1.14).

Figure 46 shows two proposed, potential mechanisms for the formation of the novel γ-lactam ring of eRF1. Both involve the initial C-4 hydroxylation step of Lys63 and two subsequent oxidation steps resulting in the +30 Da modification (**Figure 46**).

In the first mechanism (**Figure 46** in blue), after C-4 hydroxylation, a second hydroxylation occurs at the same C-4 position resulting in a geminal diol. The geminal diol is unstable, and a C-4 ketone group is formed by elimination of a water molecule. The formation of a γ-lactam ring containing a hemiaminal group occurs after nucleophilic attack by nitrogen of amide group of the Ser64 residue with the C-4 ketone group of Lys63. Finally, a third hydroxylation at the C-5 position on Lys63 leads to the +30 Da modification. In a different possible mechanism (**Figure 46** in red), after Lys63 C-4 hydroxylation, a C-5 lysyl hydroxylation occurs, followed by a second C-4 hydroxylation resulting in a C-4 ketone group. Finally, the γ-lactam ring (+30 Da modification) is formed.

The +30 Da modification was not observed, but hydroxylation occurred when Ser64 was previously substituted for a proline residue, showing that the Ser64 residue is directly involved in +30 Da modification but not in C-4 hydroxylation of Lys63 (Dr. Suzana Markolovic, unpublished data) (149).

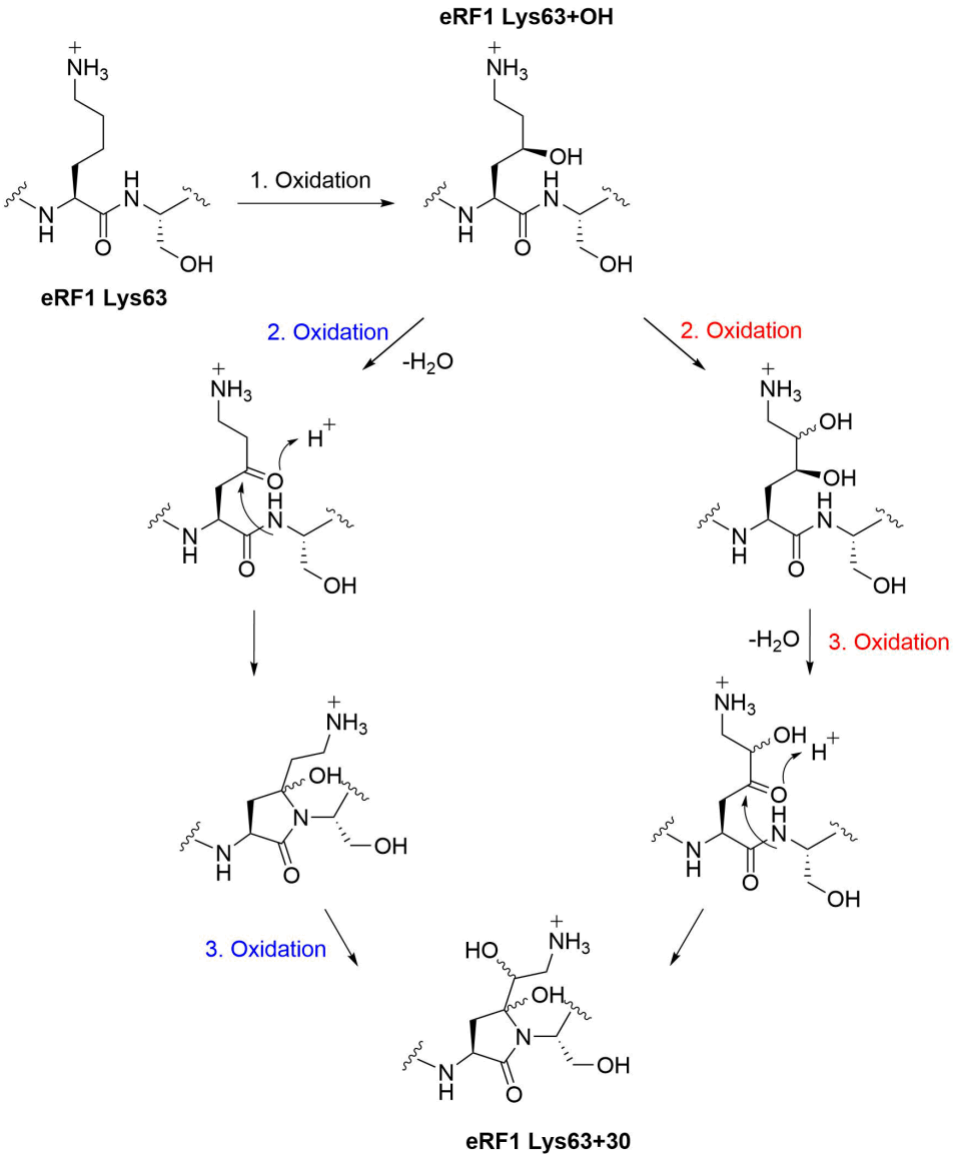

Figure 46. Two proposed reaction mechanisms for γ-lactam ring formation, catalysed by JMJD4.

5.1.2 Protein NMR studies on N-domain of eRF1

NMR studies on biophysical properties and rRNA binding of $^{15}N/^{13}C$ labelled N-domain of eRF1, eRF1+OH and eRF1+30 Da were conducted by Dr. Ivanhoe Leung and Dr. Suzana Markolovic (149). The comparative analysis of wild-type, hydroxylated, and +30 Da modified eRF1-ND revealed that the two modifications have small or no effects on global protein dynamics and interactions with rRNA. By contrast, analysis of structural and

conformational effects of the two modifications revealed that γ-lactam formation introduces significant changes in the protein structure, whereas the hydroxylation has little or no effects (149).

5.1.3 2OG oxygenase catalyse oxidative ring formation

As mentioned before in the **General Introduction**, **Section 1.9**, some members of 2OG dependent oxygenase superfamily have been reported to catalyse oxidative ring formations, e.g. the oxidase isopenicillin N synthase (IPNS) and clavaminic acid synthase (CAS). These two enzymes are involved in the biosynthesis of β-lactam penicillin and cephalosporin antibiotics and β-lactam β-lactamase inhibitor clavulanic acid, respectively (227). IPNS catalyses the cyclisation of a tripeptide (δ-(*L*-α-aminoadipyl)-*L*-cysteinyl-*D*-valine; (ACV), leading to the formation of a bicyclic core of isopenicillin N (IPN) containing a β-lactam ring bridged to a thiazolidine ring (**Figure 47A**) (228, 229). IPN is a precursor for all penicillins and cephalosporins. Interestingly, IPNS can also catalyse the formation of a γ-lactam ring derived from an ACV peptide analogue with a *L*-homocysteine residue instead of *L*-cysteine residue (**Figure 47B**).

During the biosynthesis of clavulanic acid, CAS catalyses three 2OG dependent steps: a hydroxylation, an oxidative ring formation, and a desaturation, yielding in bicyclic clavaminic acid. (**Figure 47C**) (230). A proclavaminic acid analogue containing a γ-lactam ring is accepted by CAS as a substrate analogue for the oxidative ring formation and desaturation reactions (**Figure 47D**) (230).

A further oxidative γ-lactam ring formation was observed to be catalysed by the human JmjC oxygenase factor-inhibiting hypoxia inducible factor (FIH) (231). Typically, FIH catalyses the hydroxylation of various amino acids of several natural substrates including hydroxylation of asparagine residue in a consensus ankyrin (CA) substrate (232,

233). In a substrate analogue study, the hydroxylated asparagine residue in a CA substrate peptide was replaced by other amino acids. When an asparagine residue was substituted for a serine residue in the CA substrate, the serine residue was initially hydroxylated and then further modified to an aldehyde resulting in a oxidative ring formation (**Figure 47E**) (231). An analogous ketone group is proposed as an intermediate for the formation of the +30 Da modification of eRF1 (**Figure 46**). Overall, the oxidative ring formations catalysed by IPNS, CAS, and FIH reveal similarity to the +30 Da modification potentially catalysed by JMJD4.

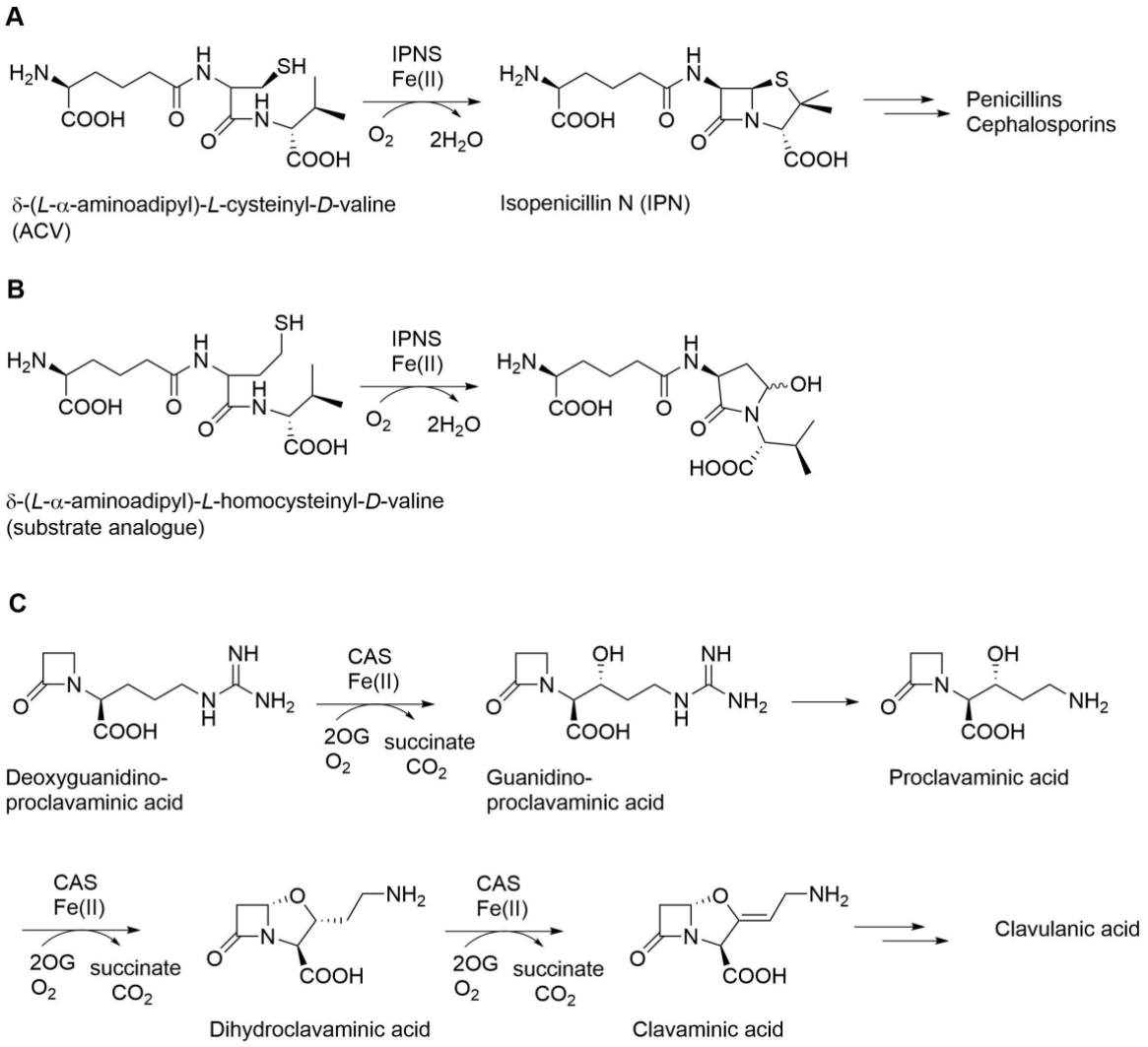

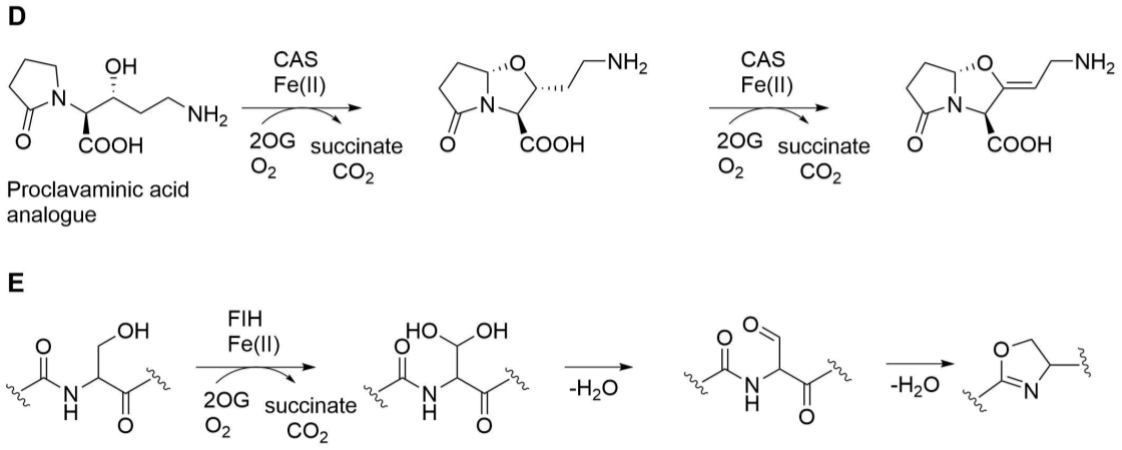

Figure 47. Members of the 2OG oxygenase family can catalyse oxidative ring formation with their natural substrate or/and substrate analogues. The reactions as shown are catalysed by IPNS (**A** and **B**), CAS (**C** and **D**) and FIH (**E**) (227–232).

2OG oxygenases employ a consensus mechanism proceeding via the Fe(IV)=O reactive intermediate. As described in **General Introduction**, the Fe(IV)=O reactive intermediate abstracts a hydrogen atom from the prime substrate giving Fe(III)-OH and a substrate radical. The subsequent reaction of the hydroxo-ferric(III) species with the substrate radical yields in hydroxylated product (**Figure 48**). Many studies on oxidative cyclisations catalysed by 2OG oxygenases confirmed consensus mechanistic steps upon the formation of the Fe(IV)=O intermediate, and the mechanistic steps are less resolved afterwards (121). For example, CAS can install a five-membered ring during the biosynthesis of clavulanic acid. Three mechanisms are proposed for the oxidative cyclisation after generating Fe(IV)=O intermediate. The first path is two hydrogen abstractions from two different positions of proclavaminic acid which are performed by CAS, resulting in cyclisation. Another option is that a hydrogen abstraction and radical transfer allow to form a positively charged carbon center reacting with the intramolecular hydroxyl group. A third mechanism involves two hydrogen abstractions and additional fragmentation forming dihydroclavaminic acid (121). The consensus 2OG oxygenase mechanism may be further adapted/modified for other cyclisation reactions.

A Hydroxylation

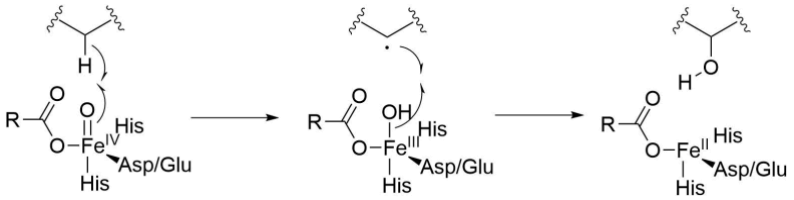

B Oxidative cyclisation

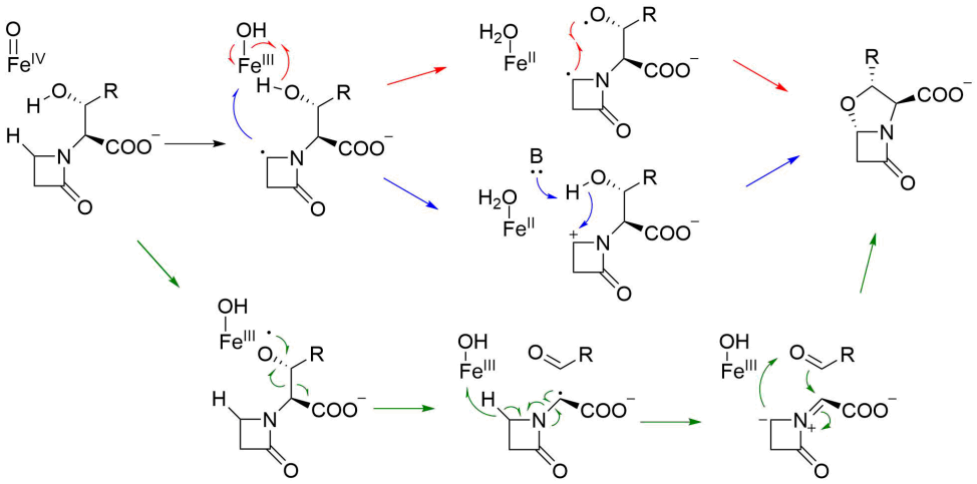

Figure 48. Consensus mechanism may adapt for different biological functions and oxidative reactions. **A.** Rebound mechanism for C-H bond hydroxylation. **B.** Proposed mechanisms for oxidative cyclisation catalysed by CAS.

Interestingly, JMJD6 has been reported to be promiscuous JmjC hydroxylase, as it can catalyse hydroxylation of various substrates (113, 114). JMJD4 and JMJD6 are both JmjC lysyl hydroxylases and they share a sequence identity of 34% (234). The sequence similarity corresponds to the active site, leading to the speculation that a structurally similar active site can accommodate different binding mode/interactions for different substrates or can catalyse multiple hydroxylations on the same substrate (consistent with the proposed mechanism for +30 Da modification). Consequently, it is possible that the catalysed reactions of (human) 2OG oxygenases including JMJD4 may be wider than previously reported.

5.1.4 Aim of the work described in this chapter

The aim of my work concerning JMJD4 was to characterise the unprecedented oxidative γ-lactam ring formation (+30 Da modification) of eRF1. The previous work has provided some evidence that a γ-lactam ring formation is catalysed by JMJD4 however, this requires further validation. Kinetic studies of γ-lactam ring formation and co-factor Fe(II), *L*-ascorbate and co-substrate 2OG dependency may provide insight into the reaction mechanism. A further aim was to explore if the hydroxylation and γ-lactam ring formation are observed also with JMJD4 and eRF1 orthologues. Ultimately, it was also investigated if the γ-lactam ring formation occurs in human cells by conducting immunoprecipitation experiments with endogenous eRF1.

5.2 Results and Discussion

5.2.1 Production and purification of recombinant hJMJD4

Human His_6-$JMJD4_{47-447}$ (hJMJD4) was produced in *E. coli* Rosetta2 (DE3) pLysS cells and purified by Ni(II)-affinity chromatography and SEC as described in the **Material and Methods**, **Section 6.3** (**Figure 49A** and **B**) (149). The purified truncated constructs of the N-domain of human $eRF1_{1-142}$-His_6 (heRF1-ND) (i.e. wild-type heRF1-ND and heRF1-ND+OH) were kindly gifted by Dr. Suzana Markolovic.

A

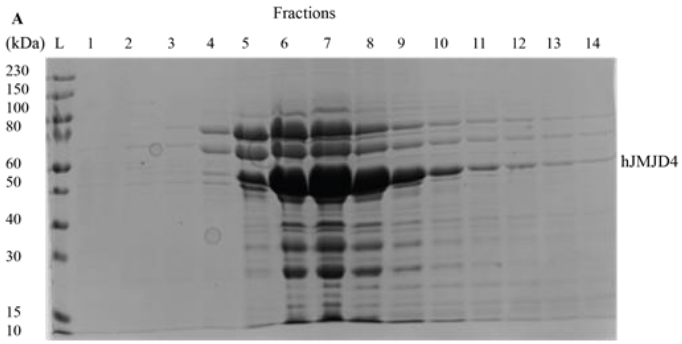

B

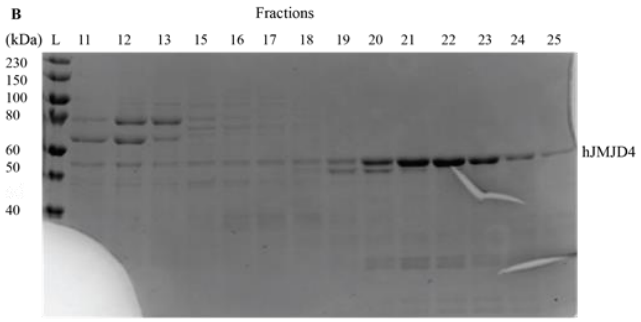

Figure 49. Purification of hJMJD4. A. and **B.** hJMJD4 was first purified using a 5 mL His-Trap column, followed by an S75 300 mL SEC column. L = Protein molecular weight marker (10-230 kDa).

5.2.2 Optimisation of an *in vitro* γ-lactam ring formation assay

To investigate the co-substrate, and co-factors dependency of JMJD4 for γ-lactam ring formation by SPE-MS, optimisation of the assay conditions was required. The work was performed in collaboration with Dr. Anthony Tumber. The previously described conditions for γ-lactam ring formation assay (50 μM heRF1-ND, 50 μM hJMJD4, 1 mM Fe(II) and 2 mM 2OG in 20 mM Tris, pH 7.5, 4 °C, 16-20 h) resulted in complete formation of +30 Da modification, but also resulted in the formation of a white protein precipitate (unpublished, DPhil Thesis of Dr. Suzana Markolovic, University of Oxford) (149). To use SPE-MS, it was necessary to stabilise the proteins to prevent precipitation, to run the assay at room temperature, and to use lower protein concentrations (**Figure 50** No 1). Protein precipitation was reduced by adding NaCl (300 mM) to the assay conditions, while retaining conversion to the +30 Da modified species (**Figure 50A** No 2 and 3). Salts, such as NaCl, can stabilise folded conformations of proteins, avoiding denaturation or aggregation in aqueous solution (235). Furthermore, these improved conditions permitted the assay to be performed at a lower enzyme concentration (1 μM), than previously (50 μM) (**Figure 50A** No 4 and 5, **Figure 50B**). Note that in heRF1-ND mass spectra a +42 Da species is present (**Figure 50**). The +42 Da peaks are likely a post-translation modification of the recombinant heRF1-ND, e.g. acetylation of the N-terminal methionine residue resulting from its production in *E. coli* (236).

A

No.	[heRF1-ND] (µM)	[hJMJD4] (µM)	T (°C)	Conversion to +30 Da	NaCl (mM)	Precipitation
1	50	50	4	Full**	0	yes
2	50	50	r.t.	Full**	100	yes
3	50	50	r.t.	Full**	300	no
4	15	15	r.t.	Full**	300	no
5	1	1	r.t.	Full**	300	no

The assay conditions were 1 mM ammonium iron(II) sulfate and 2 mM 2-oxoglutaric acid disodium salt, 20 mM Tris buffer pH 7.5, 16-20 h. With assay conditions **1** and **2** a centrifugation and dilution step was required prior to SPE-MS analysis; as previously described (149). Under conditions **3**, **4**, and **5** the proteins were stable, and the assay mixture could be analysed directly by SPE-MS. ** Partial conversion was observed when using old Tris buffer. Therefore, freshly prepared Tris buffer was used for assays.

B

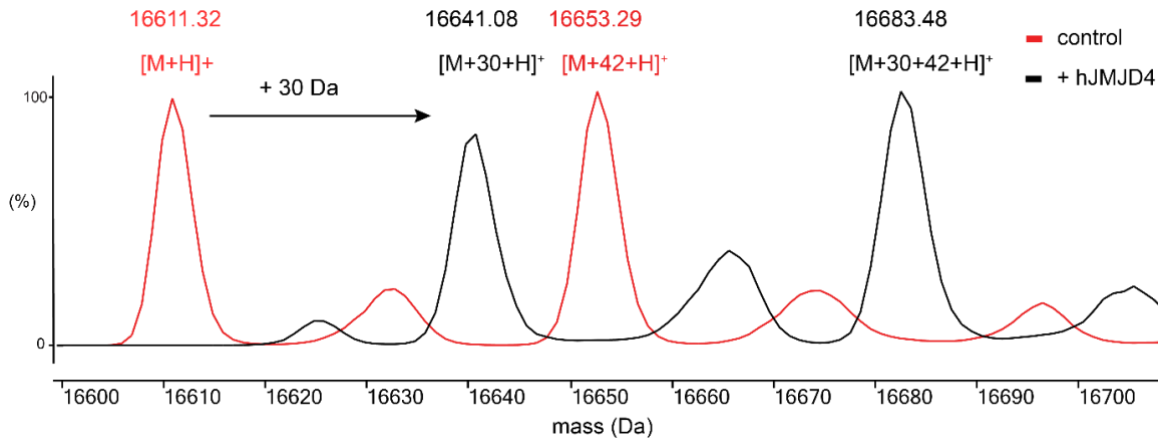

Figure 50. Optimisation of an *in vitro* γ-lactam ring formation assay. A. Screening *in vitro* heRF1-ND and hJMJD4 assay conditions. The optimised conditions were: 1 µM heRF1-ND, 1 µM hJMJD4, 1 mM ammonium iron(II) sulfate, and 2 mM 2-oxoglutaric acid disodium salt, 20 mM Tris 300 mM NaCl, pH 7.5, incubated for 16-20 h at room temperature. **B.** Representative MS spectra of heRF1-ND (control, black) and in presence of hJMJD4 under optimised γ-lactam ring formation assay conditions. Peaks were normalised.

5.2.3 Validation of *in vitro* γ-lactam ring formation catalysed by JMJD4

To test if the γ-lactam ring formation is independent of JMJD4 activity, recombinant hydroxylated heRF1-ND (heRF1-ND+OH, kindly provided my Dr. Suzana Markolovic) was incubated with Fe(II) and 2OG and analysed by SPE-MS. However, no new modification was observed, so hJMJD4 is required for γ-lactam ring formation (**Figure 51A**). It was then examined if the broad spectrum 2OG oxygenase inhibitor 2,4-pyridinedicarboxylic acid (2,4- PDCA), which blocks the active site and competes with 2OG binding (237), can prevent γ-lactam ring formation. The optimised γ-lactam ring formation assay conditions including heRF1-ND and hJMJD4 (**Figure 50**) in the presence and absence of 2,4- PDCA were used. No heRF1-ND+30 Da species was formed in presence of 2,4 PDCA, but hydroxylation of eRF1-ND was observed (**Figure 51B**). This is likely because hydroxylation is more efficient than the +30 Da modification, which under these conditions require a stoichiometric ratio of substrate and enzyme. Overall, these assay results demonstrate that formation of the +30 Da modification is dependent on the catalytic activity of JMJD4.

A heRF1-ND+OH, 2OG, Fe(II)

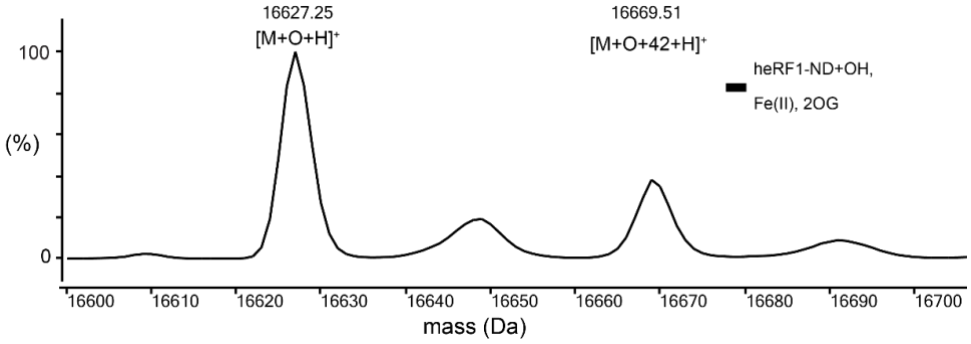

B in presence and absence of 2,4 PDCA

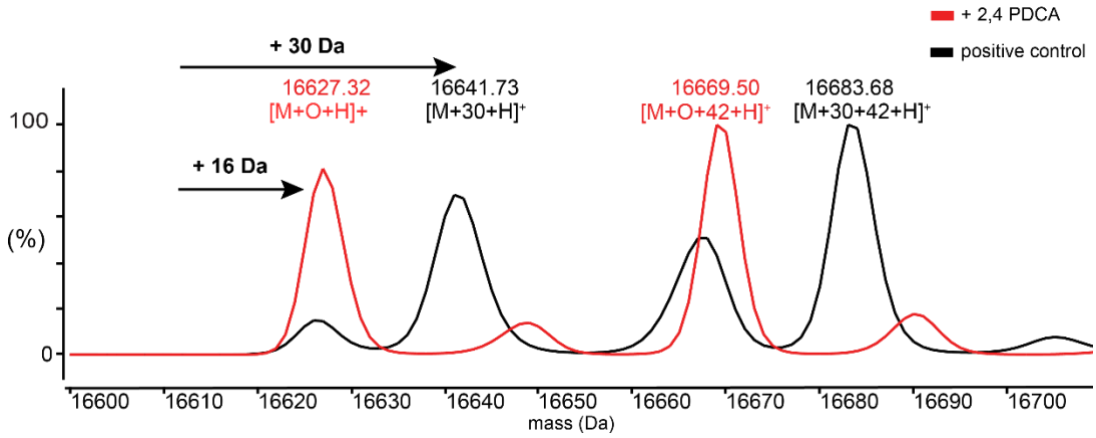

Figure 51. +30 Da modification of heRF1 is catalysed by JMJD4. A. Isolated eRF1-ND+OH in presence of Fe(II), 2OG and 20 mM Tris, pH 7.5. **B.** Optimised γ-lactam ring formation assay in presence and absence of 2,4- PDCA. Assay conditions used described in **Figure 50**.

5.2.4 Kinetic analyses on the influence of co-factors and co-substrate

5.2.4.1 Dependency on *L*-ascorbate

To investigate the dependence of γ-lactam ring formation on co-substrate (2OG) and co-factors (Fe(II) and *L*-ascorbate), the optimised γ-lactam ring formation assays using 1 µM heRF1-ND and 1 µM hJMJD4 were performed with varying concentrations of co-factors/co-substrate and monitored by SPE-MS.

First, four assays were prepared with *L*-ascorbate concentrations ranging from 0 µM to 200 µM and conversion was monitored over 50 min. Notably, the assays containing sodium *L*-ascorbate revealed significantly faster γ-lactam ring formation in a concentration

dependent manner. While the presence of *L*-ascorbate resulted in full conversion after 50 min, in the absence of *L*-ascorbate only heRF1-ND+OH was observed during this time period (**Figure 52A**).

Next, it was evaluated if in presence of *L*-ascorbate the concentration of enzyme relative to substate in assays can be reduced. Lowering the substrate:enzyme ratio to 1 µM: 100 nM led to observation of a high level of the heRF1-ND+30 Da species (~ 80 %) (**Figure 52B**). This result shows for the first time that the +30 Da modification can occur under catalytic conditions.

A

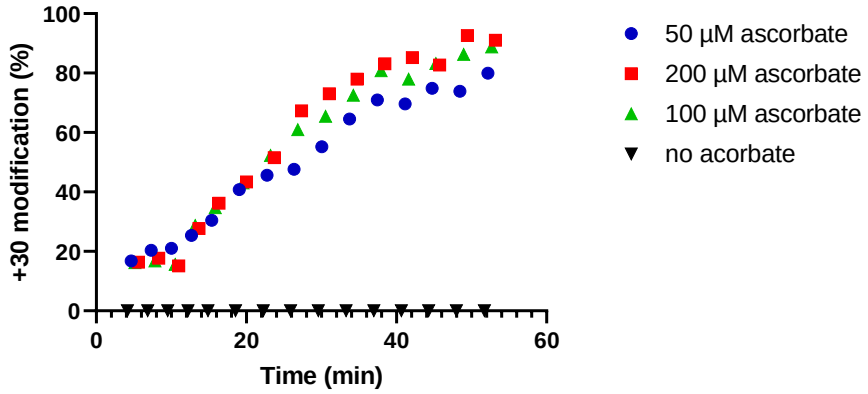

B

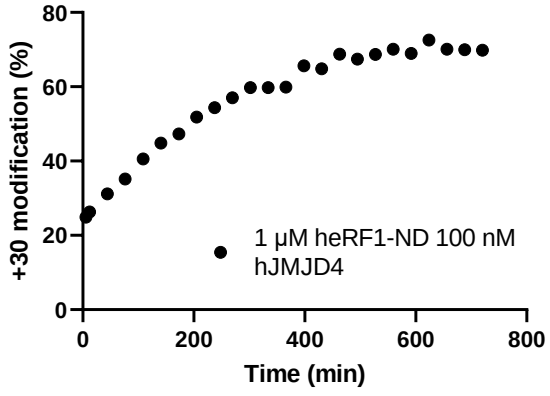

Figure 52. γ-Lactam ring formation is impacted strongly by *L*-ascorbate. A. Assay conditions used are described in **Figure 50**. These conditions were modified by varying the *L*-ascorbate concentration between 0-200 µM and using a shorter reaction time of ~ 50 min. **B.** 80% conversion of starting material to +30 modification was observed using a 10:1 substrate: enzyme ratio (1 µM heRF1-ND, 100 nM hJMJD4). For analysing the conversion, peaks at 16611 (heRF1-ND) 16627 (heRF1-ND+OH) and 16641 (heRF1-ND+30) were integrated.

The stimulation of 2OG oxygenases activity on sodium *L*-ascorbate has been previously described on many occasions (238–240). However, the precise roles of *L*-ascorbate are still unclear, including in a biological context. A possible reason for the positive effect of *L*-ascorbate on the +30 Da species is the formation of hydrogen peroxide, a strong oxidising agent, which could be involved in the +30 Da formation. Hydrogen peroxide formation can occur when ascorbate and molecular oxygen react non-enzymatically (241). However, adding catalase (which catalyses formation of water and dioxygen from hydrogen peroxide) to the optimised assay conditions did not affect the degree of +30 Da formation (**Figure 53**). For further γ-lactam ring formation assays 100 µM sodium *L*-ascorbate was added.

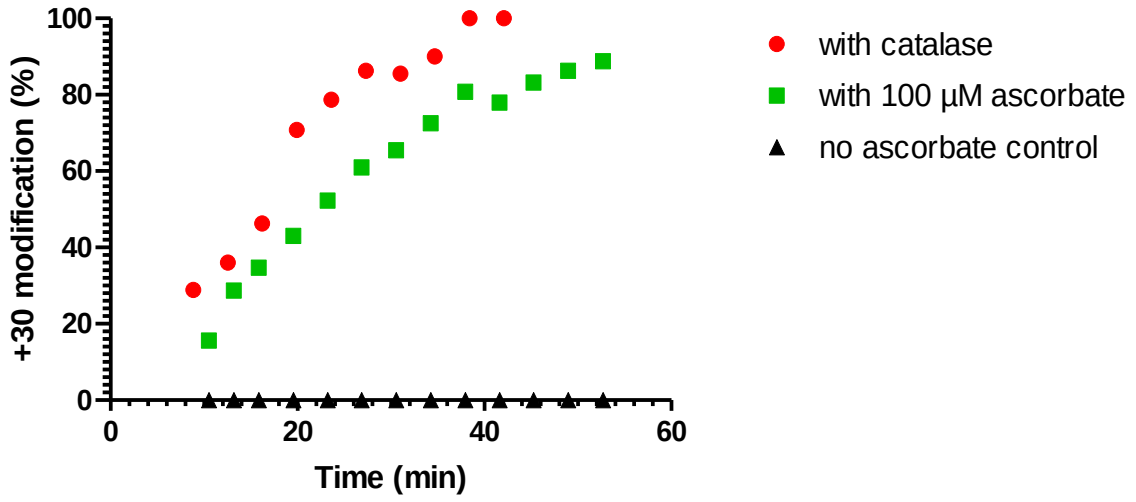

Figure 53. Assays in the presence and absence of catalase to investigate the role of *L*-ascorbate. Assay conditions used described in **Figure 50** with 10 nM catalase or 100 µM sodium *L*-ascorbate. For analysing the conversion, peaks at 16611 (eRF1-ND) 16627 (eRF1-ND+OH) and 16641 (eRF1-ND+30) were integrated.

5.2.4.2 Dependency on Fe(II)

The requirement Fe(II) for JMJD4 catalysed γ-lactam ring formation was investigated. The +30 Da modification of heRF1-ND was observed in the absence of additional Fe(II), although formation of γ-lactam ring is much less efficiently formed than when additional Fe(II) is present (**Figure 54**). As JMJD4 requires Fe(II) for its activity and some substrate conversion was observed in the no Fe(II) control sample, it is likely that JMJD4 was co-purified with some Fe(II) present in its active site.

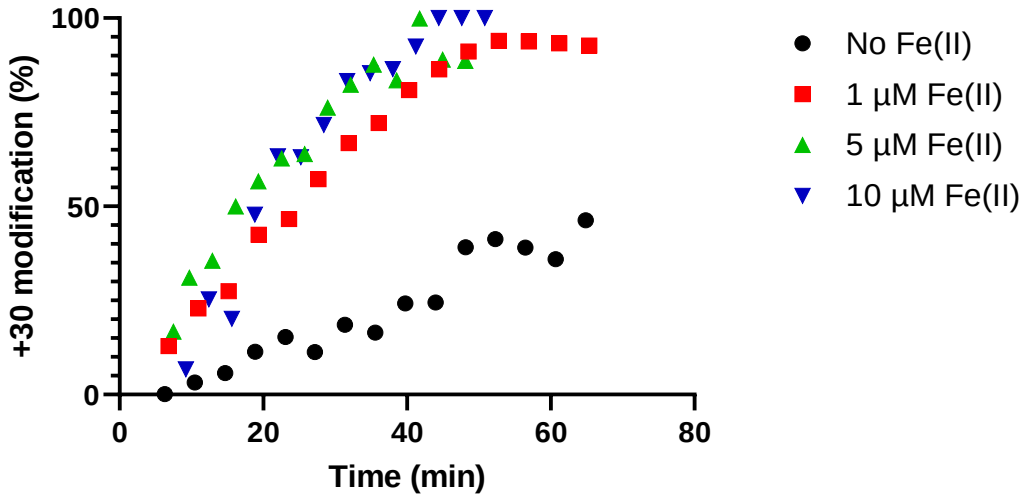

Figure 54. Dependence of Fe(II) on γ-lactam ring formation. The assay conditions used are described in **Section 5.2.4.1**. These conditions were modified by varying the Fe(II) concentration between 0-10 µM and using a shorter reaction time ~ 70 min. For analysing the conversion, peaks at 16611 (eRF1-ND) 16627 (eRF1-ND+OH) and 16641 (eRF1-ND+30) were integrated.

5.2.4.3 Dependency on 2OG

The proposed reaction mechanisms for the γ-lactam ring form described in **Figure 55** include three oxidative events, which likely require at least three 2OG molecules (assuming all three events are 2OG-dependent), i.e. one 2OG molecule for the hydroxylation of heRF1-ND and two 2OG molecules for the conversion from the hydroxylation to the γ-lactam ring formation.

Many (but not all) 2OG oxygenases catalyse uncoupled turnover of 2OG to succinate and CO_2 (both in the absence and presence of (some) substrates). Uncoupled 2OG turnover happens when decarboxylation of 2OG occurs without substrate oxidation, e.g. hydroxylation of the substrate (238–240).

Different equivalents of 2OG to wild-type heRF1-ND in the optimised γ-lactam ring formation assay were used to investigate the JMJD4 2OG dependency. The assays were performed with 1, 2, 3, 4, 5, and 100 equivalents of 2OG relative to 1 equivalent of wild-type heRF1-ND for 15 h. In the presence of only 1 equivalent of 2OG, a +16 Da peak was observed compatible with full hydroxylation of heRF1-ND (heRF1-ND+OH) (**Figure 55A**), but no +30 Da peak (or new peaks) were observed. No differences in the protein mass spectra were observed for 1, 2, and 3 equivalents of 2OG. With a greater excess of 2OG (4 and 5 equivalents), broader peaks of the heRF1-ND+OH sodium species were found (**Figure 55B**). It is unclear whether heRF1-ND+30 and/or intermediates are formed under these conditions, due to the present of broad protein signals and overlap with the sodium adduct peak. In presence of 100 equiv. of 2OG complete conversion to the +30 Da modification was observed. The results indicate no or little uncoupled turnover by JMJD4 for the initial hydroxylation, but that an excess of 2OG is required for the +30 Da modification. One possible explanation for the required excess of 2OG is that uncoupled 2OG turnover by JMJD4 occurs during formation of the +30 Da formation (as it is observed for other 2OG

oxygenases). Another potential explanation for the 2OG dependency is that binding of the hydroxylated heRF1 substrate and potential intermediates to hJMJD4 leads to weaker 2OG binding. Furthermore, there were no new products/intermediates using 2-3 equivalents of 2OG observed that implies that during catalysis of +30 Da formation following hydroxylation, intermediates may remain bound to hJMJD4.

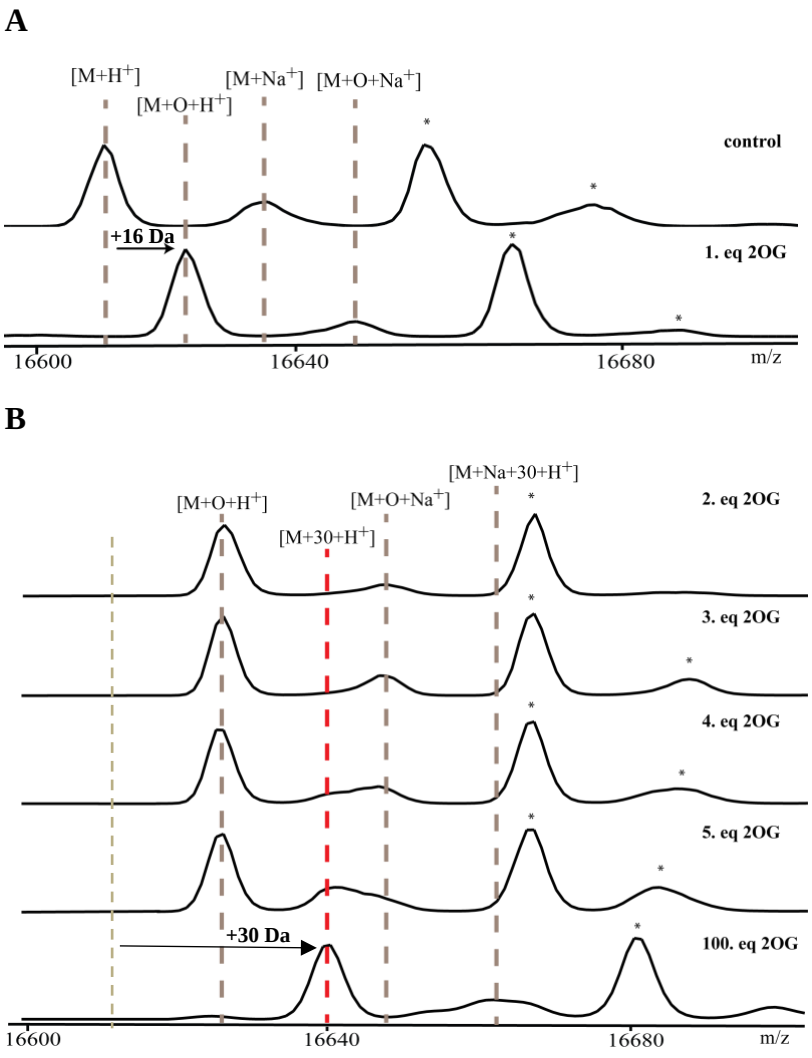

Figure 55. Dependence of heRF1-ND+OH and heRF1-ND+30 Da formation on 2OG, as analysed by SPE-MS. The assay conditions are described in **Section 5.2.4.1**. These conditions were modified by varying the 2OG concentration between 1-100 µM. Red dashed line shows the formation of heRF1-ND+30 Da. * marked all +42 Da species of heRF1-ND. Peaks were normalised.

5.2.5 JMJD4 and eRF1 orthologues

Bioinformatic analysis of eukaryotic genomes ranging from humans to yeast using BLAST (242) suggests that JMJD4/eRF1 system is highly conserved. There are (at least) 26 eukaryotic species containing orthologues of JMJD4 and eRF1 (144). However, JMJD4 orthologues were not identified in bacteria or archaea, whereas the amino acid sequence of eRF1 is highly conserved in eukaryotic species, but eRF1 eukaryotic protein orthologues differ significantly from the prokaryotic release factors in overall structure, architecture and specificity (130, 243, 244). Given the two modifications of human eRF1, hydroxylation and γ-lactam ring catalysed by recombinant hJMJD4 (144, 149), it was of interest to study the enzymatic activity of JMJD4 orthologues from different eukaryotic species. For that JMJD4 and eRF1 orthologues from *Mus musculus* (mouse) and from *Schizosaccharomyces pombe* (*S. pombe*, fission yeast) were selected.

eRF1 is a highly conserved protein in human, mouse, and *S. pombe* (133, 137). Human eRF1 (heRF1, UniProtKB Entry: P62495) share a 100% and 65% homology with the mouse (meRF1, UniProtKB Entry: Q8BWY3) and *S. pombe* (speRF1, UniProtKB Entry: P79063) orthologues, respectively (**Figure 56**). All three eRF1 orthologues contain the consensus NI**K**S motif important for stop codon recognition (133, 134, 137). Lysine residue in position 63 (numbering heRF1) is hydroxylated and lysine and serine residues in positions 63 and 64 (numbering heRF1) are involved in γ-lactam ring formation.

```
heRF1      MADDPSAADRNVEIWKIKKLIKSLEAARGNGTSMISLIIPPKDQISRVAKMLADEFGTAS 60
speR1      ---MSETAEKAIEIWKIRRLVKQLINCHGNGTSMITLIIPPGEQISRYSNMLAEEYGTAS 57
                .:*:: :*****::*:*.*  .:*******:***** :**** ::***:*:****

heRF1      NIKSRVNRLSVLGAITSVQQRLKLYNKVPPNGLVVYCGTIVTEEGKEKKVNIDFEPFKPI 120
speR1      NIKSRVNRLSVLSAITSTRERLKLYNKVPDNGLVIYCGEVIMEGNKTRKLNIDFEPFKPI 117
           **********.****.::********* ****:*** :: * .* :*:**********

heRF1      NTSLYLCDNKFHTEALTALLSDDSKFGFIVIDGSGALFGTLQGNTREVLHKFTVDLPKKH 180
speR1      NTSQYLCDNKFHTEALAELLESDQRFGFIVMDGHQTLYGVVSGSAREVLQRFTVDLPKKH 177
           *** ************: **..*.:*****:**  :*:*.:.*.:****::*********

heRF1      GRGGQSALRFARLRMEKRHNYVRKVAETAVQLFISGDKVNVAGLVLAGSADFKTELSQSD 240
speR1      GRGGQSALRFARLRDEKRHNYVRKVAEGAVQHFITDDKPNVAGIVLAGSADFKTELGQSD 237
           ************** ************ *** **:.** ****:************.***

heRF1      MFDQRLQSKVLKLVDISYGGENGFNQAIELSTEVLSNVKFIQEKKLIGRYFDEISQDTGK 300
speR1      LFDQRLQSRIIKTVDVSYGGDAGFNQAIELAADTLSNVKYVQEKKLIQRFFDEISLDSGK 297
           :*******:::* **:****: ********:::.*****::****** *:***** *:**

heRF1      YCFGVEDTLKALEMGAVEILIVYENLDIMRYVLHCQGTEEEKILYLTPEQEK---DKSHF 357
speR1      YCFGVVDTMNALQEGAVETLLCFADLDMIRYEFKNSEG-NPVITYMTKEQEEKDSTNSFL 356
           ***** **::**: **** *: : :**::** :: .   :  * *:* ***:    :*.:

heRF1      TDKETGQEHELIESMPLLEWFANNYKKFGATLEIVTDKSQEGSQFVKGFGGIGGILRYRV 417
speR1      LDKDTGAEMELVSSMLLSEWLAEHYKDYGANLEFVSDRSQEGMQFVKGFGGIGAVMRYQL 416
            **:** * **:.** * **:*::**.:**.**:*:*:**** **********.::**::

heRF1      DFQGMEYQGGDDEFFDLDDY 437
speR1      DLSMLDPE--SDEFYSDSD- 433
           *:. :: :  .***:. .*
```

Figure 56. Sequence alignment of *Homo sapiens/ Mus musculus* eRF1 and *Schizosaccharomyces pombe* eRF1. heRF1 (UniProtKB Entry: P62495) and speRF1 (UniProtKB Entry: P79063) share a protein sequence identity of 65%, analysed by Clustal Omega (78). heRF1 and meRF1 are identical proteins. The highly conserved NI**K**S motif is indicated with a red box.

Possible JMJD4 genes in the *mouse* genome (mJMJD4, UniProtKB Entry: Q8BFT6) and *S. pombe* genome (spJMJD4, UniProtKB Entry: O13977) were identified by BLAST analysis. A sequence alignment of hJMJD4 with mJMJD4 and spJMJD4 using Clustal Omega provided sequence identities of 74% and 32%, respectively. The three JMJD4 orthologues apparently have a highly conserved DSBH fold, which is characteristic of the 2OG oxygenases. Another apparently conserved structural feature between the three JMJD4 enzymes suggested by PSIPRED secondary structure analysis (245) is a C-terminal four-helical-bundle structure **Figure 57**. Furthermore, a reported global protein interaction study

in *S. pombe* shows that speRF1 (named as Sup45 in *S. pombe*) and spJMJD1 (named as JMJ1 in *S. pombe*) interact (246).

Figure 57. Sequence alignment of human JMJD4, mouse JMJD4, and *S. pombe* JMJD4. hJMJD4 (UniProtKB Entry: Q9H9V9) and mJMJD4 (UniProtKB Entry: Q8BFT6) have a protein sequence identity of 74%, whereas hJMJD4 (UniProtKB Entry: Q9H9V9) and spJMJD4 (UniProtKB Entry: O13977) share a protein sequence identity of 32%, analysed by Clustal Omega (78). The secondary structure of hJMJD4 (based on secondary structure prediction, PSIPRED (245)) is shown as blue rectangles (α-helices) and green arrows (β-strands).

5.2.5.1 Production and purification of heRF1-FL

Full-length human eRF1-His_6 (heRF1-FL) was produced in *E. coli* BL21(DE3) by Mr. Jesse Coker (Yue Lab, Structural Genomics Consortium (SGC), Oxford). The purification of heRF1-FL by Ni-affinity chromatography and SEC was performed as previously described (**Material and Methods**, **Section 6.3**; **Figure 58**) (149).

A **B**

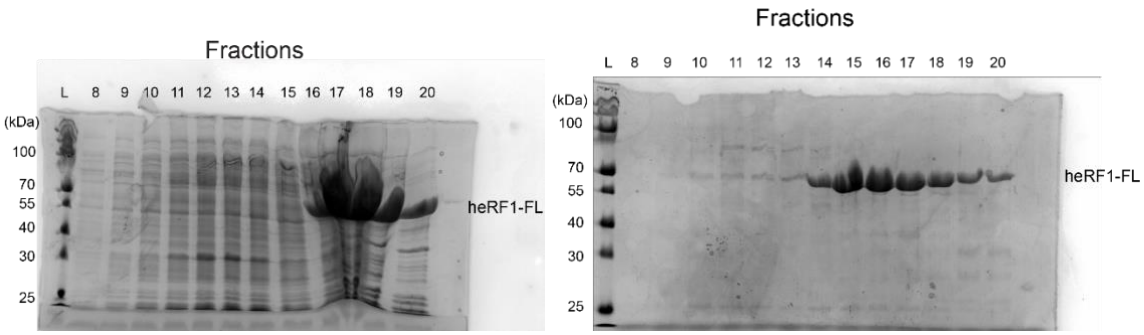

Figure 58. Purification of recombinant heRF1-FL. A. and **B.** heRF1-FL purification involves a 5 mL His-Trap column and S75 300 mL SEC column. L= Protein molecular weight marker.

5.2.5.2 Production and purification of mJMJD4

The gene encoding for full-length mJMJD4 was cloned into a pNIC28-Bsa4 vector with an *N*-terminal His_6-tag (MHHHHHHSSGVDLGTENLYFQS) for bacterial production. The pNIC28-Bsa4 mJMJD4 vector was transformed into *E. coli* Rosetta2 (DE3) pLysS cells. The new enzyme mJMJD4 was then produced following the procedure used for hJMJD4 production as described in the **Material and Methods**, **Section 7.2.12**. Recombinant mJMJD4 was purified using a combination of Ni(II) affinity chromatography and subsequent SEC following the same two-step purification protocol used for hJMJD4 purification (**Material and Methods**, **Section 6.3** and **Figure 59A** and **B**) (144). mJMJD4 mass was confirmed by intact protein LC-ESI-MS (**Figure 59C**).

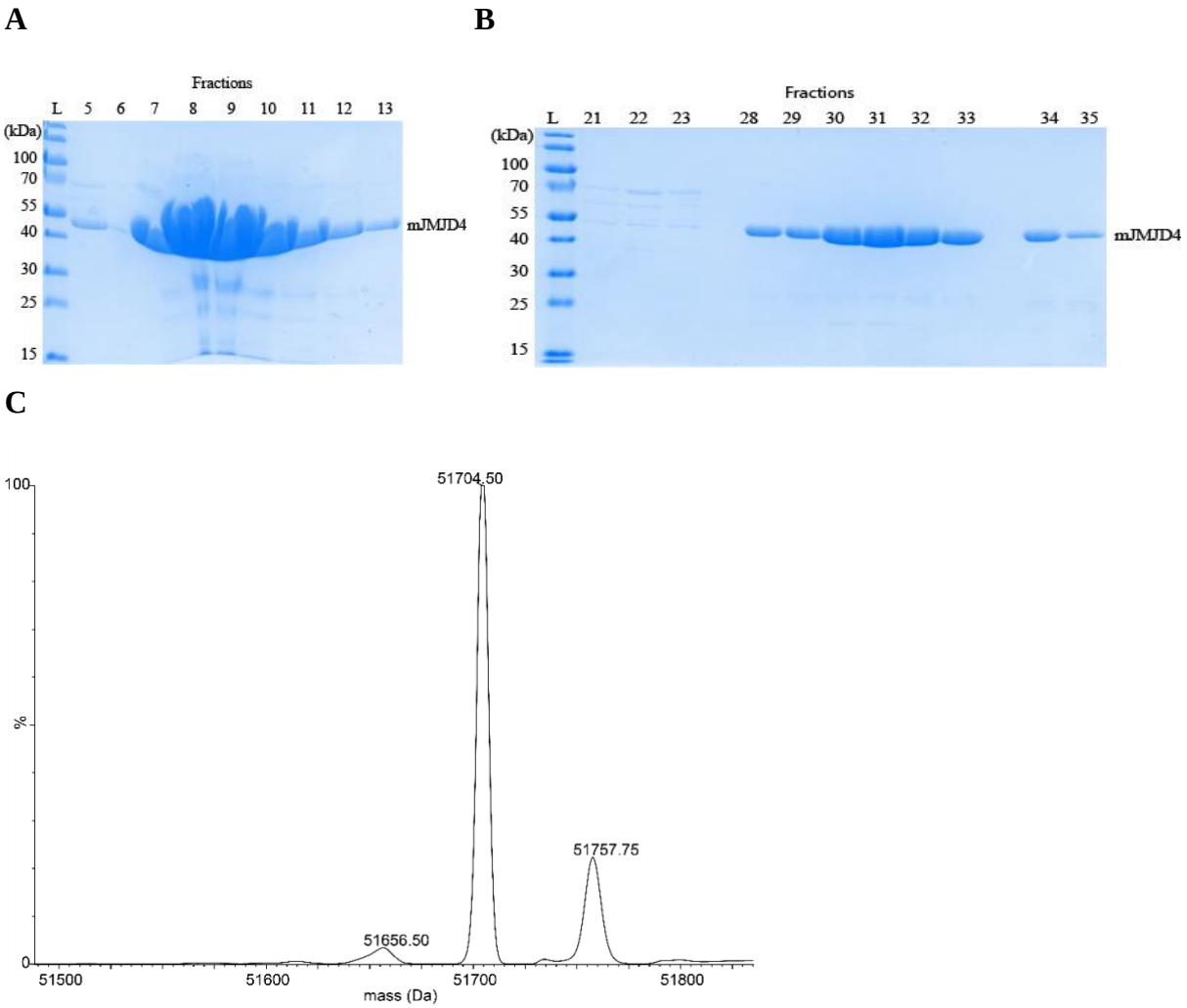

Figure 59. Coomassie-stained SDS-PAGE gels showing mJMJD4 purification and LC-ESI-MS analysis. Protein was first purified using a 5 mL His-Trap column (**A.**), then an SEC column (**B.**). L= Protein molecular weight marker. **C.** Deconvoluted mass spectra of mJMJD4. Theoretical molecular weight of mJMJD4 is 51704.75 Da and observed mass is 51704.50 Da.

5.2.5.3 Production and purification of full-length speRF1

The gene encoding for the full-length speRF1 was cloned from the *S. pombe* genome into a pNIC28-Bsa4 plasmid with an *N*-terminal His_6-tag and TEV-protease cleavage site (MHHHHHHSSGV DLGTENLYFQS) using ligation-independent cloning (247) as outlined in the **Material and Methods**, **Section 7.2.1**. Optimal production conditions of speRF1-FL in *E. coli* BL21 (DE3) were tested at 18, 28, and 37 °C and two different isopropyl β-D-1-thiogalactopyranoside (IPTG) concentrations (0.1 and 0.5 mM) (**Figure**

60A). The optimal production of speRF1-FL was induced by 0.5 mM IPTG at 18 °C with overnight (o/n) incubation. speRF1-FL was purified on a small scale using Ni(II)-affinity resin as described in the **Material and Methods**, **Section 6.3** and then buffer exchanged into hJMJD4 SEC buffer (**Figure 60B**). The presence of the speRF1-FL was validated by intact LC-ESI-MS (**Figure 60C**).

A

Vector	Cell line	Production conditions	Note
pNIC28-Bsa4 speRF1-FL	**BL21(DE3)***	**18 °C, 0.5 mM IPTG*, o/n**	**Good expression**
	BL21(DE3)	18 °C, 0.1 mM IPTG, o/n	Good expression
	BL21(DE3)	28 °C, 0.5 mM IPTG, o/n	Good expression
	BL21(DE3)	28 °C, 0.1 mM IPTG, o/n	Low expression
	BL21(DE3)	37°C, 0.5 mM IPTG, o/n	Low expression
	BL21(DE3)	37°C, 0.1 mM IPTG, o/n	Low expression

*Optimal condition for expression of soluble speRF1-FL.

B **C**

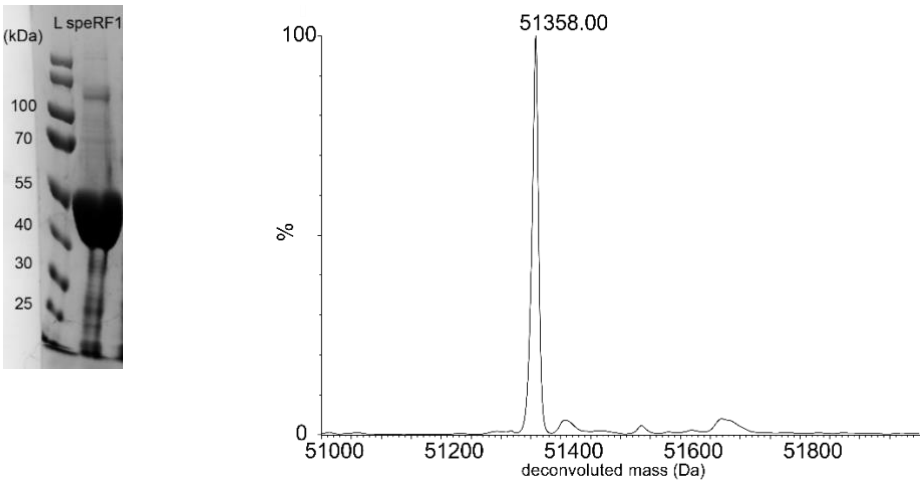

Figure 60. Expression trials and production of speRF1-FL. A. Summary of bacterial expression conditions screened for speRF1-FL. **B.** SDS-PAGE gel showing purified speRF1-FL after SEC. purification **C.** Deconvoluted mass spectrum confirms recombinant speRF1-FL. Theoretical molecular weight of speRF1-FL is 51355.93 Da and measured mass was 51358.00 Da.

5.2.5.4 Production and purification of full-length spJMJD4

The gene of JMJ1 (encoding for full-length spJMJD4) was codon-optimised for expression in *E. coli* and purchased in an expression vector pRSET-A (from GenScript) encoding for a protein with a N-terminal His_6-tag and a TEV-protease cleavage site (MRGSHHHHHHG MASMTGGQQMGRDLYDDDDKDRWGSENLYFQS). Probably due to a phage infection that occurred in our microbiology laboratory in 2018, it was not possible to grow any *E. coli* cells and all my attempts to express the recombinant proteins in *E. coli* cells failed. After a deep cleaning and disinfection, I tried again to express spJMJD4 with little success. Summary of all spJMJD4 expression attempts can be found in **Table 13**. Mr. Jesse Coker (Yue laboratory, Structural Genomics Consortium (SGC), Oxford) kindly provided me with a pellet of *E. coli* BL21 (DE3) Rosetta pRARE2 containing spJMJD4 (**Table 13**).

Table 13. Expression trails of spJMJD4 in different cell lines. In bold condition for spJMJD4 production.

Vector	**A. *coli* cell line**	**Media**	**Condition**	**Note**
pRSET-A spJMJD4	BL21(DE3)	2TY	-	No bacterial growth within 9 h*
	BL21(DE3) physS	2TY	-	No bacterial growth within 9 h*
	BL21(DE3) physS	2TY	-	No bacterial growth within 9 h
	Rosetta2 (DE3) pLysS	2TY	-	No bacterial growth within 9 h*
	Rosetta2 (DE3) pLysS	TB	-	No bacterial growth within 9 h
	BL21 Rosetta DE3 pRARE2	TB-PLUS		Schofield lab, no bacterial growth within 9 h
	BL21 (DE3) Rosetta pRARE2	**TB-PLUS**	**18 °C, 0.5 mM IPTG**	**In Yue lab (SGC)**

*Were conducted during and after phage infection in our lab.

Recombinant spJMJD4 was purified according to the purification protocol used for hJMJD4 (149). This includes Ni-affinity followed by SEC (**Material and Methods**, **Section 6.3**). The expression level of the spJMJD4 gene was found to be low and the recombinant

protein sample not very pure even after purification by a His-Trap column and S75 SEC, indicative of a high level of non-specific binding (**Figure 61**). Another batch of BL21 Rosetta DE3 pRARE2 containing spJMJD4 was purified by 5 mL His-Trap column using an extended wash step (3x longer, 60 column volumes) and a gradually increase of imidazole, aiming to remove unwanted *E. coli* proteins before the elution of spJMJD4. However, the purity, judged by SDS-PAGE gel, was not improved.

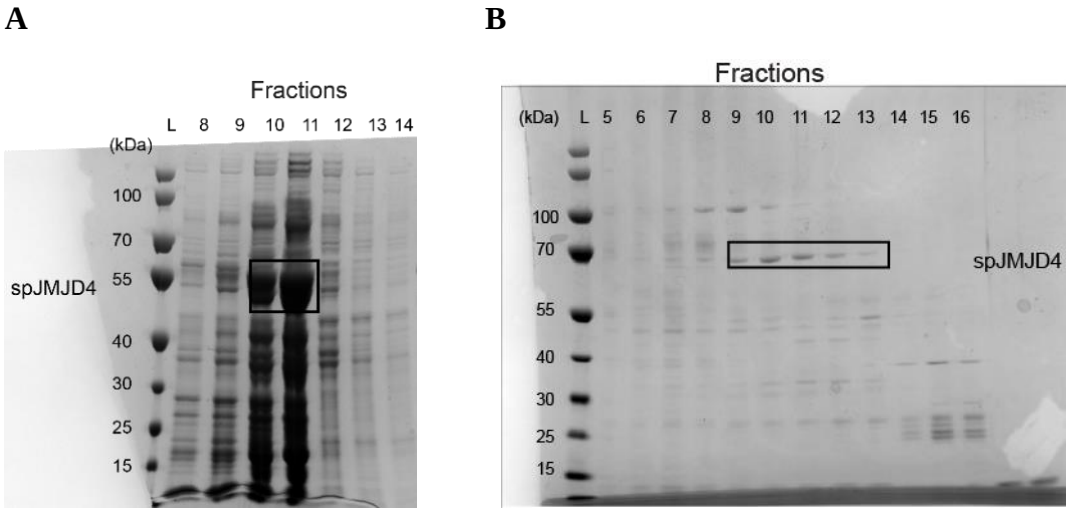

Figure 61. Purification of recombinant full-length spJMJD4. A. Ni-affinity chromatography**. B.** SEC. Black boxes indicate the spJMJD4 protein. L = protein molecular weight marker.

The production of new protein spJMJD4 was validated by trypsin catalysed digestion of potential spJMJD4 band (**Figure 61**) and subsequently analysed by LC-MS/MS, which was performed by Mr. Jesse Coker (Yue Laboratory, Structural Genomics Consortium (SGC), Oxford). The proteomic analysis shows 41% coverage of the spJMJD4 amino acid sequence (**Figure 62**). To confirm then molecular weight of the recombinant spJMJD4, intact LC-ESI-MS was performed. However, the corresponding protein mass for spJMJD4 was not detected. To improve the ionisation of spJMJD4, TFA (up to final 10% (v/v)) and freshly prepared 1,4-dithiothreitol (DTT) (final 5 mM) were added to the MS sample solution. However, the protein mass of spJMJD4 was still not detected by LC-ESI-MS.

1 MVYRPTAHEFDDLPKIEFIDSCPYQVFLEQYLKPCVPVLIGPKLTAQWKA
51 NTTWITSKGDPNILHSYILPDKPCTSRDNTSGNSLLNDNDIKNFIRSYAE
101 RIVNNEDKNVFLDSLLLSPNYEYLEENYGTIPVPLAYCNEKDRYGSQRRE
151 TVPLKSALHELRDEQVQLQCRQAPSNQALKSLYAKDMHLFRHLDPADFPY
201 STPDIFADDWLNAYVIDCESDDFRFAYLGSHLTTTGLHTDVYASHSFSVN
251 LCGVKCWLFIDPKDLQTIASLYDDQQLPSWITKDDLFRGPLVNHRHLIKI
301 LFQYPGQTVFVPSGWYHQVLNIGTTLSINHNWCNASCILQMYTALKEQYE
351 VSAESLKDLLEDGIVTKDRFSQVVTEVVEANYGWCWRRFWGMIKHQLKRR
401 DAILHSSEYFSKWPIQPEFLPPLSWEYSILKNILLNDEPGSTFDSGSPPS
451 SIVTIFKSLGDFKE

Sequence	Observed	Mr(expt)	Mr(calc)	Delta	Score	Expect	Peptide
16 – 43	1118.41	3352.208	3351.729	0.4794	77	7.80E-05	K.IEFIDSCPYQVFLEQYLKPCVPVLIGPK.L
59 – 77	728.27	2181.788	2182.084	-0.2959	68	0.00074	K.GDPNILHSYILPDKPCTSR.D
78 – 92	810.26	1618.505	1618.743	-0.238	18	75	R.DNTSGNSLLNDNDIK.N
78 – 92	810.27	1618.525	1618.743	-0.218	42	0.27	R.DNTSGNSLLNDNDIK.N
78 – 92	810.27	1618.525	1618.743	-0.218	65	0.0012	R.DNTSGNSLLNDNDIK.N
78 – 92	810.27	1618.525	1618.743	-0.218	77	8.70E-05	R.DNTSGNSLLNDNDIK.N
78 – 92	810.28	1618.545	1618.743	-0.198	98	6.30E-07	R.DNTSGNSLLNDNDIK.N
78 – 92	810.29	1618.565	1618.743	-0.178	79	5.20E-05	R.DNTSGNSLLNDNDIK.N
156 – 171	991.38	1980.745	1980.98	-0.2345	37	0.79	K.SALHELRDEQVQLQCR.Q
156 – 171	661.28	1980.818	1980.98	-0.1618	58	0.007	K.SALHELRDEQVQLQCR.Q
163 – 171	588.17	1174.325	1174.54	-0.2146	42	1	R.DEQVQLQCR.Q
264 – 283	1167.91	2333.805	2334.174	-0.3689	99	5.50E-07	K.DLQTIASLYDDQQLPSWITK.D
264 – 283	778.97	2333.888	2334.174	-0.2862	118	6.70E-09	K.DLQTIASLYDDQQLPSWITK.D
347 – 357	641.72	1281.425	1281.609	-0.1834	37	0.78	K.EQYEVSAESLK.D
347 – 357	641.73	1281.445	1281.609	-0.1634	23	18	K.EQYEVSAESLK.D
347 – 357	641.74	1281.465	1281.609	-0.1434	42	0.23	K.EQYEVSAESLK.D
347 – 357	641.75	1281.485	1281.609	-0.1234	43	0.19	K.EQYEVSAESLK.D
347 – 357	641.76	1281.505	1281.609	-0.1034	39	0.45	K.EQYEVSAESLK.D
347 – 357	641.77	1281.525	1281.609	-0.0834	25	13	K.EQYEVSAESLK.D
347 – 367	789.29	2364.848	2365.19	-0.3418	85	1.20E-05	K.EQYEVSAESLKDLLEDGIVTK.D
347 – 367	1183.47	2364.925	2365.19	-0.2646	48	0.067	K.EQYEVSAESLKDLLEDGIVTK.D
358 – 367	551.74	1101.465	1101.592	-0.1263	76	0.00013	K.DLLEDGIVTK.D
370 – 387	1115.37	2228.725	2229.031	-0.3059	73	0.00022	R.FSQVVTEVVEANYGWCWR.R
370 – 387	743.93	2228.768	2229.031	-0.2632	95	1.20E-06	R.FSQVVTEVVEANYGWCWR.R
370 – 387	743.96	2228.858	2229.031	-0.1732	35	4.4	R.FSQVVTEVVEANYGWCWR.R
401 – 412	698.78	1395.545	1395.667	-0.1216	71	0.00034	R.DAILHSSEYFSK.W
413 – 431	1172.51	2343.005	2342.235	0.7704	54	0.015	K.WPIQPEFLPPLSWEYSILK.N
432 – 457	912.33	2733.968	2734.37	-0.402	96	1.00E-06	K.NILLNDEPGSTFDSGSPPSSIVTIFK.S

Figure 62. Trypsin digestion of spJMJD4 band in SDS-PAGE gel. The red amino acid sequences indicate the peptides found by proteomic analysis. The data have been generated by Mr. Jesse Coker.

5.2.5.5 Comparison of mouse and S. pombe JMJD4 activities with human JMJD4

To compare the catalytic activities of the newly produced JMJD4 orthologues, spJMJD4 and mJMJD4, with hJMJD4, *the* optimised γ-lactam ring formation assay conditions, **Section 5.2.4.1** were used. The overnight incubation of mJMJD4 with heRF1-ND led to mixture of heRF1-ND+OH and heRF1-ND+30 Da products (**Figure 63A**), whereas the incubation of hJMJD4 with eRF1-ND resulted in complete conversion to the

heRF1-ND+30 Da (**Figure 50**) Compared to assay conditions containing heRF1-FL as substrate, the incubation with mJMJD4 resulted in a ~ +24 Da mass shift for heRF1-FL (**Figure 63B**). This is consistent with what was previously observed for heRF1-FL and hJMJD4 (~ +25 Da mass shift) (149). Previous complementary proteomic analysis of γ-lactam ring formation assay with heRF1-FL and hJMJD4 showed that heRF1-FL contained the +30 Da modification (149). The apparently different results observed (+24-25 Da instead of +30 Da mass shift) using different substrates eRF1-ND and eRF1-FL may be due to the limitations of deconvolution method employed in MassLynx. The deconvolution method may have difficulties distinguishing between the protein charge states of two large and similar sized proteins (e.g. heRF1-FL+OH, heRF1-FL+30 Da and hJMJD4 or mJMJD4) and high substrate:enzyme ratio.

By contrast, under optimised γ-lactam ring formation assay conditions using speRF1-FL and spJMJD4, speRF1-FL was hydroxylated (+16 Da), there was no +30 Da species of speRF1-FL observed (**Figure 63C**). The differences in activity of hJMJD4 and mJMJD4 to spJMJD4 may be amino acid sequence differences due to evolutionary processes.

A with heRF1-ND and mJMJD4

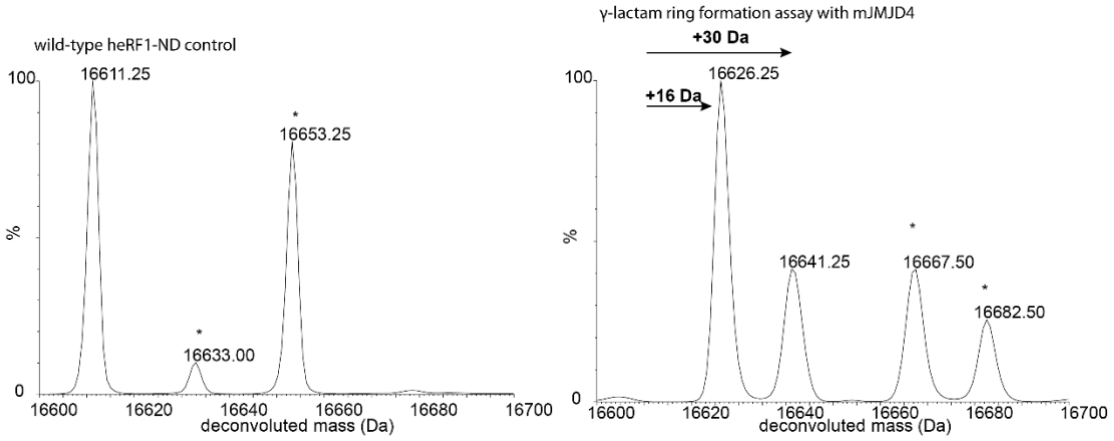

B with heRF1-FL and mJMJD4

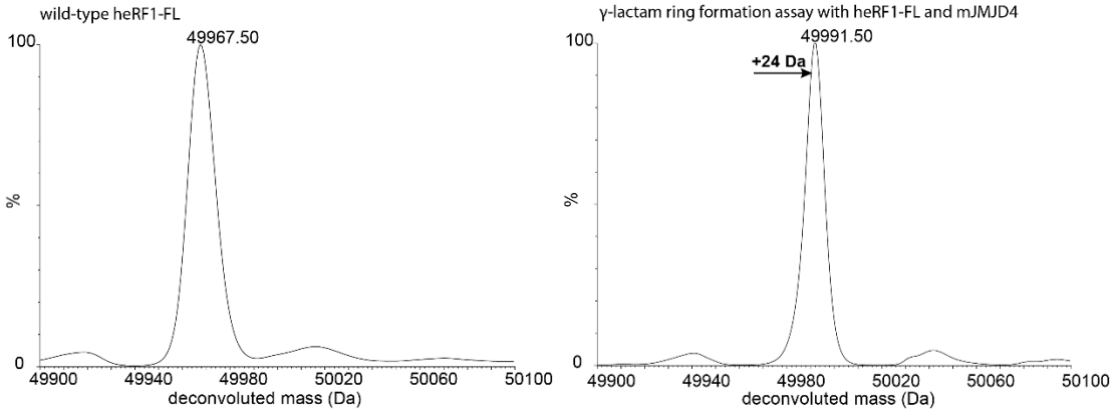

C with speRF1-FL and spJMJD4

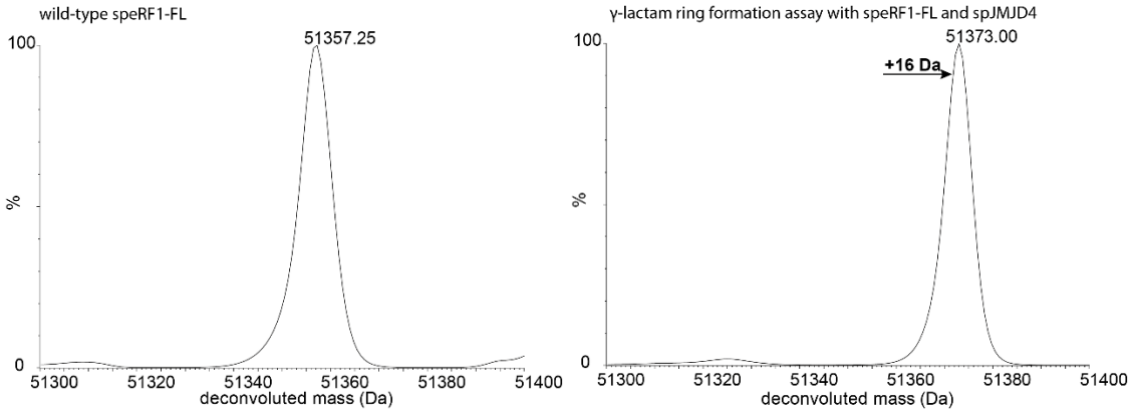

Figure 63. +30 Da modification is catalysed by mJMJD4 and hydroxylation of speRF1-FL is catalysed by spJMJD4. Assay conditions described in **Section 5.2.4.1**. Peaks were normalised. * marked all +42 Da species of heRF1-ND.

5.2.5.6 Bacterial co-expression of heRF1-FL and hJMJD4 and heRF1-FL and mJMJD4

To investigate the cellular relevance of the +30 Da modification co-expression studies in bacterial cells were carried out. Co-expression and purification of recombinant heRF1-FL and hJMJD4 and heRF1-FL and mJMJD4 in *E. coli* Rosetta2 (DE3) pLysS cells were performed on a small scale (**Material and Methods**, **Section 6.3.3.1**). Intact protein LC-MS analysis of the purified heRF1-FL and hJMJD4 mixture and heRF1 and mJMJD4 mixture revealed an apparent +27 Da mass shift for heRF1-FL (**Figure 64**). This result is consistent with the observation of a previous co-expression experiment with hJMJD4 and heRF1-FL (149). Overall, the results of the work with the JMJD4 and eRF1 orthologues suggest that the hydroxylation of eRF1 by JMJD4 is conserved among eukaryotic species. The co-expression studies and γ-lactam ring formation assay using mouse proteins support the possible physiological relevance of the γ-lactam ring formation.

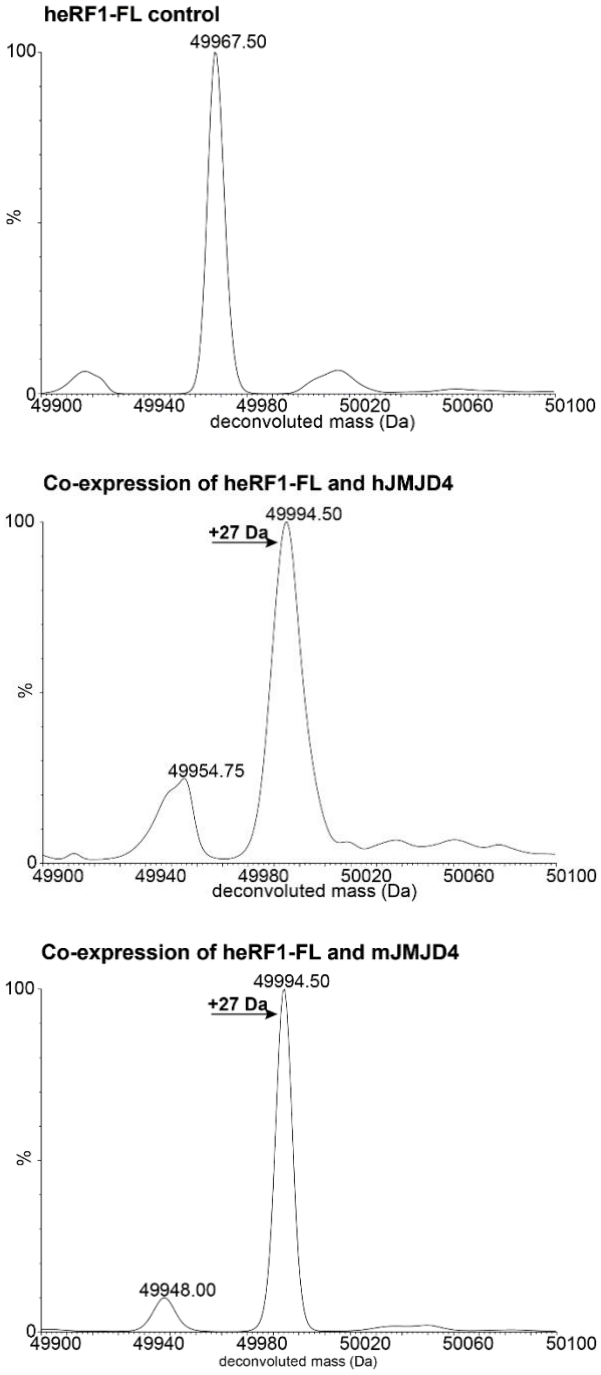

Figure 64. Bacterial co-production of heRF1-FL and hJMJD4 and mJMJD4 led to the +30 Da modification, respectively. LC-ESI-MS spectra show heRF1-FL+30 after co-expression with hJMJD4 and mJMJD4 in *E. coli*, respectively. Wild-type heRF1-FL produced in *E. coli* was used as control.

5.2.6 Investigating potential γ-lactam ring formation in human cells

The work described in this chapter reveals that the +30 Da modification of heRF1 was shown to occur in assays with isolated enzymes and in co-expression experiments in bacterial cells. If the new modification is present in human cells it would be the first oxidative ring formation catalysed by a 2OG oxygenase in humans and could be relevant for, e.g. protein translation termination or protein degradation. However, previous proteomic analysis of immunoprecipitation (IP) experiments performed on endogenous protein showed a high level of hydroxylated (+16 Da) eRF1 in HEK 293T, A549, and U2OS cells, but no presence for the +30 Da modification in endogenous eRF1 (144, 149). It is possible that the +30 Da modification may be present in human cells, but at very low abundance and so under the detection limit. To overcome this problem, a different approach was taken where total cell lysates from HepG2 cells was incubated with recombinant hJMJD4 and Fe(II), *L*-ascorbate, and 2OG. Immunoprecipitation was then performed on the samples treated with and without recombinant hJMJD4 and cofactors/co-substrate using both anti-eRF1 and anti-JMJD4 antibodies and subsequently analysed by Western Blot. The anti-JMJD4 antibody was used to try to co-immunoprecipitated endogenous/recombinant JMJD4 with endogenous eRF1. The work was performed in collaboration with Dr. Chiara Maniaci.

Prior to the immunoprecipitation experiment, the anti-eRF1 antibody (B11, Santa Cruz Biotechnology) and anti-JMJD4 antibody (JMJD4/32b/H12, Oxford) were used to evaluate the level of endogenous eRF1 and JMJD4 in total cell lysate from HepG2 cells in a Western Blot as described in the **Material and Methods**, **Section 6.10.4**. The anti-eRF1 antibody is monoclonal and his epitope is between amino acid 411-437 at the C-terminus of eRF1, whereas the Lys63 which is modified by JMJD4 is at the N-terminus of eRF1. The anti-eRF1 antibody is likely to bind to wild-type eRF1, eRF1+OH and eRF1+30 Da. The

Western Blot analysis show good expression levels for both endogenous eRF1 and JMJD4 in HepG2 cells (**Figure 65**).

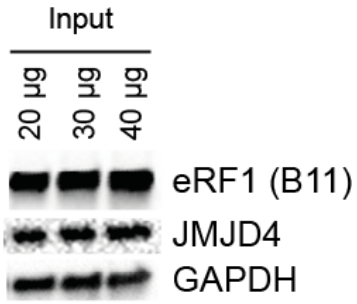

Figure 65. Western blots to evaluate endogenous level of eRF1 and JMJD4. 20, 30, and 40 µg of total cell lysate from HepG2 was used to detect endogenous eRF1 and JMJD4 using anti-eRF1 (B11) antibody anti-JMJD4 (JMJD4/32b/H12, Oxford). As the housekeeper protein GAPDH was used.

Given that lysis buffers containing various detergents, e.g. SDS and nonyl phenoxypolyethoxylethanol (NP-40) and sodium deoxycholate, it was important to determine if recombinant hJMJD4 would still retain its activity in different lysis buffers. Therefore, optimised γ-lactam ring formation assay as described in **Section 5.2.4.1** was performed using two different lysis buffers: RIPA buffer (150 mM NaCl, 1.0% NP-40, 0.5% sodium deoxycholate, 0.1% SDS, 50 mM Tris, pH 8.0) and JIES Buffer (20 mM Tris pH 7.4, 100 mM NaCl, 5 mM $MgCl_2$, 0.5 % (v/v) NP-40). After incubation for 16 h, the samples were analysed by LC-ESI-MS (**Figure 66**).

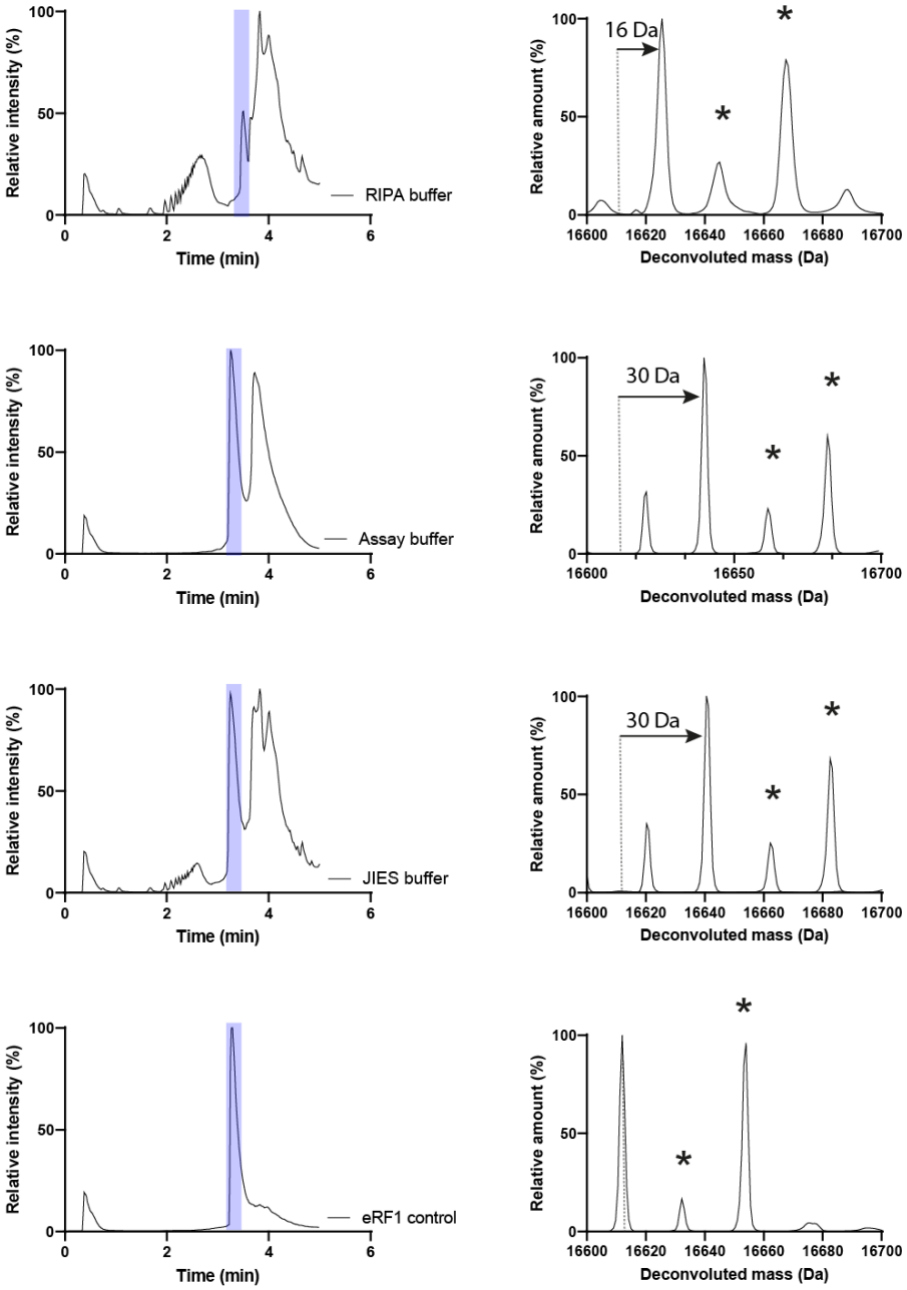

Figure 66. Lysis buffers influence activity of recombinant hJMJD4.

The results show that RIPA buffer influenced the retention time of the recombinant eRF1-ND; whereas use of the JIES buffer and the γ-lactam ring formation assay buffer (20 mM Tris pH 7.5 300 mM NaCl) gave similar retention times for the heRF1-ND species. The deconvoluted MS spectra of the peak eluted at 3.2-3.3 min showed that heRF1-ND underwent hydroxylation in RIPA buffer (+16 Da) and +30 Da modification in JIES buffer.

Consequently, JIES buffer was used as lysis buffer for the immunoprecipitation experiment with recombinant hJMJD4.

The immunoprecipitation experiments were performed on HepG2 cell lysates using anti-eRF1 and anti-JMJD4 antibodies conjugated to magnetic beads, as described in the **Material and Methods**, **Section 6.10.5**, and then analysed by Western Blots. Prior to incubation with the antibody conjugated beads, cell lysate from HepG2 was treated with recombinant hJMJD4 (2% of total protein concentration), 1 mM ammonium iron(II) sulfate, 2 mM 2-oxoglutaric acid disodium salt, and 1 mM sodium *L*-ascorbate.

To elute the antibody antigen complex from the magnetic beads prior to the Western blot, the IP samples were boiled in a loading dye buffer not containing a reducing agent, i.e. DTT. As the antibody lgG heavy chains band runs at the same expected molecular weight for eRF1 band in the SDS-PAGE gels, boiling samples in reducing conditions would have led to the degradation of the antibody and release of the heavy chains, resulting in overlap of the two bands. The Western blot analysis revealed that the anti-eRF1 (B11) antibody successfully immunoprecipitated endogenous eRF1, however co-immunoprecipitation of endogenous eRF1 with anti-JMJD4 antibody was not observed (**Figure 67**).

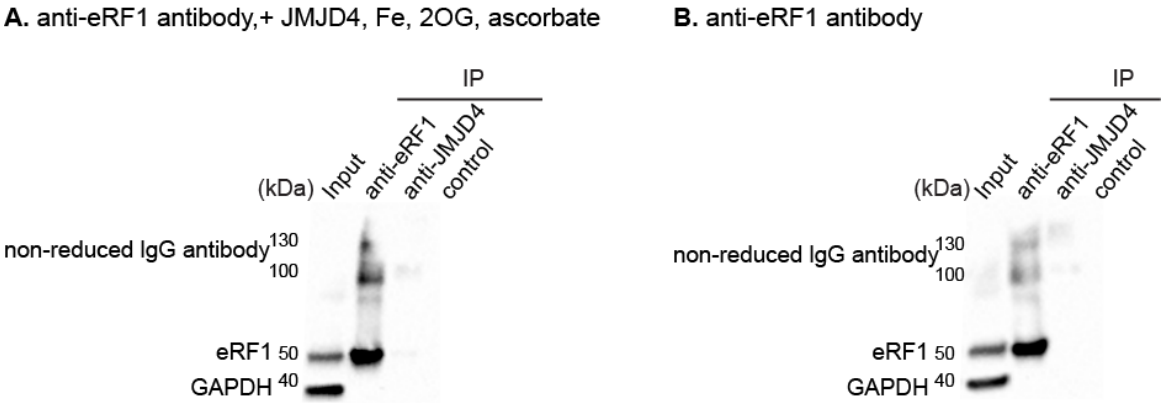

Figure 67. Western Blots of IP experiments. A. The IP product treated with recombinant hJMJD4 (2% of total protein concentration), 1 mM ammonium iron(II) sulfate, 2 mM 2-oxoglutaric acid disodium salt, and 1 mM sodium *L*-ascorbate was added to total cell lysate of HepG2 cells in JIES buffer for 16 h at 4 °C. **B.** Control IP experiment. Input is total cell lysate of HepG2. Control contains Dynabeads™ protein A magnetic beads with total cell lysate of HepG2 cells.

The IP samples were then analysed by LC-MS/MS to investigate the presence of the possible +30 Da modified eRF1 in the hJMJD4 treated samples. Previous LC-MS/MS analysis performed on tryptic digested recombinant wild-type eRF1-ND, eRF1-ND+OH, and eRF1-ND+30 Da showed presence of the following peptides: wild-type eRF1-ND [MLADEFGTASNI**K** = 698.84], eRF1-ND+OH [MLADEFGTASNI**KOH** = 706.84] and eRF1-ND+30 Da (MLADEFGTASNI**K+30**SR = 835.41]. Note that the peptide fragment containing the +30 Da modification, as anticipated, contains a missed tryptic cleavage site after Lsy63 (involved in hydroxylation and +30 Da modification). LC-MS/MS experiments were performed and analysed by Dr. Roman Fischer and Ms. Svenja Hester (TDI, University of Oxford) using PEAKS software. The presence of the hydroxylated eRF1 peptide fragments was found in both hJMJD4 treated and untreated samples, but the +30 Da modified eRF1 peptide was not detected (**Figure 68**).

It was not possible to detect the +30 Da modification on endogenous eRF1 in human cell lysate. Possible explanations are that +30 Da modification may be further modified in cells or other undetected modifications may happen. Another explanation is that the

experiment design (e.g. detection of endogenous proteins or data analysis) may prevent the observation of γ-lactam ring in endogenous eRF1.

A. Treated with hJMJD4, Fe(II), 2OG, *L*-ascorbate

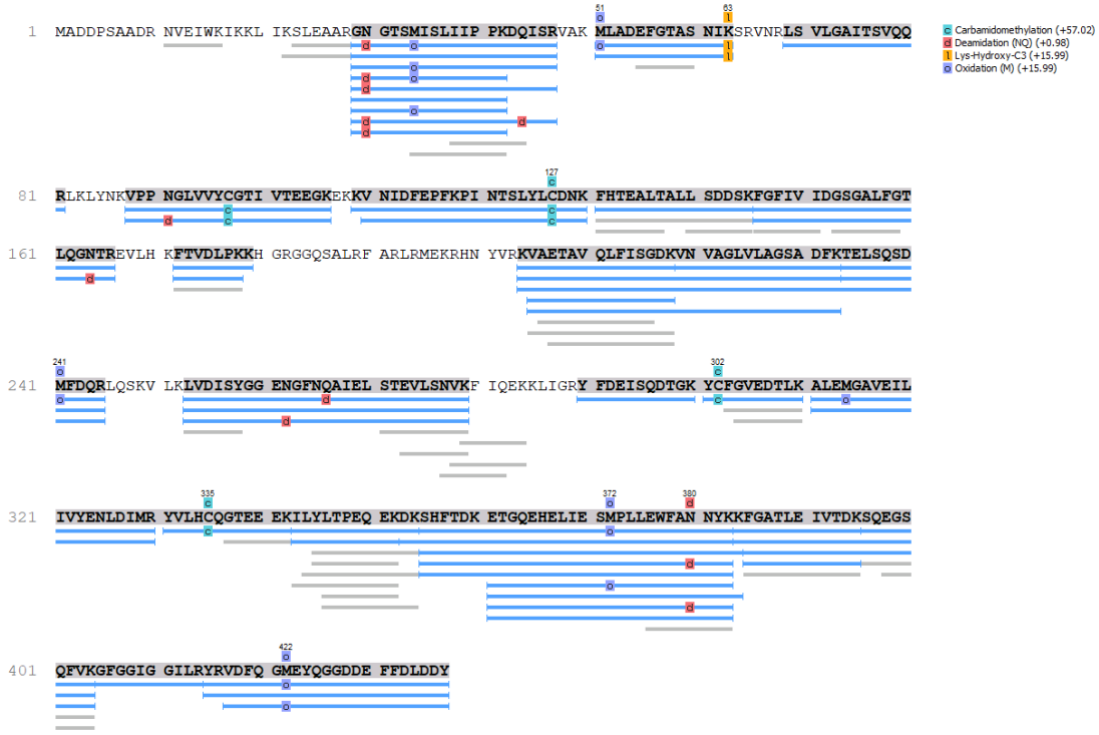

B. Untreated control

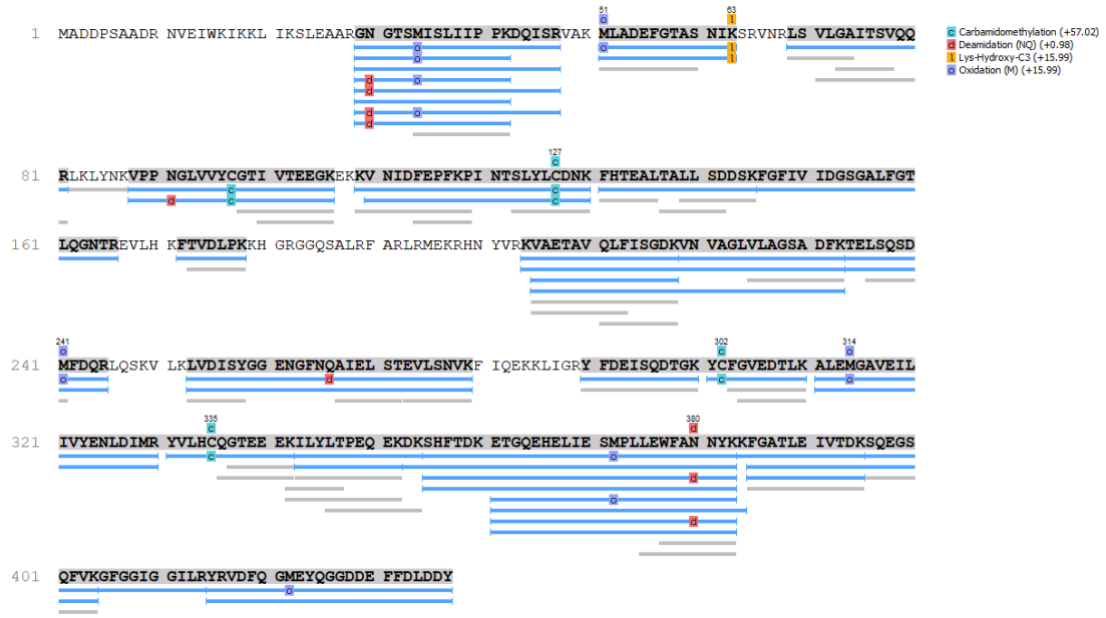

C

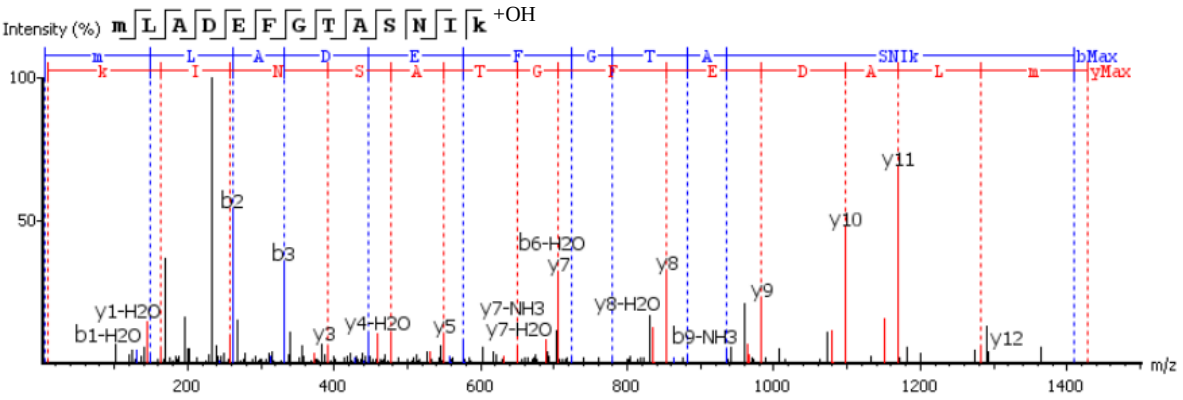

Figure 68. PEAKS analyses of the immunoprecipitation experiments described in Figure 67. Figures were kindly provided by Ms. Svenja Hester. A. IP experiment treated with JMJD4, 2OG, Fe(II) and *L*-ascorbate **B.** Control IP experiment. **C.** Fragmentation of eRF1 peptide containing hydroxylation (+16 Da). The experiments were performed by Ms. Svenja Hester.

5.3 Conclusions

The work presented in this chapter aimed to characterise the JMJD4 catalysed oxidative γ-lactam ring forming reaction occurring between Lys63 and Ser64 residues of heRF1. One focus of the work was to investigate factors required for the γ-lactam ring formation as catalysed by JMJD4 and to investigate the underlying reaction mechanism.

Previous work has reported γ-lactam ring formation of eRF1 occurs in assays with isolated enzymes (149). However, the recombinant eRF1 was unstable under the reported assay conditions resulting in precipitation. The γ-lactam ring formation assay was optimised for SPE-MS and LC-MS experiments to avoid the unwanted precipitation (**Figure 50**). The γ-lactam ring formation was inhibited by the broad-spectrum 2OG oxygenase inhibitor 2,4-PDCA (**Figure 50**). Use of the optimised γ-lactam ring formation assay with recombinant eRF1-ND+OH and co-substrate and co-factors but in absence of hJMJD4 showed no evidence for the +30 Da modification. This demonstrates that conversion of the C-4 lysyl hydroxylation to the +30 Da modification is catalysed by hJMJD4.

Further mechanistic studies on +30 Da formation suggest that the formation depends on Fe(II) and 2OG which is in agreement with JMJD4 being a Fe(II)- and 2OG-dependent oxygenase. hJMJD4 is stimulated by the presence of *L*-ascorbate, as is also commonly observed (but not always) for 2OG oxygenases. Notably, different dependencies on 2OG for Lys63 hydroxylation and +30 Da modification were observed. Only one equivalent of 2OG relative to eRF1 is required for complete hydroxylation of eRF1 (**Figure 55**). This indicates that hJMJD4 undergoes no or only a very low level of uncoupled conversion of 2OG to succinate and CO_2 during eRF1-ND hydroxylation. For the +30 Da modification an excess of 2OG relative to eRF1 is required. This indicates that the ring formation is challenging for the catalytic machinery of hJMJD4 (**Figure 55**). It is possible that the uncoupled turnover of 2OG to succinate or weaker binding of 2OG in presence of bound eRF1-ND+OH or other

intermediates. The potential uncoupled 2OG is in agreement with the strong dependence on *L*-ascorbate which was observed for the γ-lactam ring formation (**Figure 52**). The link between uncoupled 2OG turnover and *L*-ascorbate has been previously reported(248) and suggested that the physiological role of *L*-ascorbate is to provide Fe(II) for catalytically active enzyme after uncoupled turnover which result in higher Fe oxidation states (i.e. (Fe(III) and Fe(IV)). An alternative explanation for the excess of 2OG is weaker binding of 2OG in presence of bound eRF1-ND+OH or intermediates.

Future work could focus on investigating coupled and uncoupled turnover of 2OG to succinate by hJMJD4 in the presence and absence of wild-type eRF1 and hydroxylated eRF1 substrates. Additional binding and structural studies of hJMJD4 and wild-type eRF1, eRF1+OH and eRF1+30 and kinetic studies to obtain K_M values for 2OG for hydroxylation and +30 Da modification may help to further rationalise the mechanistic studies.

JMJD4 and eRF1 are evolutionary conserved in at least 26 eukaryotic species including human, mouse and *S. pombe* (144). It was investigated if JMJD4 from mouse and from *S. pombe* have the capacity to catalyse hydroxylation and γ-lactam ring formation. Recombinant JMJD4 and eRF1 orthologues from mouse and from *S. pombe* were cloned, produced in *E. coli* and purified. Similarly to hJMJD4, the mJMJD4 orthologue catalysed both hydroxylation and γ-lactam ring formation of heRF1 (amino acid sequence identical with meRF1) (**Figure 63**). Bacterial co-expression studies confirmed γ-lactam ring forming activity of mJMJD4, as it has been previously observed for hJMJD4 (**Figure 64**) (149).

In contrast to hJMJD4 and mJMJD4, the catalytic activity of spJMJD4 was apparently limited to hydroxylation of speRF1 (**Figure 63**). Biochemical assays with spJMJD4 and speRF1 did not show +30 Da modification. It may be because important interaction partners or other unknown factors, which are relevant for the oxidative ring

formation activity are not provided. Further work could verify the activity of spJMJD4 in *in vivo S. pombe* cell studies.

Additional work described in this chapter aimed at exploring the potential biological relevance of the γ-lactam ring formation of eRF1 *in vivo*. The results from IP experiments from HepG2 cells followed by Western Blot and proteomic analysis in presence and absence of recombinant hJMJD4, cofactors and co-substrate revealed hydroxylation of Lys63 in eRF1, however no additional modification was detected (**Figure 68**). Consequently, the γ-lactam species of heRF1 could not be observed in human cell proteome.

Further studies could involve the use of a specific anti-eRF1+30 Da antibody for IP experiments and Western Blots. The specific antibody could assist the mass spectrometric analysis, e.g. LC-MS/MS to detect the +30 Da modification if it exists. It is possible that in cells the +30 Da modification is only produced/stable under specific conditions or that an alternative modification occurs in cells. Given that with isolated proteins an excess of 2OG is required for its formation (at least under assay conditions) it is possible that excess (local) 2OG in cells may promote its formation. Alternatively, the +30 Da modification may be a non-biologically related artefact, albeit an interesting one.

Chapter 6 Thesis Summary and Conclusions

The work presented in this thesis focused on the characterisation of recently identified novel reactions catalysed by the bacterial class D nucleophilic serine β-lactamases (SBLs) and the human JmjC oxygenase JMJD4, which suggest that their functions are more diverse than previously believed. JMJD4 catalyses a well-characterised (4*R*)-lysyl hydroxylation reaction, as well as the unprecedented oxidative γ-lactam ring formation of eukaryotic release factor 1 (eRF1) (144, 145, 149). The class D SBLs also catalyse an unexpected cyclisation reaction, converting β-lactam antibiotics belonging to the carbapenem family into β-lactone products (88, 167).

The work described in **Chapters 2-4** focused on the class D SBLs, the mechanisms by which they degrade carbapenem antibiotics, and the clinical relevance of the results. Mutagenesis studies with OXA-48 and OXA-23 (two clinically relevant class D SBLs (59, 90)) were carried out to investigate the underlying molecular factors responsible for carbapenem-derived β-lactone formation (**Chapter 2**) (219). The results imply that the product distribution is determined by the conformations of the carbapenem-derived C-6 hydroxyethyl side chain, where one conformation favours β-lactone formation, and another is proposed to favour hydrolysis by helping position the hydrolytic water molecule in the active site. The combined results indicate that the active site residues interacting non-covalently with the dynamic C-6 hydroxyethyl side chain govern the relative levels of hydrolysis and β-lactone formation.

The OXA-48 V120L and OXA-23 V128L variants were observed to produce β-lactones from carbapenems with both 1β-methyl and 1β-hydrogen substituents (**Sections 2.2.4** and **2.2.6**). OXA-48 V120L is a clinically observed OXA variant (151) which shows efficient carbapenem turnover and demonstrates greater levels of β-lactone formation relative to wild-type OXA-48. Other class D SBL variants containing a similar Val-to-Leu substitution have been reported to be efficient carbapenemases (152, 155). Overall, the results support the proposed likely prevalence of carbapenem-derived β-lactone formation by class D SBLs and suggest that β-lactone production by class D SBLs represents a new resistance mechanism for carbapenem antibiotics.

The inhibitory activity of β-lactones against a panel of class A, C and D SBLs and class B metallo-β-lactamases (MBLs) was examined in work described in **Chapter 3**. A well-established fluorogenic assay was applied (213) to evaluate the potency of both the mixture of meropenem-derived β-lactones and meropenem as β-lactamase inhibitors. Under the tested conditions, no inhibition was observed for the class A and C SBLs and class B MBLs by the meropenem-derived β-lactones. While class D SBLs were inhibited by the mero-β-lactones, forming covalent complexes, the parent carbapenem was observed to be a more potent inhibitor (**Section 3.2.3**). NMR and MS studies suggest that recyclisation of the covalent complex occurs rapidly reforming the β-lactones. The different reactivities of meropenem and meropenem-derived β-lactones with class D SBLs are proposed to result from structural differences associated with the corresponding AECs. According to crystallographic and spectroscopic work, the tautomeric form of the pyrroline ring plays a role in determining the deacylation pathway by influencing the conformation of the C-6 hydroxyethyl side chain. Taken together, the results imply the carbapenemase activity of class D SBLs is not significantly inhibited by their β-lactones (at least compared to the parent

carbapenem), and thus these enzymes remain an efficient antibiotic resistance mechanism in spite of the potential accumulation of carbapenem-derived β-lactones.

In addition to the active site residues interacting with the carbapenem C-6 hydroxyethyl side chain, as described in **Chapter 2**, the tautomeric nature of different acyl-enzyme complexes likely influences the rate of product formation as proposed in **Chapter 3**. In the work described in **Chapter 4**, novel carbapenem analogues were used to investigate how the tautomerisation of the pyrroline ring impacts on, if at all, the stability of a carbapenem-derived AEC. A small panel of carbapenems was prepared (by co-workers) with several different C-2 phenyl thioether side chains with electron-donating and electron-withdrawing properties. The β-lactone and hydrolysis products formed by OXA-48 and carbapenem analogues were characterised by NMR spectroscopy. These studies revealed strong effects of the C-2 substituent on the degradation rate and, in some cases, the hydrolysis versus β-lactones product profile of these carbapenems with OXA-48. Notably, it was observed that two carbapenems with opposing electron-donating and electron-withdrawing effects (i.e. **TS02** and **FDK023**) behaved similarly with OXA-48, suggesting that in addition to electronic effects, other unknown factors, e.g. steric effects contribute to the carbapenemase activity of class D SBLs.

Overall, the work described in **Chapter 2-4** on carbapenem pyrroline ring tautomerisation occurring in the AECs of class D SBLs suggest that inhibition by carbapenems is reduced by β-lactone formation, consistent with the proposal that β-lactones are produced as a resistance mechanism. If that is the case this raises questions as to the extent of β-lactone formation as a resistance mechanism, including as to why non-hydrolytic resistance has not emerged previously, and whether other non-hydrolytic β-lactam inactivation mechanisms are feasible. Future studies on other classes of SBLs, especially non-carbapenemases, will be important to investigate the scope β-lactone-mediated

resistance and the precise role of carbapenem tautomerisation processes in the acyl-enzyme complexes in inhibition and hydrolysis. Future work could investigate the interaction of Class A and C SBLs with carbapenems, e.g. with respect to potential β-lactone formation.

The research described in **Chapter 5** focused on JMJD4, a member of the JmjC subfamily of 2-oxoglutarate-dependent oxygenases. After the initial hydroxylation of eRF1 by JMJD4, this enzyme can catalyse an unprecedented γ-lactam ring formation reaction with eRF1 with isolated components. γ-lactam ring formation likely ablates activity by eERF1 because it cause substantial conformational changes (149). The dependence of this reaction on the catalytic machinery of JMJD4 was confirmed by testing the impact of inhibitors, co-factors, and co-substrates. Notably, in the presence of *L*-ascorbic acid, JMJD4 showed enhanced levels of γ-lactam ring formation; the improved conditions showed that γ-lactam ring formation can be performed under catalytic conditions. This result suggests that the reactions catalysed by animal 2OG oxygenases may extend beyond the typical hydroxylation and demethylations to the complex and exotic oxidative ring formation that have been previously thought to be the provenance only of microbial 2OG oxygenases (121). Notably the reaction catalysed by JMJD4 is somewhat reminiscent of those catalysed by 2OG oxygenases and related enzymes involved in antibiotic and β-lactamase inhibitor biosynthesis (229, 230).

The γ-lactam ring formation is not limited to the human JMJD4 enzyme, as recombinant mouse JMJD4 catalysed the same modification of eRF1 (**Figure 69**). Bacterial co-production of recombinant mouse JMJD4 and eRF1 also indicated that ring formation is catalysed by the mouse orthologue. The JMJD4/eRF1 system is also highly conserved in yeast. Mass spectrometric work demonstrated that recombinant JMJD4 from the yeast *Schizosaccharomyces pombe* (*S. pombe*) was capable of hydroxylating the corresponding

eRF1 protein from *S. pombe*, but γ-lactam ring formation was not observed (**Figure 69**). The apparently evolutionarily conserved biochemical role of JMJD4 emphasises the biological importance of the hydroxylation of eRF1.

To investigate γ-lactam ring formation in a cellular context, immunoprecipitation experiments with human cells with recombinant human JMJD4 were conducted. The subsequent proteomics analysis revealed hydroxylated eRF1, but oxidative ring formation was not detected. The preliminary cellular experiments and functional analysis of *S. pombe* JMJD4 cannot preclude that the γ-lactam ring formation occurs *in vivo*; it is possible that the isolation procedures do not work well for the γ-lactam ring and that the analytical methods do not efficiently allow its detection. It is possible that unidentified interaction/binding partners for the γ-lactam ring formation complicate its isolation from cells or that it is targeted for clearance or degradation. Future work could focus on cellular studies using cell lines exogenously overexpressing JMJD4 to identify γ-lactam ring in human cells. In addition, the hydroxylation and potentially the γ-lactam ring formation could be identified of endogenous *S. pombe* eRF1 in cells.

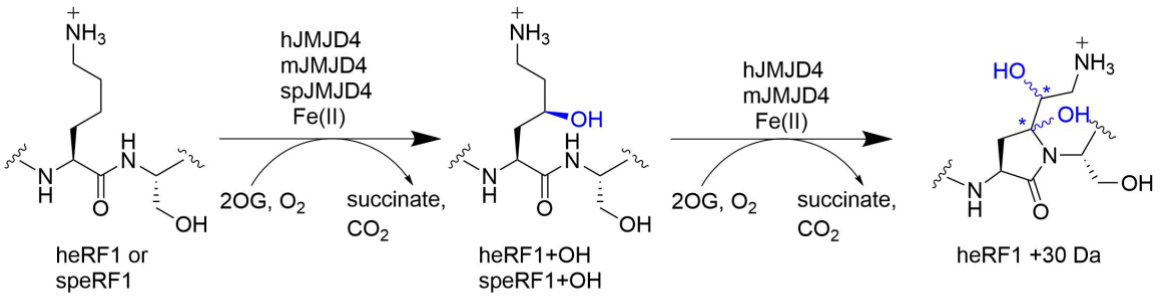

h = human, m = mouse, sp = *S. pombe*, heRF1 = meRF1

Figure 69. Overview of the activity of human, mouse and *S. pombe* JMJD4 with their corresponding eRF1 proteins.

Chapter 7 – Material and Methods

7.1 General

All chemicals, reagents and oligonucleotide primers were obtained from Sigma-Aldrich, unless otherwise specified. Biapenem, doripenem, ertapenem sodium, and meropenem trihydrate were from Glentham Life Sciences, ampicillin sodium, kanamycin sulphate, and isopropyl-β-D-1-thiogalactopyranoside (IPTG) were from Apollo Scientific, imipenem was from Molekula, panipenem was from Ontario Chemicals. Water was deionised by an Elix® system (Millipore) and then dispensed by a 0.22 μm membrane filter by a Milli-Q® system (Millipore), obtaining the so-called MQ water. For sterile work MQ water was autoclaved, and in this work referred to as sterile MQ water.

7.2 Microbiological Techniques

7.2.1 Cloning

7.2.1.1 Overview of oligonucleotide primers and plasmids used in this work

Primer was dissolved in sterile MQ water to obtain a 100 mM stock solution. A 10 mM primer working stock in sterile MQ water was prepared for ligation independent cloning (LIC) and for site-directed mutagenesis (SDM). The primers used are described in **Table 14**.

Table 14. Primer sequences used for LIC and SDM reactions.

Name of construct	**Primer**	**Sequence (5'- to 3')***
OXA-48		
OXA-48 W105A	F	TATCGCCACTGCGAATCGCGATCATAATCTAATCAC
	R	TCGCGCGTCTGTCCATCC
OXA-48 W105F	F	TATCGCCACTTTCAATCGCGATCATAATCTAATC
	R	TCGCGCGTCTGTCCATCC
OXA-23		
OXA-23 V128I	F	AGAAGCCATGAAGCTTTCTGCAATCCCAGTCTATC
	R	GATAGACTGGGATTGCAGAAAGCTTCATGGCTTCT
OXA-23 V128L	F	AGAAGCCATGAAGCTTTCTGCACTCCCAGTCTATC
	R	GATAGACTGGGAGTGCAGAAAGCTTCATGGCTTCT
JMJD4 and eRF1		
mJMJD4	F	TACTTCCAATCCATGGATCGGGAGACACGC
	R	TATCCACCTTTACTGCTAAAGGGCCTCTGCAGC
speRF1-FL	F	TACTTCCAATCCATGAGTGAGACTGCTGAGAAAGC
	R	TATCCACCTTTACTGCTAGTCGGAGTCGGAATAAAATTCATCAG

*The DNA sequences in blue are LIC overhang sequences. Start and stop codons are in red. The DNA bases in green correspond to the introduced changes.

In **Table 15** all plasmids used are summarised. The pRSET-A vector contains between the N-terminal His_6-tag and the *E. coli* codon-optimised spJMJ4 construct a tobacco etch virus (TEV) protease cleavage site (MRGSHHHHHHGMASMTGG QQMGRDLYDDDDKDRWGSENLYFQ*S, * = TEV cleavage site). The pNIC-Bio3 construct has a N-terminal His_6-tag with TEV protease cleavage site (MHHHHHHSSGVDLGTENLYFQ*SM, * = TEV cleavage site) and a termination codon at the C-terminal after the construct sequence. Therefore, the pNIC-Bio3 constructs are not biotinylated.

Table 15. Plasmids used in this work.

Name of construct	**Construct length**	**Vector**	**Tag**	**Source**
OXA-48 plasmids				
OXA-48	23-265	pNIC-Bio3	His_6	Dr. Christopher Lohans
OXA-48 V120L	23-265	pNIC-Bio3	His_6	Mr. Henry Chan
OXA-48 V120I	23-265	pNIC-Bio3	His_6	Mr. Henry Chan
OXA-48 W105A	23-265	pNIC-Bio3	His_6	SDM
OXA-48 W105F	23-265	pNIC-Bio3	His_6	SDM
OXA-48 L158I	23-265	pNIC-Bio3	His_6	Mr. Henry Chan
OXA-48 L158V	23-265	pNIC-Bio3	His_6	Mr. Henry Chan
OXA-23 plasmids				
OXA-23	18-273	pOPINF	His_6	Dr. Jürgen Brem
OXA-23 V128I	18-273	pOPINF	His_6	SDM
OXA-23 V128L	18-273	pOPINF	His_6	SDM
OXA-10 plasmid				
OXA-10	20-266	pET22 (Kan)	untagged	Dr. Christopher Lohans
JMJD4 plasmids				
hJMJD4	47-463*	pET28a(+)	His_6	Dr. Suzana Markolovic
mJMJD4	1-427	pCMV6-Entry	Myc-DKK	Origene
mJMJD4	1-427	pNIC28-Bsa4	His_6	LIC
spJMJD4	1-464	pRSET-A***	His_6	Thermo Fisher Scientific
eRF1 plasmids				
heRF1-ND**	1-142	pET23b(+)	His_6	Dr. Mat Coleman
heRF1-FL**	1-437	pET23b(+)	His_6	Dr. Mat Coleman
speRF1-FL	1-433	pNIC28-Bsa4	His_6	LIC from genomic DNA

*****It is not known if Met1 or Met47 is the initiation for translation of endogenous JMJD4.

Human and mouse eRF1 are identical. * Antibiotic selection: Ampicillin.

7.2.1.2 Ligation independent cloning

LIC insert amplification

For LIC cloning the DNA of interest was amplified by polymerase chain reaction (PCR) using the Q5® High-Fidelity DNA Polymerase and custom oligonucleotide primers (**Table 14**) with melting temperatures (T_m) of 55-67 °C. NEB protocol according to the manufacturer's instructions was applied for reaction and thermocycling conditions as outlined in **Table 16** and **Table 17** using a MJ Mini Personal Thermal Cycler (Bio-Rad). PCR performance was assessed by agarose gel electrophoresis (**Section 7.2.1.4**). The product was then purified by GeneJET Gel Extraction Kit (Thermo Fisher Scientific).

Table 16. Q5® High-Fidelity DNA Polymerase chain reaction.

Component	**Volume for 50 µL reaction (µL)**	**Final concentration**
5x Q5® Reaction Buffer	10	1x
10 mM dNTPs	1	200 µM
10 µM Forward primer	2.5	0.5 µM
10 µM Reverse primer	2.5	0.5 µM
Template DNA (plasmid or genomic DNA)	1	< 1000 ng
Q5® High-Fidelity DNA Polymerase	0.5	0.02 units μL^{-1}
5x Q5® High GC Enhancer	10	1x
Sterile MQ water	22.5	-

Table 17. Thermocycling conditions for PCR.

Step	Cycle	Temperature (°C)	Time (s)
Initial denaturation	1	98	30
Denaturation		98	10
Annealing*	25	50-62	30
Extension		72	60
Final extension	1	72	5 min
Hold	1	4	Hold

*Annealing temperature is 5 °C below the T_m of used primers.

Preparing cohesive ends for DNA insert

For the next step the cohesive ends of the DNA insert were generated using T4 DNA polymerase (Lucigen) in presence of dCTP as described in **Table 18**.

Table 18. Preparation of LIC-ready insert by generation of cohesive ends.

Component	Volume (µL) for a final volume of 10 µL
Sterile MQ water	2.05
Purified amplified DNA insert	5
Buffer A (Lucigen)	1
25 mM dCTP	1
BSA (10 mg/mL)	0.2
100 mM DTT	0.5
T4 DNA Polymerase (Lucigen)	0.25

Preparing cohesive ends for vector

To linearise the pNIC28-Bsa4 vector (kindly provided by Dr. Christopher Lohans) the vector was digested with BsaI (NEB) in CutSmart buffer (NEB) for 160 min at 50 °C, with mixing at 300 rpm (**Table 19**).

Table 19. Vector digestion by restriction enzyme BsaI.

Component	**Volume (µL) for a total of 100 µL**
Sterile MQ water	86-X
X µL plasmid (approx. 5 µg)	X
BsaI (20 units μL^{-1}, NEB)	3
10x CutSmart buffer (NEB)	10
BSA (10 mg/mL)	0.2

After digestion with BsaI the linearised vector was purified from the reaction mixture by GeneJET PCR Purification Kit (Thermo Fisher Scientific). To prepare cohesive ends, the purified linearised vector was incubated with dGTP and T4 DNA polymerase (Lucigen) for 30 min at room temperature and then for 25 min at 75 °C in order to deactivate the T4 DNA polymerase and LIC-ready vector was obtained. (**Table 20**).

Table 20. Preparation of LIC-ready vector by generation of cohesive ends.

Component	Volume (µL) for a total of 100 µL
Sterile MQ water	32.4
Linearised plasmid	50
Buffer A (Lucigen)	10
25 mM dGTP	1
BSA (20 mg/mL)	0.5
100 mM DTT	5
T4 DNA Polymerase (Luigen)	1

Annealing and Transformation

2 µL LIC-ready insert and 1 µL LIC-ready vector were mixed and incubated at room temperature for 30 minutes. The mixture was transformed into *E. coli* NEB-10β competent cells (**Section 7.2.2**) and plated onto Luria Broth (LB) plates containing 5% sucrose (selecting against uncut pNIC28-Bsa4 vectors). Single colonies were grown in starter cultures (**Section 7.2.8**). The plasmid DNA was isolated with a Plasmid Miniprep Kit (Thermo Fisher Scientific) and sequenced (**Section 7.2.10**).

7.2.1.3 SDM

QuikChange® SDM

The standard QuikChange® SDM protocol was partly modified to conditions suitable for the Q5® High-fidelity DNA polymerase (NEB) (**Table 16**). Complementary primers (**Table 14**) were used to insert the mutations. The vector was amplified using the QuikChange® SDM thermocycler programme (**Table 21**).

Table 21. Thermocycling conditions for QuikChange® SDM.

Step	Cycles	Temperature (°C)	Time (min)
Initial denaturation	1	94	2
Denaturation		94	0.45
Annealing	20	<78	1
Extension*		68	20
Final extension	1	68	20
Hold	1	4	

After amplification of the vectors, the PCR reaction was treated with 1 µL DpnI restriction enzyme (20 units µL $^{-1}$, NEB) and incubated overnight at room temperature to digest the methylated template plasmid. 5 µL of the mixture was then transformed into NEB-10β competent cells according to the procedures described in **Section 7.2.2**. The mutagenesis was confirmed by sequencing (**Section 7.2.10**).

NEBaseChanger™ SDM

In this protocol, the forward and reverse primers are designed in a back-to-back fashion. The forward primer contains the desired mutation in its middle section, while the reverse primer starts next to the 5′ end of the forward primer and is designed to be complementary to the 3′-5′ plasmid strand. PCR reactions were carried out as outlined in (**Table 16**), with the NEBaseChanger™ SDM thermocycler programme (**Table 22**).

Table 22. NEBaseChanger™ SDM thermocycler programme.

Step	Cycles	Temperature (°C)	Time (min)
Initial denaturation	1	94	2
Denaturation		94	0.45
Annealing	20	<78	1
Extension*		68	20
Final extension	1	68	20
Hold	1	4	∞

The PCR reaction mixture was mixed with 1 µL DpnI and incubated overnight at room temperature. The mixture was then treated with T4 ligase (NEB) and PNK T4 kinase (NEB) and incubated for 20 min at room temperature using following protocol (**Table 23**).

Table 23. Ligation of the blunt-ends of a plasmid.

Component	Volume for 20 µL reaction	Final concentration
Sterile MQ water	12	-
T4 DNA Ligase Buffer (10x)	2	1x (1 mM ATP, 10 mM DTT)
PCR product	4	-
PNK T4 kinase	1	0.5 units μL^{-1}
T4 kinase	1	20 units μL^{-1}

5 µL of the reaction mixture was added to NEB-10β competent cells and transformed as described in **Section 7.2.2**. Presence of the desired mutation in the plasmid was verified by sequencing (**Section 7.2.10**).

7.2.1.4 Agarose gel electrophoresis

The purity of the PCR reaction product was analysed by agarose gel electrophoresis. 1 % (w/v) agarose gel was prepared: 0.4 g agarose was dissolved in 40 mL 1x TAE buffer (Tris base, acetic acid and EDTA, **Table 24**) upon heating using microwave. After cooling down 4 µL of 10000x SYBR SAFE (Invitrogen) was added and the mixture was poured into a cast and allowed to set for 30 minutes. For the sample preparation 5 µL of 6x DNA Loading dye (NEB) was added to 25 µL amplicon. The sample (25 µL) was loaded onto the gel, and electrophoresis was run along with the appropriate 100 bp or 1 kb DNA ladder (NEB) in a Bio Rad tank filled with 1x TAE buffer at 100 V for 30 minutes. In cases where the template and cloning vectors encode resistance to the same antibiotic, the corresponding DNA construct band was cut out with a razor and DNA was extracted from the gel using GeneJET Gel Extraction Kit (Thermo Fisher Scientific). The extracted/purified DNA was stored at -20 °C.

Table 24. 50x TAE buffer.

Component	**50x TAE buffer (500 mL) (g)**
Trizma® base	121.14
Acetic acid	28.55
0.5 M EDTA	50

7.2.2 Bacterial transformations

Plasmid constructs were transformed into *E. coli* NEB-10β (NEB), BL21(DE3) (NEB), BL21(DE3) pLysS (NEB) or Rosetta (DE3) pLysS (Novagen) competent cells. Competent cells (25-50 µL) were thawed on ice and mixed with bacterial plasmid (30 -100 ng), or LIC or SDM mixture (5 µL). After incubating for 10-25 minutes on ice, reactions were heat shocked at 42 °C for 30 s and rested for 2 minutes on ice. Super Optimal Broth (SOC) medium (80 µL) was added to the bacterial cells before incubation at 37 °C for 1 h. After that, the bacterial cells were plated onto LB-agar plates with the required antibiotics (50 µg/mL kanamycin, 100 µg/mL ampicillin and/or 35 µg/mL chloramphenicol) and incubated at 37 °C overnight.

7.2.3 Bacterial co-transformations

Two bacterial plasmids (final amount 100 ng) were pre-mixed and competent cells were added. Transformation was performed as previously described (**Section 7.2.2**).

7.2.4 LB-agar plates

LB agar media was prepared in a glass bottle with components as listed in **Table 25**. The mixture was autoclaved. During cooling a pre-filtered solution of the appropriate antibiotic (50 µg/mL kanamycin, 100 µg/mL ampicillin and/or 35 µg/mL chloramphenicol) was added. 15 mL solution was poured into each Petri dish and left to solidify, before stored at 4 °C. Note that for LIC cloning, 5% sucrose was supplemented in addition to the antibiotic.

Table 25. LB agar media ingredients.

Component*	Mass (g) for 200 mL LB agar media
Agar (1.5% final)	3
Bactotryptone	2
Yeast extract	1
NaCl	2

7.2.5 2TY Growth media

2TY bacterial growth media was kindly prepared and autoclaved by Mr. Herminio Manso Jubier.

7.2.6 Terrific Broth (TB) Growth media

TB growth media containing 47.6 g L^{-1} TB powder (Sigma Aldrich) and 8 mL L^{-1} glycerol in MQ water was prepared and autoclaved.

7.2.7 TB Plus Growth media

To the autoclaved TB growth media described in **Section 7.2.6** were added 0.01% Antifoam + 1 mM $MgSO_4$ + 10 mM $(NH_4)_2SO_4$ + 0.5% (w/v) glucose + 1x *E. coli* trace metals. The 1x *E. coli* trace metals and 0.01% Antifoam solutions were kindly prepared by Mr. Jesse Coker (Yue lab, SGC).

7.2.8 Starter cultures

To 100 mL of 2TY growth media the required antibiotics was added and inoculated with a colony from a freshly transformed LB plate or using a glycerol stock. The bacterial starter culture was grown overnight at 37 °C with shaking at 180 rpm.

7.2.9 Glycerol stocks

A 700 µL aliquot from the starter culture was mixed with sterile 90% glycerol aqueous solution (700 µL) in a sterile cryotube. Glycerol stocks were stored at -80 °C.

7.2.10 Plasmid purification and sequencing

After fresh transformation, a starter culture was prepared as described in **Section 7.2.8**. Bacterial cells from 5 mL starter culture were pelleted by centrifugation (5 min, 4000 rpm, 4 °C). The plasmid DNA was isolated using a GeneJET Plasmid MiniPrep Kit (Thermo Fisher Scientific). The plasmid was eluted with 30-50 µL sterile MQ water. All recombinant plasmids were analysed by sequencing using Source Bioscience and Eurofins.

7.2.11 Expression trials

To identify optimal production conditions for new proteins, factors including temperature and IPTG concentration were varied. 100 mL 2TY growth media was supplemented with the required antibiotic as outlined in **Section 7.2.12** and inoculated with 1 mL starter culture. The culture was grown at 37 °C with shaking at 180 rpm. When an optical density at a wavelength of 600 nm (OD_{600}) of 0.6-0.8 was reached, the cultures were induced by different IPTG concentrations (0.1 and 0.5 mM) under various induction temperatures (18, 28 and 37 °C). The bacterial cell cultures were grown overnight, and then cells from a 1 mL aliquot from each overnight culture were pelleted (8000 rpm, 4 °C, 5 min).

Cell pellets were resuspended in 100 mL MQ water and 25 µL Popculture Reagent (Merck) supplemented with 0.5 µL Lysonase™ Bioprocessing Reagent (Novagen), and the mixture was then incubated for 10 min. The cell debris was separated by centrifugation (8000 rpm, 4 °C, 5 min). To analyse the amount of protein present, 10 µL of supernatant from each sample was mixed with 2x NuPAGE™ LDS (1:1 MQ water and 4x NuPAGE™ LDS with 6 mg dithiothreitol (DTT) in 100 µL) and loaded onto a SDS-PAGE gel. Alternatively, to enrich a His_6-tagged proteins loose Ni(II) resin was used (**Section 7.3.3.1**).

7.2.12 Protein production

0.1-0.6 L 2TY media (often used 12 x 0.6 L 2TY media), supplemented with the appropriate antibiotics (**Table 26**), was inoculated with a 1:100 v/v ratio of starter culture. The culture was shaken at 180 rpm at 37 °C. When the culture reached an OD_{600} of 0.6-1.0, protein production was induced by addition of IPTG, after which the culture was incubated for the optimal time period at the appropriate induction temperature (**Table 13**). The cultures were then harvested by centrifugation (8000 rpm, 8 min, 4 °C). The collected cell pellets were stored at -80 °C.

Table 26. Optimised protein production conditions.

Recombinant protein	**Vector**	**Strain**	**Antibiotic Resistance****	**Conditions**
OXA-48*	pNICBio3	BL21(DE3)	Kan^R	0.5 mM IPTG, 18 °C, o/n
OXA-23 V128I	pOPINF	BL21(DE3)	Amp^R	0.5 mM IPTG, 18 °C, o/n

OXA-23 V128L	pOPINF	BL21(DE3)	Amp^R	0.1 mM IPTG, 18 °C, o/n
OXA-10	pET22	BL21(DE3)	Kan^R	0.5 mM IPTG, 37 °C, 4 h
OXA-10 S70C	pET22	BL21(DE3)	Kan^R	0.1 mM IPTG 37 °C, 4 h
hJMJD4	pET28a(+)	Rosetta (DE3) pLysS	Kan^R Chl^R	0.5 mM IPTG, 18 °C, o/n
hJMJD4 and eRF1-ND/FL co-expressed		Rosetta (DE3) pLysS	Kan^R Amp^R Chl^R	0.5 mM IPTG, 20 °C, o/n
mJMJD4	pNIC28-Bsa4	Rosetta (DE3) pLysS	Kan^R Chl^R	0.5 mM IPTG, 18 °C, o/n
mJMJD4 and heRF1-ND/FL co-expressed		Rosetta (DE3) pLysS	Kan^R Amp^R Chl^R	0.5 mM IPTG, 20 °C, o/n
heRF1-FL	pET23b(+)	BL21(DE3)	Amp^R	0.5 mM IPTG, 20 °C, o/n
heRF1-ND	pET23b(+)	BL21(DE3)	Amp^R	0.5 mM IPTG, 20 °C, o/n
speRF1-FL	pNIC28-Bsa4	BL21(DE3)	Kan^R	0.5 mM IPTG, 18 °C, o/n

* Protein production conditions also used for OXA-48 variants. ** Kan = kanamycin, Amp = ampicillin, Chl = chloramphenicol.

7.3 Protein purification

7.3.1 Cell lysis

Cell pellets were resuspended in 3-4x (w/v) cooled lysis buffer containing DNase I (Roche) and cOmplete™ Protease Inhibitor Cocktail (Roche) and stirred at room temperature for 10 min, then at 4 °C for 30 min. Suspended cells were lysed by sonication (Sonics Vibracell VCX750 Ultrasonic Cell Disruptor) at 60% amplitude, with a repeated 3 s pulse followed by a 7 s rest time, for a total of 3.5 min. The crude lysate was centrifuged (22000 rpm, 25 minutes, 4°C), and the supernatant was filtered using a 0.45 µm syringe filter (Sarstedt).

7.3.2 Purification strategies

Table 27 provides an overview of the different purification protocols used for the recombinant proteins.

Table 27. Overview of purification protocols.

Recombinant proteins	Purification steps	Buffers
OXA-48* OXA-48 W105A OXA-48 W105F OXA-23 OXA-23 V128I OXA-23 V128L	Ni-NTA affinity chromatography (5 mL)	Buffer A: (50 mM HEPES, pH 7.5, 20 mM imidazole, 500 mM NaCl) Buffer B: (50 mM HEPES, pH 7.5, 500 mM imidazole, 500 mM NaCl) Wash: 20 CVs of HisTrap Buffer A Elution: 0-100% HisTrap Buffer B over 8 CVs
	SEC (S200, 300 mL)	50 mM sodium phosphate Buffer pH 7.5*
hJMJD4 mJMJD4	Ni-NTA affinity chromatography (5 mL)	Buffer A: (50 mM HEPES, pH 7.5, 500 mM NaCl,

		20 mM imidazole) Buffer B: (50 mM HEPES, pH 7.5, 500 mM NaCl, 250 mM imidazole) Wash: 24 CVs with Buffer A Elution: 5 CVs with Buffer B
	SEC (S75, 300 mL)	20 mM Tris, pH 7.5, 200 mM NaCl, 5% glycerol
heRF1-FL speRF1-FL	Ni-NTA affinity chromatography (5 mL)	Buffer A: (50 mM HEPES, pH 7.5, 500 mM NaCl, 20 mM imidazole) Buffer B: (50 mM HEPES, pH 7.5, 500 mM NaCl, 250 mM imidazole) Wash: 24 CVs with Buffer A Elution: 5 CVs with Buffer B
	SEC (S75, 300 mL)	50 mM HEPES, pH 7.5, 200 mM NaCl, 2% glycerol,
mJMJD4/heRF1-FL co-expression hJMJD4/eRF1-FL co-expression	Loose Ni(II) resin method (**Section 7.3.3.1)**	Buffer A: (50 mM HEPES, pH 7.5, 500 mM NaCl, 20 mM imidazole) Buffer B: (50 mM HEPES, pH 7.5, 500 mM NaCl, 250 mM imidazole) Wash: 3x 500 µL HisTrap Buffer A Elution: 400 µL HisTrap Buffer B
	Buffer exchange	20 mM Tris, pH 7.5, 200 mM NaCl, 5% glycerol

* Buffer is prepared by mixing sodium monobasic and dibasic phosphates. NAT = nitrilotriacetic acid, SEC = size exclusion column, CV = column volume

7.3.3 Protein chromatography

7.3.3.1 Loose Ni(II) resin method

Loose Ni(II) resin (20 µL resin/mL or 400 µL resin/100 mL of bacterial cell culture) was pre-washed three times with Buffer A (**Table 27**). Equilibrated resin slurry (80%) was mixed with protein samples and incubated with rocking at 4 °C for 1 h. Loose resin was pelleted by centrifugation (8000 rpm, 1 min, 4 °C) and then washed three times with 500-1000 µL buffer A (**Table 27**). The protein was eluted from the resin by incubating with 100-500 µL buffer B (**Table 27**) for 1 h with rocking. Resin and supernatant were separated by centrifugation. 10 µL of the supernatant was transferred to a new tube for SDS-PAGE gel analysis. The resulting protein solutions were flash frozen in liquid nitrogen and stored at -80 °C.

7.3.3.2 Nickel(II) affinity chromatography

A charged 5 mL HisTrap™ HP Column (GE Healthcare) was washed with 6 CVs Buffer B and pre-equilibrated with 6 CVs Buffer A (**Table 27**). The filtered supernatant was loaded onto the pre-equilibrated column at 1 mL/min. Non-specifically bound proteins (without the His_6-tag) were removed with 24 CVs Buffer A (**Table 27**). The desired protein was then eluted with Buffer B (**Table 27**) and collected in 1 mL fractions. Fractions that contained the protein of interest, as indicated by SDS-PAGE or UV trace, were subsequently combined and concentrated.

7.3.3.3 Size exclusion chromatography

Size exclusion chromatography using a Superdex 75 or Superdex 200 300 mL column (GE Healthcare) was performed. The column was washed with water and pre-equilibrated with 300 mL gel filtration buffer (**Table 27**). The protein-containing fractions

obtained from the previous chromatography step were loaded onto the size exclusion column via a pre-washed 10 mL superloop (GE Healthcare) or pre-washed 2 mL superloop (GE Healthcare). Protein was eluted in the gel filtration buffer, collected in 5 mL fractions, and analysed by SDS-PAGE and intact protein LC-ESI-MS.

7.3.3.4 Concentration of purified proteins

Purified protein was concentrated using an Amicon® Ultra Centrifugal filter (Sigma Aldrich) with a molecular weight (MW) cut off selected as appropriate for the MW of the protein. The protein concentration was measured at 280 nm using NanoDrop ND-1000 and NanoDropOne spectrophotometers.

7.3.3.5 Sodium dodecyl sulfate polyacrylamide gel electrophoresis

SDS-PAGE was used to verify purity and size of the produced proteins. SDS-PAGE gel with 12% acrylamide was prepared (**Table 28** and **Table 29**). 10 µL Protein samples were mixed with 10 µL 2x NuPAGE™ LDS (1:1 MQ water and 4x NuPAGE™ LDS with 6 mg DTT in 100 µL). The samples were loaded onto the gel with PageRuler Prestained Protein Ladder (10 to 230 kDa, Thermo Fisher Scientific). In a Mini-Protean® Tetra Cell (Bio-Rad) electrophoresis was performed at a voltage of 180 V and a current of 400 mA with the running buffer (200 mM glycine, 25 mM Tris, 0.1% SDS), for 60 min. The gel was then stained for 15 minutes with InstantBlue™ Protein Stain (Expedeon).

Table 28. SDS-PAGE gel recipe.

Component	Separating gel (mL)	Stacking gel (mL)
2x Separating buffer, pH 8.8	5	-
2x Stacking buffer, pH 6.8	-	2.5
30% Acrylamide	4	0.83
MQ water	1	1.67
10% Ammonium persulfate (APS)	0.1	0.05
N,N,N′,N′-Tetramethylethylenediamine (TEMED)	10 µL	5 µL

Table 29. Components of the 2x separating and 2x stacking gel buffers.

Reagent	2x Separating gel buffer, pH 8.8	2x Stacking buffer, pH 6.8
Trizma® base	0.75 M	0.25 M
10% SDS (w/v)	0.2%	0.2%

7.4 Lactones production and purification

10 mM Meropenem was incubated with 25 μM OXA-48 S70C in 3.2 mL 50 mM sodium phosphate,pH 7.5 solution, at room temperature for 48 h. The protein was removed by filtering the reaction mixture through an Amicon Ultra-0.5 Centrifugal Filter with a 10 kDa cut off (Millipore). The filtrate was loaded onto a Sep-Pak C18 Plus Light Cartridge (Waters), which had been pre-equilibrated with 100% acetonitrile followed by 100% MQ water. The cartridge was then washed with 2 mL MQ water, before elution of the meropenem-derived β-lactones with 2 mL 25% acetonitrile. The elute was frozen and lyophilised. The purity and concentration of the meropenem-derived β-lactones were measured by ^{1}H-NMR and ^{1}H-^{1}H COSY as described in **Section 7.6.1**.

7.5 Mass spectrometry

7.5.1 Optimised γ-lactam ring formation assay and Fe(II), 2OG, and ascorbate dependence

The following conditions were used for optimised γ-lactam ring formation assay, unless otherwise stated: 1 μM eRF1-ND, 1 μM JMJD4, 100 μM Fe(II), 200 μM 2OG in 20 mM Tris-HCl, pH 7.5, 16-20 h, room temperature. The co-factor Fe(II) was prepared as a 100x ammonium iron(II) sulfate stock solution in 20 mM aq. HCl, followed by dilution to a 10x working stock solution in MQ water. The co-substrate 2OG was prepared as a 100 mM stock of 2-oxoglutaric acid disodium salt, and then diluted to a 10x working stock in 20 mM Tris-HCl pH 7.5 or 20 mM Tris-HCl 300 mM NaCl pH 7.5. In the optimised γ-lactam ring formation assay, 100 μM sodium *L*-ascorbate was added. Sodium *L*-ascorbate was prepared as a 100x stock solution in MQ water and diluted to a 10x working stock in 20 mM Tris-HCl, 300 mM NaCl, pH 7.5. Protein assays were analysed using a Xevo G2-S Q-ToF or SPE-Q-TOF.

7.5.2 Acylation assay for class D SBLs

500 μL samples containing 1 μM enzyme and 10 μM substrate or inhibitor in 50 mM sodium phosphate, pH 7.5 were prepared. The 50 mM sodium phosphate buffer, pH 7.5 was prepared with water in the LiChrosolv® for chromatography (Millipore) grade. The reaction was monitored for 6-15 min using SPE-MS.

7.5.3 Deacylation assay for class D SBLs

For deacylation assay with carbapenem-derived β-lactones and carbapenems, 1 μM enzyme was incubated for 10 min with 10 μM meropenem-derived β-lactones to form the

AEC. Then100 μM ertapenem was added to analyse the stability of the AEC. The deacylation assay was measured by SPE-MS.

7.5.4 Intact protein LC-MS

5 μL of each protein sample (0.01-0.02 mg/mL) was injected onto a Merck Chromolith C18 2x5 mm guard column connected to a Water LCT Premier XE time-of-flight mass spectrometer. The LC method involved a gradient of 5-100% acetonitrile and 0.1% (v/v) formic acid in MQ water over 8 minutes. Data were analysed using MassLynx V4.0 (Waters).

7.5.5 XEVO G2-S Q-Tof

The Xevo G2-S Q-ToF mass spectrometer was operated in positive ion mode, employing the Lockspray™ ion source mechanism for high mass accuracy. Liquid chromatography was performed using an Acquity UPLC system with an Aeris, 3.6 μM widepore C4, 200 Å, 50 x 2.1 mm column (Phenomenex). 10 μL of each sample was injected onto the system. Elution solvents were: (A) MQ water with 0.1% (v/v) formic acid, and (B) HPLC-grade acetonitrile with 0.1% (v/v) formic acid. The 10 min elution protocol was controlled and analysed using MassLynx V4.1 (Waters).

7.5.6 SPE-MS

In the case of time course experiments, 0.5-2 mL samples were used. The reaction was monitored by electrospray ionisation MS in positive ion mode with an integrated autosampler/solid-phase extraction (SPE) RapidFire 365 system. The sample was aspirated

under vacuum for 400 ms and loaded onto a C4 SPE cartridge (Agilent Technology). Buffer salts were removed by washing the cartridge with 0.1 % formic acid in water at a flow rate of 1.5 mL/min for 4.5 s. Following the aqueous wash, the protein was eluted onto the mass spectrometer with 85% acetonitrile, 15% water (LiChrosolv® for chromatography, Millipore) containing 0.1% formic acid at a flow rate of 1.25 mL/min for 4.5 s. The cartridge was re-equilibrated with 0.1 % formic acid in water for 500 ms. Ion chromatogram data were extracted with MSHunter VB0.700 and deconvoluted with maximum entropy. For the determination of peak area, MSHunter (VB0.600) was used.

7.6 NMR experiments

Unless otherwise stated, all NMR experiments were performed using one of the following NMR spectrometers at 298 K: a Bruker Avance III 700 MHz spectrometer equipped with a TCI inverse cryoprobe, and a Bruker AVIII HD 600 MHz spectrometer equipped with a BB-F/^{1}H Prodigy N_2 cryoprobe. NMR samples of final volumes of 170 µL were prepared in 50 mM sodium phosphate, pH 7.5 buffer supplemented with 10% D_2O and measured in 3 mm NMR capillary tubes (Cortecnet).

7.6.1 β-Lactone quantification by ^{1}H-NMR

The β-lactone samples as obtained from the procedures in **Section 7.4** were dissolved in 50 mM sodium phosphate, pH 7.5 to a 10 mM working solution. The exact concentration of β-lactone in each sample was determined by ^{1}H-NMR, using trimethylsilylpropanoic acid (TSP) as the reference for quantification (226). 17 µL of 10 mM β-lactone sample, 1 µL of 3 mg/mL TSP, 17 µL D_2O (Sigma-Aldrich, 99.9% D) and 135 µL 50 mM sodium phosphate, pH 7.5 were mixed in a 1.5 mL Eppendorf tube and transferred to a 3 mm NMR tube. The NMR experiment was carried out at 600 MHz with suppression of water signal using excitation sculpting with perfect-echo. The acquired ^{1}H-NMR spectrum was processed with TopSpin 3.2 (Bruker).

7.6.2 ^{1}H-NMR turnover time courses

For β-lactamase turnover assays, each sample contained 1 mM substrate with enzyme at the optimal concentration (**Table 30**) and 10% D_2O in 50 mM sodium phosphate buffer, pH 7.5, to a total volume of 170 µL.

Table 30. Enzyme concentrations used for ^{1}H-NMR turnover time courses of carbapenems with different class D SBL variants.

Enzyme	Substrate	Enzyme concentration (µM)
Wild-type OXA-48	Meropenem	5
OXA-48 V120I	Meropenem	2.5
OXA-48 V120L	Meropenem	0.25
OXA-48 V120L	Biapenem	0.25
OXA-48 V120L	Imipenem	0.25
OXA-48 V120L	Ertapenem	0.25
OXA-48 V120L	Panipenem	0.25
OXA-48 W105A	Meropenem	100
OXA-48 W105F	Meropenem	5
OXA-48 L158V	Meropenem	2.5
OXA-48 L158I	Meropenem	2.5
Wild-type OXA-23	Meropenem	5
OXA-23 V128I	Meropenem	5
OXA-23 V128L	Meropenem	5
OXA-23 V128L	Imipenem	5
OXA-23 V128L	Panipenem	5

7.6.3 ^{13}C-Carbamylation assay

Purified wild-type OXA-48, OXA-48 V120I and OXA-48 V120L were dialysed using 3 mL Slide-A-Lyzer Dialysis Cassettes with a 10K Molecular weight cut-off (MWCO) (Thermo Fisher Scientific) against 3 × 500 mL freshly degassed 50 mM sodium phosphate buffer, pH 7.5. After 18 h of dialysis, protein samples were transferred to 1.5 mL Eppendorf tubes and stored at – 80 °C. Each sample for the NMR assay contained 700 µM OXA enzyme in 50 mM sodium phosphate pH 7.5, supplemented with 100 mM $NaHCO_3$ (Sigma Aldrich), 10% D_2O and 0.1 mM Ethylenediaminetetraacetic acid (EDTA). ^{13}C-NMR spectra were acquired at 150 MHz with 2048 scans including a relaxation delay of 2.0 s. For processing a 10 Hz line broadening was applied (80).

7.6.4 Chemical assignment of products derived from carbapenem analogues

For NMR characterisation, carbapenem-derived β-lactones were prepared by treating 1 mM carbapenem with 25 µM OXA-48 S70C in 50 mM sodium phosphate buffer, pH 7.5 and 10% D_2O for 1h. Carbapenem-derived hydrolysis products were obtained by treating 1 mM carbapenem with 25 µM wild-type OXA-48 and 10% D_2O in 50 mM sodium phosphate buffer, pH 7.5 and 10% D_2O for 1h. Chemical shifts were assigned based on a combination of ^{1}H, COSY, TOCSY, HSQC and HMBC experiments (parameters summarised in **Table 31**) performed on a Bruker Avance III 700 MHz and Bruker AVIII HD 600 MHz spectrometers.

Table 31. NMR parameters.

Experiment	**Puls-Programme**	**Size of FID (1H) / (1H) or (13C)**	**Spectral width / Centre of spectrum (1H) in ppm**	**Spectral width / Centre of spectrum (13C)**	**Number of scans**
^{1}H	zgesgppe	32768	16.0208/ 4.691		32
^{1}H ^{1}H COSY	cosygpprqf	2048/ 256	10.0041, 10.0041/ 4.703, 4.703		8
^{1}H ^{13}C HSQC	hsqcetgpprsisp2.2	2048, 256	15.9440/ 4.702	240.0072/ 100.000	16
^{1}H ^{13}C HMBC	hmbcetgpl2ndpr	2048, 128	12.0251/ 4.703	220.0066/ 100.000	128

7.7 Absorbance-based assay

7.7.1 Steady state assay

Analysis of steady state kinetics was performed based on a published procedure with modifications (249, 250). Procedures for setting up the assays were described as follows. Substrate solutions of various concentrations were prepared by a series of dilutions in a 100 mM sodium phosphate, pH 7.5 buffer supplemented with 0.01% TritionX-100. A dilute enzyme solution was prepared using the same buffer. At each substrate concentration, reaction was initiated by addition of the enzyme to an optimal concentration (described below), with an additional 10 min incubation period in the cases of meropenem and imipenem, before adding the enzyme and starting the measurement. Reactions were carried out at 25 °C in 96-well UV-star Microplates (Greiner, Bio-One) in at least triplicate. Increase in absorbance of nitrocefin-derived hydrolysis products (ε = 20500 M^{-1} cm^{-1}) (249), or depletion in absorbance of meropenem (ε = 10940 M^{-1} cm^{-1}) (250) or imipenem (ε = 9000 M^{-1} cm^{-1}) (250), was monitored using a PHERAstar FS microplate reader (BMG Labtech). For nitrocefin turnover assays, the following enzyme concentrations were used: wild-type OXA-48 (25 pM), OXA-48 V120I (25 pM), OXA-48 V120L (50 pM), OXA-48 L158V (500 pM), OXA-48 L158I (500 pM), OXA-48 W105F (500 pM), OXA-48 W105A (250 pM), wild-type OXA-23 (100 pM), OXA-23 V128I (700 pM), and OXA-23 V128L (500 pM). For meropenem turnover assays, enzyme concentrations of WT OXA-48 (75 nM), OXA-48 V120I (100 nM), OXA-48 V120L (300 nM), OXA-48 L158V (1150 nM), OXA-48 L158I (400 nM), OXA-48 W105F (100 nM), WT OXA-23 (350 nM), OXA-23 V128I (290 nM), OXA-23 V128L (320 nM) were used. For imipenem turnover assays, enzyme concentrations of WT OXA-48 (1.5 nM), OXA-48 V120I (2 nM), OXA-48 V120L (50 nM), WT OXA-23 (42.5 nM), OXA-23 V128I (50 nM), OXA-23 V128L (170 nM) were used. Fitting was

performed with the GraphPad Prism package (version X) based on a steady state approximation and the Michaelis-Menten enzyme kinetic parameters $k_{cat,}$ K_M, and k_{cat}/K_M were obtained.

7.8 Circular dichroism (CD) spectroscopy

400 µL samples containing the enzyme of interest, at 0.2 mg/mL for Class D SBL variants in 10 mM sodium phosphate pH 7.5 were transferred to a 0.1 cm pathlength cuvette. A Chirascan CD spectrometer (Applied Photophysics) equipped with a Peltier temperature-controlled cell holder was used to obtain CD spectra. Spectra were acquired at 23 °C in a wavelength range of 185 nm to 260 nm at 0.5 nm intervals and at a scan rate of 1 scan/s. The resulting spectra were processed with baseline correction and smoothing using the Savitzky-Golay filter.

OXA-enzyme samples for thermal melting temperature measurements were prepared similarly. Signal was monitored at the fixed wavelength of 222 nm and over temperatures gradually increased from 20 °C to 85 °C at 1 °C intervals. Data points were fitted to a Boltzmann sigmoidal curve using GraphPad Prism 5.

7.9 Bioinformatic analysis

7.9.1 JMJD4 alignment

For the identification of hJMJD4 orthologues, a protein BLAST search was carried out. (*H. sapiens* JMJD4 (NP_075383) was aligned with *M. musculus* JMJD4 (NP_ 848774) and *S. pombe* JMJD4 (NP-593806). Results were verified by Clustal Omega protein sequence alignment (78) and bioinformatic analysis.

7.9.2 eRF1 alignment

A protein BLAST search was used to identify eRF1 proteins from *M. musculus* and *S. pombe. H. sapiens* eRF1 (NP_004721.1) was aligned with *M. musculus* eRF1 (NP_659115.3) and *S. pombe* eRF1 (NP_594680.1) by Clustal Omega (78).

7.9.3 Class D β-lactamase database

The constantly updated Beta-lactamase DataBase (BLDB) (38) was filtered for class D serine β-lactamases and the results were exported as a csv file. Excel (Microsoft Office) was used to select and analyse the residues present at position 120 (OXA-48 numbering) across 930 class D serine β-lactamases (last update June 2020).

7.10 Human cell culture

7.10.1 General

All *in vivo* experiments were performed under sterile conditions in a class II biological safety cabinet. *H. sapiens* HepG2 cells were grown in Dulbecco's Modified Eagle's Media low glucose (DMEM, Sigma Aldrich) supplemented with 2 mM L-glutamine and 10 % fetal bovine serum (FBS, Sigma Aldrich) at 37 °C in a humidified atmosphere of 5% CO_2.

7.10.2 Cell passaging

HepG2 cells were grown in T75 cell culture flasks (Greiner Bio-one) and passaged every 3-5 days up to a total of 25 passages. Prior to each passage, trypsin-EDTA solution (Sigma Aldrich) and fresh growth media were pre-warmed in a water bath at 37 °C. The old growth media was removed, in which the HepG2 cells grew attached to the surface of the T75 cell culture flask. The attached cells were then washed with sterile 10 mL phosphate-buffered saline (PBS). Next the HepG2 cells were detached from the flask surface by adding 2.5 mL trypsin-EDTA solution and incubated at 37 °C in a humidified atmosphere of 5% CO_2 for 2-3 mins. 7.5 mL fresh growth media-low glucose was added to the trypsinised/detached cells. 2-3 mL resuspended cells were passaged on to a new T75 cell culture flask containing 10 mL fresh growth media-low glucose. For western blotting and immunoprecipitation experiments, each 10 cm dish was seeded with 3 x 10^5 cells in the presence of 10 mL growth media-low glucose.

7.10.3 Cell harvest

The 10 cm dishes were placed on ice. The growth media was removed, and the attached cells were washed with 2x 3 mL PBS. 0.3 mL Pre-cooled RIPA buffer (Sigma Aldrich) or JIES buffer (20 mM Tris-HCl pH 7.4, 100 mM NaCl, 5 mM $MgCl_2$, 0.5 % (v/v) NP-40), containing complete EDTA-free protease inhibitor cocktail (Roche) was added to each dish and cells were scraped from the dish surface. The lysed cells were transferred to a pre-cooled Eppendorf tube, incubated for 20 min on ice, and centrifuged for 10 min at 4 °C and 14k rpm. The supernatant was transferred to a new Eppendorf tube and the protein concentration was quantified using Coomassie (Bradford) Protein Assay Kit (Thermo Fisher Scientific). The supernatant (total cell lysate) was either stored at -20 °C or used directly for immunoprecipitation (IP) and western blotting experiments.

7.10.4 Western blotting

Total cell lysate, supernatant and IP samples were loaded onto a SDS-PAGE gel and were separated by SDS-PAGE electrophoresis at 130 V for 60 min. The separated proteins on the gel were transferred onto a membrane at 80 V and 4 °C for 80 min using transfer buffer (48 mM TrisBase, 39 mM Glycine + 20% Methanol). The blotting onto the membrane was validated by staining with Ponceau red. The membrane was then blocked with 5% milk in Tris-buffered saline, 0.1% Tween 20 buffer (TBST, 2.4 g Tris base, 8.8 g NaCl in 1 L) for 45 min and then washed three times with TBST for 5 min. The primary antibody, anti-eRF1 (mouse, B-11, sc-36568610, Santa Cruz Biotechnology) and anti-JMJD4 (mouse, JMJD4/32b/H12, University of Oxford), was added and incubated at 4 °C overnight. After incubation the membrane was washed three times with Tris-buffered saline (TBS) for overall 30 min, incubated with the horseradish peroxidase (HRP)-linked anti-mouse lgG secondary antibody (Cell Signaling Technology) at room temperature for 1 h, and washed again. The

proteins were visible with a 1:1 solution of Solution A (Luminol Enhancer Solution): Solution B (Peroxide Solution) from the Amersham ECL™ Prime Western Blotting Detection Reagent kit (GE Healthcare) for chemiluminescence detection.

7.10.5 Immunoprecipitation experiments

Dynabeads Protein G superparamagnetic beads (Thermo Fisher Scientific, 30 mg of beads/mL of PBS, pH 7.4, 0.01% Tween™ 20, 0.09% sodium azide and 8 μg of IgG/mg of beads, 20 μL per sample) were washed three times with citrate-phosphate buffer, pH 5.0 (200 μL per 20 μL sample). The magnetic beads were resuspended in PBS to make up a 50% slurry. Anti-JMJD4 antibody (mouse, JMJD4/32b/H12, University of Oxford) and anti-eRF1 antibody (mouse, B-11, sc-36568610, Santa Cruz Biotechnology) were incubated with washed breads for 1 h at 4 °C. Antibody conjugated beads were washed again three times with citrate-phosphate buffer, pH 5.0 (200 μL per 20 μL sample) and then with PBS (200 μL per 20 μL sample). Total cell lysate (0.5 mg per 20 μL sample) was added to the antibody conjugated beads and incubated overnight at 4 °C under rotation. The supernatant was removed from the beads complex and stored for analysis by western blotting. The beads complex was washed three times with PBS (200 μL) and resuspended in 20 μL PBP and 20 μL of 2x NuPAGE™ LDS sample (without additional reducing agents), and the mixture was heated for 15 min at 75 °C. Supernatant and total cell lysate were mixed with 4x NuPAGE™ LDS. IP, supernatant, and total cell lysate samples were used for western blotting (**Section 7.10.4**).

Chapter 8 – References

1. Van Boeckel, T. P., Gandra, S., Ashok, A., Caudron, Q., Grenfell, B. T., Levin, S. A., and Laxminarayan, R. (2014) Global antibiotic consumption 2000 to 2010: an analysis of national pharmaceutical sales data. *Lancet Infect. Dis.* **14**, 742–750

2. Nemeth, J., Oesch, G., and Kuster, S. P. (2014) Bacteriostatic versus bactericidal antibiotics for patients with serious bacterial infections: systematic review and meta-analysis. *J. Antimicrob. Chemother.* **70**, 382–395

3. Kapoor, G., Saigal, S., and Elongavan, A. (2017) Action and resistance mechanisms of antibiotics: A guide for clinicians. *J. Anaesthesiol. Clin. Pharmacol.* **33**, 300–305

4. Lorber, B. (1988) Changing patterns of infectious diseases. *Am. J. Med.* **84**, 569–578

5. Cohen, M. L. (2000) Changing patterns of infectious disease. *Nature*. **406**, 762–767

6. Howard, S. J., Catchpole, M., Watson, J., and Davies, S. C. (2013) Antibiotic resistance: global response needed. *Lancet Infect. Dis.* **13**, 1001–1003

7. Kohanski, M. A., Dwyer, D. J., and Collins, J. J. (2010) How antibiotics kill bacteria: from targets to networks. *Nat. Rev. Microbiol.* **8**, 423–435

8. Demain, A. L., and Elander, R. P. (1999) The β-lactam antibiotics: past, present, and future. *Antonie Van Leeuwenhoek*. **75**, 5–19

9. Sykes, R. B., and Bonner, D. P. (1985) Aztreonam: The first monobactam. *Am. J. Med.* **78**, 2–10

10. ABRAHAM, E. P., NEWTON, G. G. F., SCHENCK, J. R., HARGIE, M. P., OLSON, B. H., SCHUURMANS, D. M., FISHER, M. W., and FUSARI, S. A. (1955) Identity of Cephalosporin N and Synnematin B. *Nature*. **176**, 551

11. Aoki, H., Sakai, H. I., Kohsaka, M., Konomi, T., Hosoda, J., Iguchi, E., Imanaka, H., and Kubochi, Y. (1976) Nocardicin a, a new monocyclic β-lactam antibiotic I. Discovery, isolation and characterization. *J. Antibiot. (Tokyo).* **29**, 492–500

12. Kahan, F. M., Kropp, H., Sundelof, J. G., and Birnbaum, J. (1983) Thienamycin: development of imipenem-cilastatin. *J. Antimicrob. Chemother.* **12**, 1–35

13. Kahan, J. S., Kahan, F. M., Goegelman, R., Currie, S. A., Jackson, M., Stapley, E. O., Miller, T. W., Miller, A. K., Hendlin, D., Woodruff, H. B., Birnbaum, J., Mochales, S., and Hernandez, S. (1979) Thienamycin, a new β-lactam antibiotic i. discovery, taxonomy, isolation and physical properties. *J. Antibiot. (Tokyo).* **32**, 1–12

14. Zhanel, G. G., Wiebe, R., Dilay, L., Thomson, K., Rubinstein, E., Hoban, D. J., Noreddin, A. M., and Karlowsky, J. A. (2007) Comparative Review of the Carbapenems. *Drugs*. **67**, 1027–1052

15. Vollmer, W., Blanot, D., and De Pedro, M. A. (2008) Peptidoglycan structure and architecture. *FEMS Microbiol. Rev.* **32**, 149–167

16. Silhavy, T. J., Kahne, D., and Walker, S. (2010) The Bacterial Cell Envelope. *Cold Spring Harb. Perspect. Biol.* a000414

17. Anderson, J. S., Meadow, P. M., Haskin, M. A., and Strominger, J. L. (1966) Biosynthesis of the peptidoglycan of bacterial cell walls: I. Utilization of uridine diphosphate acetylmuramyl pentapeptide and uridine diphosphate acetylglucosamine for peptidoglycan synthesis by particulate enzymes from Staphylococcus aureus and Microco. *Arch. Biochem. Biophys.* **116**, 487–515

18. Buynak, J. D. (2007) Cutting and Stitching: The Cross-Linking of Peptidoglycan in the Assembly of the Bacterial Cell Wall. *ACS Chem. Biol.* **2**, 602–605

19. Sauvage, E., Kerff, F., Terrak, M., Ayala, J. A., and Charlier, P. (2008) The penicillin-binding proteins: structure and role in peptidoglycan biosynthesis. *FEMS Microbiol. Rev.* **32**, 234–258

20. Tipper, D. J., and Strominger, J. L. (1965) Mechanism of action of penicillins: a proposal based on their structural similarity to acyl-D-alanyl-D-alanine. *Proc. Natl. Acad. Sci. U. S. A.* **54**, 1133–1141

21. Silver, L. L. (2006) Does the cell wall of bacteria remain a viable source of targets for novel antibiotics? *Biochem. Pharmacol.* **71**, 996–1005

22. Cochrane, S. A., and Lohans, C. T. (2020) Breaking down the cell wall: Strategies for antibiotic discovery targeting bacterial transpeptidases. *Eur. J. Med. Chem.* **194**, 112262

23. Wise Jr, E. M., and Park, J. T. (1965) Penicillin: its basic site of action as an inhibitor of a peptide cross-linking reaction in cell wall mucopeptide synthesis. *Proc. Natl. Acad. Sci. U. S. A.* **54**, 75–81

24. Yocum, R. R., Waxman, D. J., Rasmussen, J. R., and Strominger, J. L. (1979) Mechanism of penicillin action: penicillin and substrate bind covalently to the same active site serine in two bacterial D-alanine carboxypeptidases. *Proc. Natl. Acad. Sci. U. S. A.* **76**, 2730–2734

25. Strominger, J. L., Blumberg, P. M., Suginaka, H., Umbreit, J., Wickus, G. G., Chain, E. B., and Stoeckel, H. (1971) How penicillin kills bacteria: progress and problems. *Proc. R. Soc. London. Ser. B. Biol. Sci.* **179**, 369–383

26. Pires, D., de Kraker, M. E. A., Tartari, E., Abbas, M., and Pittet, D. (2017) 'Fight Antibiotic Resistance—It's in Your Hands': Call From the World Health Organization for 5th May 2017. *Clin. Infect. Dis.* **64**, 1780–1783

27. Poole, K. (2004) Resistance to β-lactam antibiotics. *Cell. Mol. Life Sci. C.* **61**, 2200–2223

28. Giedraitienė, A., Vitkauskienė, A., Naginienė, R., and Pavilonis, A. (2011) Antibiotic Resistance Mechanisms of Clinically Important Bacteria. *Medicina (B. Aires).* **47**, 19

29. Farra, A., Islam, S., Strålfors, A., Sörberg, M., and Wretlind, B. (2008) Role of outer membrane protein OprD and penicillin-binding proteins in resistance of Pseudomonas aeruginosa to imipenem and meropenem. *Int. J. Antimicrob. Agents*. **31**, 427–433

30. Siroy, A., Molle, V., Lemaître-Guillier, C., Vallenet, D., Pestel-Caron, M., Cozzone, A. J., Jouenne, T., and Dé, E. (2005) Channel formation by CarO, the carbapenem resistance-associated outer membrane protein of Acinetobacter baumannii. *Antimicrob. Agents Chemother.* **49**, 4876–4883

31. Bajaj, H., Scorciapino, M. A., Moynié, L., Page, M. G. P., Naismith, J. H., Ceccarelli, M., and Winterhalter, M. (2016) Molecular Basis of Filtering Carbapenems by Porins from β-Lactam-resistant Clinical Strains of Escherichia coli. *J. Biol. Chem.* **291**, 2837–2847

32. Piddock, L. J. V (2006) Clinically relevant chromosomally encoded multidrug resistance efflux pumps in bacteria. *Clin. Microbiol. Rev.* **19**, 382–402

33. Bush, K. (2018) Past and Present Perspectives on β-Lactamases. *Antimicrob. Agents Chemother.* **62**, e01076-18

34. Fisher, J. F., and Mobashery, S. (2016) β-Lactam Resistance Mechanisms: Gram-Positive Bacteria and Mycobacterium tuberculosis. *Cold Spring Harb. Perspect. Med.* **6**, a025221

35. D'Costa, V. M., King, C. E., Kalan, L., Morar, M., Sung, W. W. L., Schwarz, C., Froese, D., Zazula, G., Calmels, F., Debruyne, R., Golding, G. B., Poinar, H. N., and Wright, G. D. (2011) Antibiotic resistance is ancient. *Nature*. **477**, 457–461

36. ABRAHAM, E. P., and CHAIN, E. (1940) An Enzyme from Bacteria able to Destroy Penicillin. *Nature*. **146**, 837

37. Fleming, A. (1929) On the Antibacterial Action of Cultures of a Penicillium, with Special Reference to their Use in the Isolation of B. influenzæ. *Br. J. Exp. Pathol.* **10**, 226–236

38. Naas, T., Oueslati, S., Bonnin, R. A., Dabos, M. L., Zavala, A., Dortet, L., Retailleau, P., and Iorga, B. I. (2017) Beta-lactamase database (BLDB) – structure and function. *J. Enzyme Inhib. Med. Chem.* **32**, 917–919

39. Singh, T., Singh, P. K., Das, S., Wani, S., Jawed, A., and Dar, S. A. (2019) Transcriptome analysis of beta-lactamase genes in diarrheagenic Escherichia coli. *Sci. Rep.* **9**, 3626

40. Rice, L. B., Eliopoulos, G. M., Wennersten, C., Goldmann, D., Jacoby, G. A., and Moellering Jr, R. C. (1991) Chromosomally mediated beta-lactamase production and gentamicin resistance in Enterococcus faecalis. *Antimicrob. Agents Chemother.* **35**, 272–276

41. Medeiros, A., Mayer, K. H., and Opal, S. M. (1988) Plasmid-mediated beta-lactamases. *Antimicrob. Newsl.* **5**, 61–65

42. Sirot, D. (1995) Extended-spectrum plasmid-mediated β-lactamases. *J. Antimicrob. Chemother.* **36**, 19–34

43. Bush, K. (2010) Bench-to-bedside review: The role of beta-lactamases in antibiotic-resistant Gram-negative infections. *Crit. Care*. **14**, 224

44. Paterson, D. L., and Bonomo, R. A. (2005) Extended-spectrum beta-lactamases: a clinical update. *Clin. Microbiol. Rev.* **18**, 657–686

45. Bush, K. (2010) Alarming β-lactamase-mediated resistance in multidrug-resistant Enterobacteriaceae. *Curr. Opin. Microbiol.* **13**, 558–564

46. Lamotte-Brasseur, J., Knox, J., Kelly, J. A., Charlier, P., Fonzé, E., Dideberg, O., and Frère, J.-M. (1994) The Structures and Catalytic Mechanisms of Active-Site Serine β-Lactamases. *Biotechnol. Genet. Eng. Rev.* **12**, 189–230

47. Galleni, M., Lamotte-Brasseur, J., Raquet, X., Dubus, A., Monnaie, D., Knox, J. R., and Frère, J.-M. (1995) The enigmatic catalytic mechanism of active-site serine β-lactamases. *Biochem. Pharmacol.* **49**, 1171–1178

48. Queenan, A. M., and Bush, K. (2007) Carbapenemases: the Versatile β-Lactamases. *Clin. Microbiol. Rev.* **20**, 440 LP – 458

49. Lobkovsky, E., Moews, P. C., Liu, H., Zhao, H., Frere, J. M., and Knox, J. R. (1993) Evolution of an enzyme activity: crystallographic structure at 2-A resolution of cephalosporinase from the ampC gene of Enterobacter cloacae P99 and comparison with a class A penicillinase. *Proc. Natl. Acad. Sci.* **90**, 11257 LP – 11261

50. Doi, Y., and Paterson, D. L. (2007) Detection of plasmid-mediated class C β-lactamases. *Int. J. Infect. Dis.* **11**, 191–197

51. Sykes, R. B., and Matthew, M. (1976) The β-lactamases of Gram-negative bacteria and their rôle in resistance to β-lactam antibiotics. *J. Antimicrob. Chemother.* **2**, 115–157

52. Evans, B. A., and Amyes, S. G. B. (2014) OXA β-Lactamases. *Clin. Microbiol. Rev.* **27**, 241–263

53. Danel, F., Hall, L. M., Duke, B., Gur, D., and Livermore, D. M. (1999) OXA-17, a further extended-spectrum variant of OXA-10 beta-lactamase, isolated from Pseudomonas aeruginosa. *Antimicrob. Agents Chemother.* **43**, 1362–1366

54. Danel, F., Hall, L. M., Gur, D., and Livermore, D. M. (1995) OXA-14, another extended-spectrum variant of OXA-10 (PSE-2) beta-lactamase from Pseudomonas aeruginosa. *Antimicrob. Agents Chemother.* **39**, 1881–1884

55. Nigro, S. J., and Hall, R. M. (2016) Structure and context of Acinetobacter transposons carrying the oxa23 carbapenemase gene. *J. Antimicrob. Chemother.* **71**, 1135–1147

56. Lyon, J. A. (1985) Imipenem/cilastatin: the first carbapenem antibiotic. *Drug Intell. Clin. Pharm.* **19**, 895—899

57. Héritier, C., Poirel, L., Lambert, T., and Nordmann, P. (2005) Contribution of acquired carbapenem-hydrolyzing oxacillinases to carbapenem resistance in Acinetobacter baumannii. *Antimicrob. Agents Chemother.* **49**, 3198–3202

58. Rollauer, S. E., Sooreshjani, M. A., Noinaj, N., and Buchanan, S. K. (2015) Outer membrane protein biogenesis in Gram-negative bacteria. *Philos. Trans. R. Soc. Lond. B. Biol. Sci.* **370**, 20150023

59. Poirel, L., Potron, A., and Nordmann, P. (2012) OXA-48-like carbapenemases: the phantom menace. *J. Antimicrob. Chemother.* **67**, 1597–1606

60. Petrella, S., Ziental-Gelus, N., Mayer, C., Renard, M., Jarlier, V., and Sougakoff, W. (2008) Genetic and Structural Insights into the Dissemination Potential of the Extremely Broad-Spectrum Class A β-Lactamase KPC-2 Identified in an Escherichia coli Strain and an Enterobacter cloacae Strain Isolated from the Same Patient in France. *Antimicrob. Agents Chemother.* **52**, 3725 LP – 3736

61. Aitha, M., Marts, A. R., Bergstrom, A., Møller, A. J., Moritz, L., Turner, L., Nix, J. C., Bonomo, R. A., Page, R. C., Tierney, D. L., and Crowder, M. W. (2014) Biochemical, Mechanistic, and Spectroscopic Characterization of Metallo-β-lactamase VIM-2. *Biochemistry*. **53**, 7321–7331

62. Powers, R. A., and Shoichet, B. K. (2002) Structure-Based Approach for Binding Site Identification on AmpC β-Lactamase. *J. Med. Chem.* **45**, 3222–3234

63. Docquier, J. D., Calderone, V., De Luca, F., Benvenuti, M., Giuliani, F., Bellucci, L., Tafi, A., Nordmann, P., Botta, M., Rossolini, G. M., and Mangani, S. (2009) Crystal Structure of the OXA-48 β-Lactamase Reveals Mechanistic Diversity among Class D Carbapenemases. *Chem. Biol.* **16**, 540–547

64. Page, M. I., and Badarau, A. (2008) The Mechanisms of Catalysis by Metallo Lactamases. *Bioinorg. Chem. Appl.* **2008**, 576297

65. Walsh, T. R. (2010) Emerging carbapenemases: a global perspective. *Int. J. Antimicrob. Agents*. **36**, S8–S14

66. Galleni, M., Lamotte-Brasseur, J., Rossolini, G. M., Spencer, J., Dideberg, O., Frère, J. M., and Group, M. W. (2001) Standard numbering scheme for class B beta-lactamases. *Antimicrob. Agents Chemother.* **45**, 660–663

67. Garau, G., García-Sáez, I., Bebrone, C., Anne, C., Mercuri, P., Galleni, M., Frère, J.-M., and Dideberg, O. (2004) Update of the Standard Numbering Scheme for Class B β-Lactamases. *Antimicrob. Agents Chemother.* **48**, 2347 LP – 2349

68. Mojica, M. F., Bonomo, R. A., and Fast, W. (2016) B1-Metallo-β-Lactamases: Where Do We Stand? *Curr. Drug Targets*. **17**, 1029–1050

69. Yigit, H., Queenan, A. M., Anderson, G. J., Domenech-Sanchez, A., Biddle, J. W., Steward, C. D., Alberti, S., Bush, K., and Tenover, F. C. (2001) Novel Carbapenem-

Hydrolyzing β-Lactamase, KPC-1, from a carbapenem-resistant strain of Klebsiella pneumoniae. *Antimicrob. Agents Chemother.* **45**, 1151 LP – 1161

70. Lee, C.-R., Lee, J. H., Park, K. S., Kim, Y. B., Jeong, B. C., and Lee, S. H. (2016) Global Dissemination of Carbapenemase-Producing Klebsiella pneumoniae: Epidemiology, Genetic Context, Treatment Options, and Detection Methods. *Front. Microbiol.* **7**, 895

71. Nordmann, P., and Poirel, L. (2014) The difficult-to-control spread of carbapenemase producers among Enterobacteriaceae worldwide. *Clin. Microbiol. Infect.* **20**, 821–830

72. Poirel, L., Marqué, S., Héritier, C., Segonds, C., Chabanon, G., and Nordmann, P. (2005) OXA-58, a novel class D {beta}-lactamase involved in resistance to carbapenems in Acinetobacter baumannii. *Antimicrob. Agents Chemother.* **49**, 202–208

73. Santillana, E., Beceiro, A., Bou, G., and Romero, A. (2007) Crystal structure of the carbapenemase OXA-24 reveals insights into the mechanism of carbapenem hydrolysis. *Proc. Natl. Acad. Sci.* **104**, 5354–5359

74. Paetzel, M., Danel, F., de Castro, L., Mosimann, S. C., Page, M. G. P., and Strynadka, N. C. J. (2000) Crystal structure of the class D β-lactamase OXA-10. *Nat. Struct. Biol.* **7**, 918–925

75. Kaitany, K.-C. J., Klinger, N. V, June, C. M., Ramey, M. E., Bonomo, R. A., Powers, R. A., and Leonard, D. A. (2013) Structures of the class D Carbapenemases OXA-23 and OXA-146: mechanistic basis of activity against carbapenems, extended-spectrum cephalosporins, and aztreonam. *Antimicrob. Agents Chemother.* **57**, 4848–4855

76. Kadonaga, J. T., Gautier, A. E., Straus, D. R., Charles, A. D., Edge, M. D., and Knowles, J. R. (1984) The role of the beta-lactamase signal sequence in the secretion of proteins by Escherichia coli. *J. Biol. Chem.* . **259**, 2149–2154

77. Kadonaga, J. T., Plückthun, A., and Knowles, J. R. (1985) Signal sequence mutants of beta-lactamase. *J. Biol. Chem.* . **260**, 16192–16199

78. Sievers, F., Wilm, A., Dineen, D., Gibson, T. J., Karplus, K., Li, W., Lopez, R., McWilliam, H., Remmert, M., Söding, J., Thompson, J. D., and Higgins, D. G. (2011) Fast, scalable generation of high-quality protein multiple sequence alignments using Clustal Omega. *Mol. Syst. Biol.* **7**, 539

79. Knox, J. R., Moews, P. C., and Frere, J.-M. (1996) Molecular evolution of bacterial β-lactam resistance. *Chem. Biol.* **3**, 937–947

80. Lohans, C. T., Wang, D. Y., Jorgensen, C., Cahill, S. T., Clifton, I. J., McDonough, M. A., Oswin, H. P., Spencer, J., Domene, C., Claridge, T. D. W., Brem, J., and Schofield, C. J. (2017) 13C-Carbamylation as a mechanistic probe for the inhibition of class D β-lactamases by avibactam and halide ions. *Org. Biomol. Chem.* **15**, 6024–6032

81. Leonard, D. A., Bonomo, R. A., and Powers, R. A. (2013) Class D β-Lactamases: A Reappraisal after Five Decades. *Acc. Chem. Res.* **46**, 2407–2415

82. Baurin, S., Vercheval, L., Bouillenne, F., Falzone, C., Brans, A., Jacquamet, L., Ferrer, J.-L., Sauvage, E., Dehareng, D., Frère, J.-M., Charlier, P., Galleni, M., and Kerff, F. (2009) Critical Role of Tryptophan 154 for the Activity and Stability of Class D β-Lactamases,. *Biochemistry*. **48**, 11252–11263

83. Maveyraud, L., Golemi, D., Kotra, L. P., Tranier, S., Vakulenko, S., Mobashery, S., and Samama, J.-P. (2000) Insights into Class D β-Lactamases Are Revealed by the

Crystal Structure of the OXA10 Enzyme from Pseudomonas aeruginosa. *Structure*. **8**, 1289–1298

84. Lahiri, S. D., Johnstone, M. R., Ross, P. L., McLaughlin, R. E., Olivier, N. B., and Alm, R. A. (2014) Avibactam and class C β-lactamases: mechanism of inhibition, conservation of the binding pocket, and implications for resistance. *Antimicrob. Agents Chemother.* **58**, 5704–5713

85. Fisher, J. F., and Mobashery, S. (2009) Three decades of the class A beta-lactamase acyl-enzyme. *Curr. Protein Pept. Sci.* **10**, 401–407

86. Maveyraud, L., Mourey, L., Kotra, L. P., Pedelacq, J.-D., Guillet, V., Mobashery, S., and Samama, J.-P. (1998) Structural Basis for Clinical Longevity of Carbapenem Antibiotics in the Face of Challenge by the Common Class A β-Lactamases from the Antibiotic-Resistant Bacteria. *J. Am. Chem. Soc.* **120**, 9748–9752

87. Akhter, S., Lund, B. A., Ismael, A., Langer, M., Isaksson, J., Christopeit, T., Leiros, H. K. S., and Bayer, A. (2018) A focused fragment library targeting the antibiotic resistance enzyme - Oxacillinase-48: Synthesis, structural evaluation and inhibitor design. *Eur. J. Med. Chem.* **145**, 634–648

88. Lohans, C. T., van Groesen, E., Kumar, K., Tooke, C. L., Spencer, J., Paton, R. S., Brem, J., and Schofield, C. J. (2018) A New Mechanism for β-Lactamases: Class D Enzymes Degrade 1β-Methyl Carbapenems through Lactone Formation. *Angew. Chem. Int. Ed.* **130**, 1296–1299

89. Vercheval, L., Bauvois, C., di Paolo, A., Borel, F., Ferrer, J.-L., Sauvage, E., Matagne, A., Frère, J.-M., Charlier, P., Galleni, M., and Kerff, F. (2010) Three factors that modulate the activity of class D β-lactamases and interfere with the post-translational carboxylation of Lys70. *Biochem. J.* **432**, 495–506

90. Smith, C. A., Antunes, N. T., Stewart, N. K., Toth, M., Kumarasiri, M., Chang, M., Mobashery, S., and Vakulenko, S. B. (2013) Structural Basis for Carbapenemase Activity of the OXA-23 β-Lactamase from Acinetobacter baumannii. *Chem Biol.* **20**, 1107–1115

91. Stewart, N. K., Smith, C. A., Antunes, N. T., Toth, M., and Vakulenko, S. B. (2019) Role of the Hydrophobic Bridge in the Carbapenemase Activity of Class D beta-Lactamases. *Antimicrob. Agents Chemother.* **63**, e02191-18

92. Lund, B. A., Thomassen, A. M., Nesheim, B. H. B., Carlsen, T. J. O., Isaksson, J., Christopeit, T., and Leiros, H. K. S. (2018) The biological assembly of OXA-48 reveals a dimer interface with high charge complementarity and very high affinity. *FEBS J.* **285**, 4214–4228

93. Golemi, D., Maveyraud, L., Vakulenko, S., Samama, J.-P., and Mobashery, S. (2001) Critical involvement of a carbamylated lysine in catalytic function of class D β-lactamases. *Proc. Natl. Acad. Sci.* **98**, 14280–14285

94. Danel, F., Paetzel, M., Strynadka, N. C. J., and Page, M. G. P. (2001) Effect of divalent metal cations on the dimerization of OXA-10 and -14 class D β-lactamases from Pseudomonas aeruginosa. *Biochemistry*. 10.1021/bi0025969

95. Ledent, P., Raquet, X., Joris, B., Van Beeumen, J., and Frère, J. M. (1993) A comparative study of class-D beta-lactamases. *Biochem. J.* **292**, 555–562

96. Hutton, J. J., Kaplan, A., and Udenfriend, S. (1967) Conversion of the amino acid sequence Gly-Pro-Pro in protein to Gly-Pro-Hyp by collagen proline hydroxylase. *Arch. Biochem. Biophys.* **121**, 384–391

97. Loenarz, C., and Schofield, C. J. (2011) Physiological and biochemical aspects of hydroxylations and demethylations catalyzed by human 2-oxoglutarate oxygenases.

Trends Biochem. Sci. **36**, 7–18

98. Loenarz, C., and Schofield, C. J. (2008) Expanding chemical biology of 2-oxoglutarate oxygenases. *Nat. Chem. Biol.* **4**, 152–156

99. Ivan, M., Kondo, K., Yang, H., Kim, W., Valiando, J., Ohh, M., Salic, A., Asara, J. M., Lane, W. S., and Kaelin Jr., W. G. (2001) HIFα Targeted for VHL-Mediated Destruction by Proline Hydroxylation: Implications for O2 Sensing. *Science (80-.).* **292**, 464 LP – 468

100. Mitchell, A. J., Zhu, Q., Maggiolo, A. O., Ananth, N. R., Hillwig, M. L., Liu, X., and Boal, A. K. (2016) Structural basis for halogenation by iron- and 2-oxo-glutarate-dependent enzyme WelO5. *Nat. Chem. Biol.* **12**, 636–640

101. Topf, M., Sandala, G. M., Smith, D. M., Schofield, C. J., Easton, C. J., and Radom, L. (2004) The Unusual Bifunctional Catalysis of Epimerization and Desaturation by Carbapenem Synthase. *J. Am. Chem. Soc.* **126**, 9932–9933

102. Roach, P. L., Clifton, I. J., Fülöp, V., Harlos, K., Barton, G. J., Hajdu, J., Andersson, I., Schofield, C. J., and Baldwin, J. E. (1995) Crystal structure of isopenicillin N synthase is the first from a new structural family of enzymes. *Nature*. **375**, 700–704

103. Zhang, Z., Ren, J., Stammers, D. K., Baldwin, J. E., Harlos, K., and Schofield, C. J. (2000) Structural origins of the selectivity of the trifunctional oxygenase clavaminic acid synthase. *Nat. Struct. Biol.* **7**, 127–133

104. Hausinger, R. P. (2004) Fe(II)/α-Ketoglutarate-Dependent Hydroxylases and Related Enzymes. *Crit. Rev. Biochem. Mol. Biol.* **39**, 21–68

105. Liu, H., Wang, C., Lee, S., Deng, Y., Wither, M., Oh, S., Ning, F., Dege, C., Zhang, Q., Liu, X., Johnson, A. M., Zang, J., Chen, Z., Janknecht, R., Hansen, K., Marrack,

P., Li, C.-Y., Kappler, J. W., Hagman, J., and Zhang, G. (2017) Clipping of arginine-methylated histone tails by JMJD5 and JMJD7. *Proc. Natl. Acad. Sci.* **114**, E7717 LP-E7726

106. Shen, J., Xiang, X., Chen, L., Wang, H., Wu, L., Sun, Y., Ma, L., Gu, X., Liu, H., Wang, L., Yu, Y., Shao, J., Huang, C., and Chin, Y. E. (2017) JMJD5 cleaves monomethylated histone H3 N-tail under DNA damaging stress. *EMBO Rep.* **18**, 2131–2143

107. Klose, R. J., Kallin, E. M., and Zhang, Y. (2006) JmjC-domain-containing proteins and histone demethylation. *Nat. Rev. Genet.* **7**, 715–727

108. Hewitson, K. S., McNeill, L. A., Riordan, M. V, Tian, Y.-M., Bullock, A. N., Welford, R. W., Elkins, J. M., Oldham, N. J., Bhattacharya, S., Gleadle, J. M., Ratcliffe, P. J., Pugh, C. W., and Schofield, C. J. (2002) Hypoxia-inducible Factor (HIF) Asparagine Hydroxylase Is Identical to Factor Inhibiting HIF (FIH) and Is Related to the Cupin Structural Family. *J. Biol. Chem.* . **277**, 26351–26355

109. Walport, L. J., Hopkinson, R. J., Chowdhury, R., Schiller, R., Ge, W., Kawamura, A., and Schofield, C. J. (2016) Arginine demethylation is catalysed by a subset of JmjC histone lysine demethylases. *Nat. Commun.* **7**, 11974

110. Chang, B., Chen, Y., Zhao, Y., and Bruick, R. K. (2007) JMJD6 Is a Histone Arginine Demethylase. *Science (80-.).* **318**, 444 LP – 447

111. Brejc, K., Bian, Q., Uzawa, S., Wheeler, B. S., Anderson, E. C., King, D. S., Kranzusch, P. J., Preston, C. G., and Meyer, B. J. (2017) Dynamic Control of X Chromosome Conformation and Repression by a Histone H4K20 Demethylase. *Cell*. **171**, 85-102.e23

112. Mantri, M., Krojer, T., Bagg, E. A., Webby, C. J., Butler, D. S., Kochan, G.,

Kavanagh, K. L., Oppermann, U., McDonough, M. A., and Schofield, C. J. (2010) Crystal Structure of the 2-Oxoglutarate- and Fe(II)-Dependent Lysyl Hydroxylase JMJD6. *J. Mol. Biol.* **401**, 211–222

113. Webby, C. J., Wolf, A., Gromak, N., Dreger, M., Kramer, H., Kessler, B., Nielsen, M. L., Schmitz, C., Butler, D. S., Yates, J. R., Delahunty, C. M., Hahn, P., Lengeling, A., Mann, M., Proudfoot, N. J., Schofield, C. J., and Böttger, A. (2009) Jmjd6 Catalyses Lysyl-Hydroxylation of U2AF65, a Protein Associated with RNA Splicing. *Science (80-.).* **325**, 90 LP – 93

114. Islam, M. S., McDonough, M. A., Chowdhury, R., Gault, J., Khan, A., Pires, E., and Schofield, C. J. (2019) Biochemical and structural investigations clarify the substrate selectivity of the 2-oxoglutarate oxygenase JMJD6. *J. Biol. Chem.* **294**, 11637–11652

115. Aik, W., McDonough, M. A., Thalhammer, A., Chowdhury, R., and Schofield, C. J. (2012) Role of the jelly-roll fold in substrate binding by 2-oxoglutarate oxygenases. *Curr. Opin. Struct. Biol.* **22**, 691–700

116. McDonough, M. A., Loenarz, C., Chowdhury, R., Clifton, I. J., and Schofield, C. J. (2010) Structural studies on human 2-oxoglutarate dependent oxygenases. *Curr. Opin. Struct. Biol.* **20**, 659–672

117. Koehntop, K. D., Emerson, J. P., and Que, L. (2005) The 2-His-1-carboxylate facial triad: a versatile platform for dioxygen activation by mononuclear non-heme iron(II) enzymes. *JBIC J. Biol. Inorg. Chem.* **10**, 87–93

118. Suzana Markolovic, Thomas M Leissing, Rasheduzzaman Chowdhury, Sarah E Wilkins, Xin Lu, C. J. S. (2016) Structure–function relationships of human JmjC oxygenases — demethylases versus hydroxylases. *Curr. Opin. Struct. Biol.* **41**, 62–

72

119. Chowdhury, R., McDonough, M. A., Mecinović, J., Loenarz, C., Flashman, E., Hewitson, K. S., Domene, C., and Schofield, C. J. (2009) Structural Basis for Binding of Hypoxia-Inducible Factor to the Oxygen-Sensing Prolyl Hydroxylases. *Structure*. **17**, 981–989

120. Markolovic, S., Wilkins, S. E., and Schofield, C. J. (2015) Protein Hydroxylation Catalyzed by 2-Oxoglutarate-dependent Oxygenases. *J. Biol. Chem.* **290**, 20712–20722

121. Martinez, S., and Hausinger, R. P. (2015) Catalytic Mechanisms of Fe(II)- and 2-Oxoglutarate-dependent Oxygenases. *J. Biol. Chem.* . **290**, 20702–20711

122. Zurlo, G., Guo, J., Takada, M., Wei, W., and Zhang, Q. (2016) New Insights into Protein Hydroxylation and Its Important Role in Human Diseases. *Biochim. Biophys. Acta*. **1866**, 208–220

123. Kato, M., Araiso, Y., Noma, A., Nagao, A., Suzuki, T., Ishitani, R., and Nureki, O. (2011) Crystal structure of a novel JmjC-domain-containing protein, TYW5, involved in tRNA modification. *Nucleic Acids Res.* **39**, 1576–1585

124. Songe-Møller, L., van den Born, E., Leihne, V., Vågbø, C. B., Kristoffersen, T., Krokan, H. E., Kirpekar, F., Falnes, P. Ø., and Klungland, A. (2010) Mammalian ALKBH8 Possesses tRNA Methyltransferase Activity Required for the Biogenesis of Multiple Wobble Uridine Modifications Implicated in Translational Decoding. *Mol. Cell. Biol.* **30**, 1814 LP – 1827

125. Ge, W., Wolf, A., Feng, T., Ho, C.-H., Sekirnik, R., Zayer, A., Granatino, N., Cockman, M. E., Loenarz, C., Loik, N. D., Hardy, A. P., Claridge, T. D. W., Hamed, R. B., Chowdhury, R., Gong, L., Robinson, C. V, Trudgian, D. C., Jiang,

M., Mackeen, M. M., Mccullagh, J. S., Gordiyenko, Y., Thalhammer, A., Yamamoto, A., Yang, M., Liu-Yi, P., Zhang, Z., Schmidt-Zachmann, M., Kessler, B. M., Ratcliffe, P. J., Preston, G. M., Coleman, M. L., and Schofield, C. J. (2012) Oxygenase-catalyzed ribosome hydroxylation occurs in prokaryotes and humans. *Nat. Chem. Biol.* **8**, 960–962

126. Markolovic, S., Zhuang, Q., Wilkins, S. E., Eaton, C. D., Abboud, M. I., Katz, M. J., McNeil, H. E., Leśniak, R. K., Hall, C., Struwe, W. B., Konietzny, R., Davis, S., Yang, M., Ge, W., Benesch, J. L. P., Kessler, B. M., Ratcliffe, P. J., Cockman, M. E., Fischer, R., Wappner, P., Chowdhury, R., Coleman, M. L., and Schofield, C. J. (2018) The Jumonji-C oxygenase JMJD7 catalyzes (3S)-lysyl hydroxylation of TRAFAC GTPases. *Nat. Chem. Biol.* **14**, 688–695

127. Singleton, R. S., Liu-Yi, P., Formenti, F., Ge, W., Sekirnik, R., Fischer, R., Adam, J., Pollard, P. J., Wolf, A., Thalhammer, A., Loenarz, C., Flashman, E., Yamamoto, A., Coleman, M. L., Kessler, B. M., Wappner, P., Schofield, C. J., Ratcliffe, P. J., and Cockman, M. E. (2014) OGFOD1 catalyzes prolyl hydroxylation of RPS23 and is involved in translation control and stress granule formation. *Proc. Natl. Acad. Sci.* **111**, 4031 LP – 4036

128. Van Rechem, C., Black, J. C., Boukhali, M., Aryee, M. J., Gräslund, S., Haas, W., Benes, C. H., and Whetstine, J. R. (2015) Lysine Demethylase KDM4A Associates with Translation Machinery and Regulates Protein Synthesis. *Cancer Discov.* **5**, 255 LP – 263

129. Dever, T. E., and Green, R. (2012) The Elongation, Termination, and Recycling Phases of Translation in Eukaryotes. *Cold Spring Harb. Perspect. Biol.* **4**, a013706–a013706

130. Frolova, L., Le Goff, X., Rasmussen, H. H., Cheperegin, S., Drugeon, G., Kress, M., Arman, I., Haenni, A.-L., Celis, J. E., Phllippe, M., Justesen, J., and Kisselev, L. (1994) A highly conserved eukaryotic protein family possessing properties of polypeptide chain release factor. *Nature*. **372**, 701–703

131. Drugeon, G., Jean-Jean, O., Frolova, L., Le Goff, X., Philippe, M., Kisselev, L., and Haenni, A. L. (1997) Eukaryotic release factor 1 (eRF1) abolishes readthrough and competes with suppressor tRNAs at all three termination codons in messenger RNA. *Nucleic Acids Res.* **25**, 2254–2258

132. Scolnick, E., Tompkins, R., Caskey, T., and Nirenberg, M. (1968) Release factors differing in specificity for terminator codons. *Proc. Natl. Acad. Sci. U. S. A.* **61**, 768–774

133. Song, H., Mugnier, P., Das, A. K., Webb, H. M., Evans, D. R., Tuite, M. F., Hemmings, B. A., and Barford, D. (2000) The crystal structure of human eukaryotic release factor eRF1--mechanism of stop codon recognition and peptidyl-tRNA hydrolysis. *Cell*. **100**, 311–321

134. Chavatte, L., Seit-Nebi, A., Dubovaya, V., and Favre, A. (2002) The invariant uridine of stop codons contacts the conserved NIKSR loop of human eRF1 in the ribosome. *EMBO J.* **21**, 5302–5311

135. Frolova, L. Y., Tsivkovskii, R. Y., Sivolobova, G. F., Oparina, N. Y., Serpinsky, O. I., Blinov, V. M., Tatkov, S. I., and Kisselev, L. L. (1999) Mutations in the highly conserved GGQ motif of class 1 polypeptide release factors abolish ability of human eRF1 to trigger peptidyl-tRNA hydrolysis. *RNA* . **5**, 1014–1020

136. Seit-Nebi, A., Frolova, L., Justesen, J., and Kisselev, L. (2001) Class-1 translation termination factors: invariant GGQ minidomain is essential for release activity and

ribosome binding but not for stop codon recognition. *Nucleic Acids Res.* **29**, 3982–3987

137. Cheng, Z., Saito, K., Pisarev, A. V, Wada, M., Pisareva, V. P., Pestova, T. V, Gajda, M., Round, A., Kong, C., Lim, M., Nakamura, Y., Svergun, D. I., Ito, K., and Song, H. (2009) Structural insights into eRF3 and stop codon recognition by eRF1. *Genes Dev.* . **23**, 1106–1118

138. des Georges, A., Hashem, Y., Unbehaun, A., Grassucci, R. A., Taylor, D., Hellen, C. U. T., Pestova, T. V, and Frank, J. (2014) Structure of the mammalian ribosomal pre-termination complex associated with eRF1.eRF3.GDPNP. *Nucleic Acids Res.* **42**, 3409–3418

139. Frolova, L., Seit-Nebi, A., and Kisselev, L. (2002) Highly conserved NIKS tetrapeptide is functionally essential in eukaryotic translation termination factor eRF1. *RNA.* **8**, 129–136

140. Wong, L. E., Li, Y., Pillay, S., Frolova, L., and Pervushin, K. (2012) Selectivity of stop codon recognition in translation termination is modulated by multiple conformations of GTS loop in eRF1. *Nucleic Acids Res.* **40**, 5751–5765

141. Bulygin, K. N., Khairulina, Y. S., Kolosov, P. M., Ven'yaminova, A. G., Graifer, D. M., Vorobjev, Y. N., Frolova, L. Y., Kisselev, L. L., and Karpova, G. G. (2010) Three distinct peptides from the N domain of translation termination factor eRF1 surround stop codon in the ribosome. *RNA.* **16**, 1902–1914

142. Taylor, D., Unbehaun, A., Li, W., Das, S., Lei, J., Liao, H. Y., Grassucci, R. A., Pestova, T. V, and Frank, J. (2012) Cryo-EM structure of the mammalian eukaryotic release factor eRF1–eRF3-associated termination complex. *Proc. Natl. Acad. Sci.* **109**, 18413 LP – 18418

143. Preis, A., Heuer, A., Barrio-Garcia, C., Hauser, A., Eyler, D. E., Berninghausen, O., Green, R., Becker, T., and Beckmann, R. (2014) Cryoelectron Microscopic Structures of Eukaryotic Translation Termination Complexes Containing eRF1-eRF3 or eRF1-ABCE1. *Cell Rep.* **8**, 59–65

144. Feng, T., Yamamoto, A., Wilkins, S. E., Sokolova, E., Yates, L. A., Münzel, M., Singh, P., Hopkinson, R. J., Fischer, R., Cockman, M. E., Shelley, J., Trudgian, D. C., Schödel, J., McCullagh, J. S. O., Ge, W., Kessler, B. M., Gilbert, R. J., Frolova, L. Y., Alkalaeva, E., Ratcliffe, P. J., Schofield, C. J., and Coleman, M. L. (2014) Optimal translational termination requires C4 lysyl hydroxylation of eRF1. *Mol. Cell.* **53**, 645–654

145. Li, W., Chang, S. T.-L., Ward, F. R., and Cate, J. H. D. (2020) Selective inhibition of human translation termination by a drug-like compound. *Nat. Commun.* **11**, 4941

146. Ho, Y. J., Shih, C. P., Yeh, K. T., Shi, B., Gong, Z., Lin, Y. M., and Lu, J. W. (2018) Correlation between high expression levels of jumonji domain-containing 4 and short survival in cases of colon adenocarcinoma. *Biochem. Biophys. Res. Commun.* **503**, 1442–1449

147. Ploumakis, A., and Coleman, M. L. (2015) OH, the Places You'll Go! Hydroxylation, Gene Expression, and Cancer. *Mol. Cell.* **58**, 729–741

148. Yoo, H., Son, D., Lee, Y. J., and Hong, K. (2016) Mouse JMJD4 is dispensable for embryogenesis. *Mol. Reprod. Dev.* **83**, 588–593

149. Markolovic, S. (2017) *Biochemical and biophysical studies on the Jumonji-C hydroxylases JMJD7 and JMJD4*. Ph.D. thesis

150. Pitout, J. D. D., Peirano, G., Kock, M. M., Strydom, K., and Matsumura, Y. (2019) The Global Ascendency of OXA-48-Type Carbapenemases. *Clin. Microbiol. Rev.*

33, e00102-19

151. Dabos, L., Bogaerts, P., Bonnin, R. A., Zavala, A., Sacré, P., Iorga, B. I., Huang, D. T., Glupczynski, Y., and Naas, T. (2018) Genetic and Biochemical Characterization of OXA-519, a Novel OXA-48-Like β-Lactamase. *Antimicrob. Agents Chemother.* **62**, e00469-18

152. Kotsakis, S. D., Flach, C.-F., Razavi, M., and Larsson, D. G. J. (2019) Characterization of the First OXA-10 Natural Variant with Increased Carbapenemase Activity. *Antimicrob. Agents Chemother.* **63**, e01817-18

153. Zander, E., Chmielarczyk, A., Heczko, P., Seifert, H., and Higgins, P. G. (2012) Conversion of OXA-66 into OXA-82 in clinical Acinetobacter baumannii isolates and association with altered carbapenem susceptibility. *J. Antimicrob. Chemother.* **68**, 308–311

154. Evans, B. A., Hamouda, A., Towner, K. J., and Amyes, S. G. B. (2008) OXA-51-like β-lactamases and their association with particular epidemic lineages of Acinetobacter baumannii. *Clin. Microbiol. Infect.* **14**, 268–275

155. Takebayashi, Y., Findlay, J., Heesom, K. J., Warburton, P. J., Avison, M. B., and Evans, B. A. (2020) Variability in carbapenemase activity of intrinsic OxaAb (OXA-51-like) β-lactamase enzymes in Acinetobacter baumannii. *bioRxiv*. 10.1101/2020.07.02.183822

156. Mitchell, J. M., and Leonard, D. A. (2014) Common Clinical Substitutions Enhance the Carbapenemase Activity of OXA-51-Like Class D β-Lactamases from Acinetobacter spp. *Antimicrob. Agents Chemother.* 10.1128/aac.03651-14

157. Smith, C. A., Antunes, N. T., Stewart, N. K., Frase, H., Toth, M., Kantardjieff, K. A., and Vakulenko, S. (2015) Structural Basis for Enhancement of Carbapenemase

Activity in the OXA-51 Family of Class D β-Lactamases. *ACS Chem. Biol.* **10**, 1791–1796

158. De Luca, F., Benvenuti, M., Carboni, F., Pozzi, C., Rossolini, G. M., Mangani, S., and Docquier, J.-D. (2011) Evolution to carbapenem-hydrolyzing activity in noncarbapenemase class D β-lactamase OXA-10 by rational protein design. *Proc. Natl. Acad. Sci. U. S. A.* **108**, 18424–9

159. Matagne, A., Dubus, A., Galleni, M., and Frère, J.-M. (1999) The β-lactamase cycle: a tale of selective pressure and bacterial ingenuity. *Nat. Prod. Rep.* **16**, 1–19

160. van Groesen, E., Lohans, C. T., Brem, J., Aertker, K. M. J., Claridge, T. D. W., and Schofield, C. J. (2019) 19F NMR Monitoring of Reversible Protein Post-Translational Modifications: Class D β-Lactamase Carbamylation and Inhibition. *Chem. Eur. J.* **25**, 11837–11841

161. Geoghegan, K. F., Dixon, H. B. F., Rosner, P. J., Hoth, L. R., Lanzetti, A. J., Borzilleri, K. A., Marr, E. S., Pezzullo, L. H., Martin, L. B., LeMotte, P. K., McColl, A. S., Kamath, A. V., and Stroh, J. G. (1999) Spontaneous α-N-6-Phosphogluconoylation of a “His Tag” inEscherichia coli:The Cause of Extra Mass of 258 or 178 Da in Fusion Proteins. *Anal. Biochem.* **267**, 169–184

162. Greenfield, N. J. (2006) Using circular dichroism spectra to estimate protein secondary structure. *Nat. Protoc.* **1**, 2876–2890

163. Makena, A., Brem, J., Pfeffer, I., Geffen, R. E. J., Wilkins, S. E., Tarhonskaya, H., Flashman, E., Phee, L. M., Wareham, D. W., and Schofield, C. J. (2014) Biochemical characterization of New Delhi metallo-β-lactamase variants reveals differences in protein stability. *J. Antimicrob. Chemother.* **70**, 463–469

164. Kelly, S. M., Jess, T. J., and Price, N. C. (2005) How to study proteins by circular

dichroism. *Biochim. Biophys. Acta - Proteins Proteomics*. **1751**, 119–139

165. O'Callaghan, C. H., Morris, A., Kirby, S. M., and Shingler, A. H. (1972) Novel method for detection of beta-lactamases by using a chromogenic cephalosporin substrate. *Antimicrob. Agents Chemother.* **1**, 283–288

166. Vallejo, J. A., Martínez-Guitián, M., Vázquez-Ucha, J. C., González-Bello, C., Poza, M., Buynak, J. D., Bethel, C. R., Bonomo, R. A., Bou, G., and Beceiro, A. (2016) LN-1-255, a penicillanic acid sulfone able to inhibit the class D carbapenemase OXA-48. *J. Antimicrob. Chemother.* **71**, 2171–2180

167. Lohans, C. T., Freeman, E. I., Groesen, E. van, Tooke, C. L., Hinchliffe, P., Spencer, J., Brem, J., and Schofield, C. J. (2019) Mechanistic Insights into β-Lactamase-Catalysed Carbapenem Degradation Through Product Characterisation. *Sci Rep*. **9**, 13608

168. Schneider, K. D., Karpen, M. E., Bonomo, R. A., Leonard, D. A., and Powers, R. A. (2009) The 1.4 Å crystal structure of the class D β-lactamase OXA-1 complexed with doripenem. *Biochemistry*. **48**, 11840–11847

169. Baldwin, J. E. (1976) Rules for ring closure. *J. Chem. Soc. Chem. Commun.* 10.1039/C39760000734

170. Bürgi, H. B., Dunitz, J. D., and Shefter, E. (1974) Chemical reaction paths. IV. Aspects of O...C = O interactions in crystals. *Acta Cryst.* **B30**, 1517–1527

171. Leiros, H.-K. S., Thomassen, A. M., Samuelsen, O., Flach, C.-F., Kotsakis, S. D., and Larsson, D. G. J. Structural insight to the enhanced carbapenem efficiency of OXA-655 compared to OXA-10. Protein Data Bank. 6SKQ

172. Smith, C. A., Stewart, N. K., Toth, M., and Vakulenko, S. B. (2019) Structural Insights into the Mechanism of Carbapenemase Activity of the OXA-48 beta-

Lactamase. *Antimicrob. Agents Chemother.* **63**, e01202-19

173. Schneider, K. D., Ortega, C. J., Renck, N. A., Bonomo, R. A., Powers, R. A., and Leonard, D. A. (2011) Structures of the Class D Carbapenemase OXA-24 from Acinetobacter baumannii in Complex with Doripenem. *J. Mol. Biol.* **406**, 583–594

174. Papp-Wallace, K. M., Kumar, V., Zeiser, E. T., Becka, S. A., and van den Akker, F. (2019) Structural Analysis of The OXA-48 Carbapenemase Bound to A "Poor"; Carbapenem Substrate, Doripenem. *Antibiotics*. **8**, 145

175. June, C. M., Muckenthaler, T. J., Schroder, E. C., Klamer, Z. L., Wawrzak, Z., Powers, R. A., Szarecka, A., and Leonard, D. A. (2016) The structure of a doripenem-bound OXA-51 class D beta-lactamase variant with enhanced carbapenemase activity. *Protein Sci.* **25**, 2152–2163

176. Pernot, L., Mayer, C., and Sougakoff, W. (2001) Crystal Structure of the Acyl-Enzyme Intermediate OXA-13:Imipenem. Protein Data Bank. 1H5X

177. Akhtar, A., and Chen, Y. (2019) Crystal Structure of Class D Beta-lactamase OXA-48 with Imipenem. Protein Data Bank. 6PTU

178. Akhtar, A., and Chen, Y. (2019) Crystal Structure of Class D Beta-lactamase OXA-48 with Meropenem. Protein Data Bank. 6PT1

179. Harper, T. M., June, C. M., Taracila, M. A., Bonomo, R. A., Powers, R. A., and Leonard, D. A. (2018) Multiple substitutions lead to increased loop flexibility and expanded specificity in Acinetobacter baumannii carbapenemase OXA-239. *Biochem J.* **475**, 273–288

180. Queenan, A. M., Shang, W., Flamm, R., and Bush, K. (2010) Hydrolysis and Inhibition Profiles of β-Lactamases from Molecular Classes A to D with Doripenem, Imipenem, and Meropenem. *Antimicrob. Agents Chemother.* **54**, 565–

569

181. Ambler, R. P., Baddiley, J., and Abraham, E. P. (1980) The structure of β-lactamases. *Philos. Trans. R. Soc. London. B, Biol. Sci.* **289**, 321–331

182. Hall, B. G., and Barlow, M. (2005) Revised Ambler classification of β-lactamases. *J. Antimicrob. Chemother.* **55**, 1050–1051

183. Campoli-Richards, D. M., and Brogden, R. N. (1987) Sulbactam/Ampicillin. *Drugs*. **33**, 577–609

184. Wise, R. (1993) The efficacy and safety of piperacillin/tazobactam in the therapy of bacteraemia. *J. Antimicrob. Chemother.* **31**, 97–104

185. Dhillon, S. (2018) Meropenem/Vaborbactam: A Review in Complicated Urinary Tract Infections. *Drugs*. **78**, 1259–1270

186. Papp-Wallace, K. M. (2019) The latest advances in β-lactam/β-lactamase inhibitor combinations for the treatment of Gram-negative bacterial infections. *Expert Opin. Pharmacother.* **20**, 2169–2184

187. Drawz, S. M., and Bonomo, R. A. (2010) Three Decades of β-Lactamase Inhibitors. *Clin. Microbiol. Rev.* **23**, 160 LP – 201

188. Bush, K., and Bradford, P. A. (2019) Interplay between β-lactamases and new β-lactamase inhibitors. *Nat Rev Microbiol*. **17**, 295–306

189. Reading, C., and Cole, M. (1977) Clavulanic Acid: a Beta-Lactamase-Inhibiting Beta-Lactam from Streptomyces clavuligerus. *Antimicrob. Agents Chemother.* **11**, 852 LP – 857

190. Charnas, R. L., Fisher, J., and Knowles, J. R. (1978) Chemical Studies on the Inactivation of Escherichia coli RTEM β-Lactamase by Clavulanic Acid.

Biochemistry. 10.1021/bi00604a025

191. Fisher, J., Charnas, R. L., and Knowles, J. R. (1978) Kinetic studies on the inactivation of Escherichia coli RTEM β-lactamase by clavulanic acid. *Biochemistry*. **17**, 2180–2184

192. Imtiaz, U., Billings, E. M., Knox, J. R., and Mobashery, S. (1994) A Structure-Based Analysis of the Inhibition of Class A .beta.-Lactamases by Sulbactam. *Biochemistry*. **33**, 5728–5738

193. Bush, K., Macalintal, C., Rasmussen, B. A., Lee, V. J., and Yang, Y. (1993) Kinetic interactions of tazobactam with beta-lactamases from all major structural classes. *Antimicrob. Agents Chemother.* **37**, 851 LP – 858

194. Fisher, J., Charnas, R. L., Bradley, S. M., and Knowles, J. R. (1981) Inactivation of the RTEM .beta.-lactamase from Escherichia coli. Interaction of penam sulfones with the enzyme. *Biochemistry*. **20**, 2726–2731

195. Payne, D. J., Cramp, R., Winstanley, D. J., and Knowles, D. J. (1994) Comparative activities of clavulanic acid, sulbactam, and tazobactam against clinically important beta-lactamases. *Antimicrob. Agents Chemother.* **38**, 767–772

196. Livermore, D. M., Mushtaq, S., Warner, M., Turner, S. J., and Woodford, N. (2017) Potential of high-dose cefepime/tazobactam against multiresistant Gram-negative pathogens. *J. Antimicrob. Chemother.* **73**, 126–133

197. Charbonneau, P. (1994) Review of piperacillin/tazobactam in the treatment of bacteremic infections and summary of clinical efficacy. *Intensive Care Med.* **20**, S43–S48

198. Newton, L., Kotowski, A., Grinker, M., and Chun, R. (2018) Diagnosis and management of pediatric sinusitis: A survey of primary care, otolaryngology and

urgent care providers. *Int. J. Pediatr. Otorhinolaryngol.* **108**, 163–167

199. Ehmann, D. E., Jahić, H., Ross, P. L., Gu, R.-F., Hu, J., Kern, G., Walkup, G. K., and Fisher, S. L. (2012) Avibactam is a covalent, reversible, non-β-lactam β-lactamase inhibitor. *Proc. Natl. Acad. Sci. U. S. A.* **109**, 11663–11668

200. Choi, H., Paton, R. S., Park, H., and Schofield, C. J. (2016) Investigations on recyclisation and hydrolysis in avibactam mediated serine β-lactamase inhibition. *Org. Biomol. Chem.* **14**, 4116–4128

201. Kazmierczak, K. M., Bradford, P. A., Stone, G. G., de Jonge, B. L. M., and Sahm, D. F. (2018) n Vitro Activity of Ceftazidime-Avibactam and Aztreonam-Avibactam against OXA-48-Carrying Enterobacteriaceae Isolated as Part of the International Network for Optimal Resistance Monitoring (INFORM) Global Surveillance Program from 2012 to 2015. *Antimicrob. Agents Chemother.* **62**, e00592-18

202. Livermore, D. M., Mushtaq, S., Warner, M., Zhang, J., Maharjan, S., Doumith, M., and Woodford, N. (2011) Activities of NXL104 Combinations with Ceftazidime and Aztreonam against Carbapenemase-Producing Enterobacteriaceae. *Antimicrob. Agents Chemother.* **55**, 390 LP – 394

203. Alraddadi, B. M., Saeedi, M., Qutub, M., Alshukairi, A., Hassanien, A., and Wali, G. (2019) Efficacy of ceftazidime-avibactam in the treatment of infections due to Carbapenem-resistant Enterobacteriaceae. *BMC Infect. Dis.* **19**, 772

204. Che, H., Wang, R., Wang, J., and Cai, Y. (2019) Ceftazidime/avibactam versus carbapenems for the treatment of infections caused by Enterobacteriaceae: A meta-analysis of randomised controlled trials. *Int. J. Antimicrob. Agents*. **54**, 809–813

205. Ness, S., Martin, R., Kindler, A. M., Paetzel, M., Gold, M., Jensen, S. E., Jones, J. B., and Strynadka, N. C. J. (2000) Structure-Based Design Guides the Improved

Efficacy of Deacylation Transition State Analogue Inhibitors of TEM-1 β-Lactamase. *Biochemistry*. **39**, 5312–5321

206. Kaye, K. S., Bhowmick, T., Metallidis, S., Bleasdale, S. C., Sagan, O. S., Stus, V., Vazquez, J., Zaitsev, V., Bidair, M., Chorvat, E., Dragoescu, P. O., Fedosiuk, E., Horcajada, J. P., Murta, C., Sarychev, Y., Stoev, V., Morgan, E., Fusaro, K., Griffith, D., Lomovskaya, O., Alexander, E. L., Loutit, J., Dudley, M. N., and Giamarellos-Bourboulis, E. J. (2018) Effect of Meropenem-Vaborbactam vs Piperacillin-Tazobactam on Clinical Cure or Improvement and Microbial Eradication in Complicated Urinary Tract Infection: The TANGO I Randomized Clinical Trial. *JAMA*. **319**, 788–799

207. Castanheira, M., Rhomberg, P. R., Flamm, R. K., and Jones, R. N. (2016) Effect of the β-Lactamase Inhibitor Vaborbactam Combined with Meropenem against Serine Carbapenemase-Producing Enterobacteriaceae. *Antimicrob. Agents Chemother.* **60**, 5454 LP – 5458

208. Hecker, S. J., Reddy, K. R., Totrov, M., Hirst, G. C., Lomovskaya, O., Griffith, D. C., King, P., Tsivkovski, R., Sun, D., Sabet, M., Tarazi, Z., Clifton, M. C., Atkins, K., Raymond, A., Potts, K. T., Abendroth, J., Boyer, S. H., Loutit, J. S., Morgan, E. E., Durso, S., and Dudley, M. N. (2015) Discovery of a Cyclic Boronic Acid β-Lactamase Inhibitor (RPX7009) with Utility vs Class A Serine Carbapenemases. *J. Med. Chem.* **58**, 3682–3692

209. Liu, B., Trout, R. E. L., Chu, G.-H., McGarry, D., Jackson, R. W., Hamrick, J. C., Daigle, D. M., Cusick, S. M., Pozzi, C., De Luca, F., Benvenuti, M., Mangani, S., Docquier, J.-D., Weiss, W. J., Pevear, D. C., Xerri, L., and Burns, C. J. (2020) Discovery of Taniborbactam (VNRX-5133): A Broad-Spectrum Serine- and Metallo-β-lactamase Inhibitor for Carbapenem-Resistant Bacterial Infections. *J.*

Med. Chem. **63**, 2789–2801

210. Desgrandchamps, D., and Munzinger, J. (1989) Increasing rates of in vitro resistance to ciprofloxacin and norfloxacin in isolates from urine specimens. *Antimicrob. Agents Chemother.* **33**, 595 LP – 596

211. Schechter, L. M., Creely, D. P., Garner, C. D., Shortridge, D., Nguyen, H., Chen, L., Hanson, B. M., Sodergren, E., Weinstock, G. M., Dunne, W. M., van Belkum, A., and Leopold, S. R. (2018) Extensive Gene Amplification as a Mechanism for Piperacillin-Tazobactam Resistance in Escherichia coli. *MBio*. **9**, e00583-18

212. Göttig, S., Frank, D., Mungo, E., Nolte, A., Hogardt, M., Besier, S., and Wichelhaus, T. A. (2019) Emergence of ceftazidime/avibactam resistance in KPC-3-producing Klebsiella pneumoniae in vivo. *J. Antimicrob. Chemother.* **74**, 3211–3216

213. van Berkel, S. S., Brem, J., Rydzik, A. M., Salimraj, R., Cain, R., Verma, A., Owens, R. J., Fishwick, C. W. G., Spencer, J., and Schofield, C. J. (2013) Assay platform for clinically relevant metallo-β-lactamases. *J. Med. Chem.* **56**, 6945–6953

214. Brem, J., Cain, R., Cahill, S., McDonough, M. A., Clifton, I. J., Jiménez-Castellanos, J.-C., Avison, M. B., Spencer, J., Fishwick, C. W. G., and Schofield, C. J. (2016) Structural basis of metallo-β-lactamase, serine-β-lactamase and penicillin-binding protein inhibition by cyclic boronates. *Nat. Commun.* **7**, 12406

215. Brem, J., van Berkel, S. S., Zollman, D., Lee, S. Y., Gileadi, O., McHugh, P. J., Walsh, T. R., McDonough, M. A., and Schofield, C. J. (2015) Structural Basis of Metallo-β-Lactamase Inhibition by Captopril Stereoisomers. *Antimicrob. Agents Chemother.* **60**, 142–150

216. Cahill, S. T., Cain, R., Wang, D. Y., Lohans, C. T., Wareham, D. W., Oswin, H. P.,

Mohammed, J., Spencer, J., Fishwick, C. W. G., McDonough, M. A., Schofield, C. J., and Brem, J. (2017) Cyclic Boronates Inhibit All Classes of β-Lactamases. *Antimicrob. Agents Chemother.* **61**, e02260-16

217. Brewitz, L., Tumber, A., and Schofield, C. J. (2020) Kinetic parameters of human aspartate/asparagine-β-hydroxylase suggest that it has a possible function in oxygen sensing. *J. Biol. Chem.* **295**, 7826–7838

218. He, X., Mezyk, S. P., Michael, I., Fatta-Kassinos, D., and Dionysiou, D. D. (2014) Degradation kinetics and mechanism of β-lactam antibiotics by the activation of H2O2 and Na2S2O8 under UV-254nm irradiation. *J. Hazard. Mater.* **279**, 375–383

219. Aertker, K. M. J., Chan, H. T. H., Lohans, C. T., and Schofield, C. J. (2020) Analysis of β-lactone formation by clinically observed carbapenemases informs on a novel antibiotic resistance mechanism. *J. Biol. Chem.* **295**, 16604–16613

220. Easton, C. J., and Knowles, J. R. (1982) Inhibition of the RTEM .beta.-lactamase from Escherichia coli. Interaction of the enzyme with derivatives of olivanic acid. *Biochemistry*. **21**, 2857–2862

221. Tremblay, L. W., Fan, F., and Blanchard, J. S. (2010) Biochemical and Structural Characterization of Mycobacterium tuberculosis β-Lactamase with the Carbapenems Ertapenem and Doripenem. *Biochemistry*. **49**, 3766–3773

222. Charnas, R. L., and Knowles, J. R. (1981) Inhibition of the RTEM .beta.-lactamase from Escherichia coli. Interaction of the enzyme with derivatives of olivanic acid. *Biochemistry*. **20**, 2732–2737

223. Charnas, R. L., and Knowles, J. R. (1981) Inhibition of the RTEM .beta.-lactamase from Escherichia coli. Interaction of the enzyme with derivatives of olivanic acid. *Biochemistry*. **20**, 2732–2737

224. Easton, C. J., and Knowles, J. R. (1982) Inhibition of the RTEM .beta.-lactamase from Escherichia coli. Interaction of the enzyme with derivatives of olivanic acid. *Biochemistry*. **21**, 2857–2862

225. Kalp, M., and Carey, P. R. (2008) Carbapenems and SHV-1 β-Lactamase Form Different Acyl-Enzyme Populations in Crystals and Solution. *Biochemistry*. **47**, 11830–11837

226. Reid, D. G., MacLachlan, L. K., Edwards, A. J., Hubbard, J. A., and Sweeney, P. J. (1997) Introduction to the NMR of Proteins BT - Protein NMR Techniques (Reid, D. G. ed), pp. 1–28, Humana Press, Totowa, NJ, 10.1385/0-89603-309-0:1

227. Bush, K., and Bradford, P. A. (2016) β-Lactams and β-Lactamase Inhibitors: An Overview. *Cold Spring Harb. Perspect. Med.* **6**, a025247

228. Rutledge, P. J. (2015) CHAPTER 19 Isopenicillin N Synthase. in *2-Oxoglutarate-Dependent Oxygenases*, pp. 414–424, The Royal Society of Chemistry, 10.1039/9781782621959-00414

229. Arnstein, H. R., and Clubb, M. E. (1958) The biosynthesis of penicillin. 8. Investigation of cyclic cysteinylvaline peptides as precursors. *Biochem. J.* **68**, 528–535

230. Salowe, S. P., Marsh, E. N., and Townsend, C. A. (1990) Purification and characterization of clavaminate synthase from Streptomyces clavuligerus: an unusual oxidative enzyme in natural product biosynthesis. *Biochemistry*. **29**, 6499–6508

231. Yang, M., Hardy, A. P., Chowdhury, R., Loik, N. D., Scotti, J. S., McCullagh, J. S. O., Claridge, T. D. W., McDonough, M. A., Ge, W., and Schofield, C. J. (2013) Substrate Selectivity Analyses of Factor Inhibiting Hypoxia-Inducible Factor.

Angew. Chemie Int. Ed. **52**, 1700–1704

232. Cockman, M. E., Webb, J. D., Kramer, H. B., Kessler, B. M., and Ratcliffe, P. J. (2009) Proteomics-based Identification of Novel Factor Inhibiting Hypoxia-inducible Factor (FIH) Substrates Indicates Widespread Asparaginyl Hydroxylation of Ankyrin Repeat Domain-containing Proteins. *Mol. & Cell. Proteomics*. **8**, 535 LP – 546

233. Yang, M., Chowdhury, R., Ge, W., Hamed, R. B., McDonough, M. A., Claridge, T. D. W., Kessler, B. M., Cockman, M. E., Ratcliffe, P. J., and Schofield, C. J. (2011) Factor-inhibiting hypoxia-inducible factor (FIH) catalyses the post-translational hydroxylation of histidinyl residues within ankyrin repeat domains. *FEBS J.* **278**, 1086–1097

234. Hu, Y. J., and Imbalzano, A. N. (2016) Global gene expression profiling of JMJD6- and JMJD4-depleted mouse NIH3T3 fibroblasts. *Sci. Data*. 10.1038/sdata.2016.22

235. von Hippel, P. H., and Wong, K.-Y. (1964) Neutral Salts: The Generality of Their Effects on the Stability of Macromolecular Conformations. *Science (80-.).* **145**, 577 LP – 580

236. Ree, R., Varland, S., and Arnesen, T. (2018) Spotlight on protein N-terminal acetylation. *Exp. Mol. Med.* **50**, 1–13

237. Hopkinson, R. J., Tumber, A., Yapp, C., Chowdhury, R., Aik, W., Che, K. H., Li, X. S., Kristensen, J. B. L., King, O. N. F., Chan, M. C., Yeoh, K. K., Choi, H., Walport, L. J., Thinnes, C. C., Bush, J. T., Lejeune, C., Rydzik, A. M., Rose, N. R., Bagg, E. A., McDonough, M. A., Krojer, T., Yue, W. W., Ng, S. S., Olsen, L., Brennan, P. E., Oppermann, U., Muller-Knapp, S., Klose, R. J., Ratcliffe, P. J., Schofield, C. J., and Kawamura, A. (2013) 5-Carboxy-8-hydroxyquinoline is a

Broad Spectrum 2-Oxoglutarate Oxygenase Inhibitor which Causes Iron Translocation. *Chem. Sci.* **4**, 3110–3117

238. Kuiper, C., and Vissers, M. C. M. (2014) Ascorbate as a Co-Factor for Fe- and 2-Oxoglutarate Dependent Dioxygenases: Physiological Activity in Tumor Growth and Progression. *Front. Oncol.* **4**, 359

239. Myllylä, R., Kuutti-Savolainen, E.-R., and Kivirikko, K. I. (1978) The role of ascorbate in the prolyl hydroxylase reaction. *Biochem. Biophys. Res. Commun.* **83**, 441–448

240. Flashman, E., Davies, S. L., Yeoh, K. K., and Schofield, C. J. (2010) Investigating the dependence of the hypoxia-inducible factor hydroxylases (factor inhibiting HIF and prolyl hydroxylase domain 2) on ascorbate and other reducing agents. *Biochem. J.* **427**, 135–142

241. Khan, A., Schofield, C. J., and Claridge, T. D. W. (2020) Reducing Agent-Mediated Nonenzymatic Conversion of 2-Oxoglutarate to Succinate: Implications for Oxygenase Assays. *ChemBioChem*. 10.1002/cbic.202000185

242. Sayers, E. W., Agarwala, R., Bolton, E. E., Brister, J. R., Canese, K., Clark, K., Connor, R., Fiorini, N., Funk, K., Hefferon, T., Holmes, J. B., Kim, S., Kimchi, A., Kitts, P. A., Lathrop, S., Lu, Z., Madden, T. L., Marchler-Bauer, A., Phan, L., Schneider, V. A., Schoch, C. L., Pruitt, K. D., and Ostell, J. (2019) Database resources of the National Center for Biotechnology Information. *Nucleic Acids Res.* **47**, D23–D28

243. Kisselev, L. (2002) Polypeptide Release Factors in Prokaryotes and Eukaryotes: Same Function, Different Structure. *Structure*. **10**, 8–9

244. Lind, C., Oliveira, A., and Åqvist, J. (2017) Origin of the omnipotence of eukaryotic

release factor 1. *Nat. Commun.* **8**, 1425

245. Jones, D. T. (1999) The PSIPRED secondary structure prediction method. *J. Mol. Biol.* **292**, 195–202

246. Guo, Y., Lei, B., Deng, X., Yu, Y., and Lv, H. (2014) Large scale screening of genetic interaction with sgf73(+) in fission yeast. *Yi chuan = Hered.* **36**, 723–731

247. Savitsky, P., Bray, J., Cooper, C. D. O., Marsden, B. D., Mahajan, P., Burgess-Brown, N. A., and Gileadi, O. (2010) High-throughput production of human proteins for crystallization: The SGC experience. *J. Struct. Biol.* **172**, 3–13

248. Myllylä, R., Majamaa, K., Günzler, V., Hanauske-Abel, H. M., and Kivirikko, K. I. (1984) Ascorbate is consumed stoichiometrically in the uncoupled reactions catalyzed by prolyl 4-hydroxylase and lysyl hydroxylase. *J. Biol. Chem.* . **259**, 5403–5405

249. Brammer Basta, L. A., Ghosh, A., Pan, Y., Jakoncic, J., Lloyd, E. P., Townsend, C. A., Lamichhane, G., and Bianchet, M. A. (2015) Loss of a Functionally and Structurally Distinct ld-Transpeptidase, LdtMt5, Compromises Cell Wall Integrity in Mycobacterium tuberculosis. *J. Biol .Chem.* **290**, 25670–85

250. Mehta, S. C., Samanta, M., Chow, D.-C., and Palzkill, T. (2016) Avoiding the Carbapenem Trap: KPC-2 β-lactamase Sequence Requirements for Carbapenem Hydrolysis. *FASEB J.* **30**, 1083.20-1083.20

Chapter 9 Appendix

9.1 Appendix for Chapter 2

Table 32. Chemical shift assignments for the panipenem-derived β-lactone products. The data have been generated by Mr. H. T. Henry Chan. The table is adapted from Aertker, K. M. J. et al. (2020) *J. Biol. Chem.* **295**, 16604–16613.

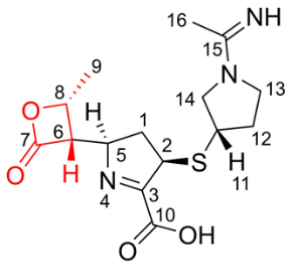

(*R*)-Δ^1

Position	^{13}C (ppm)	^{1}H (ppm)
1	36.4	1.57, 2.84
2	50.0	4.18
3	175.7	
5	66.7	4.42
6	56.5	3.82
7	172.3	
8	73.8	4.93
9	15.1	1.53
11	42.3	3.60
12	31.4	2.33, 1.96
13	154.7	3.42, 3.52
14	53.9	3.77, 3.29
15	163.0	
16	18.4	2.18

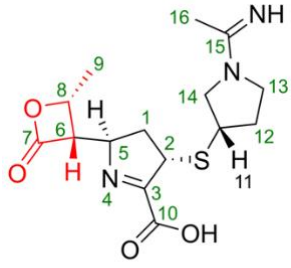

(*S*)-Δ^1

Position	^{1}H (ppm)
1	2.24, 2.25
2	4.26
3	
5	4.59
6	3.81
7	
8	4.93
9	1.54
11	
12	
13	
14	
16	

Previous chemical assignment of (*R*)-Δ^1 imine and (*S*)-Δ^1 imine of imipenem-derived hydrolysis products were used as a reference (167). The ^{13}C chemical assignments were obtained using ^{1}H ^{13}C correlations observed in ^{1}H ^{13}C HSQC and/or ^{1}H ^{13}C HMBC spectra. The chemical shift of C-10 was not observed.

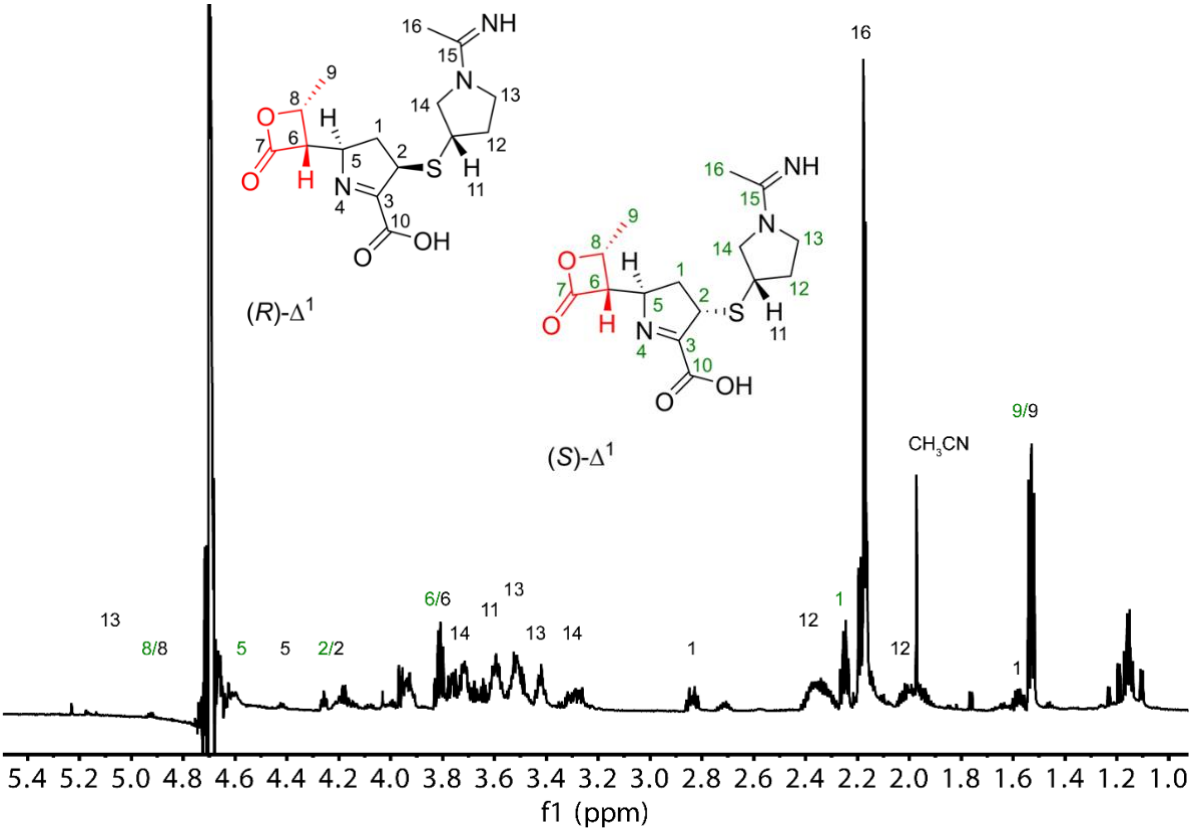

Figure 70. ^{1}H NMR (700 MHz) spectrum of the panipenem-derived β-lactone products. Solvent: 50 mM sodium phosphate buffer pH 7.5, 10% D_2O. Note, the spectrum shows the presence of hydrolysis products, and the (*R*)-Δ^1 imine form and the (*S*)-Δ^1 imine form of the panipenem-derived lactones. The (*R*)-Δ^1 imine form and (*S*)-Δ^1 imine form are present in a similar amount, however, the precise ratio is difficult to analyse due to signal overlap of the two Δ^1 imine forms. The spectrum was generated by Mr. H. T. Henry Chan and is adapted from Aertker, K. M. J. et al. (2020) *J. Biol. Chem.* 295, 16604–16613.

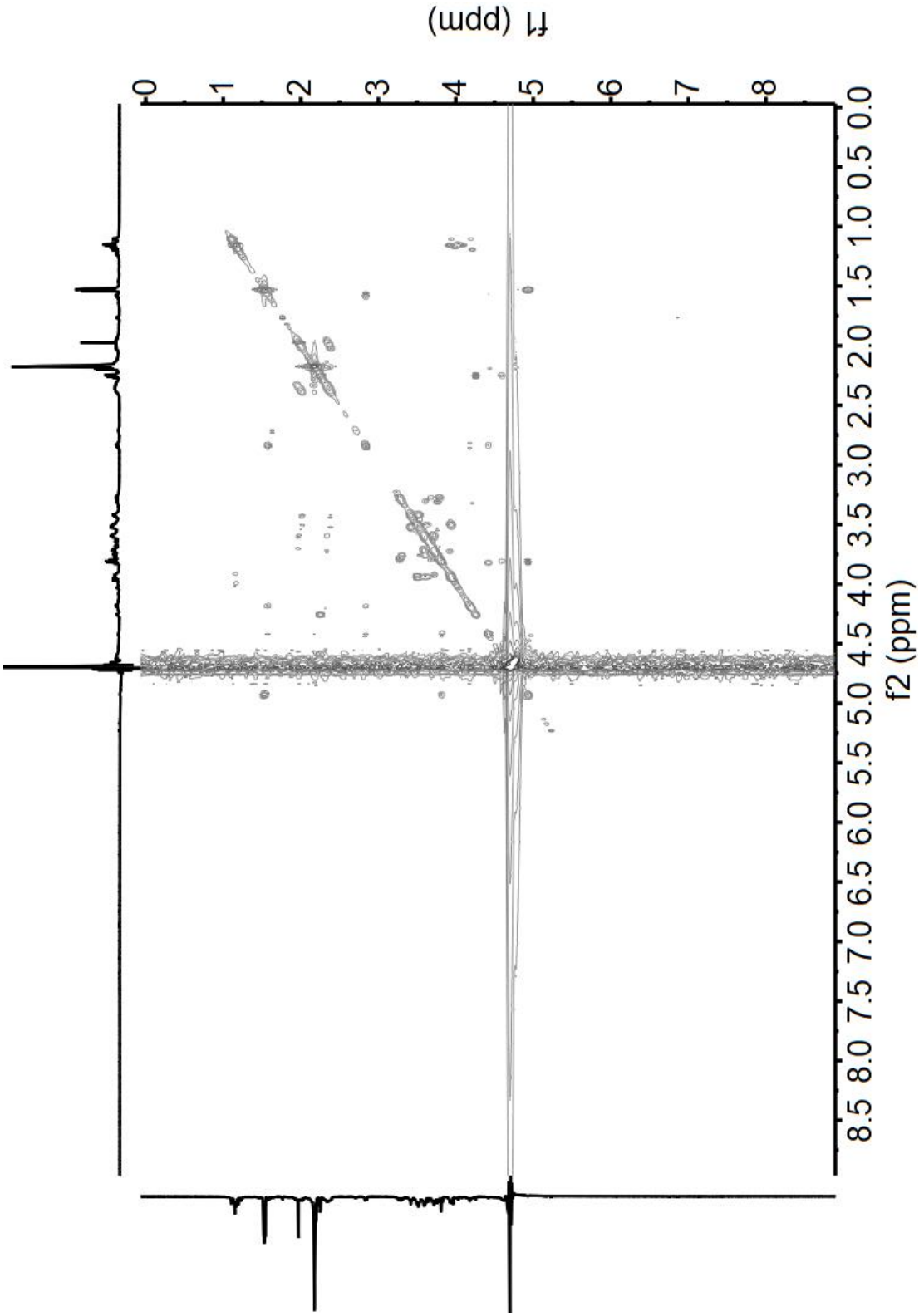

Figure 71. ^{1}H ^{1}H COSY (700 MHz) spectrum of the panipenem-derived β-lactone products. Solvent: 50 mM sodium phosphate buffer pH 7.5, 10% D_2O. The spectrum was generated by Mr. H. T. Henry Chan and is adapted from Aertker, K. M. J. et al. (2020) *J. Biol. Chem.* 295, 16604–16613.

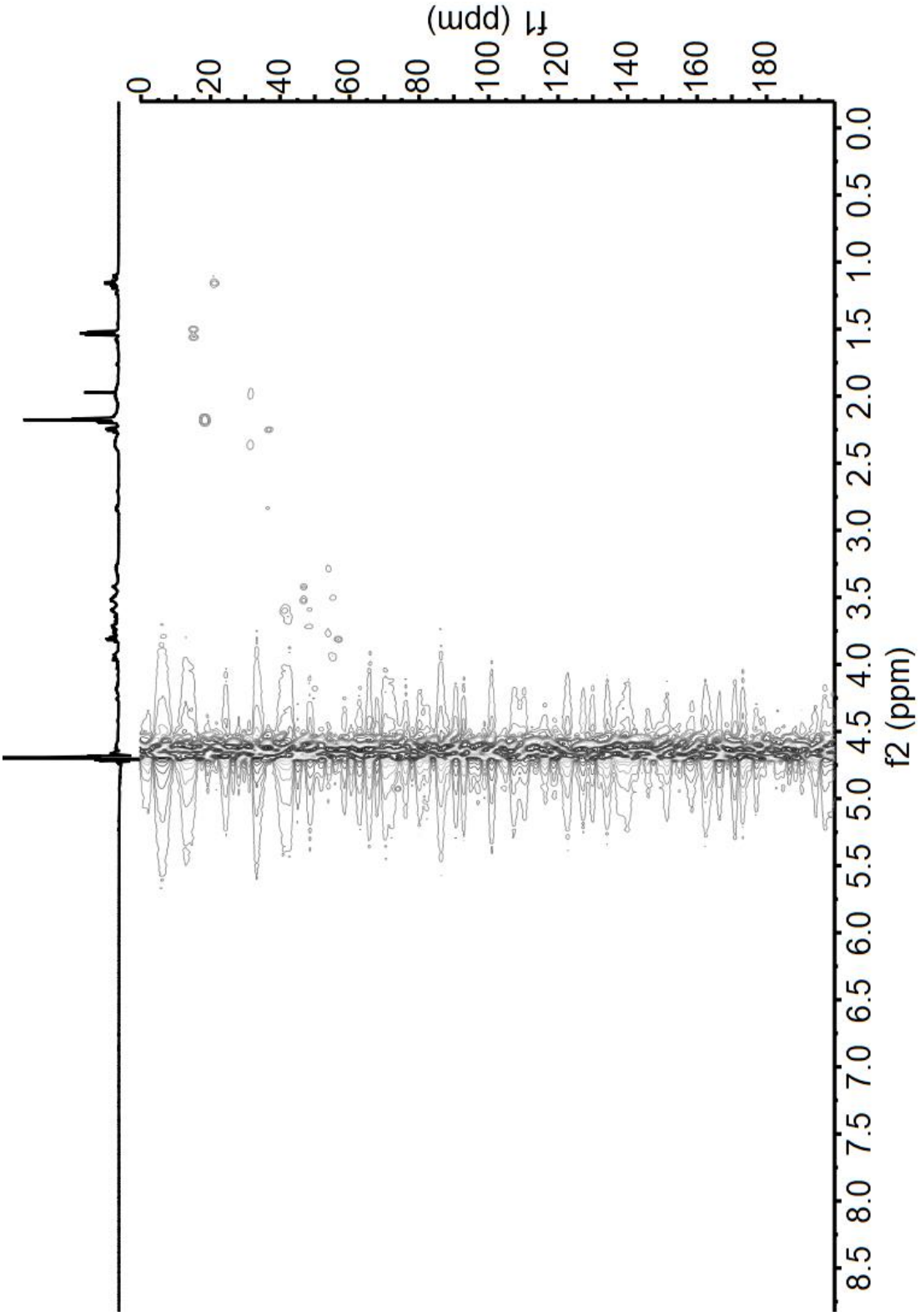

Figure 72. ^{1}H ^{13}C HSQC (700 MHz) spectrum of the panipenem-derived β-lactone products. Solvent: 50 mM sodium phosphate buffer pH 7.5, 10% D_2O. The figure is adapted from Aertker, K. M. J. et al. (2020) *J. Biol. Chem.* 295, 16604–16613.

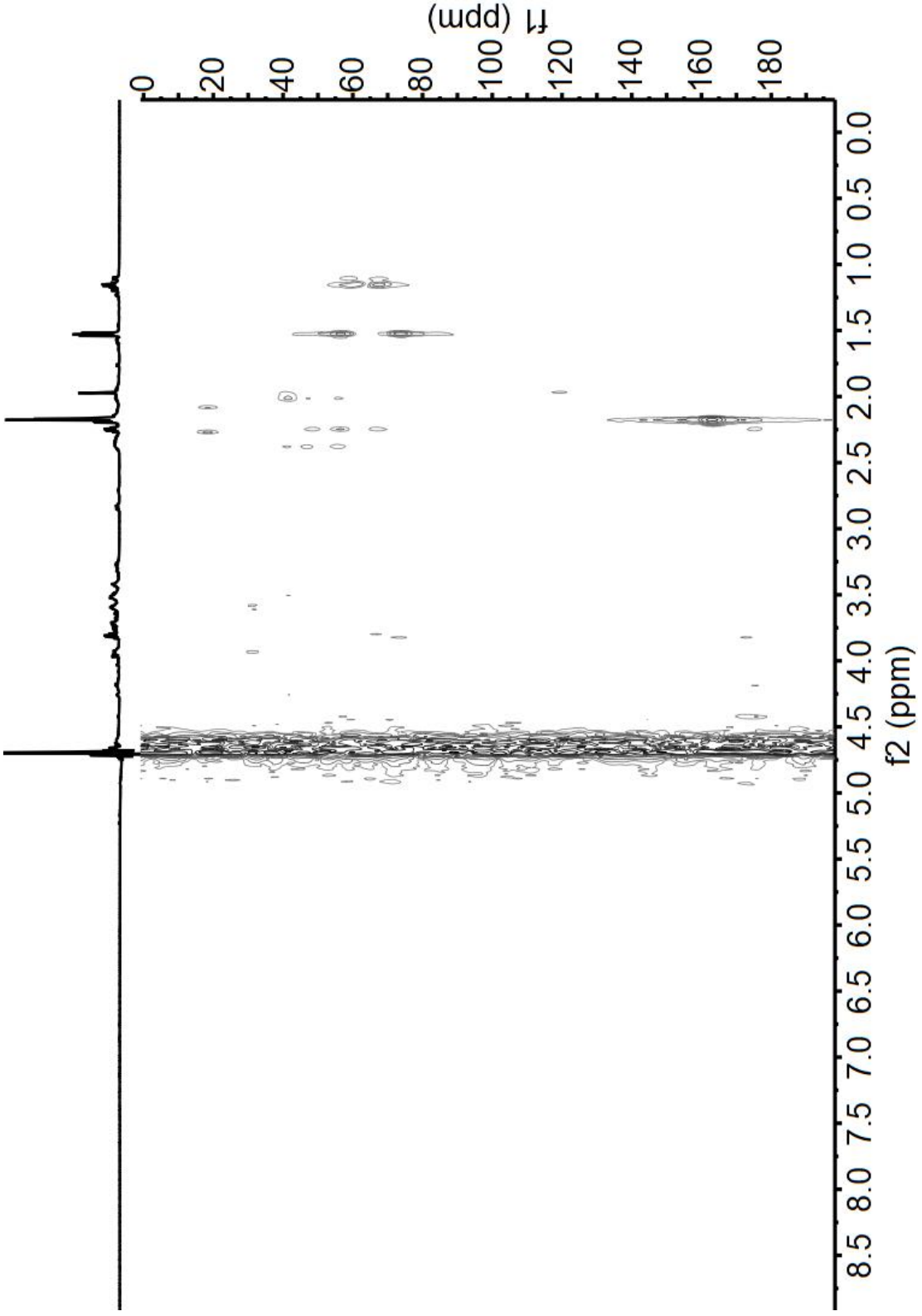

Figure 73. ^{1}H ^{13}C HMBC (700 MHz) spectrum of the panipenem-derived β-lactone products. Solvent: 50 mM sodium phosphate buffer pH 7.5, 10% D_2O. The figure is adapted from Aertker, K. M. J. et al. (2020) *J. Biol. Chem.* 295, 16604–16613.

Table 33. Chemical shift assignments for the imipenem-derived β-lactone products. The data have been generated by Mr. H. T. Henry Chan. The table is adapted from Aertker, K. M. J. et al. (2020) *J. Biol. Chem.* **295**, 16604–16613.

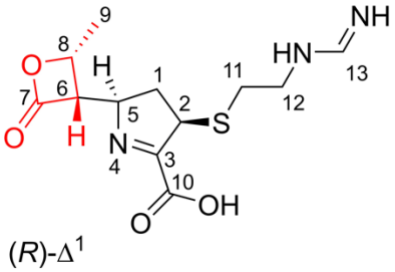

(*R*)-Δ^1

Position	^{13}C (ppm)	^{1}H (ppm)
1	35.5	1.57, 2.82
2	49.6	4.18
3	174.8	
5	66.8	4.45
6	56.6	3.84
7	172.6	
8	73.4	4.94
9	15.1	1.55
11	28.4	2.86
12	40.7	3.50
13	154.7	7.74

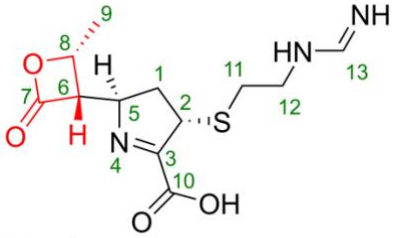

(*S*)-Δ^1

Position	^{1}H (ppm)
1	2.24, 2.25
2	4.26
3	
5	4.59
6	3.82
7	
8	4.93
9	1.56
11	
12	
13	

Previous chemical assignment of (*R*)-Δ^1 imine and (*S*)-Δ^1 imine of imipenem-derived hydrolysis products were used as a reference (167). The ^{13}C chemical assignments were obtained using ^{1}H ^{13}C correlations observed in ^{1}H ^{13}C HSQC and/or ^{1}H ^{13}C HMBC spectra. The chemical shift of C-10 was not observed.

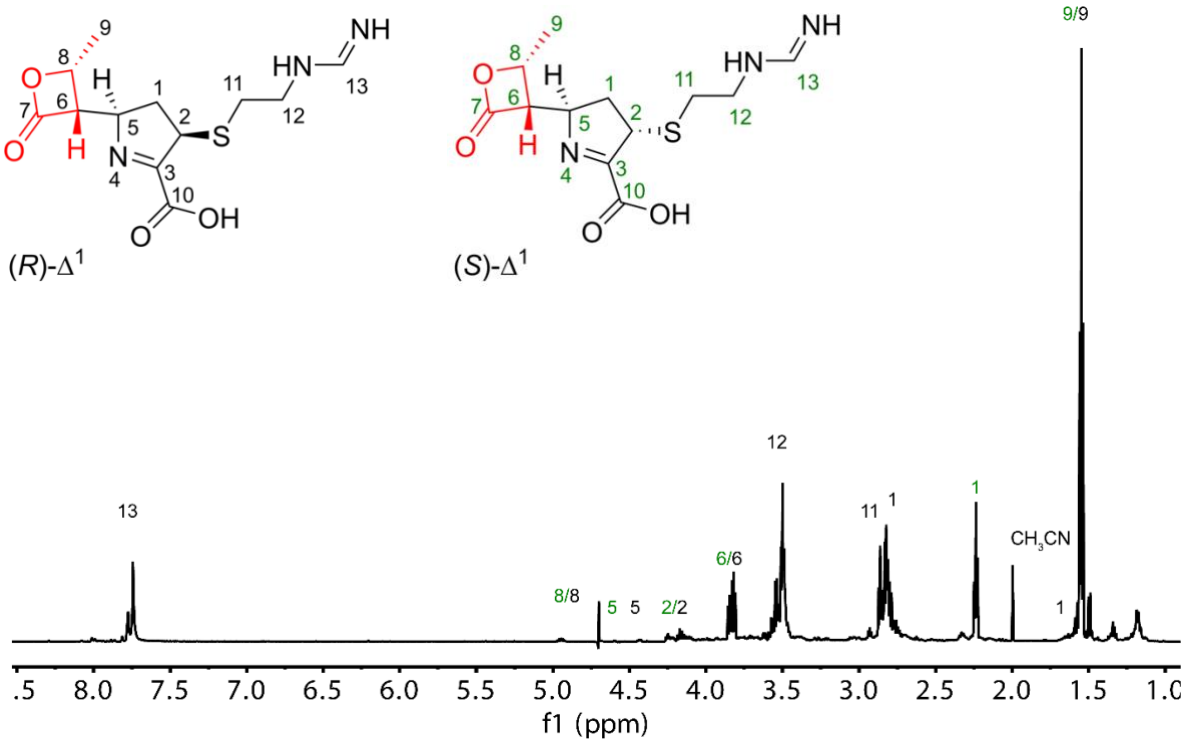

Figure 74. ^{1}H NMR (600 MHz) spectrum of the imipenem-derived β-lactone products. The spectrum shows the presence of the (*R*)-Δ^1 imine form (black numbers) and the (*S*)-Δ^1 imine form (green numbers) of the imipenem-derived β-lactones and small amount of hydrolysis products. The (*R*)-Δ^1 imine form and (*S*)-Δ^1 imine form are present in a similar amount, however, the precise ratio is difficult to analyse due to signal overlap of the two Δ^1 imine forms. The spectrum was generated by Mr. H. T. Henry Chan and is adapted from Aertker, K. M. J. et al. (2020) *J. Biol. Chem.* 295, 16604–16613.

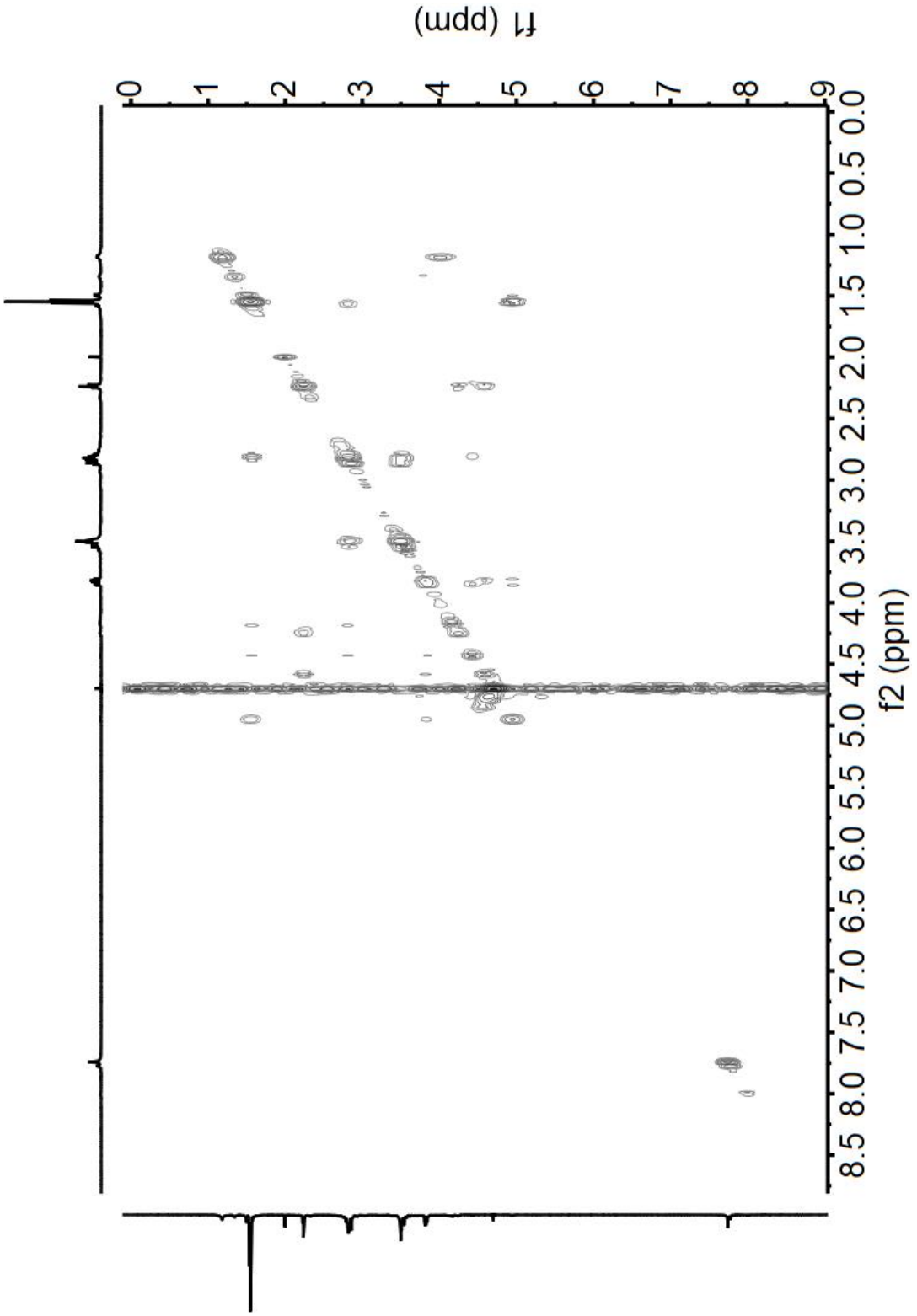

Figure 75. ^{1}H ^{1}H COSY spectrum (600 MHz) of the imipenem-derived β-lactone products. Solvent: 50 mM sodium phosphate pH 7.5, 10% D_2O. The spectrum was generated by Mr. H. T. Henry Chan and is adapted from Aertker, K. M. J. et al. (2020) *J. Biol. Chem.* 295, 16604–16613.

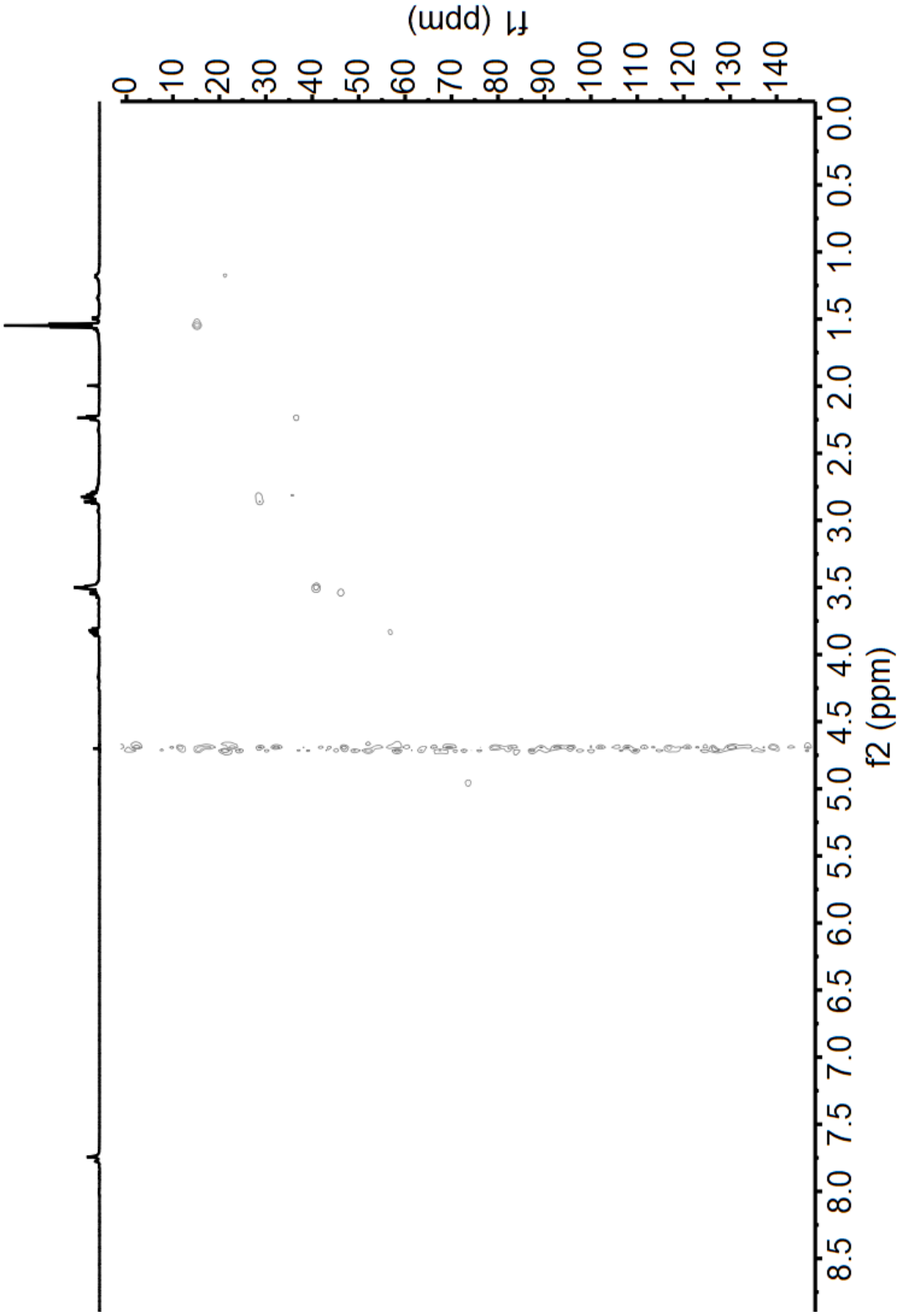

Figure 76. ^{1}H ^{13}C HSQC (600 MHz) spectrum of the imipenem-derived β-lactone products. Solvent: 50 mM sodium phosphate pH 7.5, 10% D_2O. The spectrum was generated by Mr. H. T. Henry Chan and is adapted from Aertker, K. M. J. et al. (2020) *J. Biol. Chem.* 295, 16604–16613.

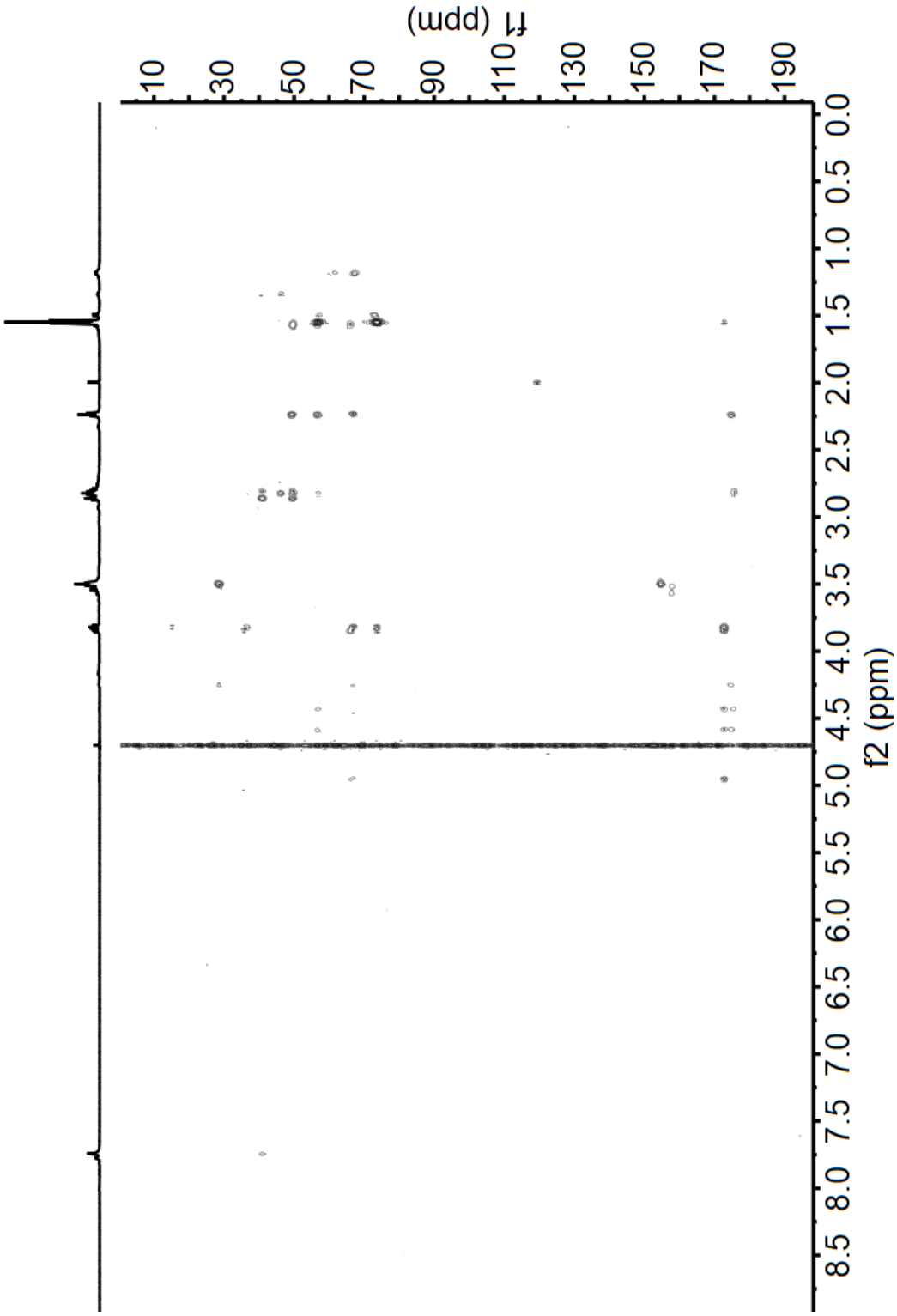

Figure 77. ^{1}H ^{13}C HMBC (600 MHz) spectrum of the imipenem-derived β-lactone products. Solvent: 50 mM sodium phosphate buffer pH 7.5, 10% D_2O. The spectrum was generated by Mr. H. T. Henry Chan and is adapted from Aertker, K. M. J. et al. (2020) *J. Biol. Chem.* 295, 16604–16613.

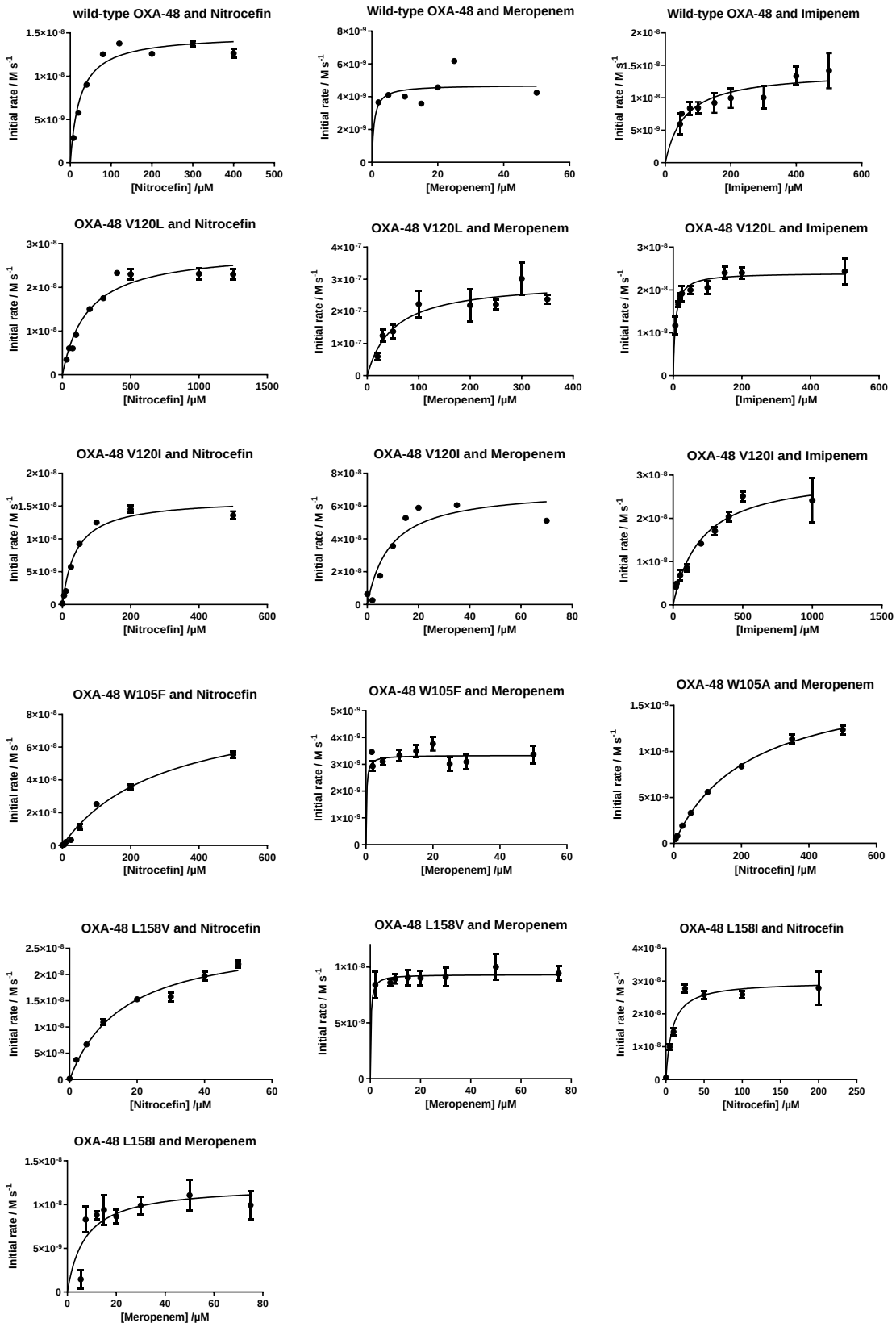

Figure 78. Michaelis-Menten kinetics of wild-type OXA-48 and its variants catalysed degradation of nitrocefin, meropenem and imipenem. Conditions: substrate (varied), enzyme concentration (depending on assay described in the **Material and Methods**, **Section 6.7.1**), 100 mM sodium phosphate pH 7.5, 0.01% Triton X-100. In assay with meropenem or imipenem as substrate 50 mM sodium bicarbonate was added. The data were fitted using the Michaelis Menten type kinetics.

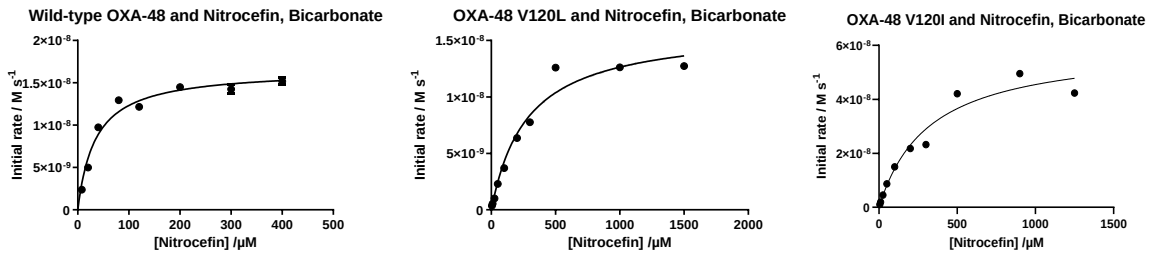

Figure 79. Michaelis-Menten kinetics of wild-type OXA-48 and OXA-48 V120I and V120L catalysed degradation of nitrocefin in presence of sodium bicarbonate. Conditions: substrate (varied), enzyme concentration (depending on assay described in the **Material and Methods**, **Section 6.7.1**), 100 mM sodium phosphate pH 7.5, 0.01% Triton X-100, 50 mM sodium bicarbonate. The data were fitted using the Michaelis Menten type kinetics.

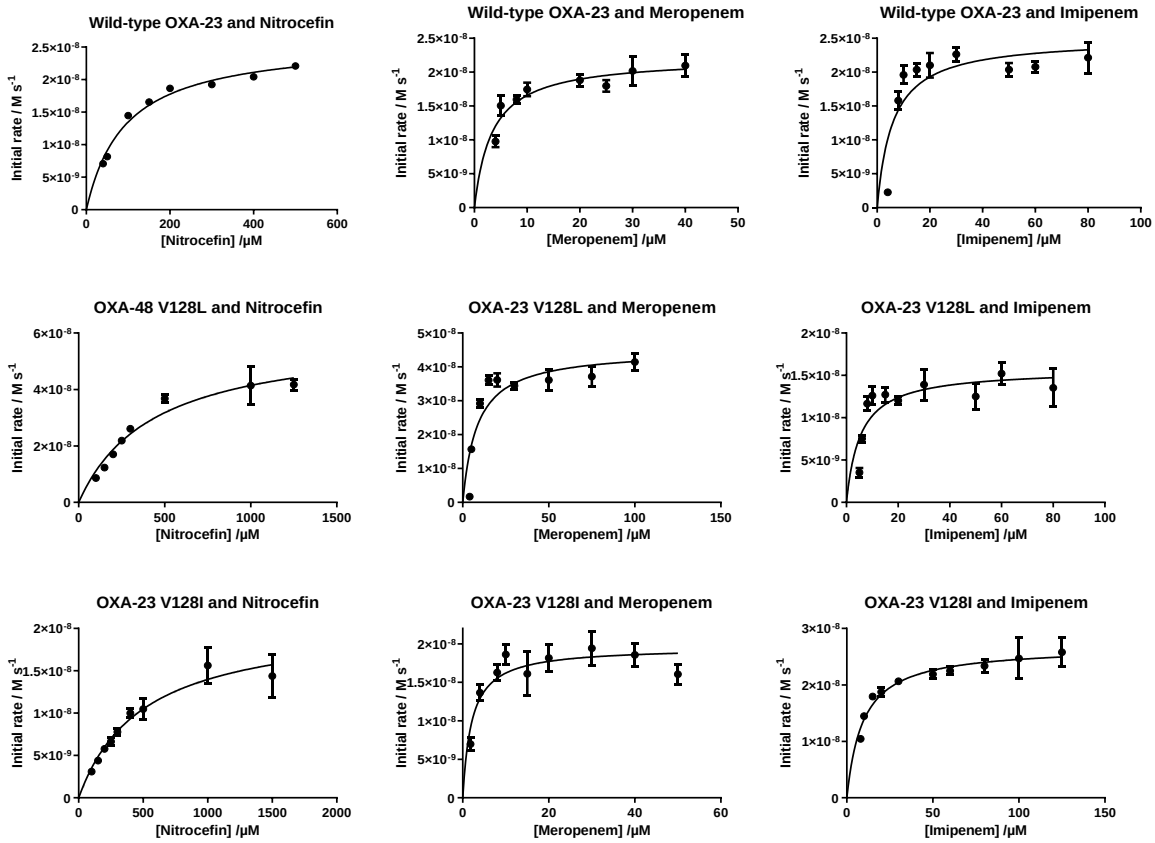

Figure 80. Michaelis-Menten kinetics of wild-type OXA-23 and its variants catalysed degradation of nitrocefin, meropenem and imipenem. Conditions: substrate (varied), enzyme concentration (depending on assay described in the **Material and Methods**, **Section 6.7.1**), 100 mM sodium phosphate pH 7.5, 0.01% Triton X-100. In assay with meropenem or imipenem as substrate 50 mM sodium bicarbonate was added. The data were fitted using the Michaelis Menten type kinetics.

9.2 Appendix for Chapter 3

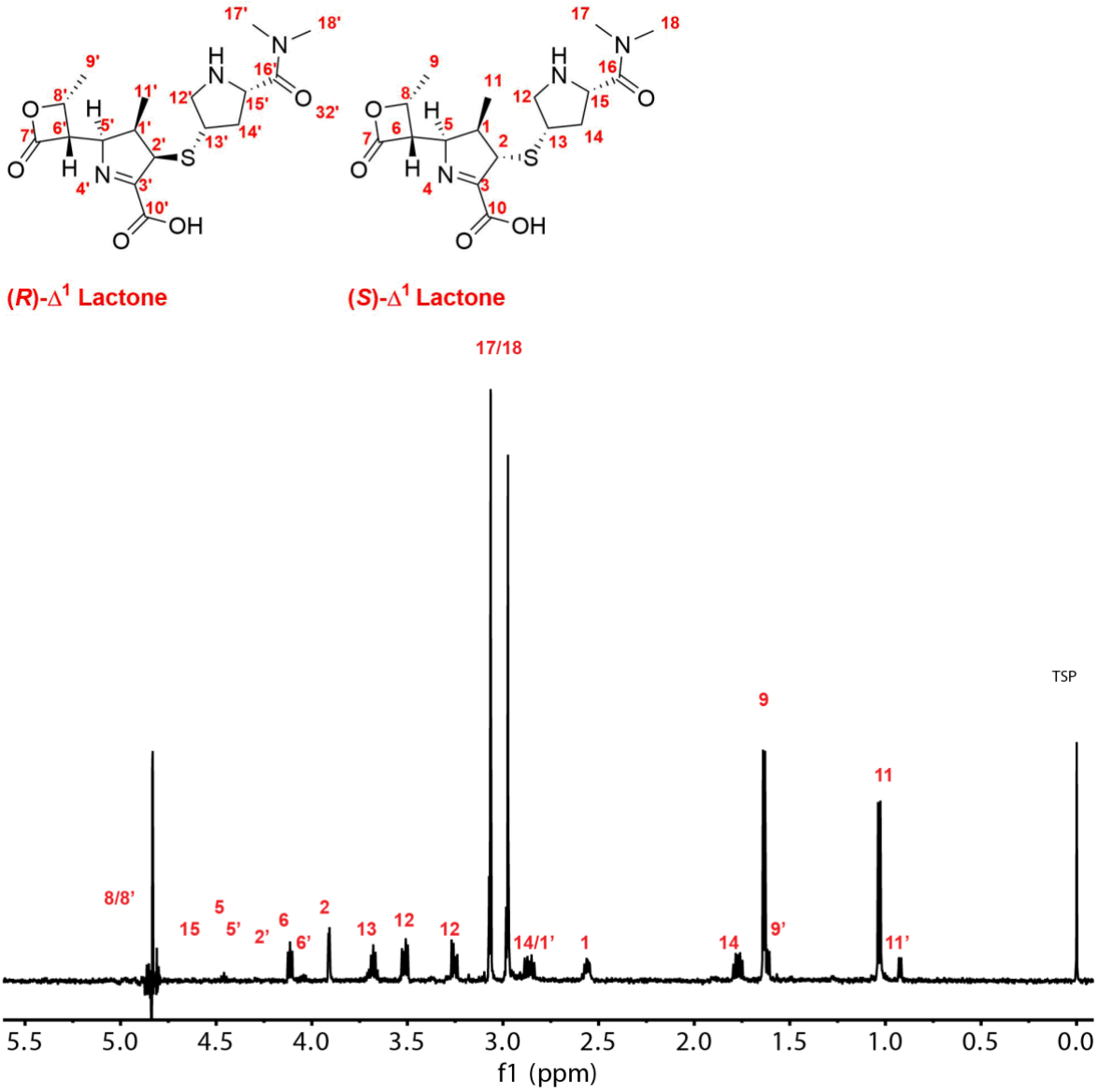

Figure 81. ^{1}H-NMR (600 MHz) spectrum of mero-β-lactones. Deuterated 3-(Trimethylsilyl) propionic-2,2,3,3-d_4 acid sodium salt (TSP) was used as a NMR reference.

TEM-1 and FC-5 (20 min Incubation)

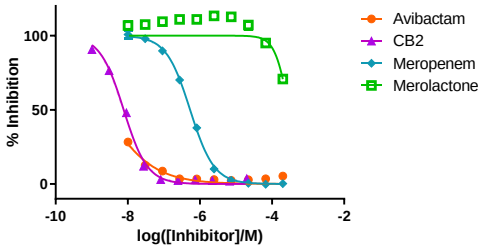

AmpC and FC-5 (20 min Incubation)

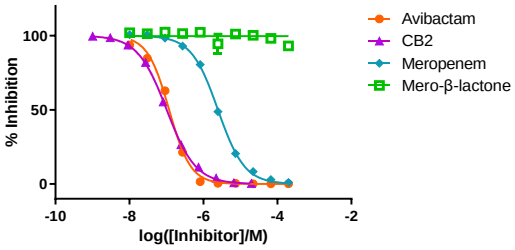

VIM-1 and FC-5 (20 min Incubation)

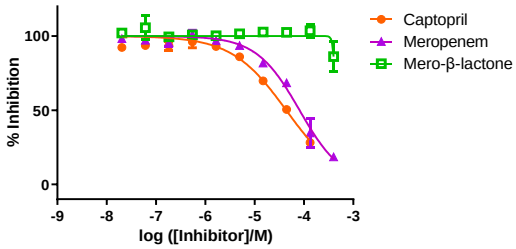

NDM-1 and FC-5 (20 min Incubation)

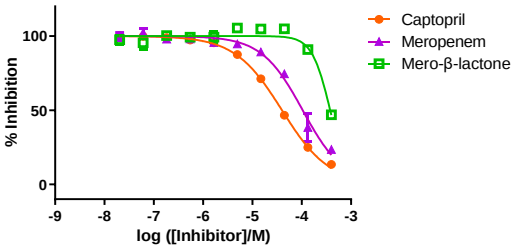

VIM-2 and FC-5 (20 min Incubation)

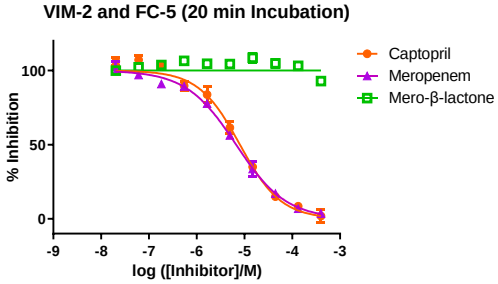

IMP-1 and FC-5 (20 min Incubation)

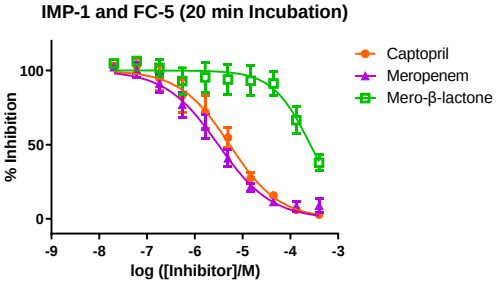

OXA-10 and FC-5 (0 min Incubation)

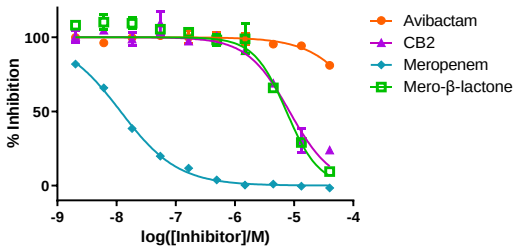

OXA-10 and FC-5 (20 min Incubation)

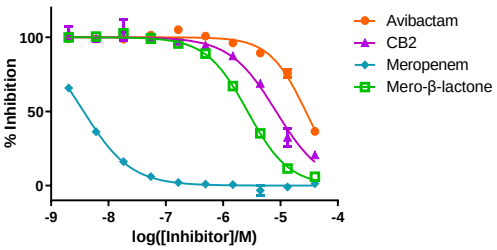

OXA-23 and FC-5 (0 min Incubation)

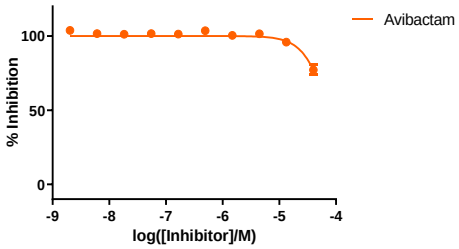

OXA-23 and FC-5 (20 min Incubation)

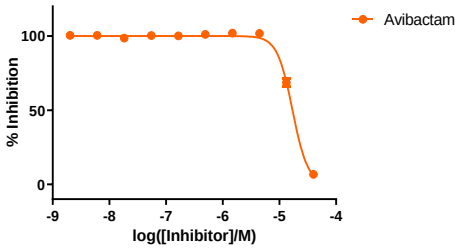

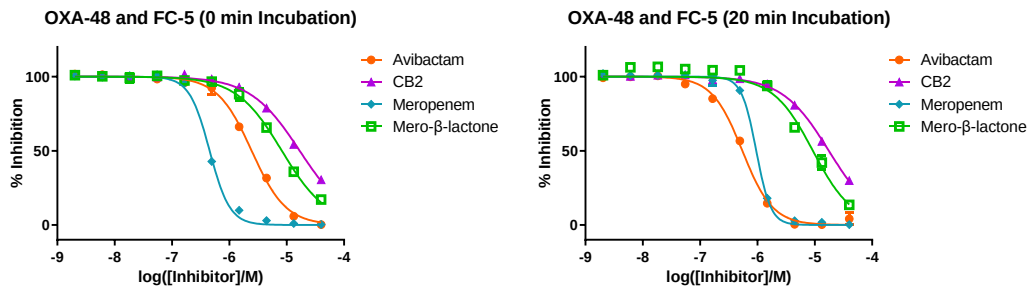

Figure 82. Dose response curves used for determining pIC$_{50}$ values. The pIC$_{50}$ values are given in **Table 7.** The data have been generated by Karina Calvopina Tapia.

Condition 1: 5 µM enzyme, 50 µM inhibitor, and 50 mM sodium phosphate in MQ water, pH 7.5.

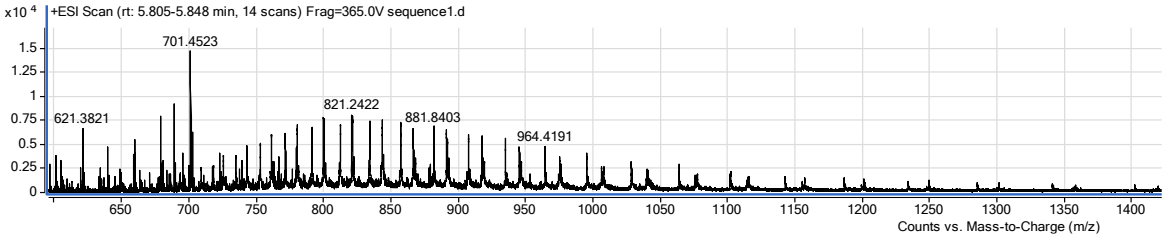

Condition 2: 1 µM enzyme, 10 µM inhibitor, and 50 mM sodium phosphate in MQ water, pH 7.5.

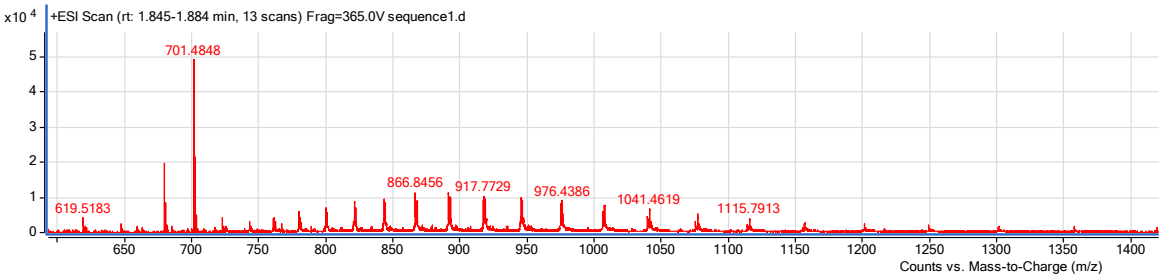

Condition 3: 1 µM enzyme, 10 µM inhibitor, and 50 mM sodium phosphate in HPLC grade water, pH 7.5.

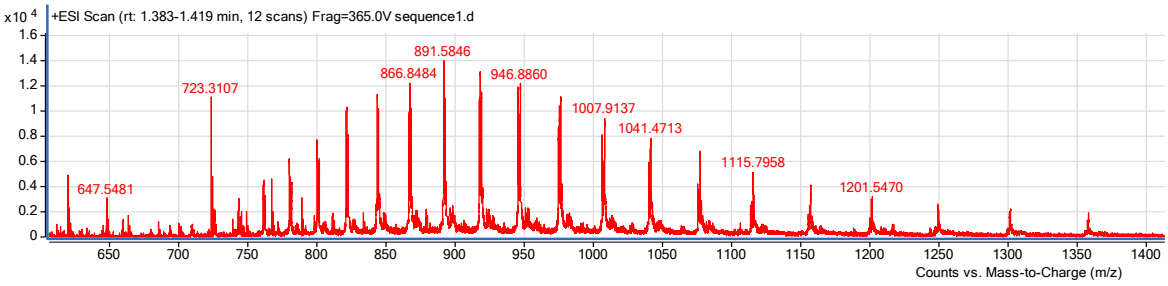

Figure 83. SPE-MS assay conditions. Optimisation of acylation assay conditions.

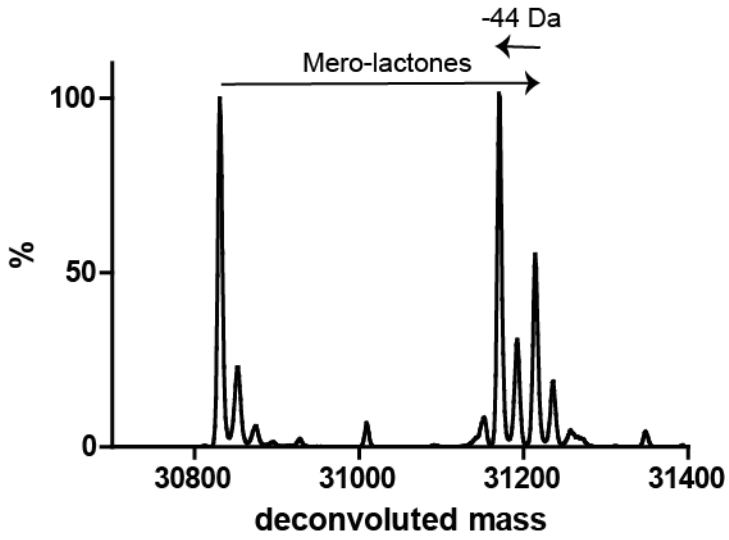

Figure 84. OXA-48 with mero-β-lactones forms AECs. The signal at -44 Da is proposed to correspond to a decarboxylated species caused by QTOF mass spectrometric analysis.

9.3 Appendix for Chapter 4

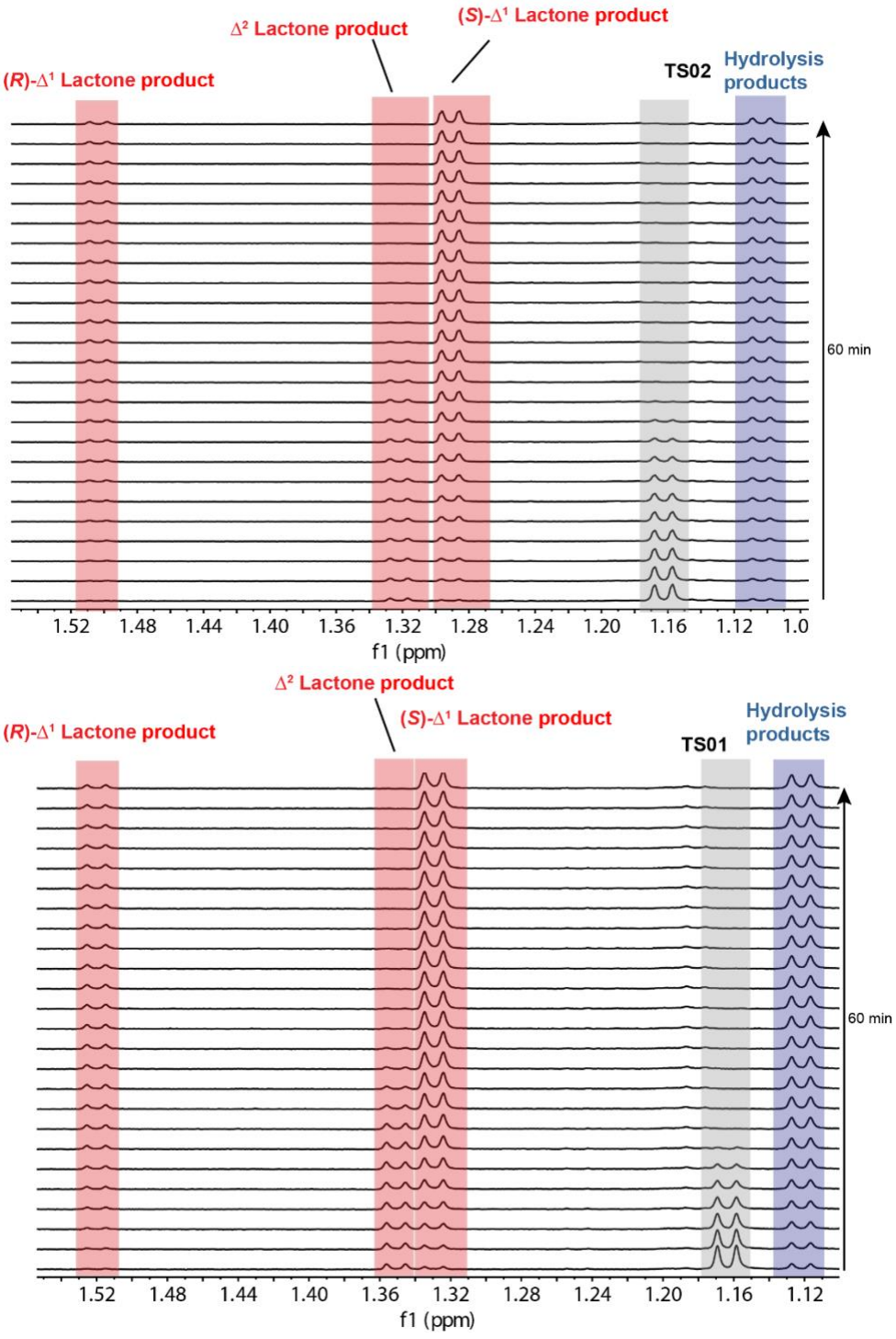

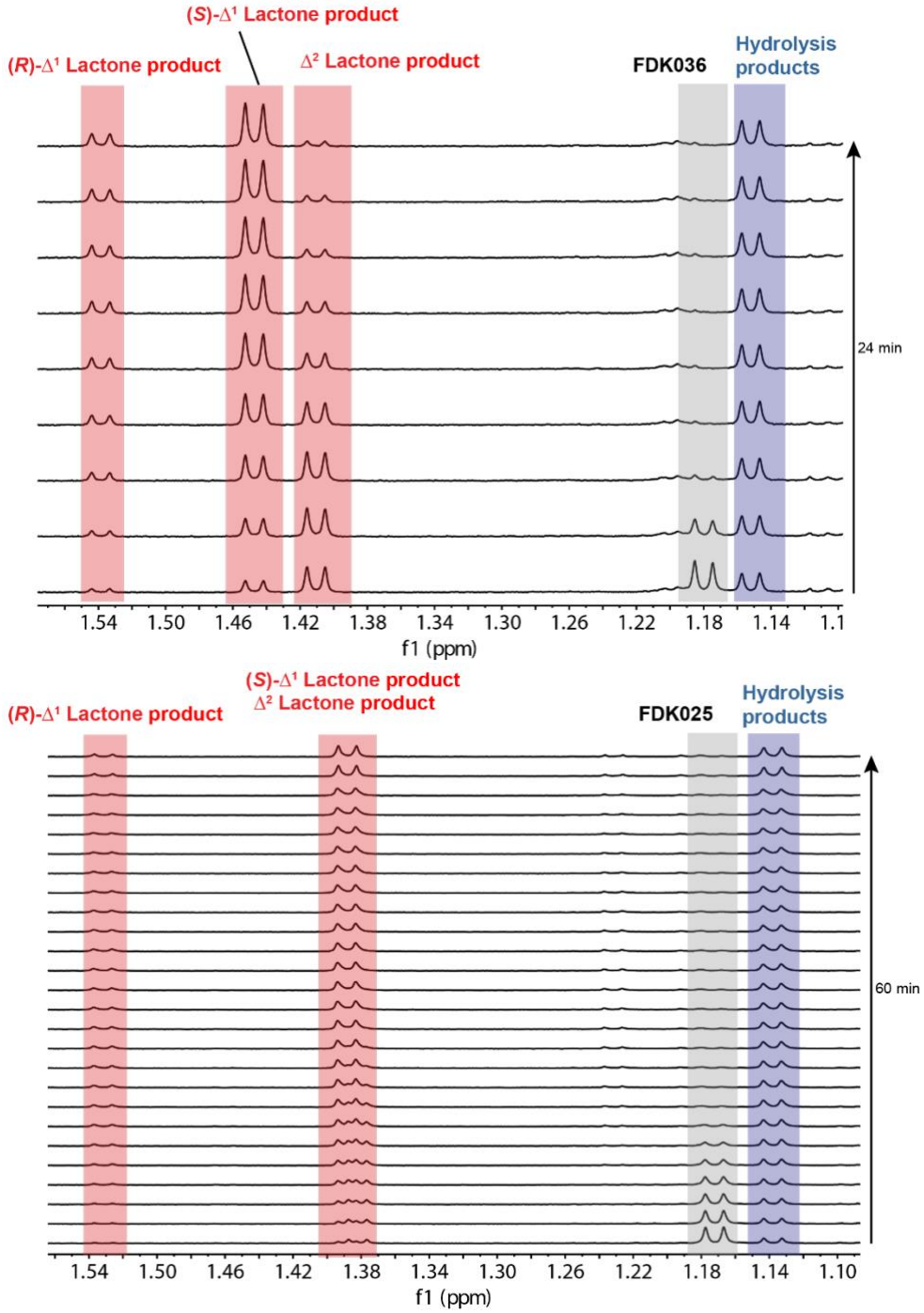
(S)-Δ¹ Lactone product
(R)-Δ¹ Lactone product
Δ² Lactone product
FDK036
Hydrolysis products
24 min
1.54 1.50 1.46 1.42 1.38 1.34 1.30 1.26 1.22 1.18 1.14 1.1
f1 (ppm)
(S)-Δ¹ Lactone product
Δ² Lactone product
(R)-Δ¹ Lactone product
FDK025
Hydrolysis products
60 min
1.54 1.50 1.46 1.42 1.38 1.34 1.30 1.26 1.22 1.18 1.14 1.10
f1 (ppm)

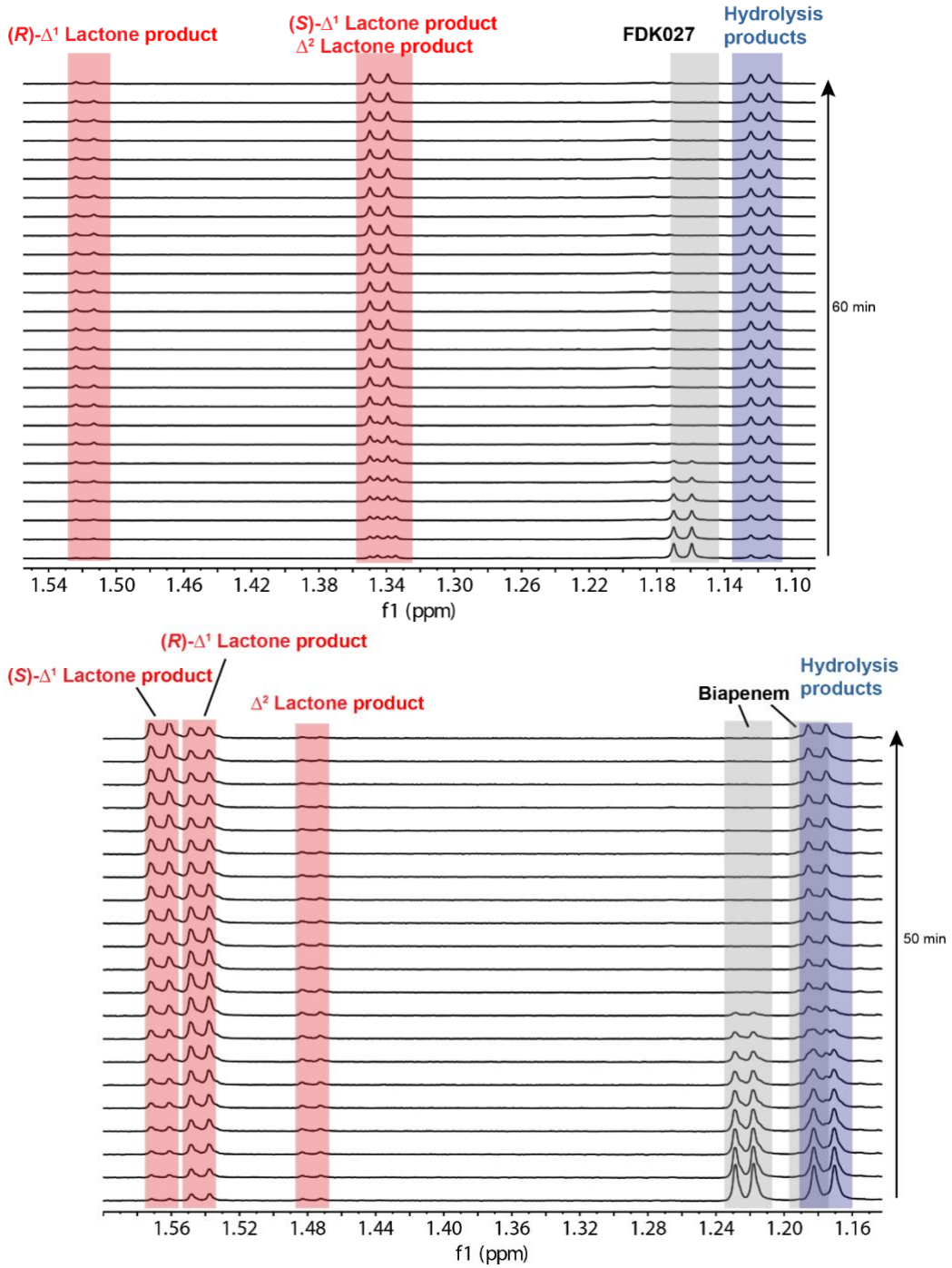

Figure 85. ^{1}H-NMR time courses with wild-type OXA-48 and carbapenem analogues and biapenem. Assay conditions: 1 mM carbapenem analogues, 5 µM wild-type OXA-48, 50 mM sodium phosphate buffer pH 7.5, 10% D_2O. The spectra with **FDK036**, **FDK025**, and **FDK037** have been generated with Ms. Fraula Daka.

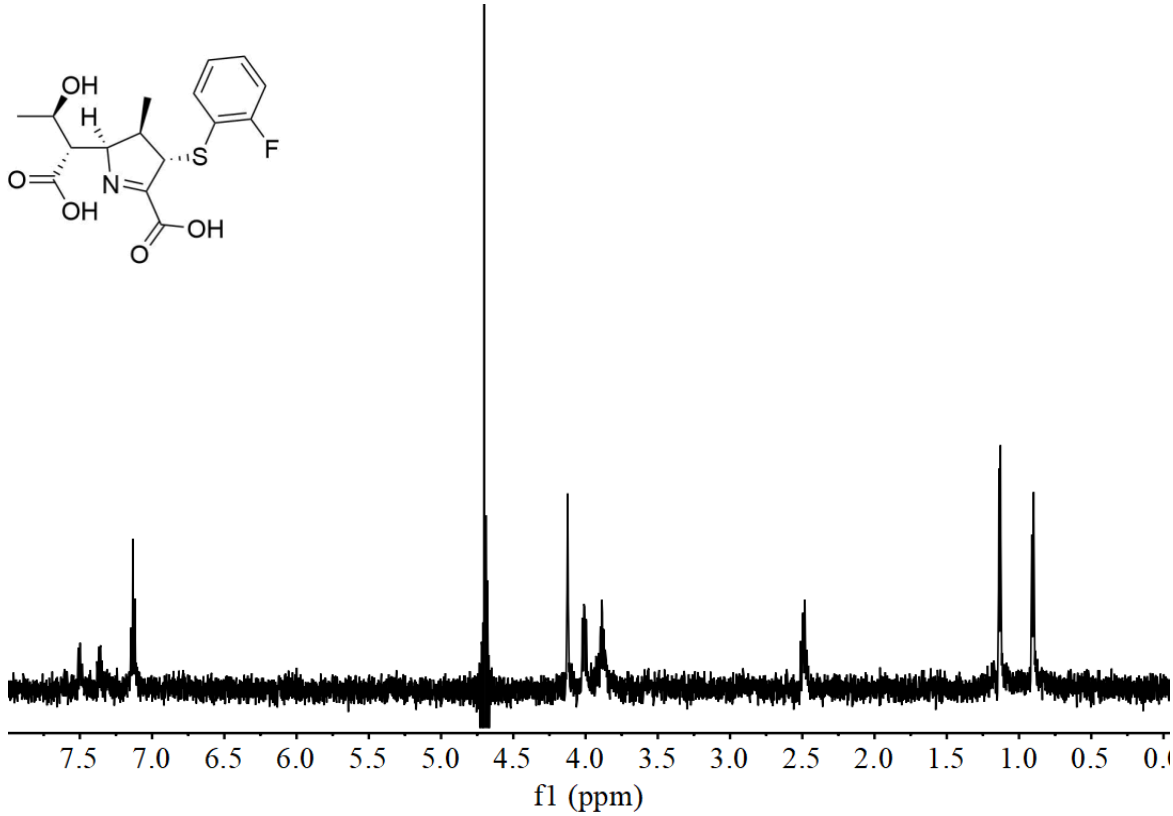

Figure 86. ^{1}H-NMR (600 MHz) spectrum of (*S*)-Δ^{1} imine hydrolysis products of FDK023. The spectrum has been generated with Ms. Fraula Daka.

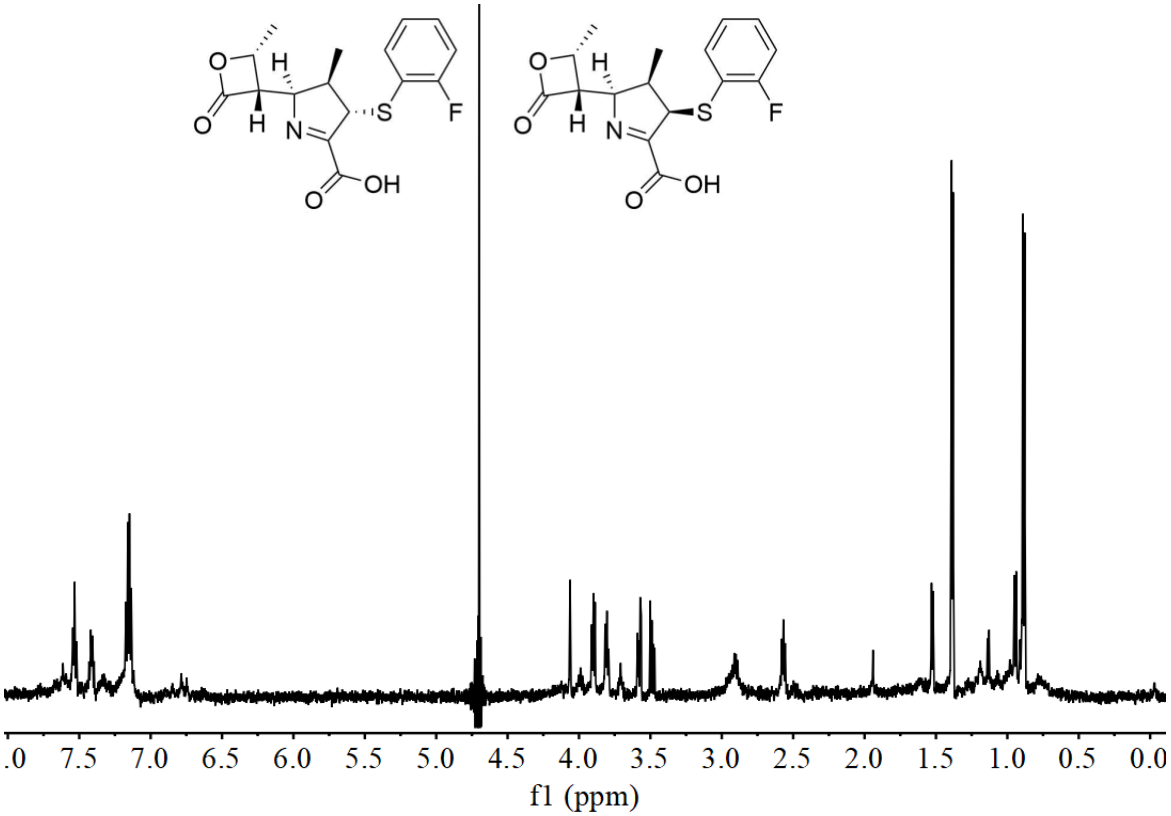

Figure 87. ^{1}H-NMR (600 MHz) spectrum of (*S*)-Δ^{1} and (*R*)-Δ^{1} imine lactones of FDK023. The spectrum has been generated with Ms. Fraula Daka.